Theory of Electrochemical Pattern Formation under Global Coupling

von
Diplom-Physiker
Florian Plenge

Von der Fakultät II – Mathematik und Naturwissenschaften
der Technischen Universität Berlin
zur Erlangung des akademischen Grades

Doktor der Naturwissenschaften
– Dr.rer.nat. –

genehmigte Dissertation

Promotionsausschuss:

Vorsitzender: Prof. Dr. E. Sedlmayr
Berichter: Prof. Dr. K. Krischer
Berichter: Prof. Dr. E. Schöll
Berichter: Prof. Dr. H. Engel

Tag der wissenschaftlichen Aussprache: 10.07.03

Berlin 2003
D 83

Abstract

Pattern formation during electrochemical reactions is a common phenomenon. It is decisively influenced by the control of the reactions via the external applied voltage or current that introduces a global coupling into the system. In this thesis pattern formation under global coupling with different characteristics is investigated by means of analytical and numerical tools in one spatial dimension. Three systems that are representative for almost all known electrochemical oscillators are studied. Moreover, the three systems possess structurally different homogeneous dynamics on which the global coupling acts. Results contributing to the understanding of general mechanisms of self-organization in electrochemical systems are obtained. Furthermore, a realistic model for the electrooxidation of hydrogen in the presence of poisons displaying quantitative agreement with experiments using parameters taken almost exclusively out of the literature is given.

A general expression for the global coupling strength due to the external control as a function of readily accessible parameters is derived. The consequences for the common operation mode of ohmic drop compensation that is shown to introduce a negative global coupling into the system are discussed.

The dynamics of a bistable system subject to a global constraint displays stationary spatial structures (domains) that exhibit an oscillatory instability leading to previously unreported (chaotically) breathing domains. We present novel patterns termed asymmetric standing waves and pulse-like behavior displayed by a two variable system with no-flux boundary conditions in which a desynchronizing global coupling acts on the activator. The response of a relaxation oscillator to negative global coupling is investigated using the hydrogen oxidation in the presence of poisons as the model system. We report the observation of in part novel phenomena, e.g., modulated oscillations, target patterns, asymmetric target patterns and cluster patterns in accordance with experiments.

We present the phase space structure in the vicinity of an unusual point in parameter space. Indications for the existence of a codimension-one bifurcation at which a homogeneous steady state loses stability and simultaneously a homoclinic orbit to this fixed point is present are given. This represents a novel mechanism of a hysteresis-free transition from a homogeneous fixed point to mixed-mode oscillations.

All results are put into the frame of nonlinear dynamics by extensive comparison

with other models, in particular a closely related model describing pattern formation in semiconductors. In part quantitative agreement with experiments is demonstrated for all three systems for the homogeneous as well as the spatially extended systems with and without global coupling.

Thus, the results of this work contribute to the understanding of emergent structures in systems subject to global coupling in general as well as to the detailed understanding of electrochemical self-organization phenomena.

Zusammenfassung

Raum-zeitliche Strukturbildung an Elektrodenoberfl¨achen ist ein weitverbreitetes Ph¨anomen. Die Musterbildung wird entscheidend durch die Kontrolle der Reaktionen mittels der angelegten Spannung oder des angelegten Stroms beeinflusst, die eine globale Kopplung im System bewirken. In der vorliegenden Arbeit wird Strukturbildung in Systemen mit globaler Kopplung verschiedener Auspr¨agung mit Hilfe analytischer und numerischer Methoden in den drei repr¨asentativen Oszillatorklassen untersucht. Diese drei Systeme zeigen unterschiedliche homogene Dynamik, auf die die global Kopplung wirkt. Dadurch werden allgemeine Resultate in Bezug auf den Einfluss globaler Kopplungen in selbstorganisierten Systemen erhalten. Desweiteren wird ein quantitatives Modell zur Beschreibung der Elektrooxidation von Wasserstoff an Platin hergeleitet. Die Modellvorhersagen stimmen quantitativ mit experimentellen Daten ¨uberein, die fast ausschließlich auf Parametern beruhen, die aus unabh¨angigen Messungen stammen.

Ein allgemein g¨ultiger Ausdruck f¨ur die globale Kopplungsst¨arke als Funktion von experimentell gut zug¨anglichen Parametern wird hergeleitet. Die Konsequenzen f¨ur den Operationsmodus, bei dem der Ohm'sche Spannungsabfall im Elektrolyten elektronisch kompensiert wird und der eine negativ-globale Kopplung bedingt, werden diskutiert.

Die Dynamik eines bistabilen Systems mit globaler Kopplung zeigt station¨are r¨aumliche Strukturen (Dom¨anen), die oszillatorisch instabil werden. Dies f¨uhrt zu bisher unbekannten periodisch und chaotisch "atmenden" Dom¨anen. Wir berichten von neuartigen Strukturen, sogenannten asymmetrischen stehenden Wellen und pulsartigem Verhalten, in einem zwei-Variablen System mit von Neumann Randbedingungen, in dem die globale Kopplung auf den Aktivator wirkt. Mithilfe des zuvor hergeleiteten Modells zur Oxidation von Wasserstoff in Anwesenheit von Elektrodengiften wird die Antwort eines Relaxationsoszillators auf desynchronisierende globale Kopplung untersucht. Der Erfolg der Modellierung zeigt sich im Auftreten von zum Teil neuartigen Ph¨anomenen, z.B. modulierten Oszillationen, (asymmetrischen) Zielscheibenmustern und verschiedenen oszillatorischen Dom¨anenmustern, die vorher in Experimenten beobachtet wurden.

Die Phasenraumstruktur in der N¨ahe eines ungew¨ohnlichen Punktes im Parameterraum wird untersucht. Hinweise auf die Existenz einer Kodimension-eins Bifurkation, an der ein homogener station¨arer Zustand instabil wird und gleichzeitig ein zu diesem

Punkt homokliner Orbit existiert, werden dargestellt. Damit wird ein neuer Mechanismus aufgedeckt, der ohne Hysterese von einem Fixpunkt zu komplexer raum-zeitlicher Dynamik f¨uhrt.

Alle Ergebnisse werden durch ausf¨uhrliche Vergleiche mit anderen selbstorganisierenden Systemen in einen gr¨oßeren Zusammenhang gestellt. Besonders hervorzuheben ist die enge Korrespondenz vieler Resultate zu einem dynamischen System, das zur Beschreibung von Halbleitern hergeleitet wurde. Zum Teil quantitative Übereinstimmung von Ergebnissen aus allen drei betrachteten Oszillatorklassen bez¨uglich der homogenen und der raum-zeitlichen Dynamik, sowohl ohne als auch mit globaler Kopplung, mit experimentellen Daten wird demonstriert.

Somit tr¨agt diese Arbeit sowohl zum allgemeinen Verst¨andnis von Selbstorganisationsph¨anomenen unter dem Einfluss globaler Kopplungen als auch zum detaillierten Verst¨andnis raum-zeitlicher Strukturen in der Elektrochemie bei.

Contents

1 Introduction **1**

2 Background **5**

2.1 Foundations of Electrochemistry 5

2.1.1 The Electrochemical Cell and the Double Layer Potential 5

2.1.2 Kinetics of Electrode Reactions 8

2.2 Homogeneous Dynamics 11

2.2.1 (Hidden) N-shaped Negative Differential Resistance ((H)N-NDR) Systems 12

2.2.2 S-shaped Negative Differential Resistance (S-NDR) Systems . . . 14

2.3 Migration Coupling 16

2.3.1 General Formulation 16

2.3.2 Ring Geometry and Fourier Mode Decomposition 19

2.3.3 Accelerated Fronts and Turing Patterns 23

2.4 Global Coupling Induced by the Control Mode 25

2.4.1 External Resistor and Galvanostatic Operation Mode 29

2.4.2 Close Reference Electrode 30

2.5 Detailed Description of the Model Systems 32

2.5.1 A Prototype N-NDR System – Peroxodisulfate Reduction 32

2.5.2 A Prototype S-NDR System – Periodate Reduction in the Presence of Camphor 34

2.5.3 A Prototype HN-NDR System – Hydrogen Oxidation in the Presence of Poisons 37

2.6 Methods 40

2.6.1 Spatial Discretization - Pseudo Spectral Method 40

2.6.2 Integration 43

2.6.3 Continuation 44

3 Pattern Formation in the Presence of Ohmic Drop Compensation **45**

3.1 General Equation for the Double Layer Dynamics 46

3.2 Discussion . . . 47
3.3 Conclusions . . . 48

4 S-NDR Systems – Breathing Domains and Turing Patterns 49
4.1 Stationary and Breathing Domains . . . 50
4.1.1 Introduction . . . 50
4.1.2 Model . . . 51
4.1.3 Stability Analysis and Simulations . . . 54
4.1.4 Comparison with a Semiconductor Model and Discussion . . . 67
4.1.5 Conclusions . . . 71
4.2 Turing Patterns Revisited . . . 72
4.2.1 Spatially Varying Double Layer Capacity . . . 74
4.2.2 Modeling Attractive Lateral Adsorbate Interactions . . . 75
4.2.3 Discussion . . . 78
4.2.4 Conclusions . . . 78

5 N-NDR Systems – Prototype Oscillator under Negative Global Coupling 81
5.1 Spatio-temporal Dynamics . . . 85
5.1.1 Bifurcation Analysis and Simulations . . . 85
5.1.2 Discussion and Conclusions . . . 90
5.2 Subcritical Bifurcations to a Homoclinic Saddle-Focus . . . 93
5.2.1 Electrochemical System . . . 93
5.2.2 Semiconductor System . . . 98
5.2.3 Discussion and Conclusions . . . 102

6 HN-NDR Systems – Pattern Formation during Hydrogen Oxidation 105
6.1 Realistic Model and Homogeneous Dynamics . . . 107
6.1.1 Model . . . 107
6.1.2 Results . . . 110
6.1.3 Conclusions . . . 117
6.2 Pattern Formation under Desynchronizing Global Coupling . . . 118
6.2.1 Overview of Observed Patterns . . . 121
6.2.2 Pulses and Anti-phase Oscillations . . . 123
6.2.3 Modulated Oscillations and Target Patterns . . . 124
6.2.4 Asymmetric Target Patterns . . . 128
6.2.5 Cluster Patterns . . . 129
6.2.6 Discussion . . . 131
6.2.7 Conclusions . . . 136

7 Summary and Outlook 137

A Appendix **143**
A.1 Non-dimensionalization 143
A.1.1 N-NDR Model 143
A.1.2 S-NDR Model 144
A.1.3 HN-NDR Model 146
A.2 The Jacobian in Pseudo Spectral Space - An Explicit Example 146

List of Abbreviations **151**

Bibliography **153**

Chapter 1

Introduction

The spontaneous formation of patterns in time and space is a fascinating phenomenon displayed by many systems in our environment. The basic mechanisms of self-organization in complex nonlinear systems were revealed only recently. The emergence of nonlinear dynamics was motivated by several key observations made in various quite different systems during the last century. Spatio-temporal self-organization phenomena in such diverse fields as fluid dynamics, chemistry, laser physics and biology were reported [1–8]. It was discovered almost simultaneously that also low dimensional dynamics can lead to complex motion today know as chaos [9–11]. Both phenomena stimulated the development of unifying concepts for the description of systems far from thermodynamic equilibrium.

It was realized that the second law of thermodynamics that counteracts pattern formation in closed systems does not forbid the spontaneous emergence of sustained structures in open, dissipative, systems that are able to export entropy into their environment [3]. Haken emphasized the mean field approach motivated by the 'enslavement' of photoemission in lasers by the electric field generated by the very same emissions. The concept that the dynamics of individual elements does not have to be considered if a coarse grained mean field variable can be introduced that enslaves the individual elements reduces the dimension of the dynamics to be considered enormously [2].

Thus, a common mathematical framework was established. The similarities in the experimental observations are due to the fact that pattern formation far from thermodynamic equilibrium is governed by nonlinear evolution equations of the mean field variables. Amplitude equations that are valid regardless of the specific system of interest in the vicinity of qualitative changes in the dynamics, so called bifurcations, emphasize the general nature of the mechanisms in effect [4, 6].

A prominent subclass of the systems considered in nonlinear dynamics are so called reaction-diffusion systems. They are described by evolution equations of the form

$$\dot{\boldsymbol{u}} = \boldsymbol{f}(\boldsymbol{u}) + \boldsymbol{D}\boldsymbol{\Delta}\boldsymbol{x}.$$

The evolution of the state vector $\boldsymbol{u}$ in time can be divided in a 'local' term $\boldsymbol{f}(\boldsymbol{u})$ that is called the 'reaction' part of the dynamics and a term modeling the spatial transport mechanism that usually is given by diffusion.

Common phenomena described by such equations are homogeneously catalyzed chemical reactions, most prominently the Belousov-Zhabotinsky (BZ) reaction [12], as well as heterogeneously catalyzed reactions in the gas phase [13]. Reaction-diffusion equations are used to model scroll waves in the heart [14] and pattern formation in semiconductors [15]. Turing introduced reaction-diffusion equations to describe morphogenesis [7, 16]. The most significant patterns displayed are homogeneous oscillations, chaos, stationary spatially periodic patterns, spirals, traveling waves, target patterns, and turbulence [5].

Surprisingly, electrochemical systems never played a key role in the development of nonlinear dynamics although first reports of oscillations in electrochemistry date back to 1828 [17]. Several authors published the observation of waves during electro-dissolution of Fe at the beginning of the 20^{th} century [18, 19]. Lillie and Ostwald already speculated about a connection of these waves with the waves in nerve cells which is now well established [20, 21]. Indeed, the necessary conditions for pattern formation, i.e., a system far from thermodynamic equilibrium and appropriate positive feedback mechanisms, are realized during almost all electrochemical reactions. Yet, it was not until the 1990's that the common origin of oscillatory behavior observed earlier in many electrochemical systems [22, 23] could be clarified [24, 25]. It turned out that the interplay of the electric control circuit with the reaction dynamics at the solid-liquid interface is responsible for most positive feedback mechanisms in electrochemistry.

The decisive variable for the dynamics of the electric circuit is the voltage drop over the solid-liquid interface, the so called *double layer potential*. If an external voltage is applied the double layer potential drives electrochemical reaction(s) that result in a *reaction current*. The functional dependence of the reaction current on the double layer potential, the so called *current-potential characteristic*, is determined by the specific reaction under consideration. The positive feedback loop in electrochemical systems is caused by the interaction of the electric control circuit and a region of *negative differential resistance* (NDR) of some form in the current-potential characteristic [26].

Based on the (electro-)chemical nature of the activatory and inhibitory variables and their interplay electrochemical oscillators can be divided into two classes. In the first class the positive feedback mechanism is due to an N-shaped current potential characteristic (N-NDR). In some cases the N-shape is (partially) hidden due to a different interplay of the (electro-)chemical variables (HN-NDR) [27]. In systems displaying an S-shaped current-potential characteristic (S-NDR) the positive feedback mechanism is not of genuine electrochemical nature.

Spatio-temporal pattern formation in electrochemistry was investigated systematically

only recently due to the development of suitable experimental techniques [28–32]. An exception is the above mentioned electro-dissolution of metals since the passivating oxide waves are visible with the naked eye. Electrochemical evolution equations taking the spatial degree of freedom into account were derived simultaneously [31, 33–38]. In electrochemical systems one variable typically is of electrical nature and the associated transport mechanism is migration rather than diffusion. Local perturbations in the double layer potential are mediated through the electric field in the liquid phase. Thus, spatial inhomogeneities in the double layer potential are felt not only by its nearest neighbors but by a whole range of neighboring sites which makes the coupling nonlocal [36, 39, 40]. Still, the equations are of the reaction-diffusion type in a broader sense since the dynamics can be described by a local function and a spatial coupling term. Furthermore, it was demonstrated that, depending on the operation mode, global coupling is present in the system [36, 41–46].

Over the last decade global coupling has been an active area of research. Global coupling is present in systems that are subject to external control, e.g., via an electric circuit (such as in electrochemical, semiconductor [15, 47–53] and gas discharge [54] systems) or via the electric control of the temperature in catalytic reactors [55–60]. But global coupling may also be due to transport processes that take place on time scales much faster than all other relevant time scales in the system, e.g., fast mixing in the gas phase [61–66]. A variety of other systems are described by dynamics that include global coupling, e.g., ferromagnetic [67], biological [68], and chemical systems in which the global coupling can be light induced [69]. Abstract theoretical models are discussed, e.g., in [70–73]. Furthermore, methods for the control of complex dynamics often employ global feedback mechanisms [74–81].

It is shown in chapter 3 of this contribution that global coupling is routinely present in electrochemical experiments. Additionally, the character of the global coupling, whether it has a tendency to stabilize or destabilize the dynamics, can be chosen freely. Also the strength of the global coupling can be readily varied since it is introduced by the external control circuit. Furthermore, the global coupling may act on the activator as well as on the inhibitor depending on the electrochemical reaction under consideration. Thus, electrochemical systems present a suitable model system to investigate the influence of different global couplings on pattern formation. Additionally, the interplay of global and nonlocal coupling can be studied as theoretically discussed in [73]. It is demonstrated in this contribution that the modeling of electrochemical pattern formation is capable of quantitative predictions and thus compelling tests of the proposed mechanisms are feasible.

Hence, the aim of this work is twofold. The theory of general mechanisms of nonlinear dynamics in electrochemistry focusing on patterns induced by global coupling as well as realistic modeling of electrochemical systems is discussed. The dynamics in one spa-

tial dimension employing different boundary conditions of systems displaying S-NDR, N-NDR and HN-NDR current-potential characteristics subject to global coupling is presented in this work. Paradigmic reactions out of the respective class of systems are investigated. Additionally, results contributing to the understanding of the mechanisms governing these reactions and the respective modeling are given. The theoretical data are compared with experiments where possible.

The interdisciplinary nature of nonlinear dynamics is emphasized by a close connection of part of the presented results with dynamical systems used to describe self-organization phenomena in semiconductors [15]. The similarities and the generalizations suggested by this correspondence are explored in the respective chapters.

The detailed outline of this thesis is as follows. In the next chapter a description of the background of this work is given. After the introduction of the main concepts of electrochemistry, the homogeneous dynamics of the main classes of oscillators is discussed. The peculiarities of the migration coupling and earlier results concerning the origin of global coupling in electrochemistry and its consequences are explained. Finally, the model systems studied in this work and the methods for these studies are presented.

In Chapter 3 the stability of uniform electrode states in the presence of ohmic drop compensation is considered. An alternative, explicit formulation of the global coupling term governing the evolution of the double layer potential in terms of experimentally easily measurable quantities is derived. The result has far reaching implications. It is demonstrated that any electronic drop compensation introduces a negative global coupling (NGC) into the system that potentially destabilizes homogeneous potential distributions.

The dynamics of an S-NDR oscillator is explored in chapter 4. In the first part pattern formation under a previously not discussed form of global coupling arising due to a high electrolyte conductivity is investigated and compared with results obtained earlier in a closely related semiconductor system [49, 52, 82–84]. Mechanisms of oscillatory instabilities of inhomogeneous stationary structures are the main focus in this section. Conditions for the occurrence of stationary periodic patterns in S-NDR systems given earlier [85] are reevaluated using a more realistic approach in the second part.

A prototype N-NDR model subject to desynchronizing global coupling is studied in chapter 5. An overview of the patterns induced by the global coupling as well as the underlying mechanisms are given in section 5.1. Section 5.2 explores an unusual bifurcation point encountered in the N-NDR dynamics again in close connection with the dynamics in semiconductors.

A realistic model for the hydrogen oxidation in the presence of poisons is derived in chapter 6. Spatio-temporal pattern formation of this HN-NDR system on a one dimensional ring under negative global coupling is investigated. Herewith, the instabilities of a relaxation oscillator under negative global coupling are elaborated. Finally, the results given in this thesis are summarized in chapter 7. The appendix compiles calculations of technical nature.

Chapter 2

Background

This chapter summarizes the foundations of electrochemical pattern formation as well as the methods employed to study such dynamics. It is assumed that the reader is familiar with the common terminology and phenomena of nonlinear dynamics and pattern formation. The necessary background is compiled in a huge number of excellent textbooks, e.g., Refs. [2–6, 8, 86–88].

The first section gives an introduction into electrochemistry focusing on the control conditions in effect in electrochemical cells and the kinetics governing electrode reactions. A more detailed picture can be found, e.g., in Refs. [89–92]. In the next three sections pattern formation in electrochemistry is reviewed. After introducing the prototype systems displaying dynamic instabilities and their homogeneous dynamics, the peculiarities of spatial couplings in electrochemical systems are outlined. Similar and more extensive reviews can be found in Refs. [25, 26, 93–95]. Section 2.5 introduces earlier results on the model systems investigated in this work. Finally, the methods used to study the dynamical systems are presented in section 2.6.

2.1 Foundations of Electrochemistry

2.1.1 The Electrochemical Cell and the Double Layer Potential

The schematic setup of a typical electrochemical cell is pictured in the upper part of Fig. 2.1. A constant voltage, U, is applied between working electrode (WE) and reference electrode (RE). Current is flowing between WE and counter electrode (CE). In this way the applied voltage or current can be controlled in a well defined manner via a potentiostat or galvanostat, respectively. In the following it is assumed that U is fixed at a certain value (potentiostatic control mode). It was shown that the galvanostatic mode can be modeled by a limiting case of the potentiostatic one (s.b.). The RE can be positioned freely in the cell. The distance between the WE and the CE is denoted by w. The WE defines $z = 0$

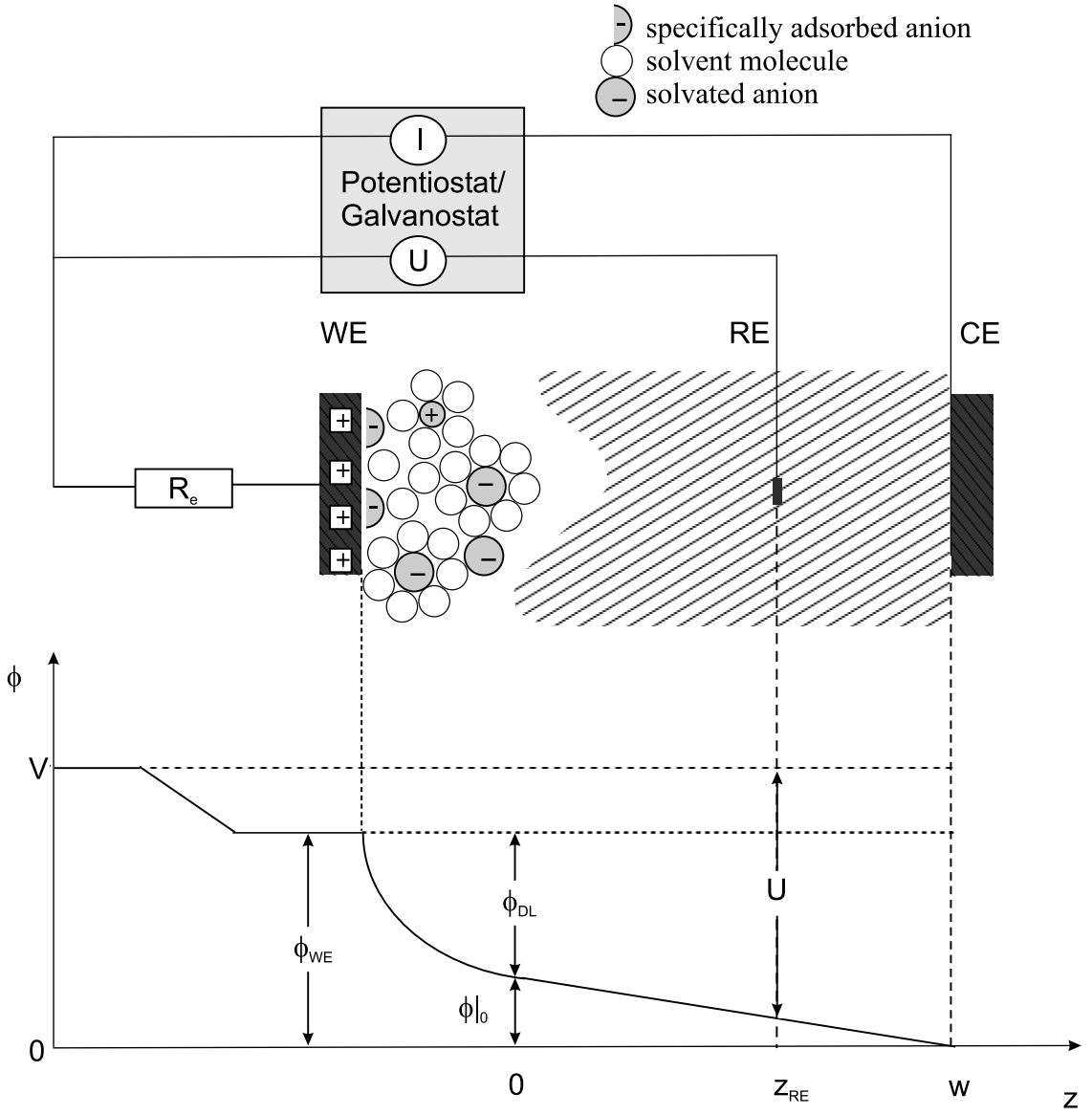

Figure 2.1: *Upper part: Schematic setup of an electrochemical system. Lower part: Definition of the different voltage drops (see text). z-axis not to scale. The potentiostat/galvanostat either fixes the voltage U between WE and RE or the current, I, between WE and CE.*

and the position of the RE is given by z_{RE}. All electrodes are taken to be point like in this section (spatially extended electrodes are discussed in section 2.3).

The so called migration current, I_m, is transported by the ions in the aqueous solution containing a conducting electrolyte. In addition one or more reacting species are present in the solution such that electron transfer through the phase boundaries WE|electrolyte|CE can take place, i.e., a reaction current I_r flows.

These phase boundaries can be well described by a capacitor. At a given potential hydrated ions will accumulate in front of the WE and will cause an equal excess charge in the metal. This structure is called the *electric double layer* and its capacitance per unit area is denoted by C_{DL}. The charge layer in the metal is of only $< 0.1\mathring{A}$ thickness. The solution side of the double layer can extend up to some 10 nm and can be thought of being made of various layers. The most common model defines two layers: The inner Helmholtz layer is given by the distance of specifically adsorbed ions to the metal surface. The outer Helmholtz layer is defined by the distance of the solvated ions to the WE. A diffuse layer connects the outer plane to the bulk solution. The thickness of the diffuse layer depends on the concentration of the solution. The intricate processes taking place in the double layer are not considered in this work. The double layer is assumed to be of zero thickness and is described by a capacitor with fixed specific capacity C_{DL} (see definition of I_C on page 8) in space and time (exceptions: sections 4.2.1 and 4.2.2).

The voltage drop over the double layer, denoted by ϕ_{DL}, cf. the lower part of Fig. 2.1, is the main driving force of all electrochemical processes and thus the central variable in electrochemistry. A significant portion of the applied potential is compensated by ϕ_{DL}. Similar processes take place at the phase boundary electrolyte|CE but are considered irrelevant for the dynamics. (I.e., a constant potential drop is assumed.) This is achieved experimentally by choosing suitable materials and reactions at the CE. In the following the potential in the electrolyte is denoted by ϕ and the electrolyte potential in front of the CE is set to $\phi = 0$. Introducing an optional external resistor, R_e, into the circuit the potential drop of interest is, cf. the lower part of Fig. 2.1,

$$V = IR_e + \phi_{\mathrm{DL}} + \phi|_0. \tag{2.1}$$

I denotes the total current. The potential drop in the bulk electrolyte is due to the finite conductivity σ of the solution. The total cell resistance, R_Ω, between WE and CE is given by $R_\Omega = w/\sigma$ for a one dimensional (1d) electrolyte. The resistance between WE and RE is denoted by $R_u = \sigma/z_{RE}$. With

$$U = V - \phi|_{z_{RE}} \tag{2.2}$$

the potential of the metal WE, ϕ_{WE}, is

$$\phi_{WE} = \phi_{\mathrm{DL}} + \phi|_0 = U + \phi|_{z_{RE}} - IR_e. \tag{2.3}$$

The potential at the RE can be expressed by

$$\phi|_{z_{RE}} = \sigma^{-1} z_{RE} R_\Omega \phi|_0 = R_\Omega^{-1} \left(R_\Omega - R_u\right) \phi|_0 \tag{2.4}$$

and $I = I_m$.

The equation governing the dynamics of the double layer potential can be derived considering Kirchhoffs Law [24]

$$I_m = I_r\left(\phi_{\mathrm{DL}}\right) + I_C. \tag{2.5}$$

The capacitive current, I_C, is given by

$$I_C = C_{DL} A \dot{\phi}_{\mathrm{DL}}, \tag{2.6}$$

where A denotes the surface area of the WE. The migration current is given by Ohm's Law

$$I_m = R_\Omega^{-1} \phi|_0. \tag{2.7}$$

Thus, the time evolution of $\phi_{\mathrm{DL}}$is

$$C_{DL} A \dot{\phi}_{\mathrm{DL}} = -I_r(\phi_{\mathrm{DL}}) + R_\Omega^{-1} \phi|_0$$

with

$$\begin{aligned} \phi|_0 &= U + \phi|_{z_{RE}} - IR_e - \phi_{\mathrm{DL}} \\ &= U - \phi_{\mathrm{DL}} + \phi|_0 \left[R_\Omega^{-1} (R_\Omega - R_u) - R_\Omega^{-1} R_e \right] \\ \Leftrightarrow \qquad \phi|_0 &= \left[1 + R_\Omega^{-1} (R_e - R_\Omega + R_u) \right]^{-1} (U - \phi_{\mathrm{DL}}) \end{aligned} \tag{2.8}$$

and it follows

$$C_{DL} A \dot{\phi}_{\mathrm{DL}} = -I_r(\phi_{\mathrm{DL}}) + (R_u + R_e)^{-1} (U - \phi_{\mathrm{DL}}). \tag{2.9}$$

The slope of the load line is thus given by the total effective resistance, R, of the circuit, $R = R_u + R_e$. The temporal dynamics in the case of galvanostatic control can be written as

$$C_{DL} A \dot{\phi}_{\mathrm{DL}} = -I_r(\phi_{\mathrm{DL}}) + I_0 \tag{2.10}$$

where I_0 denotes the applied current set by the galvanostat. This is formally identical to the potentiostatic case (Eq. (2.9)) in the limit of $R_e \to \infty$ and $U = R_e I_0$.

The functional dependence of the reaction current on the double layer potential, the so called current-potential characteristic, is determined by the specific reaction under consideration. The basic current-potential curves are introduced in the following sections.

2.1.2 Kinetics of Electrode Reactions

Any electrochemical reaction involving continuous current flow is governed by Faraday's Law. The electron transfer causes oxidation or reduction of the reactants in the electrolyte. The reaction rate is given by

$$v = A_{ox} c_{ox} k_{ox} - A_{red} c_{red} k_{red}.$$

c_{red} and c_{ox} are the concentrations of the species to be reduced and oxidized, respectively; A_{ox} and A_{red} are the areas available for oxidation and reduction, respectively. k_{ox} and

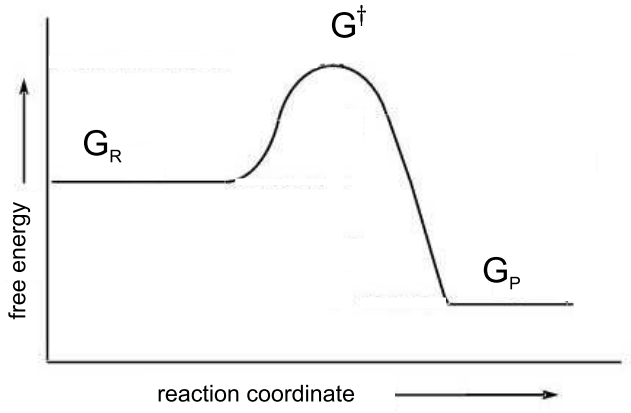

Figure 2.2: *Illustration of transition state theory. G_R, $G^\dagger$, and G_P denote the standard free energy of the reactant, the activated complex, and the product, respectively. The standard free energy landscape is traveled along the reaction coordinate during reaction and the activation energy $\Delta G = G^\dagger - G_R$ has to be overcome.*

k_{red} denote the rate functions of oxidation and reduction, respectively. The reaction rate v gives rise to a reaction current $I_r = nFv$. n denotes the number of transferred electrons per reaction and F denotes Faraday's constant. We use the convention that oxidation currents are positive.

A common ansatz to determine the dependence of the rate functions on ϕ_{DL} (and potentially other variables) is the *transition state theory*. Since this theory can be applied in a more general context of the transition from one state to another (e.g., adsorption of molecules at the electrode interface) we will speak more generally of reactants and products rather than of reduced and oxidized species,

$$R \underset{k_{PR}}{\overset{k_{RP}}{\rightleftharpoons}} P.$$

It is assumed that the reaction takes place along some reaction coordinate and that it proceeds through a well known transition state, called *activated complex* (see Fig. 2.2). Reactant, activated complex, and product are assigned standard free energies denoted by G_R, $G^\dagger$, and G_P, respectively. Now, G_P depends on ϕ_{DL} (and potentially other variables) and thus, also $G^\dagger$ depends on ϕ_{DL} weighted with the so called asymmetry parameter (or transfer coefficient), most often denoted by α. α normally varies between 0.3 and 0.7 and can be well approximated by 0.5 in most cases. With these assumptions and the

introduction of $G_P^0 = G_P(\phi_{DL} = 0)$ and $G_0^\dagger = G^\dagger(\phi_{DL} = 0)$ we can write

$$G_P = G_P^0 + G_P(\phi_{DL}) \tag{2.11}$$

$$G^\dagger = G_0^\dagger + G^\dagger(\phi_{DL}) \tag{2.12}$$

$$G^\dagger(\phi_{DL}) = \alpha G_P(\phi_{DL}). \tag{2.13}$$

The rate functions are related to the standard free energies via Arrhenius Law

$$k_x = k_x^{0'} e^{-\Delta G/RT}. \tag{2.14}$$

Using Eqs. (2.11 - 2.14) and lumping parts independent of ϕ_{DL} into the rate constants (which then depend on temperature) the rate functions can be written as

$$\begin{aligned} k_{RP} &= k_R^{0'} \exp\left(-\frac{G^\dagger - G_R}{RT}\right) \\ k_{PR} &= k_P^{0'} \exp\left(-\frac{G^\dagger - G_P}{RT}\right) \\ \Leftrightarrow v_{RP} &= c_R k_R^0 A_R \exp\left(-\alpha\frac{G_P}{RT}\right) \qquad (2.15) \\ v_{PR} &= c_P k_P^0 A_P \exp\left((1-\alpha)\frac{G_P}{RT}\right). \qquad (2.16) \end{aligned}$$

Considering a simple one step electron transfer reaction, $A^x \rightleftharpoons A^{x+1} + e^-$, the activation energy depends only on the so called overpotential $\phi_{DL} - \phi_{DL}^0$. The equilibrium potential, ϕ_{DL}^0, is defined as the potential at which no net current is flowing, $I_r(\phi_{DL}^0) = 0$.

Expanding the activation energy in a Taylor series around the equilibrium potential and keeping only first order terms, the Butler-Volmer equation is derived

$$I_r = nF\left[c_{ox} k_0^{ox} A_{ox} e^{-\alpha f(\phi_{DL} - \phi_{DL}^0)} - c_{red} k_0^{red} A_{red} e^{(1-\alpha) f(\phi_{DL} - \phi_{DL}^0)}\right] \tag{2.17}$$

with $f := nF(RT)^{-1}$. Due to the exponential factors one reaction can be dropped already for low overpotentials, e.g., for positive overpotentials the oxidation current dominates.

But the electron transfer reaction is not the only process governing the reaction current. Often other processes such as

- mass transfer of the reactants and products from the bulk to the WE and back (cf. section 5),
- other surface phenomena, e.g., adsorption of an organic molecule that inhibits the reaction (cf. section 4),
- or chemical reactions preceeding or following the electron transfer (cf. section 6)

are the *rate determining steps*. These other mechanisms are 'hidden' in Eq. (2.17) in the dependence of c, k, and/or A on these processes.

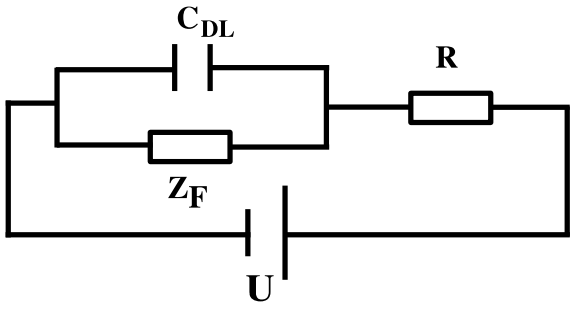

Figure 2.3: *Equivalent circuit of an electrochemical cell.*

2.2 Homogeneous Dynamics

In all genuine electrochemical instabilities the double layer potential is an essential variable. It will be seen in the following that all pattern forming electrochemical systems possess a common property: The current-potential characteristic displays a region of negative differential resistance in some form [24]. This can easily be rationalized when considering the stability of the steady states, ϕ_{DL}^{ss}, of a one variable electrochemical system. For this purpose it is useful to introduce the equivalent circuit displayed in Fig. 2.3 that describes point like electrochemical systems. Z_F denotes the *zero frequency faradaic impedance* defined by $Z_F := \left(\frac{\mathrm{d}I_r}{\mathrm{d}\phi_{\mathrm{DL}}}\Big|_{\phi_{\mathrm{DL}}^{ss}} \right)^{-1}$. A straight forward calculation of the stability of the circuit yields that the steady state is unstable if (cf. Eq. (2.9))

$$\left\{ \frac{\mathrm{d}}{\mathrm{d}\phi_{\mathrm{DL}}} \left[-I_r\left(\phi_{\mathrm{DL}}\right) + \frac{U-\phi_{\mathrm{DL}}}{R} \right] \right\}\Big|_{\phi_{\mathrm{DL}}^0} > 0$$

$$\Leftrightarrow \qquad \frac{\mathrm{d}I_r}{\mathrm{d}\phi_{\mathrm{DL}}}\Big|_{\phi_{\mathrm{DL}}^0} < -\frac{1}{R}. \tag{2.18}$$

Eq. (2.18) points to two central conditions for instabilities in one variable electrochemical systems.

1. The current-potential characteristic has to display an NDR

$$\frac{\mathrm{d}I_r}{\mathrm{d}\phi_{\mathrm{DL}}}\Big|_{\phi_{\mathrm{DL}}^0} < 0.$$

2. The total effective resistance of the circuit has to be larger than the absolute value of the faradaic impedance

$$|Z_F| < R. \tag{2.19}$$

Recalling that galvanostatic control is equivalent to $R_e \to \infty$ it becomes apparent that condition one suffices for the galvanostatic operation mode.

If additional variables have to be taken into account, the above arguments do not apply in general. The systems under consideration can be divided into two classes: In the first and most common class the double layer potential acts as the activator. It is shown in the next section that the underlying positive feedback mechanism stems from an N-shaped current potential characteristic (N-NDR). Though in some cases the NDR is hidden by a second potential dependent process (HN-NDR) [27].

The positive feedback mechanism in the second class is provided by a process that is not of genuine electrochemical nature and thus, the double layer potential plays the role of the inhibitor in these systems. The systems falling into this class display an S-shaped current-potential characteristic (S-NDR).[1]

2.2.1 (Hidden) N-shaped Negative Differential Resistance Systems

Instabilities in (H)N-NDR systems have their origin in the interplay of the processes at the electrode|electrolyte interface with the electronic control circuit. The occurrence of an N-NDR can stem from several mechanisms and does not have to be directly visible in the current-potential characteristic. Considering Eq. (2.17) the possible origins of an N-NDR are [24]:

- The available area for the reaction decreases with increasing overpotential, e.g., due to the enhanced adsorption of a species that completely inhibits the reaction.
- The concentration of the electro-active species decreases with increasing overpotential. The most prominent mechanism for this effect was discovered by Frumkin and involves more complex models of the double layer structure.
- The electron transfer rate decreases with increasing overpotential, e.g., if adsorption of a species that increases the activation energy is enhanced for higher overpotentials.

These mechanisms are in effect for a certain range of applied voltages and are embedded by regions of positive differential resistance. In Fig. 2.4(a) the resulting N-shaped current potential characteristic for this case is displayed together with some examples of the load-line $I = R^{-1}(U - \phi_{\mathrm{DL}})$.

The most basic nonlinear phenomenon, namely *bistability*, arises in such a system if the load line has three intersections with the current voltage curve (and no other variables are essential for the dynamics, this condition resembles Eq. (2.19)). The positive feedback loop causing the instability of the NDR-branch can be described as follows: Suppose the system is in a state defined by the intersection of the load line and the NDR-branch of

[1] It turns out that only systems with S-shaped I/ϕ_{DL}-characteristic involve ϕ_{DL} as an essential variable, thus Z-shaped characteristics will not be discussed here.

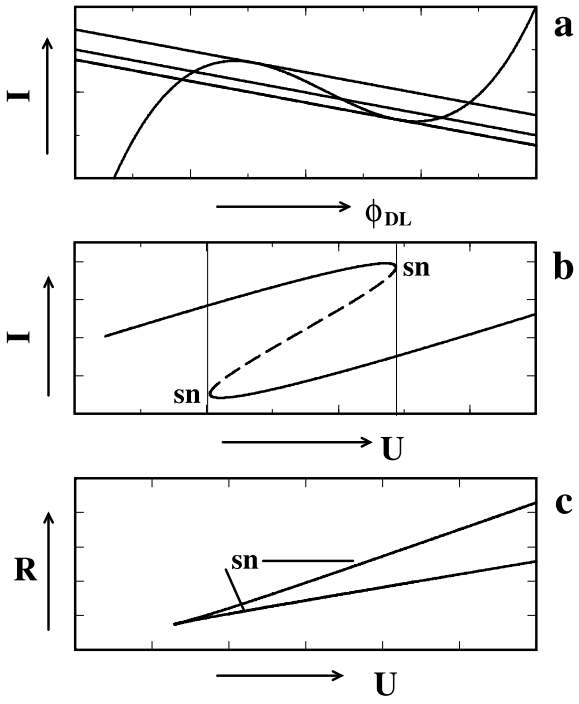

Figure 2.4: *(a) Typical N-shaped current-potential characteristic. Also shown are three examples of the load line. Two just at the border to bistability and one in between. (b) Schematic one parameter bifurcation diagram of the stationary solutions of an electrochemical system with an N-shaped I/ϕ_{DL}-characteristic. The region with three steady states is enclosed by saddle-node bifurcations (sn). (c) Existence region of two stable steady states in the R-U-parameter plane. After [95].*

the I/ϕ_{DL}-characteristic. A small perturbation of ϕ_{DL} to more positive values causes the reaction current to decrease. This will also prompt a decrease in the total current through the electrolyte given by the potentiostatic control condition. Inequality (2.19) now ensures that this decrease is smaller than the one in the reaction current, thus leading to a further increase in ϕ_{DL}. Finally the system will arrive on the right stable branch where $\frac{dI_r}{d\phi_{DL}} > 0$. The two stable states are depicted in Fig. 2.5. The *active state* is defined as the state where the reaction current is high and thus ϕ_{DL} is low. The stationary stable state for higher double layer potentials corresponds to the *passive state*.

Typical bifurcation scenarios are displayed in Figs. 2.4(b) and (c). When sweeping the applied voltage the bistability region is entered via saddle-node (sn) bifurcations. In Fig. 2.4(c) the typical shape of the existence region of bistability suggested by inequality (2.19) is documented in the *R-U* parameter plane.

If a second process introduces a negative feedback loop in an N-NDR system, self sustained *oscillations* arise for some combinations of the system parameters. Since this second essential variable takes on the role of the inhibitor, it must be slower than the

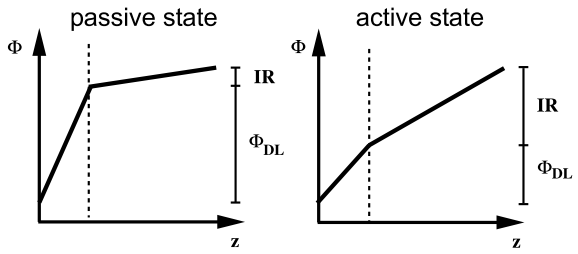

Figure 2.5: *Illustration of the active and passive state in a bistable electrochemical system.*

potential dynamics. This condition is generally satisfied by any process of chemical nature or if the time scale of the dynamics is set by mass transport processes such as diffusion. The later is a common mechanism for oscillations in electrochemical systems (cf. section 2.5.1).

Consider again a point on the NDR branch of the current potential characteristic where now the concentration variations of the reacting species in front of the electrode are explicitly taken into account. If ϕ_{DL} is shifted to higher values, I_r decreases and thus the concentration in front of the electrode increases since the depletion of the reacting species in front of the electrode is a slow process. The negative feedback loop is closed by observing that a higher concentration leads to a larger faradaic current, thus the concentration has a stabilizing effect on the dynamics.

In Fig. 2.6(a) a schematic picture of the oscillatory region of an N-NDR oscillator is shown. The typical two parameter bifurcation diagram displayed in Fig. 2.6(b) shows that the oscillations normally exist in an interval of total effective series resistances and are followed by a bistability region for higher *R*. I.e., N-NDR systems do not oscillate under galvanostatic conditions.

As stated above, the NDR does not necessarily have to be visible in the I/ϕ_{DL}-characteristic. It can be 'hidden' ($\partial I/\partial\phi_{DL} < 0$ but $\mathrm{d}I/\mathrm{d}\phi_{DL} > 0$), if a second slow potential dependent process is present. Thus, the autocatalytic feedback loop is the same as in N-NDR oscillators, just the coupling to and the nature of the inhibitor are different in HN-NDR oscillators. This has one important consequence, as can be seen in Fig. 2.6(d): The oscillatory region in the *R-U* parameter plane is not bounded from above, i.e., HN-NDR systems also oscillate under galvanostatic control.

2.2.2 S-shaped Negative Differential Resistance Systems

Electrochemical oscillators in which the double layer is the inhibitory variable are very rare if they exist at all. The reason being that the time scale of the activator must exceed the one of the inhibitor, i.e., ϕ_{DL}. Nevertheless they are introduced here since S-NDR systems favor spatial instabilities as will be seen in the next sections.

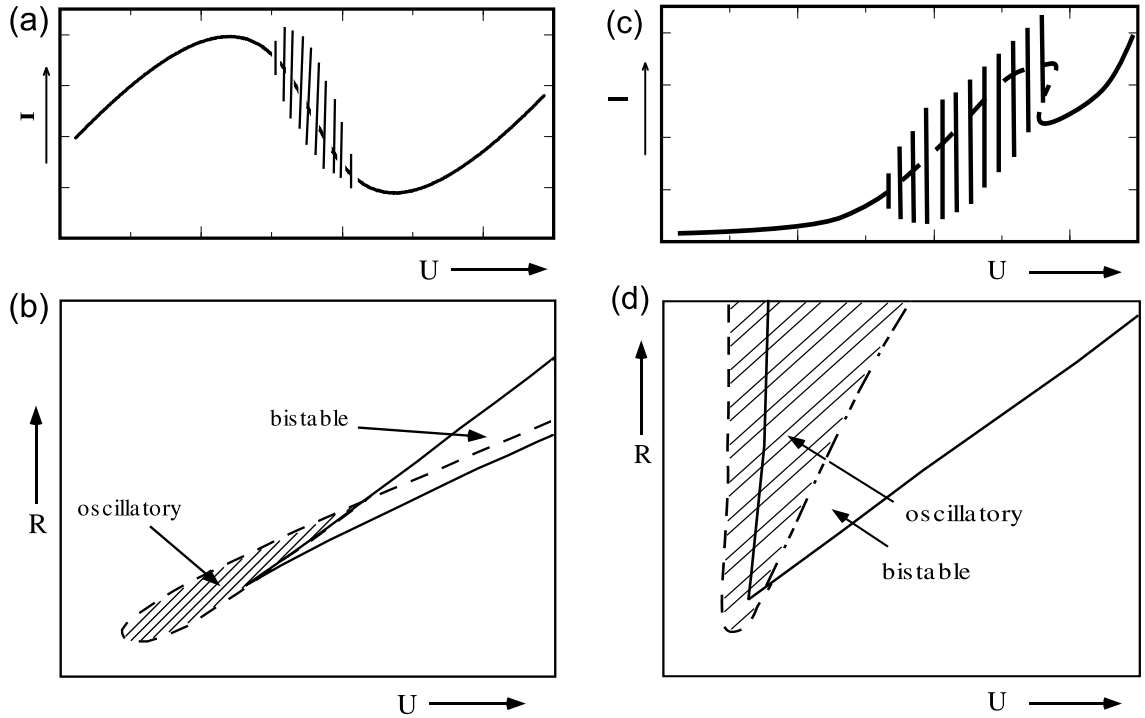

Figure 2.6: *Schematic current-voltage characteristic of an (a) N-NDR and (c) HN-NDR oscillator, respectively. Shown is the total current as a function of the applied voltage U. (a) N-NDR system: For suitable values of the total effective resistance (cf. (b)) oscillations are observed in a wide voltage interval on the branch of negative differential resistance. (c) HN-NDR system: If the total effective resistance, R, exceeds a certain threshold (cf. (d)) oscillations are observed in a wide voltage interval on a branch of positive differential resistance. (b),(d) Typical bifurcation diagrams of an (b) N-NDR and (d) HN-NDR oscillator, respectively, displaying the regions of oscillatory and bistable behavior in the R-U-parameter plane. After [26].*

In Figs. 2.7(a) and (b) schematic current potential and current voltage characteristics of an S-NDR system are displayed. The autocatalysis in systems with an S-shaped current potential characteristic has to be provided by a chemical process. This implies that the characteristic has to display a bistable region, i.e., $I(\phi_{\mathrm{DL}})$ is multivalued in some parameter interval (cf. Fig. 2.7(a)). The typical bifurcation diagram displaying universal relative positions of sn and Hopf bifurcations (h) in the *R-U* parameter plane for S-NDR oscillators is displayed in Fig. 2.7(c). It is again important to note that S-NDR systems oscillate also in the galvanostatic control mode.

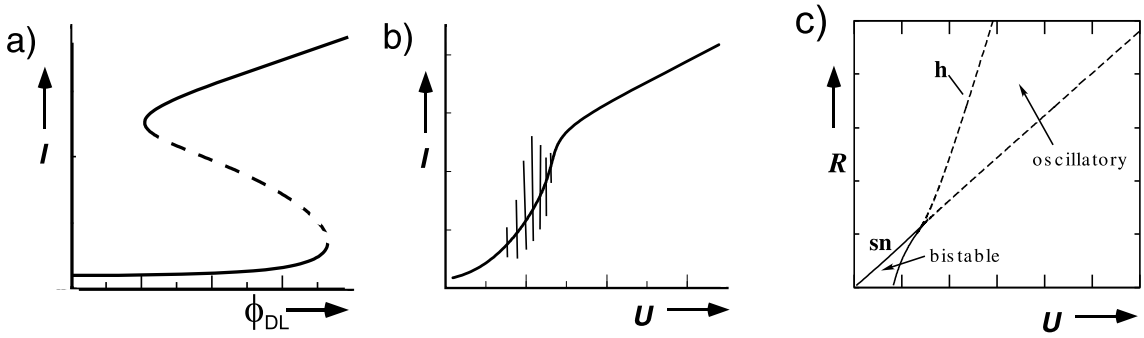

Figure 2.7: *(a) Schematic S-NDR current-potential characteristic. (b) Typical current-voltage characteristic of an S-NDR oscillator. Shown is the total current, I, as a function of the applied voltage, U. Note that the S-shape is not directly visible in this diagram due to the IR drop in the electrolyte. If the total effective resistance R exceeds a certain threshold (cf. (c)) oscillations are observed in a wide voltage interval on a branch with positive slope in the I/U-characteristic. (c) Bifurcation diagram of an S-NDR oscillator displaying the regions of oscillatory and bistable behavior in the R-U-parameter plane. sn and h denote the points of saddle-node and Hopf bifurcations, respectively. After [26].*

2.3 Migration Coupling

2.3.1 General Formulation

In this section the spatial degree of freedom is included in the double layer dynamics. Since we want to consider pure migration coupling in this section, no external resistance is included here and the RE is positioned in the plane of the CE (R_e=0=$\phi|_{z_{RE}}$). Other configurations would introduce spatial couplings stemming from the control mode (cf. next section). To derive the dependence of the double layer potential on $\boldsymbol{x}$ and t the migration currents in the electrolyte driven by the electric field $-\boldsymbol{\nabla}\phi(\boldsymbol{x},t)$ have to be considered. In the Nernst-Planck approximation the ion flux density, $\boldsymbol{j_i}$, of each charge carrying species i is given by

$$\boldsymbol{j_i} = -D_i \boldsymbol{\nabla} c_i - \mu_i n_i c_i \boldsymbol{\nabla}\phi,$$

where D_i denotes the diffusion constant, μ_i the mobility and n_i the number of charges carried by each ion. The migration current density in the electrolyte is then given by

$$\begin{aligned} \boldsymbol{i_m} &= F \sum n_i \boldsymbol{j_i} \\ &= -F \sum n_i D_i \boldsymbol{\nabla} c_i - F \boldsymbol{\nabla}\phi \sum \mu_i n_i^2 c_i. \end{aligned}$$

To simplify this expression some common approximations can be introduced. Most importantly the electrolyte is considered to be *electro-neutral*, $\sum n_i c_i = 0 \forall \boldsymbol{x}$. This is a very

good approximation for almost all electrolytes since any charges in the electrolyte are balanced very quickly by counter-ions [96]. Thus, Laplace's equation rather than Poisson's equation is valid for the potential in the entire electrolyte

$$\Delta\phi = 0. \tag{2.20}$$

Assuming additionally that all diffusion constants are equal, $D_i = D$, the migration current density is given by

$$\begin{aligned} \boldsymbol{i_m} &= -FD\boldsymbol{\nabla}\sum n_i c_i - \boldsymbol{\nabla}\phi\sum F\mu_i n_i^2 c_i \\ &= -\sigma\boldsymbol{\nabla}\phi \end{aligned}$$

with the conductivity defined by $\sigma := \sum F\mu_i n_i^2 c_i$. Another consequence of electro-neutrality is that the conductivity is constant in space.

The dynamic equation for $\phi_{\mathrm{DL}}(\boldsymbol{x},t)$ can now be written as the local charge balance at the WE surface

$$\begin{aligned} C_{DL}\frac{\partial}{\partial t}\phi_{\mathrm{DL}} &= -i_r + i_m|_{WE} \\ &= -i_r - \sigma\left.\frac{\partial\phi}{\partial z}\right|_{WE} \end{aligned} \tag{2.21}$$

(cf. Eq. (2.5)) where total currents are replaced by current densities and z is the normal direction at the WE surface pointing into the electrolyte. Eq. (2.21) is a well posed equation for the dynamics of ϕ_{DL} since ϕ is determined only by Eq. (2.20) and the boundary conditions at the cell walls and the electrodes. Typically the CE is taken as an equipotential plane, which is a good approximation if the reactions at the CE are reversible and fast. In this work we set

$$\phi|_{CE} = 0 \tag{2.22}$$

and no-flux conditions are imposed at the cell walls. The only time dependent boundary condition is the Dirichlet-type control condition relating applied potential, U, double layer potential, ϕ_{DL}, the potential drop over the electrolyte, $\phi|_{WE}$, and the potential at the RE, $\phi|_{z_{RE}}$ (Eq. (2.8)). Thus, ϕ and also $\left.\frac{\partial\phi}{\partial z}\right|_{WE}$ are given by the boundary conditions, most importantly ϕ_{DL}, and Laplace's equation. (The time ϕ needs to adjust to changes in ϕ_{DL} is given by the cell dimension over the speed of light and is much faster than any timescale considered in electrochemical pattern formation.)

Up to now there exist three standard approaches to calculate the migration current density at the WE.

The straight forward method is to directly solve Laplace's equation in the entire electrolyte for every time step (cf., e.g., [37,38,97–102]). This approach is quite time consuming and neglects the possibility to reduce the dimensionality of the system considerably. It

turns out that computation time is a serious limitation for this method if small time steps have to be used to perform the integration in time. Another draw back is that a straight forward calculation of ϕ does not give insight in the nature of the spatial coupling parallel to the WE. This spatial coupling is effectively mediated by ϕ and stems physically from the tendency of the electrolyte to stay electro-neutral. But it will be seen below that it is possible to give closed expressions for the spatial coupling acting on ϕ_{DL} revealing the special nature of the migration coupling. On the other hand the calculation of ϕ in the entire electrolyte yields precise information of the potential distribution in the cell, thus enabling the validification (or falsification) of certain approximations made below. Additionally, it offers the possibility to introduce chemical kinetics also at the CE. Furthermore, it facilitates the investigation of arbitrary arrangements of the electrodes as well as the implementation of various boundary conditions.

Another approach explicitly takes advantage of the fact that the potential distribution in the electrolyte is uniquely determined by the boundary conditions. With the use of a Green's function, G, this dependence can be expressed in integral terms

$$\phi(\boldsymbol{x},t) = \int_{WE} G(\boldsymbol{x},\boldsymbol{x'})\phi|_{WE}(\boldsymbol{x'},t)\,\mathrm{d}\boldsymbol{x'} \tag{2.23}$$

and the derivative of ϕ with respect to the normal direction z at the WE is given by [36,103]

$$\left.\frac{\partial\phi}{\partial z}\right|_{WE} = -h(\boldsymbol{x})(\phi_{WE}-\phi_{\mathrm{DL}}) - \int_{WE} H(\boldsymbol{x},\boldsymbol{x'})\left(\phi_{\mathrm{DL}}(\boldsymbol{x'},t)-\phi_{\mathrm{DL}}(\boldsymbol{x},t)\right)\mathrm{d}\boldsymbol{x'}. \tag{2.24}$$

$H(\boldsymbol{x},\boldsymbol{x'})$ and $h(\boldsymbol{x})$ have to be calculated for every cell geometry and shape and position of the electrodes. In general this can only be achieved numerically. In [104] some cases where h and H can be calculated analytically are elaborated.

The representation of $i_m|_{WE}$ in the form of Eq. (2.24) provides numerous important insights into the nature of the migration current density, the spatial coupling and the influence of the cell geometry on the dynamics:

- $i_m|_{WE}$ can be decomposed into a local part and a part describing only the spatial coupling. This becomes apparent when comparing the equation for the homogeneous dynamics, Eq. (2.9), and for the extended system, Eq. (2.21).

- The local dynamics of ϕ_{DL} depend on the cell geometry that enters via $h(\boldsymbol{x})$. A hint to this fact was already seen in section 2.1.1 where it was derived that the local dynamics depends, e.g., on the position of the RE via the total effective resistance.

- Additionally, the local dynamics in general even depend on the position of the respective point on the WE [37, 97, 98, 101, 103, 104]. This can be understood if one considers that the distribution of the electric field at the WE is, in general, not uniform. E.g., if a point like RE is positioned in front of a disk shaped WE under potentiostatic control.

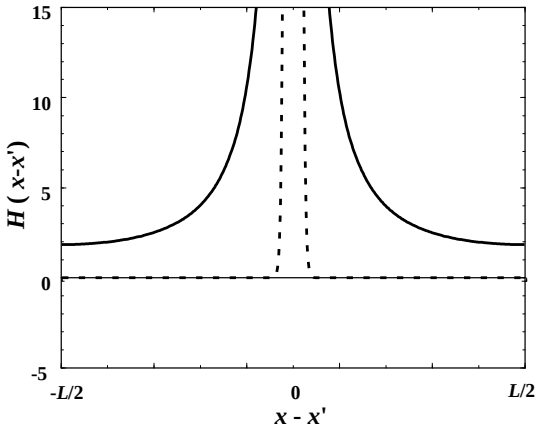

Figure 2.8: *Nonlocal electrochemical coupling function H (solid line) compared with the schematic local coupling function for diffusive coupling (dashed line). H was calculated for a ring WE. The RE is positioned on the axis of the ring and the CE is placed at infinity (R_e=0, $\phi|_{z_{RE}} = \phi|_{CE} = 0$) [36]. H approaches the diffusive case if the ratio of the length of the WE divided by the distance between WE and CE goes to infinity. After [104].*

- In general the coupling function H does not depend on $|\boldsymbol{x'} - \boldsymbol{x}|$ but on the absolute values of $\boldsymbol{x'}$ and $\boldsymbol{x}$, the reason being again the non-uniformity of the potential distribution at the WE.

- The spatial coupling can be visualized by plotting the coupling function H. It becomes apparent that the nature of the electrochemical coupling is *nonlocal*, i.e., not only nearest neighbor sites interact but all points on the electrode are affected instantaneously by changes at a certain position. In Fig. 2.8 the typical form of H is depicted for a 1d electrode.

- If the solution to H can be derived analytically the dependence of the spatial coupling on parameters of the system such as the distance between WE and CE can be investigated explicitly.

2.3.2 Ring Geometry and Fourier Mode Decomposition

Most often the dependence of the local dynamics on the position on the WE is an undesired complication. For this reason the ring geometry depicted in Fig. 2.9(a) is used in most studies of electrochemical pattern formation in both, theory and experiment. WE and CE are ring electrodes positioned on a common axis. The RE is positioned in the plane of the CE on the ring axis or behind the CE and $\phi|_{CE} = \phi|_{z_{RE}}$ is assumed. The WE is considered to be a very thin ring so that the radial dimension can be neglected. In this symmetric configuration $h(x)$ is a constant. x denotes the angular position on the ring.

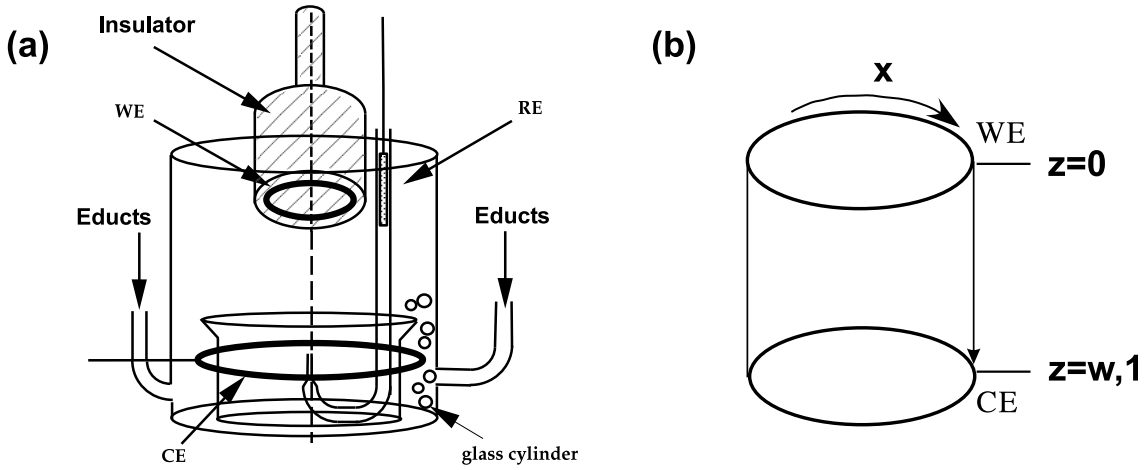

Figure 2.9: *(a) Typical electrochemical setup using ring electrodes. WE and CE are ring electrodes with a common axis on which the RE is positioned. (b) Simplified 2-d model of the geometry in (a).*

The coupling function only depends on the point distance $H(x',x) = H(|x'-x|)$ and is plotted in Fig. 2.8. For this calculation the distance between WE and CE was taken to be infinitely large. The strong nonlocal nature of H is apparent. Due to the finite length of the WE, H does not drop to zero at $x = \pm L/2$. Thus, the migration coupling includes a small contribution of positive global coupling.

The simplified two dimensional (2d) geometry shown in Fig. 2.9(b) was used to derive the first results on the nature of the spatial coupling in electrochemical systems [30, 31, 33, 39, 40, 42, 105]. The electrolyte is confined to a cylindrical surface bounded by CE and WE. The reference electrode is considered to be behind or in the plane of the CE and $\phi|_{z_{RE}}$=0, since the CE is an equipotential plane with $\phi|_{CE} = 0$. The coordinate parallel to the ring WE is denoted by x. The WE is again positioned at $z = 0$ and the CE at $z = w$.

The 2d-geometry proved to be a successful approximation and facilitates the formulation of the spatial coupling term in a third and most simple way by using an expansion into Fourier modes. The 2d-geometry, Fig. 2.9(b), is used throughout this work since 1d pattern formation is investigated and all key features of electrochemical dynamics in 1d can be captured by this geometry.[2]

For the derivation of the migration current density in Fourier space z and x are rescaled for convenience as follows: $z \to z/w$, $x \to 2\pi x/L$, where L denotes the circumference of the ring WE. Thus the boundary conditions for the potential $\phi(x,z,t)$ in the electrolyte

[2] excluding effects caused by inhomogeneous electric fi elds

read:

$$\phi(x,0,t) = \phi|_0 \tag{2.25}$$
$$\phi(x,1,t) = 0 \tag{2.26}$$
$$\phi(x,z,t) = \phi(x+2\pi,z,t). \tag{2.27}$$

The following expansion for ϕ solves the Laplace Equation supplemented with these boundary conditions

$$\phi(x,z,t) = a_0^\phi(1-z) + \sum_{n=1}^{\infty}\left(a_n^\phi \cos nx + b_n^\phi \sin nx\right)\sinh(\beta n(1-z)), \tag{2.28}$$

with the aspect ratio $\beta := 2\pi w L^{-1}$. The migration current density at the WE is then given by ($\frac{\partial}{\partial z} \to \frac{1}{w}\frac{\partial}{\partial z}$)

$$\begin{aligned} i_m &= -\frac{\sigma}{w}\left.\frac{\partial\phi}{\partial z}\right|_0 \\ &= \frac{\sigma}{w}\left[a_0^\phi + \beta\sum_{n=1}^{\infty} n\left(a_n^\phi\cos nx + b_n^\phi \sin nx\right)\cosh(\beta n)\right]. \end{aligned} \tag{2.29}$$

Now also ϕ_{DL} is written as a Fourier series

$$\phi_{\mathrm{DL}}(x,t) = a_0^{\phi_{\mathrm{DL}}} + \sum_{n=1}^{\infty}\left(a_n^{\phi_{\mathrm{DL}}}\cos nx + b_n^{\phi_{\mathrm{DL}}}\sin nx\right). \tag{2.30}$$

The coefficients of the expansion can be related to each other via the control condition $U = \phi_{\mathrm{DL}} + \phi|_0$. Note that the conditions R_e=0 and $\phi|_{z_{RE}}$=0 enter here. Inserting expansions (2.28) and (2.30) yields

$$a_0^\phi = U - a_0^{\phi_{\mathrm{DL}}} \tag{2.31}$$
$$a_n^\phi = -a_n^{\phi_{\mathrm{DL}}}\sinh^{-1}(\beta n) \tag{2.32}$$
$$b_n^\phi = -b_n^{\phi_{\mathrm{DL}}}\sinh^{-1}(\beta n). \tag{2.33}$$

Entering these relations into Eq. (2.29) gives the migration current density as a function of ϕ_{DL}

$$i_m = \frac{\sigma}{w}(U - a_0^{\phi_{\mathrm{DL}}}) - \frac{\sigma\beta}{w}\sum_{n=1}^{\infty} n\left(a_n^{\phi_{\mathrm{DL}}}\cos nx + b_n^{\phi_{\mathrm{DL}}}\sin nx\right)\coth(\beta n). \tag{2.34}$$

Eq. (2.34) resembles the statement that the migration current density includes a homogeneous term. The constant h is determined to $1/w$. Realizing that $\frac{\sigma}{w} = \frac{1}{\beta}\frac{\sigma\beta}{w}$ suggests to reduce the number of effective parameters by one through the substitution $\sigma \to \sigma\beta w^{-1} = 2\pi\sigma L^{-1}$.

Using Eqs. (2.21) and (2.30) the dynamics of ϕ_{DL} in Fourier space is then given by

$$C_{DL}\dot{a}_0^{\phi_{\mathrm{DL}}} = \int_0^{2\pi} i_r \,\mathrm{d}x + \frac{\sigma}{\beta}(U - a_0^{\phi_{\mathrm{DL}}}) \tag{2.35}$$

$$C_{DL}\dot{a}_n^{\phi_{\mathrm{DL}}} = \int_0^{2\pi} i_r \cos nx \,\mathrm{d}x - \sigma n \coth(\beta n) a_n^{\phi_{\mathrm{DL}}} \tag{2.36}$$

$$C_{DL}\dot{b}_n^{\phi_{\mathrm{DL}}} = \int_0^{2\pi} i_r \sin nx \,\mathrm{d}x - \sigma n \coth(\beta n) b_n^{\phi_{\mathrm{DL}}}. \tag{2.37}$$

The separation of i_m in a local and a spatial coupling term can also be given in physical space. Recalling Ohm's Law for i_m and using $AR_\Omega = \beta/\sigma$ the migration current density in a homogeneous situation is given by $i_m = \sigma/\beta\phi|_0$. Comparing this with Eq. (2.21), Eq. (2.21) can be rewritten for the 2d-case as follows

$$C_{DL}\frac{\partial}{\partial t}\phi_{\mathrm{DL}} = -i_r + \frac{\sigma}{\beta}(U - \phi_{\mathrm{DL}}) - \frac{\sigma}{\beta}\left(\frac{\partial\phi}{\partial z} - \phi\right)\Big|_0 \tag{2.38}$$

and the migration current is given by

$$i_m = \frac{\sigma}{\beta}(\phi_{WE} - \phi_{\mathrm{DL}}) - \frac{\sigma}{\beta}\left(\frac{\partial\phi}{\partial z} - \phi\right)\Big|_0. \tag{2.39}$$

ϕ_{WE}-ϕ_{DL} is written in the local function here since this includes the more general cases discussed in the next section and $\phi_{WE} = U$ for R_e=0=$\phi|_{z_{RE}}$ (cf. Eq. (2.8)).

Entering expansions (2.28) and (2.29) into the spatial coupling term and using Eqs. (2.35)-(2.37) leads to the damping factor of the Fourier mode *n* stemming from the spatial coupling

$$d(n) = -\sigma\left(n\coth(n\beta) - \beta^{-1}\right). \tag{2.40}$$

In Fig. 2.10 $d(n)$ is compared with the damping factor for diffusive coupling ($-n^2$).

The migration coupling thus depends on two parameters, the conductivity σ and the aspect ratio β. In particular the dependence of the migration coupling on β differs strongly from a diffusive coupling term that depends only on the diffusion constant and not on global properties of the system such as system length. Looking at Eqs. (2.36),(2.37) it is apparent that σ controls the *coupling strength* whereas β defines the *coupling range*. Thus, σ can be interpreted as the electrochemical analogon of the diffusion constant. It sets the time scale of the spatial communication with respect to the characteristic time of reaction. σ determines such properties as the front width and the relaxation time for inhomogeneities in the double layer potential.

Eq. (2.38) points to another peculiarity of electrochemical systems. The coupling range β also enters into the local dynamics. Thus, the consequences of changing the coupling range can never be studied independently of other system parameters in a real

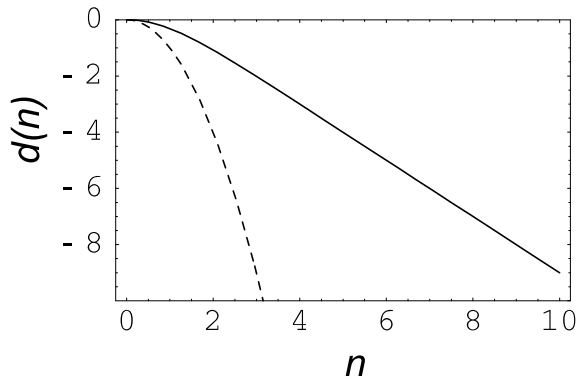

Figure 2.10: *Electrochemical coupling function in Fourier space for* $\beta = \sigma = 1$ *(Eq. (2.40), solid line). The long range coupling is apparent in the comparison with the nearest neighbor coupling given by* $-n^2$ *(dashed line).*

electrochemical system, thus hampering insight into the spatial coupling. This problem can be overcome by, unphysically, fixing the local dynamics in theoretical investigations.

It is instructive to investigate the behavior of the migration coupling in the limit of small and large β to clarify the influence of β on the coupling range. The following relations hold for the spatial damping factor [40]

$$\lim_{\beta\to 0} d(n) = -\frac{\sigma\beta}{3}n^2 + O(\beta^3 n^4)$$
$$\lim_{\beta\to\infty} d(n) = -\sigma n.$$

Obviously diffusive coupling ($-n^2$-dependence) is retained for small aspect ratios (close CE) and an easy expression can be given for the nonlocal coupling for large β. Typical values of β range from 0.1 to 10, meaning that the spatial coupling is nonlocal in most situations and none of the above limits apply in general.

2.3.3 Accelerated Fronts and Turing Patterns

Accelerated Fronts

The most striking feature of the nonlocal coupling is the observation of accelerated fronts [31, 40, 103, 106] opposed to constant front velocities observed for diffusive coupling [8]. In Fig. 2.11 the transition from a metastable to a globally stable state in a bistable electrochemical system is depicted for three different values of β. The local dynamics was fixed retaining the same steady states for all values of β (s.a.). For $\beta = 0.01$ no front acceleration is visible and the approximation of a diffusion-like coupling is valid. The intermediate value of $\beta = 1$ leads to a small front acceleration, especially close to the state of full transition. At $\beta = 10$ front acceleration is clearly visible.

Figure 2.11: *Illustration of the front acceleration for different values of the coupling range* β*. The local dynamics was fixed. Shown is the double layer potential as a function of time and space during a transition from a metastable to a globally stable state. Blue equals low and red symbolizes high* ϕ_{DL}*, repsectively. (a)* $\beta = 0.01$ *(b)* $\beta = 1$ *(c)* $\beta = 10$*.* $\sigma = 0.5$ *in all plots. Taken from [107].*

The acceleration effect can be explained straightforwardly if the migration coupling is approximated by a local-global coupling. The global part can be formally included in the local dynamics, which then depend on a time dependent parameter, namely the average double layer potential. Accordingly, also the front velocity changes when changing ϕ_{DL} [103, 104].

Turing Patterns

The most prominent example of spatial pattern formation in nonlinear dynamics is the Turing mechanism [7, 16]. It predicts the occurence of stationary periodic patterns with an intrinsic wavelength for systems that can be described by partial differential equations of the form

$$\dot{a} = f(a,v) + D_a \Delta a$$
$$\dot{v} = g(a,v) + D_v \Delta v.$$

a and v denote the activator and the inhibitor variables, respectively. The central condition for the existence of stationary patterns is that the diffusion constant of the inhibitor, D_v, must be larger than that of the activator, D_a. For chemical systems this condition is rarely met since usually diffusion constants of chemical species do not differ sufficiently. Thus, Turing patterns in chemical systems were observed only almost 40 years after their prediction by Turing in 1952 [108–111].

The above condition can be generalized for nonlocal couplings in the sense that the coupling mechanism acting on the inhibitor must be faster than the one acting on the

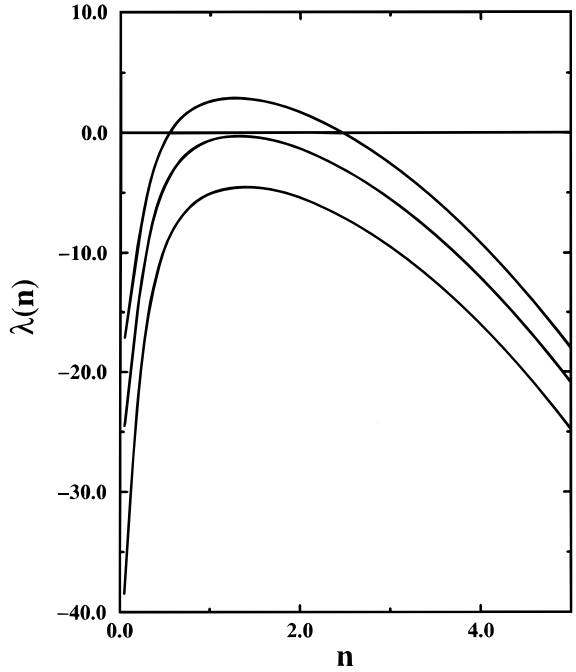

Figure 2.12: *Real part of the growth rates of perturbations of the homogeneous steady state of an S-NDR system as a function of the wavenumber of the perturbation, n, for three different parameter sets close to the Turing bifurcation. Taken from [85].*

activator. This condition is generally met for electrochemical systems with an S-shaped current potential characteristic. As stated above, in these systems the double layer potential constitutes the inhibitor and the spatial coupling term acting on v is given by the migration coupling. The ratio of the rate of migration and diffusion is proportional to $L\sigma/(D_a C_{DL})$ [85]. Inserting typical values yields a ratio of the order 10^3 to 10^4. Thus, the double layer potential spreads far more rapidly than the chemical species a does. In Fig. 2.12 the real part of the maximum growth rate of perturbations of the homogeneous steady states, $\max(\mathrm{Re}(\lambda(n)))$, are displayed in the Turing-unstable region of an S-NDR system [85].

Li *et al.* took advantage of this fact and reported the first observation of stationary Turing-type patterns in an electrochemical system in 2001 [112].

2.4 Global Coupling Induced by the Control Mode

In the previous section we excluded the external resistor and placed the RE in the plane of the CE to concentrate on the migration coupling describing the 'communication' between different sites on the WE mediated by the electric fields in the electrolyte. In this section we are going to complete the picture of standard electrochemical couplings by taking the

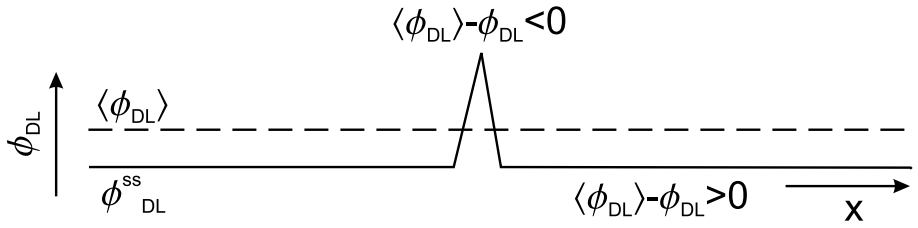

Figure 2.13: *Illustration of the effect of the global coupling term.*

above mentioned control methods into account. It is shown that both of these modes introduce a global coupling into the equation governing the dynamics of the double layer potential of the form

$$C_{DL}\frac{\partial}{\partial t}\phi_{\mathrm{DL}} = -i_r + \frac{\sigma}{\beta}(U-\phi_{\mathrm{DL}}) + \alpha(\langle\phi_{\mathrm{DL}}\rangle - \phi_{\mathrm{DL}}) - \frac{\sigma}{\beta}\left(\frac{\partial\phi}{\partial z} - \phi\right)\Big|_0 .$$

The brackets $\langle\rangle$ denote the average over space

$$\langle\phi_{\mathrm{DL}}\rangle = \frac{1}{A}\int_{WE}\phi_{\mathrm{DL}}\,\mathrm{d}\boldsymbol{x}$$

The global coupling described by $\alpha(\langle\phi_{\mathrm{DL}}\rangle - \phi_{\mathrm{DL}})$ is called negative or desynchronizing if $\alpha < 0$. Positive or synchronizing global coupling is present if $\alpha > 0$. The origin of this terminology becomes clear if one considers the situation depicted in Fig. 2.13. Suppose the system is in a homogeneous steady state, $\phi_{\mathrm{DL}}(x) = \phi_{\mathrm{DL}}^{ss}$. A small perturbation of ϕ_{DL} at a certain location on the WE to more positive values leads to an increase of $\langle\phi_{\mathrm{DL}}\rangle$. $\langle\phi_{\mathrm{DL}}\rangle - \phi_{\mathrm{DL}} < 0$ in the region of the perturbation, thus, if $\alpha < 0$, the perturbation will increase. Accordingly, this type of global coupling enhances spatial perturbations and is called desynchronizing. The opposite is true for $\alpha > 0$.

If the dynamics of the system of interest is governed by more than one essential variable, a linearization around the homogeneous steady state can give some insight into the possible effects of the global coupling [46, 107]. Since the coupling is global, it can only affect the stability of the homogeneous mode. The growth rates of perturbations with wavenumbers $n > 0$ are not changed by the global coupling. Thus, the dispersion relation of systems with $\alpha \neq 0$ are discontinuous at $n = 0$. If the jump of $\max(\mathrm{Re}(\lambda(n)))$ from $n = 0$ to $n > 0$ is positive, equivalent to saying that the global coupling stabilizes the homogeneous steady state, pattern formation can be expected. Consider the situation depicted in Fig. 2.14(a). The decrease in the dispersion relation in a vicinity of $n = 0$ is the generic situation in all 2-variable reaction-diffusion systems not displaying a Turing instability. Assuming that $\max(\mathrm{Re}(\lambda(n))) < 0$ also for larger n,[3] the most unstable

[3] Otherwise interactions with bifurcations at higher wavenumbers would have to be taken into account, cf., e.g., [85, 113]

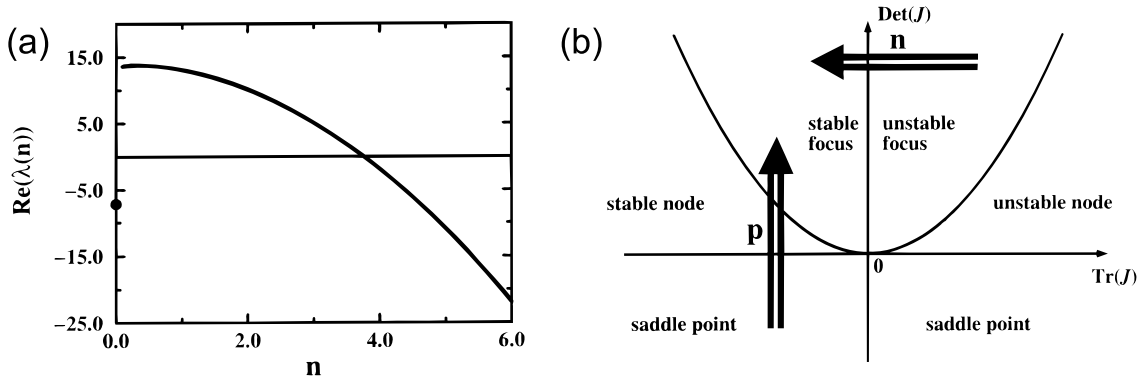

Figure 2.14: *(a) Dispersion relation for a system with global coupling. The stabilizing effect of the global coupling on the homogeneous mode manifests itself in a positive jump of max*$(Re(\lambda(n)))$ *when going from* $n = 0$ *to* $n > 0$*. (b) Stability diagram displaying how* tr$J$ *and* det$J$ *determine the stability of a two dimensional dynamical system. The arrows indicate how positive (p) or negative (n) global coupling can stabilize the homogeneous steady state if it acts on the inhibitor. Taken from [46].*

wavenumber will always be $n = 1$.[4] Depending on the imaginary part of $\lambda(1)$ two different patterns are to be expected. If $\mathrm{Im}(\lambda(1)) = 0$ stationary structures with wavenumber one, so called stationary domains, are observed. For $\mathrm{Im}(\lambda(1)) \neq 0$ symmetry breaking will occur in both, time and space, and the spatio-temporal dynamics will either resemble standing waves with wavenumber one or pulses. Often the nonlinearities neglected in the above discussion also excite the homogeneous mode. Since the resulting dynamics does not show the characteristic nodes, it was termed anti-phase oscillations rather than standing waves.

Thus, important insight on the role of global coupling for pattern formation can be deduced from the effect it has on the stability of the homogeneous steady state. Note however, that in order to predict the effect of the global coupling on homogeneous limit cycles or turbulent dynamics, a more extensive analysis has to be performed.

For a two variable system of the form

$$\begin{aligned} \dot{\phi_{\mathrm{DL}}} &= f(\phi_{\mathrm{DL}}, v) + \alpha(\langle\phi_{\mathrm{DL}}\rangle - \phi_{\mathrm{DL}}) + \text{spatial coupling} \\ \dot{v} &= g(\phi_{\mathrm{DL}}, v) + \text{spatial coupling} \end{aligned}$$

the stability of the homogeneous steady state is determined by the trace (tr) and determinant (det) of the Jacobian matrix

$$J = \begin{pmatrix} f_{\phi_{\mathrm{DL}}} + \alpha & f_v \\ g_{\phi_{\mathrm{DL}}} & g_v \end{pmatrix},$$

[4] Whether $\max(\mathrm{Re}(\lambda(1))) > 0$ depends on system size. Pattern formation is suppressed below a minimal system size such that $\mathrm{Re}(\lambda(n)) < 0 \forall n > 0$.

where subscripts denote partial derivatives with respect to the subscripted variable and evaluation at the steady state $\left(\text{e.g., } f_{\phi_{\mathrm{DL}}} = \frac{\partial f}{\partial \phi_{\mathrm{DL}}}\Big|_{(\phi_{\mathrm{DL}}^{ss}, v^{ss})}\right)$. The growth rate of perturbations is then given by

$$\lambda_{1,2} = \frac{\mathrm{tr}J}{2} \pm \sqrt{\frac{(\mathrm{tr}J)^2}{4} - \det J}$$

and stability $(\max(\mathrm{Re}(\lambda)) < 0)$ implies that $\det J > 0$ and $\mathrm{tr}J < 0$. The stability diagram of the homogeneous steady state in the plane of $\mathrm{tr}J$ and $\det J$ is depicted in Fig. 2.14(b). Now $\mathrm{tr}J$ and $\det J$ of the globally coupled system are related to the original one by

$$\mathrm{tr}J(\alpha) = \mathrm{tr}J(0) + \alpha$$
$$\det J(\alpha) = \det J(0) + g_v \alpha.$$

If v is the activator, i.e., in S-NDR systems, $g_v > 0$ in the region of negative differential resistance. Thus, the homogeneous stationary state can be stabilized for $\alpha > 0$ if it is a saddle point without global coupling (route 'p' in Fig. 2.14(b)). Since $\mathrm{Im}(\lambda(0) = 0)$ on this route, *stationary structures with wave number one can be expected in S-NDR systems under positive global coupling*. Desynchronizing global coupling can stabilize the homogeneous steady state in an S-NDR system by decreasing $\det J$ (route 'n' in Fig. 2.14(b)). The imaginary part of λ is different from zero on this route, consequently *systems with an S-shaped current potential characteristic subject to negative global coupling will exhibit pulses or standing waves with wavenumber one in the oscillatory regime*.

The autocatalysis in (H)N-NDR systems stems from ϕ_{DL}, thus $g_v < 0$. Therefore *positive global coupling tends to have a homogenizing effect in systems with an (H)N-shaped characteristic*. The opposite is true for desynchronizing global coupling. Both routes, starting from a saddle point or from an unstable focus, may stabilize the homogeneous steady state. Indeed *pulses and stationary structures with wavenumber one were observed in (H)N-NDR systems subject to negative global coupling* [36, 45, 114, 115].

It should be pointed out here that a close resemblance exists between two variable reaction-diffusion systems with global coupling and three variable reaction-diffusion systems with two inhibitors of the form

$$\dot{u} = f(u,v) + D_g(s-u) + D_u \Delta u \tag{2.41}$$
$$\dot{v} = \varepsilon g(u,v) + D_v \Delta v \tag{2.42}$$
$$\dot{s} = \gamma(u-s) + D_s \Delta s. \tag{2.43}$$

So called wave instabilities or Turing instabilities of second kind are observed in such systems. At this bifurcation point a mode with positive wavenumber and non-vanishing imaginary part of the respective eigenvalue crosses the imaginary axis. In the limit $D_s \to \infty$ and $\gamma \gg 1$ these systems display stability diagrams and spatio-temporal dynamics

similar to the ones observed in two variable reaction-diffusion systems with global coupling, see, e.g., [116–119]. Note however that the genuine three and more variable effects like mixed-mode oscillations or chaos that are also observed in these systems are absent in two variable reaction-diffusion equations with global coupling.

It should be emphasized again that the above arguments only apply to the homogeneous steady state. Indeed, the quite different effects may be observed when global coupling acts on oscillatory states. E.g., Pismen *et al.* and Hudson *et al.* reported the observation of anti-phase oscillations in an N-NDR system subject to positive global coupling [28, 44, 120].

2.4.1 External Resistor and Galvanostatic Operation Mode

To realize the global nature of the feedback introduced by an external resistance it is most instructive to consider the galvanostatic case. If the faradaic current density changes at a certain position of the WE due to a local perturbation so does the total current I. Consequently the galvanostatic control unit provides the difference current to keep the total current fixed by changing the potential of the WE. Thus, all locations of the WE are instantaneously affected by a change of the local properties of the WE.

If an external resistor is present in the circuit, the potential of the WE is given by (Eq. (2.3), $\phi|_{z_{RE}}$=0)

$$\phi_{WE} = U - IR_e - \phi_{\mathrm{DL}} \tag{2.44}$$

To express i_m in terms of ϕ_{DL} the total current has to be calculated as a function of the double layer potential. I is given by the sum of all migration currents entering the double layer. Using the expansion of i_m into Fourier modes, Eq. (2.34), I can be calculated

$$\begin{aligned} I &= \int_{WE} i_m \,\mathrm{d}\boldsymbol{x} \\ &= -\frac{\sigma}{\beta}\int_0^{2\pi} \left.\frac{\partial\phi}{\partial z}\right|_0 \mathrm{d}x \\ &= \frac{2\pi\sigma}{\beta} a_0^{\phi} = \frac{\sigma}{\beta}\langle\phi|_0\rangle \\ &= \frac{\sigma}{\beta}(\phi_{WE} - \langle\phi_{\mathrm{DL}}\rangle). \end{aligned} \tag{2.45}$$

Inserting Eq. (2.45) into Eq. (2.44) and performing some rearrangements leads to

$$\phi_{WE} - \phi_{\mathrm{DL}} = (1 + R_e\sigma/\beta)^{-1}(U - \phi_{\mathrm{DL}}) + \frac{R_e\sigma/\beta}{1 + R_e\sigma/\beta}(\langle\phi_{\mathrm{DL}}\rangle - \phi_{\mathrm{DL}}). \tag{2.46}$$

Together with Eq. (2.39) and realizing that $\sigma/\beta(1 + R_e\sigma/\beta)^{-1} = [A(R_e + R_\Omega)]^{-1}$ the dy-

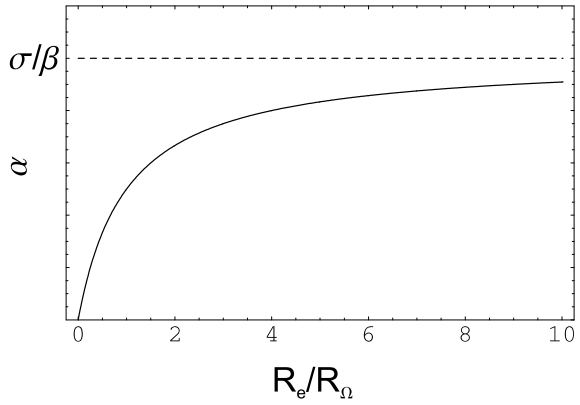

Figure 2.15: *Increase of the global coupling strength with the external resistance. Shown is the pre-factor* α *of* $(\langle\phi_{\mathrm{DL}}\rangle - \phi_{\mathrm{DL}})$ *as a function of* R_e/R_Ω.

namics of the double layer in the presence of an external resistance is given by

$$C_{DL}\frac{\partial}{\partial t}\phi_{\mathrm{DL}} = -i_r + \frac{U-\phi_{\mathrm{DL}}}{A(R_e+R_\Omega)} + \frac{R_e\sigma/\beta}{A(R_e+R_\Omega)}(\langle\phi_{\mathrm{DL}}\rangle - \phi_{\mathrm{DL}}) - \frac{\sigma}{\beta}\left(\frac{\partial\phi}{\partial z} - \phi\right)\Bigg|_0 . \tag{2.47}$$

Since β, σ, $R_e > 0$ the global coupling introduced by the external resistance is positive. The pre-factor of the global coupling term increases monotonically with R_e and approaches σ/β for large R_e, cf. Fig. 2.15.

In Fourier space only the homogeneous mode is affected by the global coupling and Eq. (2.35) becomes

$$C_{DL}\dot{a}_0^{\phi_{\mathrm{DL}}} = \int_0^{2\pi} i_r\,\mathrm{d}x + \frac{1}{A(R_e+R_\Omega)}(U - a_0^{\phi_{\mathrm{DL}}}).$$

The galvanostatic control mode can now be treated as the limit

$$\lim_{R_e,U\to\infty}[A(R_e+R_\Omega)]^{-1}(U - a_0^{\phi_{\mathrm{DL}}}) = i_0,$$

where i_0 denotes the applied current density. Thus, galvanostatic control represents the maximum positive global coupling induced by an external resistor.

Following the argument in the previous section, an external resistor or the galvanostatic control mode leads to a pronunciation of the accelerated front effect already present for R_e=0. Additionally it counteracts pattern formation in systems with an N-shaped current potential characteristic [42] and induces stationary patterns in S-NDR systems [46].

2.4.2 Close Reference Electrode

To derive the global coupling term that arises due to a close RE we consider again the control condition and represent all variables by the double layer potential. The global

nature of the coupling introduced by a close RE can be seen as follows. A local change of the double layer potential at the WE causes a redistribution of the electric field in the electrolyte. If the RE is not positioned in an equipotential plane, this redistribution is measured by the RE and the potentiostat will change ϕ_{WE} to fulfill the control condition.

If the RE is not positioned in the plane of the CE but between WE and CE, and no external resistor is present, the applied voltage is given by (Eq. (2.3), R_e=0)

$$U = \phi_{WE} - \phi|_{z_{RE}} = \phi_{\mathrm{DL}} + \phi|_0 - \phi|_{z_{RE}}. \tag{2.48}$$

The dependence of $\phi|_{z_{RE}}$ on ϕ_{DL} can be investigated with the help of the integral formulation of $\phi(\boldsymbol{x},t)$, Eq. (2.23). Using again the ring geometry and positioning the RE on the ring axis, it follows for symmetry reasons that

$$\begin{aligned}\phi(\boldsymbol{x}_{RE},t) &= \int_{WE} H(\boldsymbol{x}_{RE},\boldsymbol{x}')\phi|_0(\boldsymbol{x}',t)\,\mathrm{d}\boldsymbol{x}' \\ &= c_{RE}\langle\phi|_0\rangle \\ &= c_{RE}(\phi_{WE} - \langle\phi_{\mathrm{DL}}\rangle)\end{aligned} \tag{2.49}$$

with some constant c_{RE}.

Going back to the simplified 2d geometry, a symmetric position of the point like RE is not possible. A suitable choice is to assume that the RE is located at $z = z_{RE}$ (cf. Fig. 2.1). Using this assumption, the expansion (2.28) gives for the homogeneous situation the simple linear decrease of ϕ as a function of z

$$\phi|_{z_{RE}} = (1 - z_{RE})\phi|_0 \tag{2.50}$$

and thus $c_{RE} = 1 - z_{RE}$. One should keep in mind that z_{RE} can only be decreased to a certain value that is essentially given by the radius of the ring WE and that the approximation $c_{RE} = 1 - z_{RE}$ is a rather crude one. The true dependence of c_{RE} on the position of the RE will differ in its functional form as well as quantitatively from this expression. A generally valid expression is derived in chapter 3.

Together with Eqs. (2.48),(2.49) and after some rearrangements the potential drop over the electrolyte is given by

$$\phi_{WE} - \phi_{\mathrm{DL}} = \frac{U - \phi_{\mathrm{DL}}}{z_{RE}} - \frac{1 - z_{RE}}{z_{RE}}\left(\langle\phi_{\mathrm{DL}}\rangle - \phi_{\mathrm{DL}}\right). \tag{2.51}$$

Therefore the dynamics of the double layer potential in the case of a close reference electrode is given by

$$\begin{aligned}C_{DL}\frac{\partial}{\partial t}\phi_{\mathrm{DL}} = &-i_r + \frac{U - \phi_{\mathrm{DL}}}{AR_\Omega z_{RE}} \\ &- \frac{1}{AR_\Omega}\frac{1 - z_{RE}}{z_{RE}}(\langle\phi_{\mathrm{DL}}\rangle - \phi_{\mathrm{DL}}) - \frac{\sigma}{\beta}\left(\frac{\partial\phi}{\partial z} - \phi\right)\Big|_0.\end{aligned} \tag{2.52}$$

The pre-factor of the global coupling, α, is always negative in this case, and is bounded from below at a certain value determined by the radius of the ring WE, $\alpha \in]-\alpha_{min}(L), 0]$. Systems in which the above mentioned effects were observed due to NGC in (electro-) chemical systems are compiled, e.g., in [93].

2.5 Detailed Description of the Model Systems

As described in the introduction, the aim of this work is twofold. General mechanisms of pattern formation in electrochemistry as well as a detailed insight into the dynamics of real electrochemical systems is presented. The three model systems introduced in this section represent different degrees of abstraction. The prototype N-NDR presented in the next section is a general model for N-NDR systems with which most early results of spatio-temporal pattern formation in electrochemistry were derived [25, 34, 39, 40, 42, 95, 104, 107]. The periodate reduction in the presence of camphor, displaying an S-shaped current potential characteristic, is an intermediate case. The faradaic reaction current density entering into the double layer dynamics is modeled in the most general way, on the other side the mechanism given rise to an autocatalysis is modeled following the specific reaction. The model describing the oxidation of hydrogen in the presence of poisons is motivated by the rich dynamics found in this system in experiments. It does not resemble the minimal model of an HN-NDR oscillator [95]. Thus, the models are presented here in order of increasing complexity.

2.5.1 A Prototype N-NDR System – Peroxodisulfate Reduction

Reaction Current

The reaction current density during peroxodisulfate ($S_2O_8^{2-}$) reduction displays a genuine NDR that originates from the Frumkin effect. It is a common source of NDRs in systems in which the oxidation or reduction of an ion takes place close to the potential of zero charge (PZC).[5] Due to electrostatic interaction of the reactant ion with the WE, the potential within the double layer as well as the concentration of the reactant in the double layer change with changing double layer potential.

A general approach to model a current potential characteristic with an N-NDR is to fit the reaction current density with a polynomial of third order

$$i_r = \chi n F c k_0 (\phi_{\mathrm{DL}}^3 + k_1 \phi_{\mathrm{DL}}^2 + k_2 \phi_{\mathrm{DL}}). \tag{2.53}$$

The double layer potential is measured relative to the equilibrium potential. The constants $k_{0,1,2}$ are fitted to the reaction under consideration. χ equals $+1$ or -1 for oxidation or

[5] The potential of zero charge is defined as the potential at which no excess charge is present in the WE.

reduction reactions, respectively. In this work the reduction of peroxodisulfate is used. The respective constants were first given in [39] (cf. section 5 and appendix A.1.1).

Mass Transport Limited Negative Feedback

As described in section 2.2.1, the negative feedback in N-NDR oscillators is normally provided by the limited rate of diffusion from the bulk electrolyte to the double layer. Thus, the dynamics of the concentration at the double layer, $c(x,z=0,t)$, has to be derived. A good approximation of the concentration profile in the direction perpendicular to the WE is a linear increase/decrease of the concentration in a 'diffusion layer' of thickness δ [121]. In first order the value of δ depends on the diffusion constant of the reacting species, D, and on the viscosity of the electrolyte, ν. For a rotating ring WE it is given by [91]

$$\delta = 1.61 D^{1/3} \nu^{1/6} w^{-1/2} (r_o^3 - r_i^3)^{1/3} (0.5(r_o + r_i))^{-1}, \tag{2.54}$$

where r_o and r_i denote the outer and inner radius of the ring WE, respectively. w is given by the rotation rate of the WE. For $z > \delta$ the concentration equals the bulk concentration, denoted by c^b,

$$\begin{aligned} c(x,z,t) &= c(x,0,t) + (c^b - c(x,0,t))z/\delta && 0 < z \leq \delta \\ c(x,z,t) &= c^b && z > \delta. \end{aligned}$$

The temporal dynamics of the concentration in the double layer is given by the difference of two competing processes: The consumption of the reactant by the reaction with the rate $j_r = i_r/(nF)$ and the replenishment by diffusion from the bulk $j_d|_0 = D \left.\frac{\partial c(x,z,t)}{\partial z}\right|_0 = D\delta^{-1}(c^b - c(x,0,t))$.[6] On the other hand the rate of change of the number of reactant molecules in the diffusion layer, N, is given by

$$\frac{\mathrm{d}N}{\mathrm{d}t} = A\frac{\mathrm{d}}{\mathrm{d}t}\int_0^\delta c(x,z,t)\,\mathrm{d}z = A\frac{\delta}{2}\frac{\mathrm{d}c(x,0,t)}{\mathrm{d}t}$$

and also

$$\frac{\mathrm{d}N}{\mathrm{d}t} = A(j_d - j_r)$$

thus

$$\frac{\delta}{2}\frac{\partial c(x,0,t)}{\partial t} = -\frac{1}{nF}i_r + \frac{D}{\delta}(c^b - c(x,0,t)). \tag{2.55}$$

[6] Migration flux densities are neglected.

2.5.2 A Prototype S-NDR System – Periodate Reduction in the Presence of Camphor

The model used in this work to study electrochemical systems with an S-shaped current potential characteristic was introduced in Refs. [85, 107]. As mentioned in section 2.2.2 the autocatalysis in S-NDR systems has to be provided by a chemical step. Motivated by experiments [112], the positive feedback mechanism chosen is a first order phase transition of organic adsorbates that inhibit the faradaic reaction. It turned out that the most suitable compounds for this set up are camphor as the organic adsorbate that inhibits the reduction of periodate (IO_4^-) on a gold (111) electrode [122]. The phase transition is due to attractive interactions of the adsorbed camphor molecules. The density of adsorbed camphor on the WE surface changes reversiblely as a function of the double layer potential from a dilute to a dense phase and back [123].

Adsorbate Coverage Dynamics

The coverage of the electrode by camphor is denoted by θ. θ is measured with respect to the maximum number of adsorbed molecules per unit area, N_{max}, $\theta = N/N_{max}$, where N denotes the number of occupied surface sites. Following the arguments in section 2.1.2, the dynamics of the camphor coverage can be derived using the adsorption enthalpy. Frumkin proposed to introduce a global coupling between all adsorbed molecules which decreases the free adsorbed enthalpy linearly with increasing coverage (i.e., attractive interaction) [124]

$$G_{ad}(\theta) = q'\theta \quad (q' < 0). \tag{2.56}$$

The dependence of G_{ad} on the double layer potential originates from the change of the double layer capacitance due to adsorbed molecules.[7] We assume that the double layer capacitance varies linearly between the capacity at zero coverage denoted by C_{DL}^0 and C_{DL}^1 at $\theta = 1$

$$\frac{\mathrm{d}C_{DL}}{\mathrm{d}\theta} = C_{DL}^1 - C_{DL}^0. \tag{2.57}$$

For adsorbing organic molecules $C_{DL}^1 - C_{DL}^0 < 0$.[8] The change of the capacity due to an adsorbtion step leads to a changed energy stored in the double layer

$$\frac{\mathrm{d}E_{DL}}{\mathrm{d}C_{DL}} = -\frac{1}{2}\,{\phi_{\mathrm{DL}}}^2. \tag{2.58}$$

In order to be able to write Eq. (2.58) in this form the double layer potential has to be measured with respect to the PZC.

[7] In the following we neglect the change of the energy stored in the double layer due to dipole moments of the adsorbed organic molecules.

[8] This can be rationalized by considering that $C_{DL} = \varepsilon A d^{-1}$, where d denotes the thickness of the double layer that increases due to adsorption of organic molecules.

Table 2.1: *Parameter meaning and dimension*

k_{ad}	adsorption rate	$[\frac{\mathrm{cm}^3}{\mathrm{mol\,s}}]$
k_d	desorption rate	$[\mathrm{s}^{-1}]$
$c^b_{ad,r}$	bulk concentration of the adsorbing and reacting species, respectively	$[\frac{\mathrm{mol}}{\mathrm{cm}^3}]$
$C^{0,1}_{DL}$	capacity density of the WE at $\theta = 0$ and $\theta = 1$, respectively	$[\frac{\mathrm{C}}{\mathrm{V\,cm}^2}]$
N_{max}	maximum number of adsorbed molecules per cm^{-2}	$[\mathrm{cm}^{-2}]$
D_θ	diffusion constant of the coverage molecules	$[\frac{\mathrm{cm}^2}{\mathrm{s}}]$
q'	interaction strength of the adsorbate	$[\frac{\mathrm{J}}{\mathrm{mol}}]$
χ	equals ± 1 for oxidation or reduction reactions, respectively	[1]
$\alpha_{\theta,\phi_{\mathrm{DL}}}$	transfer coefficient for adsorption and reaction, respectively	[1]
$\mathrm{k_B}$	Boltzmann constant	$[\frac{\mathrm{J}}{\mathrm{K}}]$
k_r	reaction rate	$[\frac{\mathrm{cm}}{\mathrm{s}}]$
f	nF/RT	[1/V]

Thus, the energy change if one molecule is adsorbed, which results in a coverage change of $\Delta\theta = N_{max}^{-1}$, is given by

$$\frac{\mathrm{d}E}{\mathrm{d}\theta} = \frac{\mathrm{d}E}{\mathrm{d}C_{DL}}\frac{\mathrm{d}C_{DL}}{\mathrm{d}\theta} = -\frac{1}{2}(C^1_{DL} - C^0_{DL})\,{\phi_{\mathrm{DL}}}^2 \tag{2.59}$$

$$\rightsquigarrow \quad \Delta E = (2N_{max})^{-1}(C^0_{DL} - C^1_{DL})\,{\phi_{\mathrm{DL}}}^2 > 0. \tag{2.60}$$

The shift of the PZC due to the adsorption of organic adsorbates is neglected here for simplicity (it is taken into account in section 4.2.2). Taking the two independent influences together $G_{ad}(\theta, \phi_{\mathrm{DL}})$ reads

$$G_{ad}(\theta, \phi_{\mathrm{DL}}) = q'\theta + (2N_{max})^{-1}(C^0_{DL} - C^1_{DL})N_A\,{\phi_{\mathrm{DL}}}^2, \tag{2.61}$$

where N_A denotes Avogadro's constant.

This can now be entered into the suitable adapted 'reaction' rates introduced in section 2.1.2. The equivalents of the product and educt concentrations times the available area are the covered and free surface fractions, respectively

$$\nu_{ad} = k_{ad}c^b_{ad}(1-\theta)\exp\left(-\alpha_\theta\frac{G_{ad}(\theta,\phi_{\mathrm{DL}})}{RT}\right) \tag{2.62}$$

$$\nu_d = k_d\theta\exp\left((1-\alpha_\theta)\frac{G_{ad}(\theta,\phi_{\mathrm{DL}})}{\mathrm{RT}}\right). \tag{2.63}$$

The parameter meanings and dimensions are compiled in Table 2.1.[9]

[9] Notice in particular the three different units of the rate constants k_x.

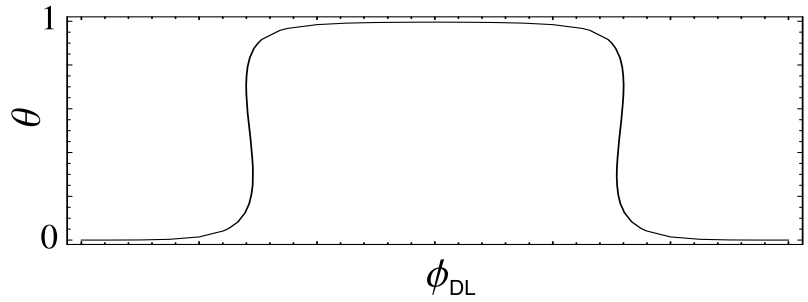

Figure 2.16: *Isotherm of the adsorbate coverage displaying two multivalued regions.*

The only relevant transport process for non-charged adsorbed particles is diffusion on the electrode surface. The attractive interactions between the adsorbed molecules are neglected for the moment. The consequences of these interactions, especially in the region of the first order phase transition, are considered in section 4.2.2. Thus, the spatio-temporal dynamics of the coverage is given by

$$\begin{aligned}\frac{\partial\theta(\boldsymbol{x},t)}{\partial t} &= v_{ad} - v_d + D_\theta\Delta\boldsymbol{x} \\ &= k_{ad}c^b_{ad}(1-\theta)e^{-\alpha_\theta\Delta G_\theta/RT} - k_d\theta e^{(1-\alpha_\theta)\Delta G_\theta/RT} + D_\theta\Delta\boldsymbol{x}.\end{aligned} \tag{2.64}$$

with

$$\frac{\Delta G_\theta}{RT} = \frac{q'\theta}{RT} + \frac{C^0_{DL} - C^1_{DL}}{2N_{max}k_BT}. \tag{2.65}$$

The isotherm of the adsorbate coverage for $\alpha_\theta = 0.5$ reads

$$\frac{\theta}{1-\theta} = \frac{k_{ad}c^b_{ad}}{k_d}e^{\Delta G_\theta/RT},$$

and is plotted in Fig. 2.16. For q' values above a critical interaction strength the isotherm exhibits two multivalued regions that indicate the presence of a first order phase transition. Which of the two regions is displayed as an S-shaped current potential curve depends on the sign of the reaction current.

Reaction Current

The reaction current density is modeled using Butler-Volmer kinetics (cf. Eq. (2.17)). The back reaction is neglected since the region of the autocatalytic behavior in θ is well separated from the equilibrium potential, ϕ^0_{DL}. Thus, the reaction current density is given by

$$i_r(\theta,\phi_{\mathrm{DL}}) = \chi nFc^b_r k_r(1-\theta)\exp\left(\chi\alpha_{\phi_{\mathrm{DL}}}f(\phi_{\mathrm{DL}} - \phi^0_{\mathrm{DL}})\right). \tag{2.66}$$

2.5.3 A Prototype HN-NDR System – Hydrogen Oxidation in the Presence of Poisons

Phenomenological Overview

The hydrogen oxidation reaction (HOR) on platinum electrodes is one of the most widely studied electrochemical reactions. Oscillations in this system are known to exist since 1930 [125]. Horányi was the first to show that the HOR exhibits oscillations in the presence of electrosorbing metal ions under galvanostatic conditions [126]. Furthermore, Krischer *et al.* showed that oscillations also occur under potentiostatic conditions for sufficiently high series resistance (either through the electrolyte solution or due to an external resistance) [127].

Additionally, a multitude of more intricate temporal dynamics was observed already a decade ago [128–131]. The system exhibits period doubling cascades, chaotic dynamics with an interior crisis and mixed-mode oscillations in certain parameter regions.

In recent measurements of spatiotemporal pattern formation during the HOR in the presence of Cu^{2+} and Cl^{-} Krischer *et al.* observed novel spatio-temporal phenomena which seem to be connected to the relaxation like form of the underlying oscillations [132, 133]. These included pulses, 1d target patterns[10], so termed asymmetric target patterns, modulated oscillations and a variety of other patterns, partly build upon the above mentioned ones.

In recent experiments conducted by Varela *et al.* even more complex patterns were observed, including low dimensional turbulence, clusters and spatiotemporal intermittent transitions into the turbulent regime [26, 133, 134].

Mechanistic View

The mechanism that leads to oscillations during the HOR is well understood and is made up of reaction steps that are independently studied. In a series of papers at the beginning of the 90s Krischer *et al.* proofed the essential role anions play in the oscillation mechanism [127, 135, 136] speculated about earlier [126, 137].

As stated in section 2.1.2, electro-catalytic reactions involve the adsorption of reaction intermediates or an educt on the WE surface. This causes a strong dependence of the reaction rate on the composition of the electrolyte since species dissolved in the electrolyte may also adsorb on the electrode surface. These adsorbates often accelerate or inhibit the reaction under consideration. The essential ingredient of the model presented in [127, 135, 136] to rationalize the occurrence of oscillations during H_2 oxidation in the presence of electrosorbing ions is that both dissolved species adsorb at the electrode surface and block the occupied surface sites for the HOR. The third variable necessary to describe

[10] These are not connected to an excitable medium but are observed in the oscillatory domain.

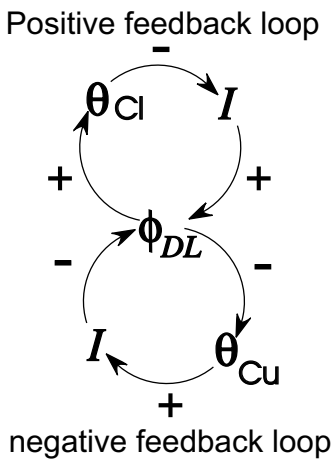

Figure 2.17: *Schematic diagram of activator (positive feedback) and inhibitor (negative feedback) loops.*

the oscillations is the double layer potential, ϕ_{DL}. The metal ion adsorption occurs at low potentials and the electrode is practically free of metal ions above a certain ϕ_{DL}. The halide ions behave in just the opposite way. For the rest of the thesis underpotential deposition of Cu^{2+} (occurring at low potentials) and specific adsorption of Cl^- (favored at more positive potentials) are taken to be the metal and halide ions, respectively, if not stated otherwise.

Since Cl^- adsorption is by far faster than adsorption of Cu^{2+}, the oscillatory mechanism can be described as follows (cf. Fig. 2.17) (the following applies to potentiostatic control, but the general mechanism is the same for the galvanostatic case):

Consider a situation where the Pt-surface is almost free of adsorbates, i.e., the oxidation current density is high and ϕ_{DL} is low. At low ϕ_{DL} Cu^{2+}-ions adsorb slowly, which causes the current to decrease, and thus, for a non-negligible cell resistance, ϕ_{DL} increases. At more positive values of ϕ_{DL} Cu starts eventually to desorb and Cl^- ions to adsorb. As illustrated in Fig. 2.17, the increase in chloride coverage with increasing potential initiates an autocatalytic process (positive feedback loop, N-NDR sub-system): An increase in the Cl^- coverage, θ_{Cl}, leads to a smaller current density, a smaller current density to a larger value of ϕ_{DL}, and thus to a further increase in θ_{Cl}. The decrease in Cu coverage with increasing potential, on the other hand, causes an increase in current density which inhibits the further growth of ϕ_{DL}. Thus, it generates a negative feedback loop. Owing to the faster adsorption/desorption rates of Cl as compared to Cu, the characteristic time of the positive feedback loop is shorter than the one of the negative feedback loop. This causes the above mentioned initial increase in ϕ_{DL} due to Cu adsorption to be enhanced owing to Cl^- adsorption. Only at these larger values of ϕ_{DL} will Cu desorption be sufficiently fast to cause a decrease in ϕ_{DL} again. This decrease of ϕ_{DL} now prompts a decrease in Cl^- coverage, initiating again the autocatalytic process, this time to smaller

values of ϕ_{DL}. In this way, the system arrives back at a state where the surface is almost copper and chloride free, and the cycle starts anew.

Mathematical Model(s)

Taking into account the potential dependent coverages of metal and halide ions the oscillations could be modeled [127, 135, 136]. The model presented in [135] included the two coverages and the double layer potential, but neglected the dependence of the hydrogen current density, i_{H_2}, on ϕ_{DL}.[11] This seemed justified since the hydrogen oxidation current density is limited by the rate of diffusion of the H_2 molecules from the bulk electrolyte to the WE already for very low overpotentials, reflecting that the HOR is one of the fastest known electrochemical reactions so that mass transport becomes the rate determining step. In the absence of poisons the hydrogen current density thus reaches a diffusion limited plateau for overpotentials of ca. 50 mV. Consequently, the hydrogen current density only depends on the available free surface sites $(1-\theta_{Cu}-\theta_{Cl})$, where θ_{Cu} and θ_{Cl} denote the portion of the WE covered by Cu^{2+} and Cl^-, respectively. Since it can be assumed that the hydrogen oxidation is preceded by dissociative adsorption of H_2 [91], i_{H_2} was modeled proportional to the square of the free adsorption sites

$$i_{H_2} = \frac{k_H^a c_H^b (1-\theta_{Cu}-\theta_{Cl})^2}{1+(k_H^a/k_{diff})(1-\theta_{Cu}-\theta_{Cl})^2}.$$

k_H^a denotes the adsorption rate, c_H^b the bulk concentration of hydrogen and k_{diff} the rate of diffusion from the bulk to the electrode. The adsorption and desorption of Cu^{2+} and Cl^- contribute $i_{Cu^{2+}}$ and i_{Cl^-} to the total faradaic current density, respectively. The current originating from halide ad- or desorption can be neglected since it is in general small. The copper current density is given by $i_{Cu^{2+}} = q_M \dot{\theta}_{Cu}$, where q_m is the charge flowing during the adsorption of one monolayer of Cu^{2+}.

The evolution of the coverages was modeled with Butler-Volmer kinetics [136]

$$N\dot{\theta}_{Cu} = k_{Cu}^a c_{Cu}^b (1-\theta_{Cu}-\theta_{Cl}) - k_{Cu}^d \theta_{Cu}$$
$$N\dot{\theta}_{Cl} = k_{Cl}^a c_{Cl}^b (1-\theta_{Cu}-\theta_{Cl}) - k_{Cl}^d \theta_{Cl}$$

with

$$k_{Cu/Cl}^a = k_{Cu/Cl}^{a,0} e^{-f_{Cu/Cl}\left(\phi_{DL}-\phi_{DL}^{Cu/Cl,0}\right)}$$
$$k_{Cl/Cu}^d = k_{Cu/Cl}^{d,0} e^{f_{Cu/Cl}\left(\phi_{DL}-\phi_{DL}^{Cu/Cl,0}\right)}.$$

[11] In [136] also a model with potential dependent hydrogen current density was presented, but the potential dependence was phenomenological and based on a non-langmuiric behavior of the current which was falsifi ed by the realistic model presented here (see section 6).

c^b_{Cu} and c^b_{Cl} denote the bulk concentrations of copper and chloride, respectively. N denotes the number of free surface sites per unit area on Pt. f_x quantifies the potential dependence of the adsorption/desorption processes, which (since $\alpha_x = 0.5$ for simplicity) are determined by $f_x = \alpha_x n_x F(RT)^{-1} = (1-\alpha_x) n_x F(RT)^{-1}$ and n_x is the number of transferred electrons during the adsorption/desorption process. The rate constants of adsorption and desorption of Cu^{2+} and Cl^- are given by $k^{a,0}_{Cu/Cl}$ and $k^{d,0}_{Cu/Cl}$, respectively.

The above model was able to reproduce the general oscillatory behavior, i.e., it showed qualitative agreement of theoretical and experimental bifurcation diagrams.

2.6 Methods

2.6.1 Spatial Discretization - Pseudo Spectral Method

Solving partial differential equations (PDEs) numerically requires a suitable discretization of space. A common approach is the approximation of space by a grid with fixed grid spacing. Spectral decomposition explicitely uses the form of the spatial operator. Suppose one wants to solve a PDE of the form

$$\frac{\partial u}{\partial t} = Lu + F(u, u_x, \ldots, u^k_x) \tag{2.67}$$

numerically, where $u(x,t)$ is a state vector, L a spatial operator and F a nonlinear function of $u^k_x = \frac{\partial^k u}{\partial x^k}$. Eq. (2.67) has to be supplemented with some boundary conditions to be well posed. Now, the functional form of the spatial operator together with the boundary conditions is taken into account by the use of a set of orthonormal functions $\varphi_i(x)$ which are eigenfunctions of the spatial operator L, $L\varphi_i = \lambda_i \varphi_i$ with the eigenvalues λ_i and fulfill the boundary conditions. The generic example being Fourier modes with periodic boundary conditions. u can then be expanded in an infinite series of the basis functions

$$u(x,t) = \sum_{n=0}^{\infty} a_n \varphi_n,$$

which yields an infinite set of coupled ordinary differential equations

$$\frac{\partial a_n}{\partial t} = \lambda_n a_n + P_n F \qquad n = 0, \ldots, \infty.$$

$P_n F$ denotes the projection of F on the subspace of the respective mode n. In any numerical procedure the series has to be truncated at some fixed N. This leads to a projection of function space B into a subspace $B_N \subset B$, defined through a projection operator, which we will denote P_N. If one also expands the projected nonlinear function

$$P_N F(u_N, (u_N)_x, ..., (u_N)^k_x) = \sum_{n=0}^{N} f_n(a_0, \ldots, a_N)\varphi_n(x)$$

the result is a set of $N+1$ coupled equations for the mode coefficients a_n, which can now be integrated in time

$$\dot{a}_n = \lambda_n a_n + f_n(a_0, \ldots, a_N)$$

The Jacobian of the system is given by

$$J_{nm} = \frac{\partial \dot{a}_n}{\partial a_m} = \lambda_n \delta_{nm} + \frac{\partial f_n}{\partial a_m} \tag{2.72}$$

The straight forward method to determine $f_n(a_0, \ldots, a_N)$ and $\frac{\partial f_n}{\partial a_m}$ is the so called Galerkin or true spectral method. The expansion of u is entered in $F(u, \ldots)$ analytically and the respective projection on the subspace φ_i is calculated. Unfortunately, this method is too time consuming for the problems that are the subject of the present contribution. Therefore, the *pseudo spectral method*, which is outlined in the following paragraph, is applied in this work.

Pseudo Spectral Method

The idea of the pseudo spectral method is to fulfill the approximation of F through the basis functions φ_n not in the entire space interval $[0, L]$ but at $N+1$ *collocation points* x_i [138]

$$\begin{aligned} F(x_i) &= P_N F(x_i) \\ &= \sum_{n=0}^{N} f_n(a_0, \ldots, a_N) \varphi_n(x_i), \end{aligned}$$

which can be written in the more convenient form

$$\begin{pmatrix} F(x_0) \\ \vdots \\ F(x_N) \end{pmatrix} = \begin{pmatrix} \varphi_0(x_0) & \cdots & \varphi_N(x_0) \\ \vdots & & \vdots \\ \varphi_0(x_N) & \cdots & \varphi_N(x_N) \end{pmatrix} \begin{pmatrix} f_0(a_0, \ldots, a_N) \\ \vdots \\ f_N(a_0, \ldots, a_N) \end{pmatrix}. \tag{2.73}$$

We will sometimes abbreviate this with the notation

$$\boldsymbol{F} = \widehat{\boldsymbol{\varphi}} \boldsymbol{f}.$$

Thus, the following steps are followed after choosing the orthonormal basis set when using the pseudo spectral method to solve Eq. (2.67)

1. Choose an appropriate value of N, that is, an approximation of the true function space through the functions $\varphi_0, \ldots, \varphi_N$.

2. Choose N collocation points x_i in the space interval.

3. Perform a discrete transform of the series $F(x_0),\ldots,F(x_N)$ to obtain the coefficients $f_i(\boldsymbol{a})$.

To obtain the Jacobian of the resulting coupled system of ordinary differential equations (ODEs) one has to compute [139]

$$\frac{\partial \boldsymbol{f}}{\partial \boldsymbol{a}} = \widehat{\varphi}^{-1}\frac{\partial \boldsymbol{F}}{\partial \boldsymbol{a}}$$

with

$$\begin{aligned}\left(\frac{\partial \boldsymbol{F}}{\partial \boldsymbol{a}}\right)_{nm} &= \left(\frac{\partial F}{\partial a_m}\right)\Big|_{x_n} \\ &= \sum_{k=0}^{p}\frac{\partial F}{\partial u_x^k}\frac{\partial u_x^k}{\partial a_m}\Big|_{x_n} \\ &= \sum_{k=0}^{p}\frac{\partial F}{\partial u_x^k}\frac{\partial}{\partial a_m}\frac{\partial^k}{\partial x^k}\sum a_i\varphi_i \\ &= \left[\sum_{k=0}^{p}\frac{\partial F}{\partial u_x^k}\frac{\partial^k\varphi_m}{\partial x^k}\right]_{x_n}\end{aligned}$$

To simplify the above further, let us assume that we want to use a full Fourier set for the expansion and let $F = F(u)$, $L = \frac{\partial^2}{\partial x^2}$. It then follows that

$$L\varphi_n = -n^2\varphi_n$$

and

$$\left(\frac{\partial \boldsymbol{F}}{\partial \boldsymbol{a}}\right)_{nm} = \varphi_m(x_n)\frac{\partial F}{\partial u}\Big|_{x_n}.$$

The part of the Jacobian determined by the local dynamics is now given by the discrete Fourier transform of $\left(\varphi_m(x_0)\frac{\partial F}{\partial u}\Big|_{x_0},\ldots,\varphi_m(x_N)\frac{\partial F}{\partial u}\Big|_{x_N}\right)$ which gives $\left(\frac{\partial f_0}{\partial a_m},\ldots,\frac{\partial f_N}{\partial a_m}\right)$ for all $m = 0,\ldots,N$. Entering the Fourier-transform in Eq. (2.72) the full Jacobian can be computed.

Aliasing

There remains one important point to be discussed. In general $F(u_N,\ldots,(u_N)_x^k) \notin B_N$ and thus, the sampling of F with N collocation points will in general yield "wrong" results in a sense which will become clear in the following example. Let $F = uu_x$. It follows that if $u = \sin 2x$, $F(\sin 2x) = \sin 4x$. For only two collocation points, F is sampled as

$-\sin 2x$ ("aliasing"). But the best approximation (in terms of $\|F(u) - F_N(u)\|$) of $\sin 4x$ in $B_N = \text{span}(1, \sin x, \sin 2x)$ is $F(\sin 2x) = 0$. The solution to this problem is to sample F at $M > N$ collocation points. The best value of M for a given N depends on the nonlinearity in F. After choosing M, aliasing errors can be kept below a desired threshold with the following procedure

1. Compute F at M collocation points x_m.
2. Solve the M-dimensional linear system (2.73) for f_m. (Equivalent to performing M discrete Fourier transforms.)
3. The best $N-$dimensional approximation of F is then given by the first N of the M Fourier-coefficients f_m of F.

As stated above, there remains the question on how many collocation points one should use for a given nonlinearity and a given N. This question is not solved for general nonlinearities, so one has to choose an appropriate relation between M and N that keeps the aliasing error below a desired level. In this work $M = 4N$ is used.

Numerical Correctness

To determine the minimum number of modes to solve a certain set of equations correctly, the minimal size of a spatial structure that can be expected in the system must be known. In a reaction-diffusion system this size is approximately given by the diffusion length, l_D. If the dynamics of a variable v are governed by an equation of the form

$$\tau \dot{v} = f(v) + D\Delta v$$

the diffusion length is – roughly speaking – of the order $\sqrt{\tau D}$.

Using Fourier modes and rescaling space to $[0, 2\pi[$, the diffusion length has to exceed one over the number of the highest mode, N, $l_D \gg 1/N$. In cases in which the typical size of the smallest structure to be expected is only poorly known, the proper modeling of the spatio-temporal dynamics can be checked by ensuring that, e.g., 99% of the dynamics is covered already by taking $m \ll N$ modes into account.

2.6.2 Integration

A common issue when integrating systems of ODEs that describe electrochemical dynamics are the different time scales on which the dynamics of the individual variables takes place. The rate of change of the double layer potential is in general much higher than that of the other, chemical, variables. The slower timescales determine the time span of interest, thus a typical stiff dynamical system is to be investigated. A dynamical system

is defined as ‘stiff’, if the Jacobian matrix has an eigenvalue whose real part is negative and large in magnitude, compared to the reciprocal of the time span of interest. The common methods to integrate such systems are so called *Predictor-Corrector* algorithms that combine explicit and implicit steps [140].

In this work the Livermore Solver for Ordinary Differential Equations (lsode) with the option for stiff systems is used. The method implemented in lsode is the so called backward differentiation method (or BDF method, or Gear’s method) with order up to five [141].

2.6.3 Continuation

The bifurcation diagrams presented in this work are calculated using the continuation software AUTO [142]. In AUTO the pseudo-arclength continuation technique is implemented. Limit cycles are continued via discretization in time opposed to the so called ‘shooting’ method implemented, e.g., in [143]. The time discretization imposes limits on the feasibility of the continuation of relaxation like oscillations which would require a huge number of collocation points.

Chapter 3

Pattern Formation in the Presence of Ohmic Drop Compensation

In this chapter we derive an extension of an equation describing the double layer dynamics in the presence of an external resistor as well as a close RE. In particular, it includes the experimentally very important case of (external) electronic drop compensation. By comparing the results obtained earlier, we demonstrate that the cell resistance which is compensated when placing the RE on the axis of the cell and close to the WE manifests itself in the evolution equation of the double layer potential in exactly the same way an external series resistor of the same magnitude but negative impedance would do. This implies not only that the strength of the global feedback can easily be measured and thus its impact on the system's behavior predicted but also that any external electronic cell compensation exerts the same destabilizing global coupling on the system, independent of relative arrangement and geometry of the electrodes.

The impact of the global coupling on the dynamics of the system depends strongly on the strength of the coupling. In the case of the external resistor, the strength of the coupling is readily obtained (Eq. (2.47)). It depends on cell resistance and external resistance, i.e., on two parameter values that are readily accessible in an experiment. This is not the case for the global coupling caused by a close RE. Eq. (2.52) was derived for the 2d-geometry and is not valid in this simple form in 3d. Geometric factors depending on the ring width and the positions of the RE and possibly also the CE have to be included. The most developed approach is discussed in [36], where a closed expression for the coupling strength is derived for a ring WE of arbitrary width, the RE on the axis of the ring and - for mathematical simplicity - the (infinitely extended) CE at infinity. For this electrode arrangement the coupling strength depends on the electrolyte conductivity, the (scaled) distance between the WE and the RE and the geometric contribution to the cell resistance. From a practical aspect, the geometric contribution to the cell resistance is difficult to obtain. Furthermore, it remains to be proven that the given expression is

independent of the special choice of geometry and position of the CE.

3.1 General Equation for the Double Layer Dynamics

A more general formulation of the evolution equation in the presence of some compensated electrolyte resistance can be obtained using Eq. (2.4) and comparing it with Eq. (2.50). The proportionality factor between $\phi|_0$ and $\phi|_{z_{RE}}$, c_{RE}, can be expressed by the cell resistance and the uncompensated resistance $c_{RE} = R_\Omega^{-1}(R_\Omega - R_u)$. This expression will be used from now on, since it is demonstrated in [102] that it also holds for realistic geometries. Consequently, the double layer dynamics with a close RE is given by

$$C_{DL}\frac{\partial}{\partial t}\phi_{\mathrm{DL}} = -i_r + \frac{U-\phi_{\mathrm{DL}}}{AR_u} - \frac{1}{AR_\Omega}\frac{(R_\Omega - R_u)/R_\Omega}{1-(R_\Omega - R_u)/R_\Omega}(\langle\phi_{\mathrm{DL}}\rangle - \phi_{\mathrm{DL}}) - \frac{\sigma}{\beta}\left(\frac{\partial\phi}{\partial z} - \phi\right)\Big|_0 . \tag{3.1}$$

Comparing the evolution equation derived for the double layer potential in the presence of an external resistor, Eq. (2.47), and Eq. (3.1), we arrive at the following formulation of the evolution law of the electrode potential for the general case

$$C_{DL}\frac{\partial}{\partial t}\phi_{\mathrm{DL}} = -i_r + \frac{U-\phi_{\mathrm{DL}}}{AR_\Omega(1+\rho)} + \frac{1}{AR_\Omega}\frac{\rho}{1+\rho}(\langle\phi_{\mathrm{DL}}\rangle - \phi_{\mathrm{DL}}) - \frac{\sigma}{\beta}\left(\frac{\partial\phi}{\partial z} - \phi\right)\Big|_0 \tag{3.2}$$

with

$$\rho = \frac{R_e}{R_\Omega} - \frac{R_\Omega - R_u}{R_\Omega}. \tag{3.3}$$

Eq. (3.2) is the central equation in electrochemical dynamics.[1] ρ defines a universal global coupling parameter in electrochemical systems. ρ varies in the interval $]-1,\infty[$. The left boundary is approached for very close distances of WE and RE. Some uncompensated resistance will always be present in the ring geometry if a close RE is used since the RE is positioned on the ring axis and can thus not be brought arbitrarily close to the WE. If external *IR*-compensation is used this limitation is lifted. $\rho \to \infty$ corresponds to the galvanostatic operation mode. The NGC strength $\alpha = \rho(AR_\Omega(1+\rho))^{-1}$ is displayed in Fig. 3.1 as a function of ρ.

As mentioned in section 2.3 some positive global coupling is present in electrochemical systems for $\rho = 0$ due to the migration coupling. It is useful to define a critical $\rho_c < 0$

[1] The spatial coupling must be rewritten in the form of a Green's function for general cell and electrode geometries (cf. Eq. (2.24)) since the above formulation is only valid for certain setups [26].

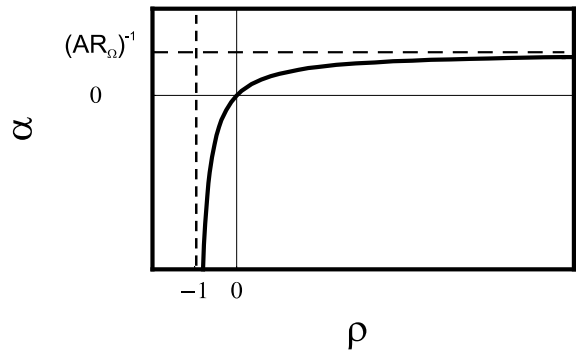

Figure 3.1: *Global coupling strength* α *as a function of* ρ.

such that no residual global coupling is left for $\rho = \rho_c$. The definition of ρ_c is not unique.[2] ρ_c depends on β and σ.

To suppress the dependence of the local dynamics on parameters determining essentially the global coupling strength, σ is redefined as follows $\sigma \to \sigma(1+\rho)^{-1}$. Thus

$$C_{DL}\frac{\partial}{\partial t}\phi_{\mathrm{DL}} = -i_r + \frac{\sigma}{\beta}(U-\phi_{\mathrm{DL}}) + \frac{\sigma\rho}{\beta}(\langle\phi_{\mathrm{DL}}\rangle - \phi_{\mathrm{DL}}) - \frac{\sigma(1+\rho)}{\beta}\left(\frac{\partial\phi}{\partial z} - \phi\right)\Big|_0 . \quad (3.4)$$

Eq. (3.4) will be used in the studies presented in this thesis to investigate the influence of ρ on electrochemical pattern formation. It is important to keep in mind that, by fixing the local dynamics using the redefinition of σ, the spatial coupling strength in the physical system is changed whenever the global coupling is varied (σ is lowered for NGC and increased in the presence of an external resistor with positive impedance).[3]

3.2 Discussion

Examining the definition for ρ, it becomes apparent that the compensated resistance, $R_\Omega - R_u$, acts exactly in the same way an external resistor with negative impedance of the same magnitude as the compensated resistance would. Consequently, this prediction was tested in 3d-simulations and experiment. It was found that the dynamics observed in an explicit 3d-model implementing the ring geometry on the one side with a close RE and on the other side with a suitable negative external resistor is indistinguishable. Also experimental tests gave the same result within the limits of experimental accuracy [102].

This suggests that a global coupling through the potentiostatic control is present whenever there is some compensated resistance. This is, however, exactly what is realized

[2] One possibility is to define $\rho_c := -\alpha_p$ where α_p is given by the pre-factor of the global coupling if the migration coupling is compared with a global-diffusive coupling $\alpha_p(\langle\phi_{\mathrm{DL}}\rangle - \phi_{\mathrm{DL}}) + D\Delta\phi_{\mathrm{DL}}$ and it is required that the dynamics of the homogeneous and the first mode is equal [104].

[3] Note that still $\sigma > 0\ \forall\rho$.

when the ohmic drop of the cell is compensated by electronic compensation, as it is possible with most commercial potentiostats. This represents an important insight since in most electrochemical experiments the *IR* drop through the electrolyte which is inevitably present is undesired. Hence, routinely, *IR* compensation is invoked. Through the reformulation of the global coupling in terms of the uncompensated resistance it becomes apparent that any compensation of the cell resistance, be it by means of a close RE or by means of an external electronic circuit introduces a NGC into the system and thus causes the 'danger' of destabilizing the uniform electrode [36, 37, 41, 43, 45, 97, 98, 100, 114, 115, 133, 144–146].

In this view, it might turn out to be necessary to reinterpret some results such as rate constants which were obtained under the assumption that the measured global quantities are representing the respective local densities at the entire WE. There exists another advantage of formulating the double layer potential dynamics in the form of Eq. (3.2). Now also for a close RE it is straight forward to experimentally determine the strength of the global coupling: one only needs to measure the cell resistance and the uncompensated resistance and the factor in front of the global coupling can be calculated.

3.3 Conclusions

The formulation of the strength of the global coupling in terms of the compensated and the total cell resistances for a ring-shaped WE and the RE on the axis of the ring originally derived for the 2d-geometry is valid in general. It enables the measurement of the global coupling strength. Moreover, it revealed that also any external, electronic ohmic drop compensation exerts a NGC whose strength is given by the same mathematical expression. An implication of this fact is that it might make a difference for the dynamic behavior of an electrochemical system whether a cell with an a priori small cell resistance is used or whether the cell resistance is compensated, either by use of a close RE or electronically.

For a ring-shaped WE with the RE on the axis of the ring these two means of ohmic drop compensation are completely equivalent. However, whenever the RE still compensates some cell resistance but is not located on the symmetry axis of the cell or when the WE has a different shape, the strength of the negative feedback is a function of the position of the electrode (cf. section 2.3.1), whereas the feedback through the external, electronic ohmic drop compensation is always strictly global. Hence, in these cases the resulting dynamics is different for the two modes of *IR*-compensation even if the magnitude of the compensated resistance is the same. This opens the possibility to study the dynamics of two-dimensional electrodes in the presence of strictly NGC [122], and of a weighted global coupling [101]. Both are areas of wide interest that have only little been explored so far.

Chapter 4

S-NDR Systems – Breathing Domains and Turing Patterns

This section deals with pattern formation in S-NDR systems. As stated in section 2, S-NDR systems in general favor the occurrence of spatial patterns. In the first section of this chapter the interaction of a spatial instability caused by global coupling with a temporal instability is investigated. The global coupling is mediated through a very high electrolyte conductivity and thus introduces a new form of global coupling not yet discussed in electrochemical systems. This research was motivated by fascinating results obtained in formally similar semiconductor systems [15].

The second section is concerned with more extensive studies on the afore mentioned Turing patterns. The earlier studies on Turing patterns in electrochemical systems [46,85] made far reaching approximations whose validity is tested. In section 4.2.1 the condition for the occurrence of a Turing instability is given without the assumption of a spatially constant double layer capacity. The second assumption tested is if a more realistic model of the attractive adsorbate-adsorbate interaction is compliant with the experimentally observed structures.

The local functions f and g we use to model the S-NDR system were given in section 2.5.2. The transformations of time and potential and the derivation of the non-dimensional parameters used in the following is given in appendix A.1.2. Note that slightly different rescalings are used in the next sections, accounting, e.g., for different boundary conditions. For simplicity, we use an oxidation reaction, $\chi = 1$, to model the reaction current (opposed to the periodate reduction reaction in the experiment). The following functions result for the local dynamics of the activator and the reaction current density i_r (cf. Eqs. (2.64),(2.66))

$$i_\mathrm{r}(\phi_\mathrm{DL},\theta) = \gamma(1-\theta)e^{\phi_\mathrm{DL}} \tag{4.1}$$

$$f(\phi_\mathrm{DL},\theta) = \mu\left[(1-\theta)e^{-\nu\phi_\mathrm{DL}^2-q\theta} - p\theta e^{\nu\phi_\mathrm{DL}^2+q\theta}\right]. \tag{4.2}$$

Note the non-polynomial nature of the function f.

The parameters ν, q and p correspond to such physical values as free adsorption sites or interaction strength. γ depends on the well accessible concentration of the reacting species, which can be varied over several decades; γ and μ are proportional to L^2. The parameters ν, p and g are fixed throughout this chapter at $\nu = 0.025$, $p = 0.5$ and $q = -2.4$ (cf. appendix A.1.2) .

4.1 Stationary and Breathing Domains

4.1.1 Introduction

Complex spatio-temporal behavior in reaction-diffusion equations, which is in a wider sense the class of equations dealt with also in electrochemistry, might be found when instabilities breaking time and space symmetries interact. A generic case is the interaction of Turing and Hopf bifurcation in a two component activator-inhibitor system in which the involved species diffuse. Complex spatio-temporal dynamics has been found near this codimension-two point theoretically [147–149] as well as experimentally [150–152].

In this section, we consider systems with high electrolyte conductivity. In such systems the migration coupling is so efficient that any spatial variation in ϕ_{DL} can be neglected which results in an additional global coupling. The set of equations to be investigated is thus of the general form

$$\tau_{\phi_{\mathrm{DL}}} \frac{\mathrm{d}\phi_{\mathrm{DL}}}{\mathrm{d}t} = g(\phi_{\mathrm{DL}}, \langle\theta\rangle_A) \tag{4.3}$$

$$\tau_{\theta} \frac{\partial\theta}{\partial t} = f(\phi_{\mathrm{DL}}, \theta) + D\Delta\theta, \tag{4.4}$$

where θ stands for the activator variable, whose dynamics comprises an autocatalytic chemical step. The angular brackets denote the spatial average over the spatial domain A. f is autocatalytic in θ; g exhibits a monotonic characteristic as a function of ϕ_{DL} and θ (cf. Eqs. (4.1),(4.2)). $\tau_{\phi_{\mathrm{DL}}(\theta)}$ denote the characteristic times for changes in ϕ_{DL} and θ, respectively.

A formally very similar set of equations describes the dynamics in bistable semiconductor systems operated via an external load resistance [15, 47, 48, 153]. The formation and dynamics of current density patterns in bistable semiconductors was extensively studied [49, 52, 82–84]. In this respective class of semiconductor systems the current-voltage characteristic also resembles the shape of an S, which points to the fact that the roles of the dynamic variables are very similar to the electrochemical model: The voltage drop u across a semiconductor device acts effectively as inhibitor, and it is subject to a global constraint imposed by the external electric circuit. The role of the activator variable

might be played by different physical quantities, such as the electron temperature [47], the concentration of excess carriers [154], the charge density in resonant tunneling structures [84, 155, 156],[1] the voltage drop across pn-junctions in thyristors [51, 157] or the interface charge density in a heterostructure hot electron diode (HHED) [83]. The dynamic equations are of the same structural form as Eqs. (4.3),(4.4); only the local nonlinear functions f and g differ from the electrochemical model.

For the current density dynamics in a class of models originally derived for the HHED in one or two spatial dimensions under galvanostatic (current-controlled) conditions, interesting complex spatio-temporal patterns termed "spiking" and "breathing" current filaments were found [82, 153]. Recently, a sufficient condition for the onset of such complex spatio-temporal dynamics was given [52].

Realizing the obvious similarities, we show in this section that the methods (e.g., for analyzing the dynamics) developed for the semiconductor system can be applied to gain insight into the interaction of different instabilities in the electrochemical system. Results regarding the possibility of the occurrence of complex spatio-temporal behavior and the mechanisms that lead to such behavior are given. It is emphasized whether the different dynamical regimes depend upon the general structural form of the equations, especially regarding the influence of global coupling, or if they are due to special properties of the underlying physical or chemical system, and thus the local dynamics. Hence a comparison of electrochemical and semiconductor systems gives considerable insight into generic complex dynamics of globally coupled bistable systems.

In the next section the electrochemical model is given in its dimensionless form and its important parameters and the mechanisms leading to global coupling in the model are discussed. In the following section we characterize the dynamics of the model by linear stability analysis along the lines developed for the semiconductor model [84] and by numerical simulations. In the discussion we compare the important features of the two models. The mechanism leading to complex spatio-temporal behavior in both models is different and this difference is explored in this section in some depth. We summarize our results in section 4.1.5 and give a short outlook to applications in terms of experimental verifications and transfer of the electrochemical results to the semiconductor model.

4.1.2 Model

To make things as transparent as possible and to facilitate later comparison with the semiconductor model, we employ the idealized geometry shown in Fig. 4.1. WE and CE are equally sized rectangular plates positioned parallel to each other in a box-like cell with otherwise insulating walls. This geometry imposes no-flux boundary conditions for ϕ_{DL}

[1] Note that for bistable resonant tunneling structures the current-voltage characteristic is Z-shaped resulting in an *activatory*, not inhibitory effect of the global constraint.

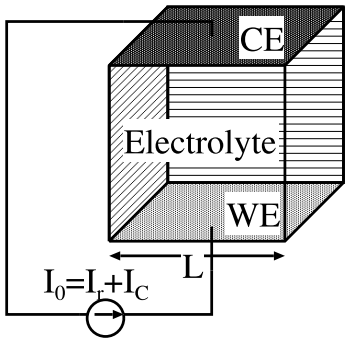

Figure 4.1: *Schematic setup of an electrochemical system realizing a rectangular WE with no-flux boundary conditions. WE and CE form top and bottom of the box-like cell with otherwise insulating walls.*

and θ; there will be no spatial inhomogeneities of the electric field at the interface imposed by this geometry.

Moreover, for very high electrolyte conductivities σ, spatial inhomogeneities in the double layer potential are damped out very fast via the efficient coupling through migration currents. It follows that spatial variations of ϕ_{DL} can be neglected. This effectively introduces a global coupling in the system, since local perturbations in ϕ_{DL} are felt instantaneously in the entire double layer.

In the following we additionally assume current controlled conditions. The dynamics of the activator variable θ are modeled by an equation of the form (4.4), where we restrict our system to 1d since the qualitative behavior should also be captured on 1d domains. 1d domains also resemble the situation of a very large aspect ratio of the rectangular domain, where one spatial dimension is too small to allow for spatial instabilities and can thus be eliminated. In this section we normalize space to the interval $[0,\pi]$ for computational convenience.

The dimensionless set of equations is thus

$$\frac{\partial \phi_{\mathrm{DL}}}{\partial t} = \gamma(i_0 - (1 - \langle\theta\rangle)e^{\phi_{\mathrm{DL}}}) \tag{4.5}$$

$$\frac{\partial \theta}{\partial t} = \mu\left((1-\theta)e^{-\nu\,\phi_{\mathrm{DL}}{}^2 - q\theta} - p\theta e^{\nu\,\phi_{\mathrm{DL}}{}^2 + q\theta}\right) + \frac{\partial^2 \theta}{\partial x^2} \tag{4.6}$$

subject to the boundary conditions

$$\left.\frac{\partial \theta}{\partial x}\right|_{x=0,\pi} = 0.$$

The brackets again denote the average over the spatial domain

$$\langle\theta\rangle = \frac{1}{\pi}\int_0^\pi \theta(x)\,\mathrm{d}x.$$

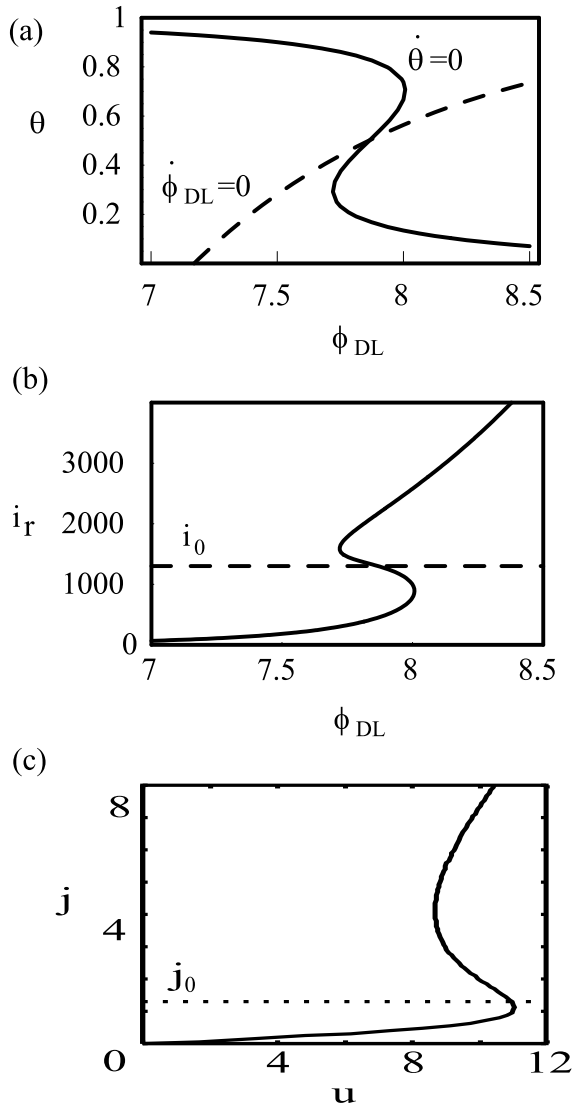

Figure 4.2: *(a) Nullclines of the model (4.5),(4.6) for an imposed current density in the autocatalytic regime (solid line* $\dot{\theta} = 0$*, dashed line* $\dot{\phi}_{\mathrm{DL}} = 0$*,* $i_0 = 1300$*,* $\nu = 0.025$*,* $q = -2.4$*,* $p = 0.5$*). (b),(c) S-shaped current-potential (voltage) curve together with the load line* i_0 *(*j_0*) for the electrochemical (Eq. (4.5),(4.6)) and the semiconductor (Eq. (4.12),(4.13)) system (s.b.), respectively.*

Eq. (4.5) suggests to define $i_r := (1-\theta)e^{\phi_{\mathrm{DL}}}$ as reaction current in the following, since the nullclines are not changed when changing γ.

In Fig. 4.2(a) the nullclines of the system are depicted for a current density i_0 that is set in the range of the negative differential resistance in the current-potential characteristic (see Fig. 4.2(b)). The S-shaped current-potential characteristic is depicted together with the load line $i = i_0$ in Fig. 4.2(b). This physically more intuitive (i-ϕ_{DL})-plane representa-

tion will be used in the following.

The dynamics is determined by the model parameters $\mu \propto L^2$, the relaxation time ratio of activator and inhibitor γ/μ (independent of L), and the general excitation level controlled by the imposed current density i_0. i_0 can be set by the galvanostatic control unit and typical values are of the order 10^3–10^4. The relaxation time ratio can be accessed easily via the concentrations of the reacting and adsorbing species.

The numerical results discussed in the following sections were obtained using 15 spatial cosine-modes (the results do not change when a larger number of modes is chosen). Recalling section 2.6.1, 15 modes only suffice if patterns of the size of the diffusion length can be captured. The diffusion length is given here by $l_D = \sqrt{\mu^{-1}}$, thus 15 modes can be used up to $\mu \simeq 100$.

4.1.3 Stability Analysis and Simulations

Homogeneous Steady State

In this section we consider the spatially uniform fixed points of the system (4.5),(4.6) and their bifurcations. The uniform steady state $(\phi_{\mathrm{DL}}^{ss}, \theta^{ss})$ is given by $i_r(\phi_{\mathrm{DL}}^{ss}, \theta^{ss}) = i_0$, $f(\phi_{\mathrm{DL}}^{ss}, \theta^{ss}) = 0$ and corresponds to the homogeneous S-shaped current-potential characteristic (Fig. 4.2(b)). Perturbing the steady state with a perturbation $(\delta_{\phi_{\mathrm{DL}}} e^{\lambda t}, \delta_\theta \cos(nx) e^{\lambda t})$ (consistent with the boundary conditions), the temporal evolution of the perturbation is given by the eigenvalues of the Jacobian matrix

$$J = \begin{pmatrix} -\gamma\sigma_{\mathrm{r}} & -\gamma i_{\mathrm{r}_\theta} \\ \mu f_{\phi_{\mathrm{DL}}} & \mu f_\theta - n^2 \end{pmatrix}.$$

For brevity we denote $\sigma_r := \left.\frac{\partial i_r}{\partial \phi_{\mathrm{DL}}}\right|_{(\phi_{\mathrm{DL}}^{ss}, \theta^{ss})}$. The stability of the fixed point with respect to homogeneous fluctuations $(n = 0)$ can be determined by inspecting

$$\begin{aligned} \det J &= -\gamma\mu f_\theta (\sigma_{\mathrm{r}} - \frac{f_{\phi_{\mathrm{DL}}}}{f_\theta} i_{\mathrm{r}_\theta}) \\ &= -\gamma\mu f_\theta \left(\sigma_{\mathrm{r}} + i_{\mathrm{r}_\theta} \frac{\mathrm{d}\theta^{\mathrm{ss}}(\phi_{\mathrm{DL}})}{\mathrm{d}\phi_{\mathrm{DL}}} \right) \\ &= -\gamma\mu f_\theta \frac{\mathrm{d}i_r(\theta^{\mathrm{ss}}(\phi_{\mathrm{DL}}), \phi_{\mathrm{DL}})}{\mathrm{d}\phi_{\mathrm{DL}}} \end{aligned}$$

and

$$\mathrm{tr} J = \mu f_\theta - \gamma\sigma_{\mathrm{r}}.$$

$\det J > 0$ for any parameter set since $\mu, \gamma > 0$ and $f_\theta \frac{\mathrm{d}i_r(\theta^{ss}(\phi_{\mathrm{DL}}), \phi_{\mathrm{DL}})}{\mathrm{d}\phi_{\mathrm{DL}}} < 0$, which follows from the fact that the branch of negative differential resistance $\left(\frac{\mathrm{d}i_r(\theta^{ss}(\phi_{\mathrm{DL}}), \phi_{\mathrm{DL}})}{\mathrm{d}\phi_{\mathrm{DL}}} < 0 \right)$ is

caused solely by the activator variable θ, equivalent to saying that $\sigma_r > 0$ in general, thus

$$f_\theta < 0, \quad \mathrm{d}i_r/\mathrm{d}\phi_{DL} > 0, \quad \text{if } (\phi_{DL}^{ss}, \theta^{ss}) \notin \text{NDR region}$$
$$f_\theta > 0, \quad \mathrm{d}i_r/\mathrm{d}\phi_{DL} < 0, \quad \text{if } (\phi_{DL}^{ss}, \theta^{ss}) \in \text{NDR region.}$$

However, tr J might change sign on the NDR-branch since $f_\theta > 0$ and $\sigma_r > 0$, which leads to an oscillatory instability of the homogeneous steady state (denoted by a superscript "h") at

$$\left(\frac{\gamma}{\mu}\right)^h := \frac{f_\theta}{\sigma_r}. \tag{4.7}$$

Thus, for $\gamma/\mu < (\gamma/\mu)^h$ (low concentration of the reacting species or high concentration of the adsorbate) the homogeneous steady state is unstable in a certain i_0-interval, since $f_\theta \sigma_r^{-1}$ depends on the imposed current density via the steady state condition. When plotting the critical value $(\gamma/\mu)^h$ as a function of the imposed current density Fig. 4.3(a) is obtained.

For $\gamma/\mu > (\gamma/\mu)^h_{max} = 2.2 \cdot 10^{-4}$ no oscillatory solutions exist for any i_0. If $\gamma/\mu \ll (\gamma/\mu)^h_{max}$, the oscillatory instability takes place close to the turning points of the current-potential characteristic at $i_0 = 889$ and $i_0 = 1587$.

To determine the stability with respect to spatially inhomogeneous fluctuations, it is sufficient to consider the activator variable θ, since sinusoidal perturbations do not affect the average value of θ and thus the double layer dynamics. Therefore the steady state becomes unstable with respect to the n^{th}-mode for

$$\mu > \frac{n^2}{f_\theta},$$

and the first mode to become unstable is always the mode with wavenumber one [8]. The wavelength of the first unstable mode depends on the system size and is equal to $2L$ for von Neumann boundary conditions. In the following we term this instability *domain bifurcation* (d). The critical parameter value is thus:

$$\mu^d := f_\theta^{-1}. \tag{4.8}$$

This critical value is depicted in Fig. 4.3(b) as a function of i_0. For system sizes $\mu < \mu_{min} = 3.54$ the spatial instability is suppressed; this defines a natural length scale for the system. For system sizes much larger than this natural length scale the spatial instabilities occur once again close to the turning points of the current-potential characteristic.

The spatial and oscillatory instabilities may coincide in a codimension-two point (Domain-Hopf bifurcation, "DH") if

$$\gamma^{DH} = \sigma_r^{-1}, \tag{4.9}$$

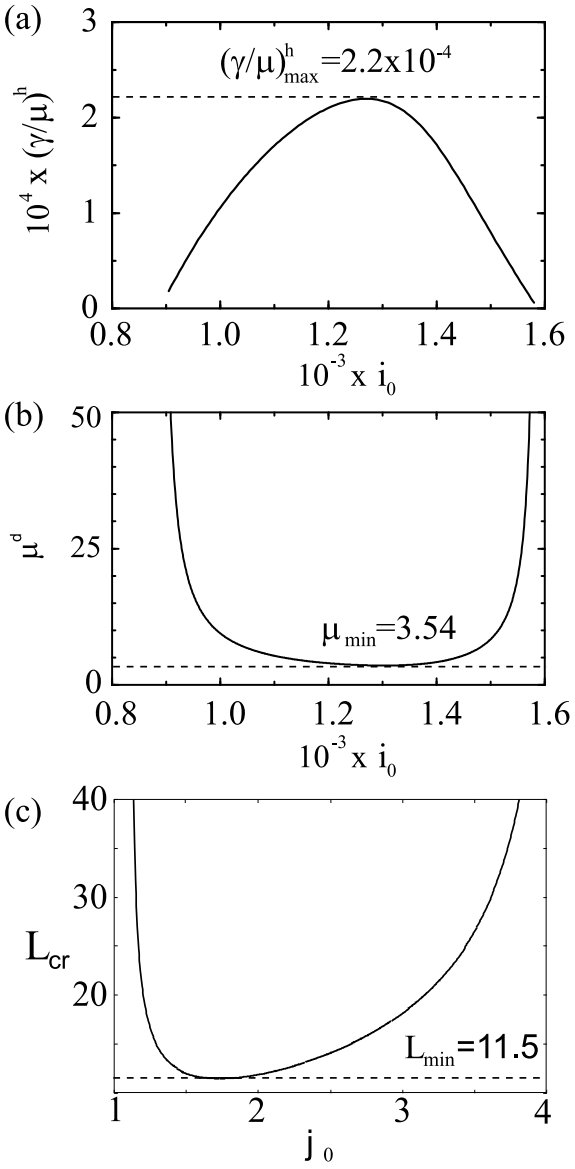

Figure 4.3: *(a) Location of the Hopf-bifurcation of the homogeneous steady state in the (γ/μ-i_0)-parameter-plane for the electrochemical model (4.5),(4.6). For $\gamma/\mu > 2.2 \cdot 10^{-4}$ the system is stable with respect to homogeneous fluctuations. (b) Threshold for the spatial instability of the uniform steady state in the (μ-i_0)-plane. For system sizes smaller than $\mu_{\min} = 3.54$ the system is stable with respect to spatial fluctuations. (c) Critical system size L_{cr} of the spatial instability for the semiconductor model (Eqs. (4.12),(4.13)) as a function of the imposed current density j_0.*

analogous to the Turing-Hopf bifurcation mentioned in the introduction, section 4.1.1. The respective imposed current density value $i_0^{\mathrm{DH}}(\mu)$ is defined as the solution of (4.8) with respect to i_0. For each set (μ, i_0) two γ values satisfy the condition for the codimension-

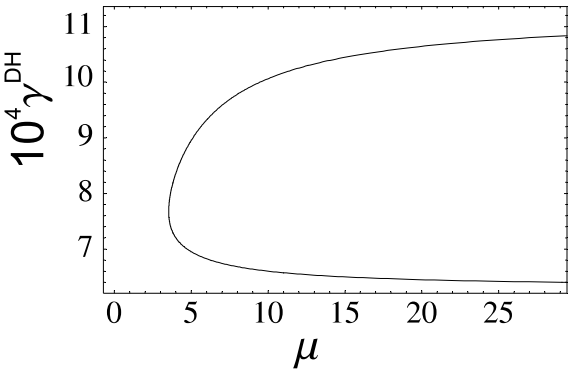

Figure 4.4: *Location of codimension-two domain-Hopf bifurcations, $\gamma^{DH}(\mu)$, in the γ-μ-parameter plane. Note that i_0 also changes along the curve.*

two point. This is illustrated in Fig. 4.4 showing the dependence of γ^{DH} on μ. The upper part of the curve (higher values of γ) corresponds to the domain bifurcation taking place at the upper part of the S-shaped current-potential characteristic also. Consequently, the codimension-two point close to the lower turning point of the characteristic is found for lower γ values.

Homogeneous Limit Cycle and Stationary Domains

In this section we complete the picture of the different basic attractors of the model by including limit cycles and stationary current domains into our stability analysis. Analytical methods fail in most cases since the involved bifurcations are either subcritical and thus do not allow for an amplitude equation analysis and/or the considered system sizes are intermediate, which excludes methods like singular perturbation theory [158] to describe domain interface dynamics.

For common concentrations and system sizes the double layer dynamics is much faster than the dynamics of the activator. For these conditions the parameters γ and μ are of the order 10 and 100, respectively. It follows that in most cases oscillatory instabilities are not present in the system and the only nontrivial mode is a stationary current domain as depicted in Fig. 4.5(a) for two values of i_0. This current domain is the final state of the system in the spatially unstable regime and the mechanism leading to such a stationary domain is well known (e.g., [8, 46]):

The activator is bistable as a function of the double layer potential. An over-critical local fluctuation in a system without global coupling that is prepared in the metastable state would lead to the formation of a transition front to the globally stable state. The global constraint, however, forces the system to maintain an average current. The system meets this constraint by taking on an inhomogeneous state in which two phases coexist. With other words, the front velocity becomes zero. The final state of the system is described by

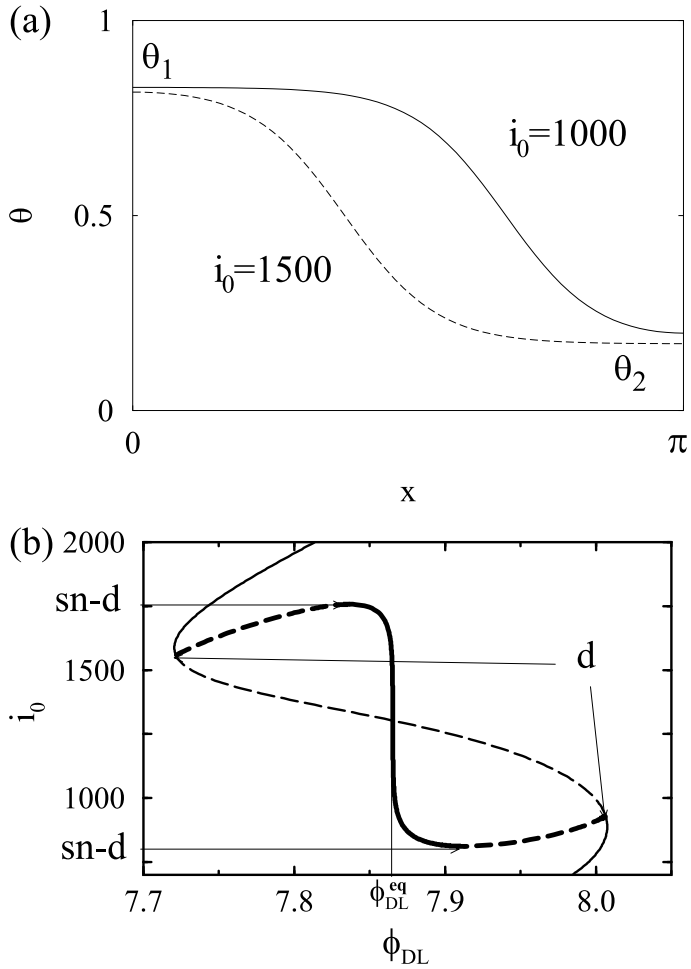

Figure 4.5: *(a) Stable domains for two values of the imposed current density i_0 for the electrochemical model ($\mu = 25$, $\gamma = 10$). (b) Bifurcation diagram for $\mu = 25$ and $\gamma = 10$. Shown is ϕ_{DL} as a function of the bifurcation parameter i_0 in the familiar current-potential plane. The branch of negative differential resistance is unstable (thin dashed line) with respect to domain formation. The domain branches (thick lines) bifurcate subcritically (d) near the turning points of the current-potential characteristic. The stable and unstable domain branches (solid and dashed thick lines, respectively) are born in a saddle-node bifurcation of domains (sn-d). The domain branch can be approximated by an equal-areas rule, Eq. (4.10), in a huge i_0 interval yielding an equistability potential ϕ_{DL}^{eq}.*

a Maxwell type construction: the intermediate, equistability double layer potential ϕ_{DL}^{eq}, which is established in the stationary structure is determined by the equal-areas rule [8,15]

$$\int_{\theta_1}^{\theta_2} f(\phi_{DL}^{eq}, \theta)\, d\theta = 0. \tag{4.10}$$

In Fig. 4.5(b) the bifurcation diagram with respect to i_0 is shown for $\mu = 25$, $\gamma = 10$.

Even though the system size is comparable to the interface width, as can be seen in Fig. 4.5(a), the above construction holds for a wide i_0-interval. This manifests itself in the approximately constant value of ϕ_{DL} on the domain branch, cf. Fig. 4.5(b), which is close to the numerically determined $\phi_{\mathrm{DL}}^{\mathrm{eq}} = 7.865$. However, since the arguments given above apply strictly only for infinite systems, deviations near the turning points of the current-potential characteristic of the domain are clearly visible. These deviations represent a boundary effect.

States with several domains are unstable due to the winner takes all principle [47, 53]. Domains with an extremum not located at the boundaries are unstable with respect to translation and are attracted by the boundary.

Fig. 4.5(b) also shows that spatially patterned solutions typically bifurcate subcritically from the homogeneous state and meet the stable domain-branch in a saddle-node bifurcation (sn-d). The domains remain stable in the entire i_0-interval in which the current-potential characteristic of the domain exhibits a negative differential resistance for these parameter values. This behavior can also be rationalized analytically [48, 49]. The domain bifurcation is supercritical only in a small μ-interval close to the minimal system size μ_{min}.

When μ is fixed at a value $\mu > \mu_{\mathrm{min}}$ and the double layer dynamics is slowed down to γ below $\mu(\gamma/\mu)^{\mathrm{h}}_{\mathrm{max}}$, the additional mode of homogeneous oscillations becomes present in the system. For $\gamma \lesssim \mu(\gamma/\mu)^{\mathrm{h}}_{\mathrm{max}}$ it bifurcates supercritically from the spatially unstable state, therefore small amplitude oscillations are unstable with respect to spatial fluctuations for any i_0. With increasing oscillation amplitude (decreasing γ) the oscillations become stabilized in a pitchfork bifurcation (pf) (cf. Fig. 4.6a). This results in bistability of stationary domains and an uniform limit cycle in an intermediate i_0-interval. The basins of attraction are separated by an unstable inhomogeneous limit cycle.

If γ is lowered even further, the stationary current domain will become unstable also. This can be rationalized by recalling that the stabilization mechanism of the domains is the global coupling mediated by ϕ_{DL}. If the delay of the double layer dynamics becomes too large, ϕ_{DL} can no longer control the interface stability. We denote the critical value of this oscillatory instability of the domain by $\gamma^{\mathrm{hd}}(\mu, i_0)$. Numerical simulations show that the threshold for an oscillatory instability of the current domain typically lies below the threshold for the Hopf bifurcation of the homogeneous steady state

$$\gamma^{\mathrm{hd}}(\mu, i_0) < \gamma^{\mathrm{h}}(\mu, i_0). \tag{4.11}$$

This can be understood in the frame of the eigenmodes of the current domain for large system sizes if we recall that in the absence of global coupling the domain state has only one positive eigenvalue that tends to zero with increasing system size. The respective arguments are given in [49]. The numerical investigations show that relation (4.11) in general holds for small and intermediate system sizes also.

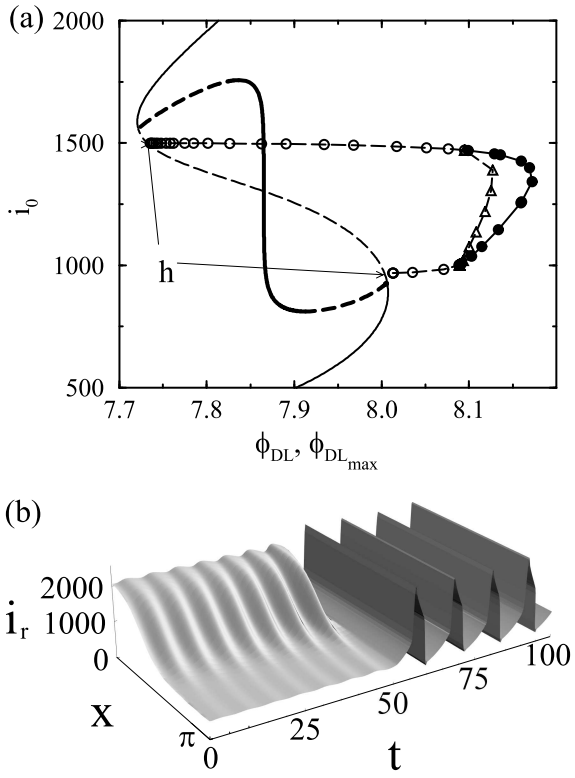

Figure 4.6: *(a) Bifurcation diagram for the electrochemical model for slower ϕ_{DL}-dynamics ($\mu = 25$, $\gamma = 3 \cdot 10^{-3}$). Apart from the branches shown in Fig. 4.5(b), a branch of unstable homogeneous oscillatory solutions (open circles) bifurcates supercritically (h) near the turning points of the current-potential characteristic. Shown is the maximum value of ϕ_{DL} during one oscillation cycle. After stabilization through a pitchfork bifurcation, the stable homogeneous oscillations (full circles) are separated from the stable domains by an unstable inhomogeneous limit cycle (open triangles). (b) Typical scenario of an oscillatory instability of a domain for lower values of γ than in (a) ($\mu = 25$, $\gamma = 1 \cdot 10^{-4}$, $i_0 = 1000$). Shown is the reaction current density $i_r = (1-\theta)e^{\phi_{DL}}$ as a function of space and time. At these parameter values the oscillatory instability of the domain is subcritical and the system finally settles down to homogeneous relaxation oscillations (standard scenario).*

It follows that, in general, the homogeneous relaxation oscillations represent an attractor when the domain loses stability. The oscillatory instability of the domain is usually subcritical; a state close to the domain is eventually attracted by the stable homogeneous limit cycle (see Fig. 4.6(b)). This can be regarded as the standard scenario (i.e., it exists in a wide parameter range) of a domain instability in globally coupled electrochemical systems with an S-shaped current-potential characteristic. In this case no complex spatio-temporal behavior arises in the model.

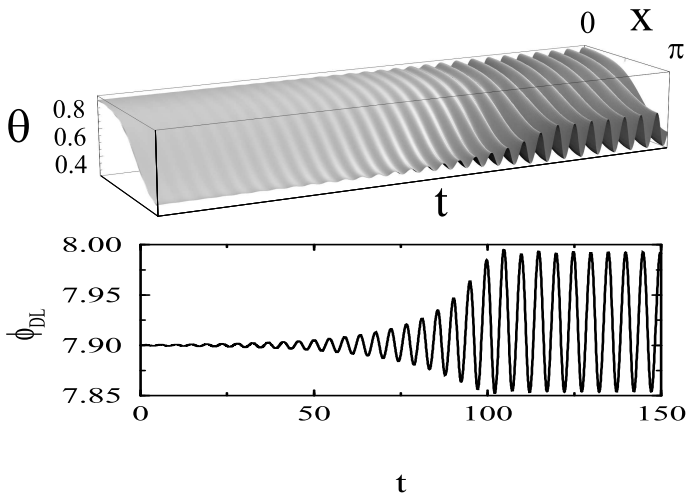

Figure 4.7: *Oscillatory instability of a domain leading to stable, periodically breathing current domains for the electrochemical model ($\mu = 10$, $\gamma = 7 \cdot 10^{-4}$, $i_0 = 1000$). (In this simulation a stable domain was prepared, γ was lowered to $\gamma = 7 \cdot 10^{-4}$, and a small random fluctuation was added.)*

Breathing Current Domains

We would expect complex spatio-temporal behavior if the branch of inhomogeneous limit cycle solutions that bifurcates from the domain-branch at the point of the oscillatory instability of the domain becomes stabilized or bifurcates supercritically. In this case the system would exhibit bistability between a stable inhomogeneous limit cycle and a stable homogeneous one. We did indeed find such a situation in the model for comparatively small system sizes ($\mu \sim 10$) and relaxation times well below the onset of homogeneous oscillations ($\gamma/\mu \sim 7 \cdot 10^{-5}$). The instability leading to such complex spatio-temporal behavior is shown in Fig. 4.7. In Fig. 4.8(a) the corresponding bifurcation diagram for $\mu = 10$ and $\gamma = 7 \cdot 10^{-4}$ is depicted. Fig. 4.9 displays the stable inhomogeneous limit cycle in the (i_r,ϕ_{DL})-plane-projection together with the main solution branches (cf. Fig. 4.8) discussed in the following paragraph.

Decreasing the imposed current density from values in the regime of bistability between a stable domain and homogeneous oscillations, the domain branch exhibits an oscillatory instability (hd). The branch of oscillatory domains that bifurcates subcritically is stabilized via a saddle-node bifurcation of oscillatory domains, i.e., periodic orbits (snp) which can be seen in the enlarged bifurcation diagram, Fig. 4.8(b). The spatio-temporal behavior becomes more involved as the imposed current density i_0 is decreased. The limit cycle undergoes a period doubling cascade leading to chaotic spatio-temporal motion (Fig. 4.10). Decreasing i_0 further, a reversed period doubling cascade occurs which leads again to stable period one breathing domains. This branch then ends in a supercrit-

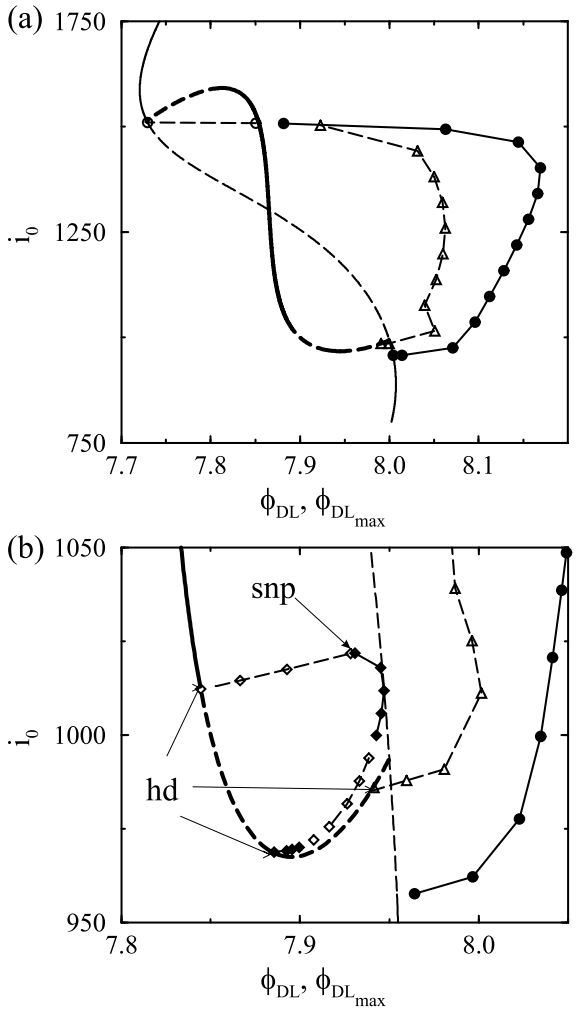

Figure 4.8: *(a) Basis bifurcation diagram for stable periodic breathing for the electrochemical model ($\mu = 10$, $\gamma = 7 \cdot 10^{-4}$). The oscillatory branch of the homogeneous limit cycles bifurcates supercritically before the spatial instability and thus homogeneous oscillations are stable nearly in the entire i_0-interval (full circles). The equal areas rule, Eq. (4.10), fails for this system size. The domain branch (thick line) is unstable in a region of negative differential resistance (dashed thick line) near the lower saddle-node bifurcation of the domains. Marked with open triangles is an unstable inhomogeneous limit cycle. It is born in a subcritical pitchfork bifurcation of the homogeneous limit cycle at high i_0 and terminates in the unstable domain branch. (b) Enlargement of the bifurcation diagram at the lower turning point. Here also the branches of the inhomogeneous breathing mode are shown (diamonds). The breathing mode bifurcates subcritically (hd) from the domain branch at higher i_0 (open diamonds) and stable breathing (full diamonds) originates in an snp. In the projection of the limit cycle on the double layer potential it gets close to the homogeneous steady state but not in real phase space (cf. text). In the current density interval between approx. $i_0 = 1000$ and $i_0 = 975$ the inhomogeneous limit cycle undergoes a period doubling cascade leading to chaotic breathing (open diamonds). Note that solutions were calculated at more i_0-values but are omitted here for clarity.*

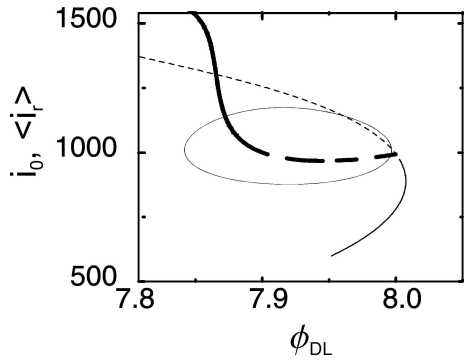

Figure 4.9: *Phase space plot of the breathing domain (circle) in a projection on the (i_r,ϕ_{DL})-plane. Also shown are the main solution branches as a function of i_0. Same parameters as in Fig. 4.7.*

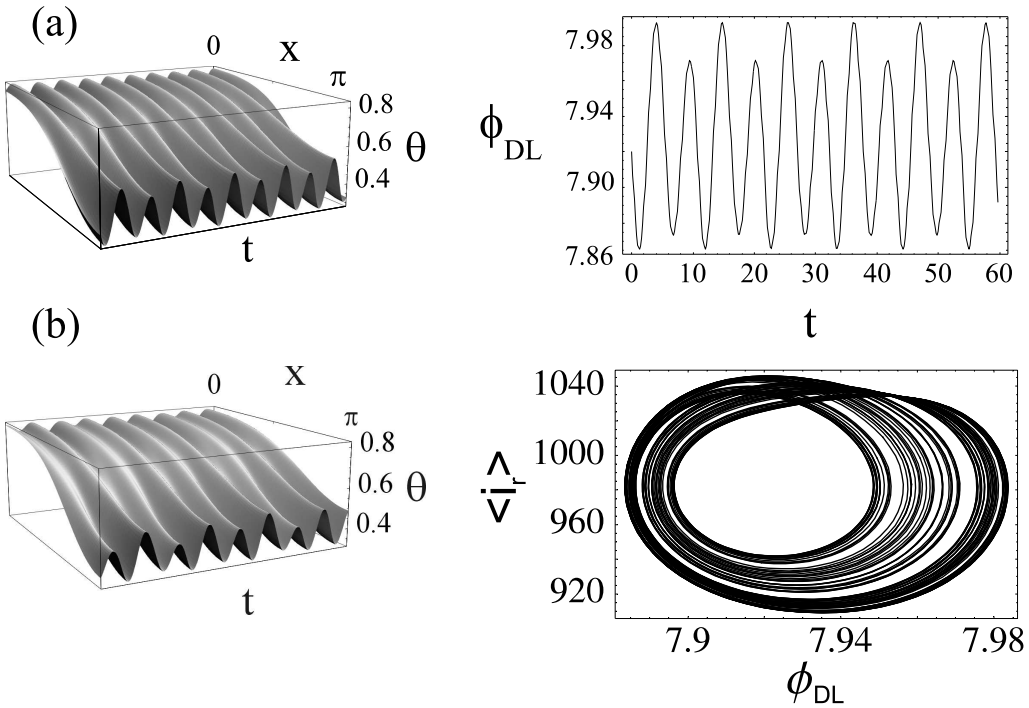

Figure 4.10: *(a) Periodically breathing domains with period two at $i_0 = 990$. Left: $\theta(x,t)$; Right: Period doubled time series, $\phi_{DL}(t)$. (b) Chaotically breathing domains at $i_0 = 980$. Left: $\theta(x,t)$; Right: Chaotic attractor in the projection on the $(\langle i_r \rangle$-$\phi_{DL})$-plane ($\mu = 10$, $\gamma = 7 \cdot 10^{-4}$).*

ical Hopf bifurcation of the domain very close to the saddle-node bifurcation, in which stable and unstable domains originate (sn-d). It is interesting to note that the dynamic nature of the invariant set that separates the basins of attraction of the two limit cycles is changing with increasing imposed current density from the unstable stationary domain

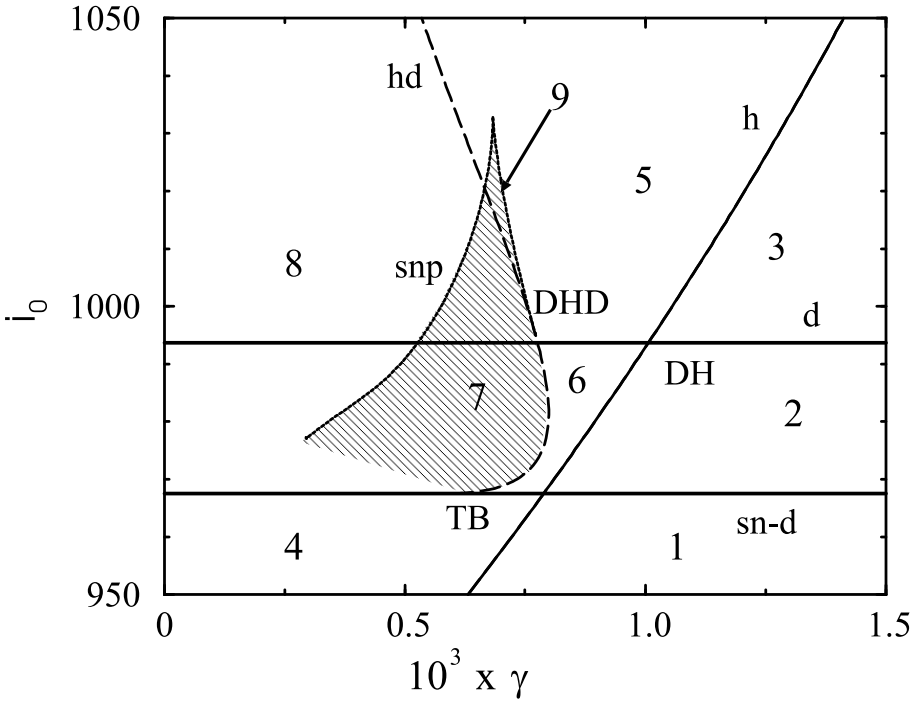

Figure 4.11: *Existence region of stable breathing in the (i_0-γ)-control-parameter plane (hatched region) for the electrochemical model ($\mu = 10$). The main dynamic regimes, characterized by attractors, are indicated by the numbers 1–9; the attractors are given in Table 4.1. Shown in solid lines are the points of the domain bifurcation (d) and the saddle-node bifurcation in which the domains originate (sn-d) (both independent of γ). The domain bifurcation and the Hopf bifurcation of the homogenous steady state (h, solid) intersect in a Turing-Hopf-type codimension-two point (DH). The dashed line shows the oscillatory instability of the domain (hd). Denoted by snp (solid line) is the line of the saddle node bifurcation of periodic orbits, i.e., breathing domains.*

(saddle point) to an unstable inhomogeneous limit cycle (see Fig. 4.8(b) for low i_0).

The region in the (i_0-γ)-parameter plane in which such complex spatio-temporal dynamics is found is depicted in Fig. 4.11 for $\mu = 10$. The lines of the Hopf bifurcation and the domain bifurcation of the homogeneous steady state and their intersection point (DH) are shown. The main regions that were discussed above (and in part also exist for different values of μ) are indicated. Note the existence of three codimension-two points: The point in which domain and Hopf bifurcation coincide (DH) was discussed in section 4.1.3. At the DH the system has a pair of purely imaginary eigenvalues and a real eigenvalue equal to zero [87]. Unfoldings of the DH have a further fine structure as discussed in the next section; it is not shown in Fig. 4.11 for clarity. Denoted by TB is the point where saddle-node and Hopf-bifurcation meet (Takens-Bogdanov point) [87]. Note that in our case both bifurcations involve inhomogeneous steady states (i.e., domains) rather

Table 4.1: *Dynamic regimes indicated in Fig. 4.11*

(1)	One stable homogeneous fixed point.
(2)	Bistability between stable domain and homogeneous fixed point.
(3)	One stable domain.
(4)	One stable homogeneous limit cycle.
(5)	Stable or unstable homogeneous limit cycle (cf. section 4.1.3) and stable domain.
(6)	Stable homogeneous limit cycle and stable domain.
(7)	Stable breathing current domains (periodic or chaotic) and a stable homogeneous limit cycle.
(8)	The Hopf bifurcation of the domain is subcritical, thus only stable homogeneous oscillations are present.
(9)	Region in which three attractors exist (cf. Fig. 4.8 for $i_0 \cong 1010$): Stable domains, stable breathing domains, and stable homogeneous limit cycle.

than homogeneous solutions. Left of the TB two saddle fixed points with one and two unstable directions, respectively, originate from the saddle-node bifurcation, right of it a saddle fixed point and a stable node. Again the fine structure, most remarkably a homoclinic bifurcation that should be present in the vicinity of the TB, is omitted. The third codimension-two point is a degenerate Hopf bifurcation of domains (DHD), in which the saddle-node bifurcation of periodic orbits (snp) coincides with the Hopf-bifurcation of the domain (hd).

We omitted in the bifurcation diagram (Fig. 4.11) some of the branches mentioned above. Furthermore there are indications of the presence of additional bifurcations that determine the exact location of the lower boundary of the regime of complex behavior.

Bifurcations and Phase Portraits Near the DH-Codimension-Two Point

In Fig. 4.12 the bifurcations and phase portraits near the codimension-two point in which the domain bifurcation and Hopf bifurcation of the homogeneous steady state meet (DH) is shown. The additional branches not shown in Fig. 4.11 are a Hopf bifurcation of the unstable stationary domain leading to an unstable inhomogeneous limit cycle and the pitchfork bifurcation of periodic orbits that stabilizes the homogeneous limit cycle born in the Hopf bifurcation of the homogeneous steady state and which is the origin of another unstable inhomogeneous limit cycle (cf. Fig. 4.6(a)). Both branches terminate in the DH. The respective phase portraits (insets) depict the dynamics schematically in a projection on the plane spanned by the eigenvectors of the two complex conjugate eigenvalues describing the Hopf bifurcation of the homogeneous fixed point and the stationary unstable domain, respectively. The third direction describes the subcritical domain bifurcation (spatial mode).

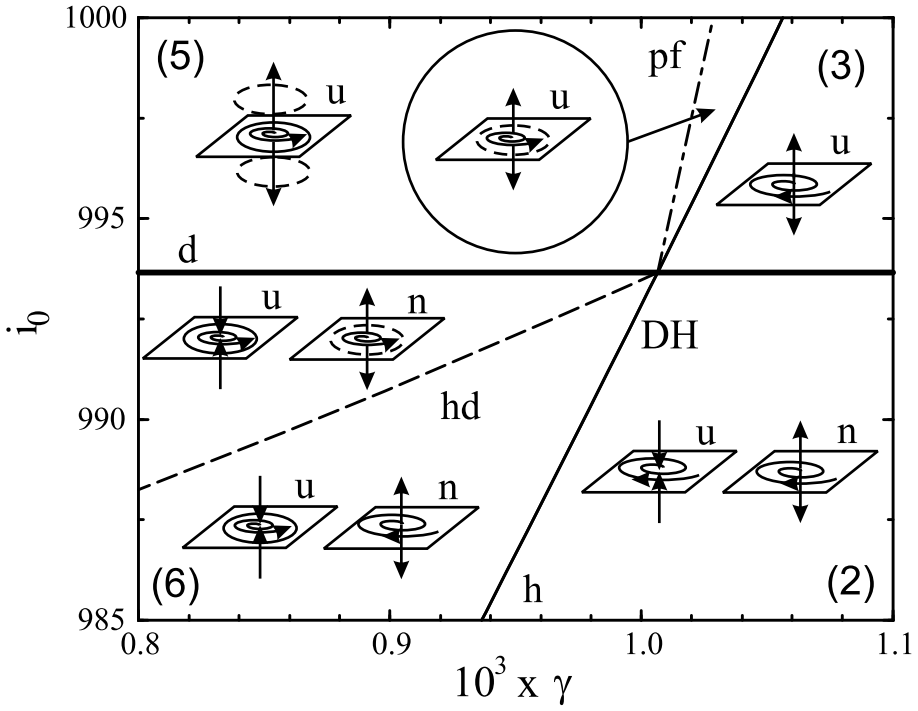

Figure 4.12: *Bifurcations and projections of phase portraits close to the codimension-two domain-Hopf-bifurcation (DH). Note that when two phase portraits are shown they refer to different parts of the phase space and are representative for the phase flow close to different fixed points. Thick solid line: spatial instability of the homogeneous steady state (d). Thin solid line: Hopf bifurcation of the homogeneous steady state (h). Dashed line: Hopf bifurcation of the stationary unstable domain (hd). Dash-dotted line: Pitchfork bifurcation of limit cycles that stabilizes the homogeneous limit cycle (pf). "u" and "n" denote the planes of uniform and (nonuniform) domain modes, respectively. Note that the nonuniform fixed point also exists in regions (3) and (5) where it is not shown. The numbers in the corners correspond to the numbers in Table 4.1 indicating the stable attractors in the respective parameter region.*

Thus, starting from the lower right corner, region (2) (cf. Table 4.1) in Fig. 4.12, the following bifurcations in the vicinity of the homogeneous steady state (plane "u") take place in counter clock wise order. In (2) the homogeneous steady state is stable. The plane symbolizes the homogeneous modes having imaginary eigenvalues, the perpendicular direction denotes the domain modes. It coexists with an unstable domain (plane "n"). Crossing the domain bifurcation, the uniform steady state loses stability in the eigen direction of the domain modes. When the Hopf bifurcation is passed, the focus in the homogeneous plane reverses direction (inset). The resulting limit cycle is unstable with respect to spatial fluctuations since it originated from the spatially unstable homogeneous steady state. The unstable limit cycle is stabilized by a Pitchfork bifurcation (pf) giv-

ing birth to two unstable inhomogeneous limit cycles that don't play a role in the further discussion.[2] The following domain bifurcation (d) changes the sign of the eigenvalue associated with the domain modes. Crossing the Hopf bifurcation of a domain (hd) does not affect the uniform state. Traversing again the Hopf bifurcation line (h), this time in the lower plane, removes the stable homogeneous limit cycle and we arrive back at the stable homogeneous fixed point. Similar arguments can be given for the nonuniform steady state symbolized by the "n"-plane. Note that it is not shown in regions (3) and (5) where it also exists.

4.1.4 Comparison with a Semiconductor Model and Discussion

In this section we compare the different dynamic instabilities and regimes described in the previous section with results obtained earlier for the semiconductor model. The semiconductor model used has the (nondimensionalized) form

$$\dot{a} = \frac{u-a}{(u-a)^2+1} - 0.05a + \frac{\partial^2 a}{\partial x^2} \tag{4.12}$$

$$\dot{u} = \alpha(j_0 - u + \langle a \rangle_L), \tag{4.13}$$

where u denotes the potential drop across the semiconductor device (corresponding to ϕ_{DL}) and a describes the interface charge density in the HHED (corresponding to θ). The system length is L and thus $\langle a \rangle_L = L^{-1} \int_0^L a \, \mathrm{d}x$. The current-voltage characteristic of the HHED is given by $j = u - a$. It also has the shape of an 'S' (Fig. 4.2(c)). If space is rescaled to the interval $[0, \pi]$, the model exhibits the same structural dependence on three parameters as Eqs. (4.5),(4.6)

$$\dot{a} = \mu^{\mathrm{s}} \left(\frac{u-a}{(u-a)^2+1} - 0.05a \right) + \frac{\partial^2 a}{\partial x^2} \tag{4.14}$$

$$\dot{u} = \gamma^{\mathrm{s}}(j_0 - u + \langle a \rangle_\pi), \tag{4.15}$$

with $\mu^{\mathrm{s}} = \left(\frac{L}{\pi}\right)^2$ and $\gamma^{\mathrm{s}} = \left(\frac{L}{\pi}\right)^2 \alpha$. These parameters can be interpreted in the same way as in the electrochemical model.

The two models possess equivalent basic modes: The branch of negative differential conductivity is unstable with respect to spatial perturbations for sufficiently large system sizes $L > L_{\min}$ (cf. Fig. 4.3(c)) and with respect to homogeneous oscillations for sufficiently slow dynamics of the voltage drop u (small α). However the temporal instability of the filament may lead to qualitatively different spatio-temporal dynamics. Apart from the breathing mode that the semiconductor models also exhibit, [15,52,83,159] the latter system displays a complex spatio-temporal mode termed *spiking* (see Fig. 4.13(a)) [82,153].

[2] The two limit cycles are identical in the projection on the global variable ϕ_{DL}, cf. Figs. 4.6 and 4.8, open diamonds.

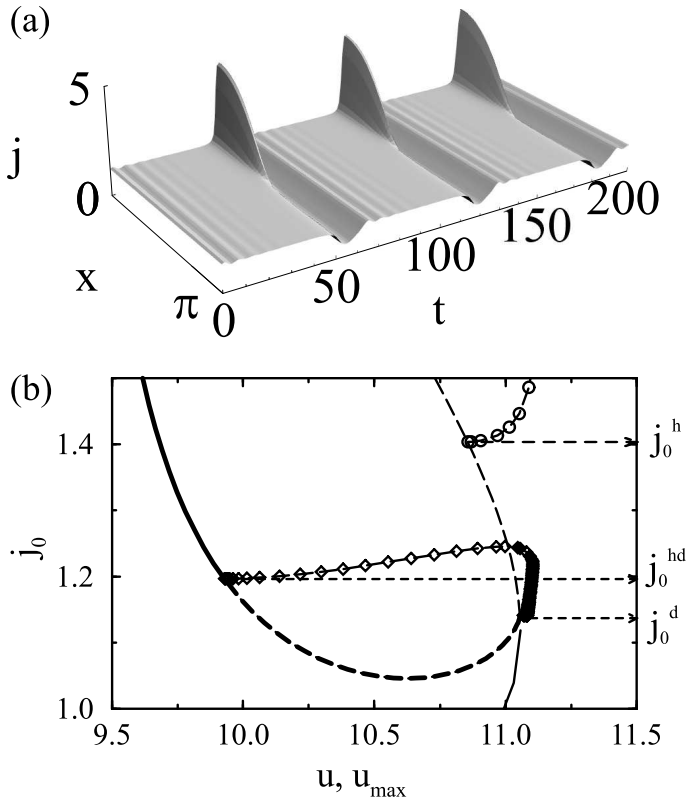

Figure 4.13: *(a) Spiking current filament in 1d ($L = 40$, $\alpha = 0.035$, $j_0 = 1.2$). (b) Bifurcation diagram for the semiconductor system for complex spatio-temporal dynamics ($L = 40$, $\alpha = 0.06$). Shown is the potential drop across the semiconductor, u, respectively the maximum u during one oscillation versus the imposed current density j_0 at the lower turning point of the current-voltage characteristic. In the current interval $[j_0^d, j_0^{hd}]$ indicated by the horizontal dashed lines no trivial state of the system is stable. The lower boundary of this parameter interval is the spatial instability of the homogeneous steady state (thin lines) and the upper one is the oscillatory instability of the filament (thick lines). Homogeneous oscillations are not present in this current density interval, they bifurcate at higher current density values (open circles in the upper right corner). The resulting inhomogeneous oscillations (diamonds) that bifurcate subcritically from the stable domain branch are born by a saddle-node bifurcation of periodic orbits.*

This mode evolves because the spatially inhomogeneous limit cycle that constitutes breathing comes eventually, with decreasing γ, very close to the homogeneous fixed point. This points to a structurally different dynamic regime as compared to the electrochemical system and facilitates the formulation of a sufficient condition for the occurrence of complex spatio-temporal dynamics [52]. In the following this is explained in some detail.

Consider the bifurcation diagram of the semiconductor model for parameter values at which complex spatio-temporal dynamics is found (Fig. 4.13(b)). Let us denote by

$j_0^{\mathrm{d}}(\mu)$, $j_0^{\mathrm{h}}(\mu,\gamma)$ and $j_0^{\mathrm{hd}}(\mu,\gamma)$ the parameter values at which the spatial instability of the homogeneous steady state, the oscillatory instability of the homogeneous steady state and the oscillatory instability of the filament, respectively, occur. For an interval of imposed current densities j_0 no trivial state is stable, since, in contrast to the electrochemical model, homogeneous oscillations are not present in the system for imposed current density values within this interval, however the filament is already oscillatorily unstable ($\gamma^{\mathrm{hd}}(\mu,i_0) > \gamma^{\mathrm{h}}(\mu,i_0)$). Thus, a sufficient condition for complex dynamics is

$$j_0^{\mathrm{h}}(\mu,\gamma) > j_0^{\mathrm{d}}(\mu) \quad \wedge \quad j_0^{\mathrm{hd}}(\mu,\gamma) > j_0^{\mathrm{d}}(\mu). \tag{4.16}$$

The limit case $j_0^{\mathrm{hd}}(\mu,\gamma) = j_0^{\mathrm{h}}(\mu,\gamma) = j_0^{\mathrm{d}}(\mu) \equiv j_0^{\mathrm{DH}}(\mu)$[3] can be reformulated as a condition for the timescale of the inhibitor γ such that the condition can be tested for different system sizes [52]:

$$\gamma^{\mathrm{hd}}(i_0^{\mathrm{d}}(\mu)) > \gamma^{\mathrm{DH}}(\mu). \tag{4.17}$$

The above inequality becomes clear if one considers that the oscillatory instability of the filament is shifted toward higher imposed current density values when lowering γ, whereas the Hopf bifurcation point of the homogeneous steady state behaves in the opposite way and the spatial instability does not depend on γ.

In Fig. 4.14 both critical timescales are plotted for both models. For the electrochemical model the critical timescales are also shown for the upper part of the S-shaped current-potential characteristic. The above arguments apply equally for this region. As indicated by the hatched region for the semiconductor system in Fig. 4.14(a), condition (4.17) is fulfilled for a large interval of system sizes L (respectively μ^{s}) for the lower part of the S-shaped current-voltage characteristic. Apart from spiking, a broad variety of periodic and chaotic spatio-temporal modes has been found in this interval [52]. Condition (4.17) is never found to hold for the upper part for the semiconductor model (not shown). It can be seen in Figs. 4.14(b) and 4.14(c) for the lower and upper part of the S-shaped current-potential characteristic, respectively, that condition (4.17) is apparently never fulfilled in the electrochemical system for any system size.

Thus, also the absence of spiking in the electrochemical system is easily understood; spiking evolves when the breathing mode eventually comes very close to the plane of homogeneous modes which constitutes a stable focus in this plane. The relaxation close to the homogeneous fixed point in the plane of the homogeneous modes leads to the small, almost homogeneous, oscillations and then the spike evolves again as the trajectory leaves the plane of homogeneous dynamics along the unstable direction of the homogeneous fixed point (cf. Fig. 4.13). In the electrochemical system the plane of homogeneous modes always constitutes an unstable focus for parameter values in which the domain

[3] The concurrence of three bifurcations is not a codimension-three point since two fi xed points (a homogeneous and an inhomogeneous steady state) are involved.

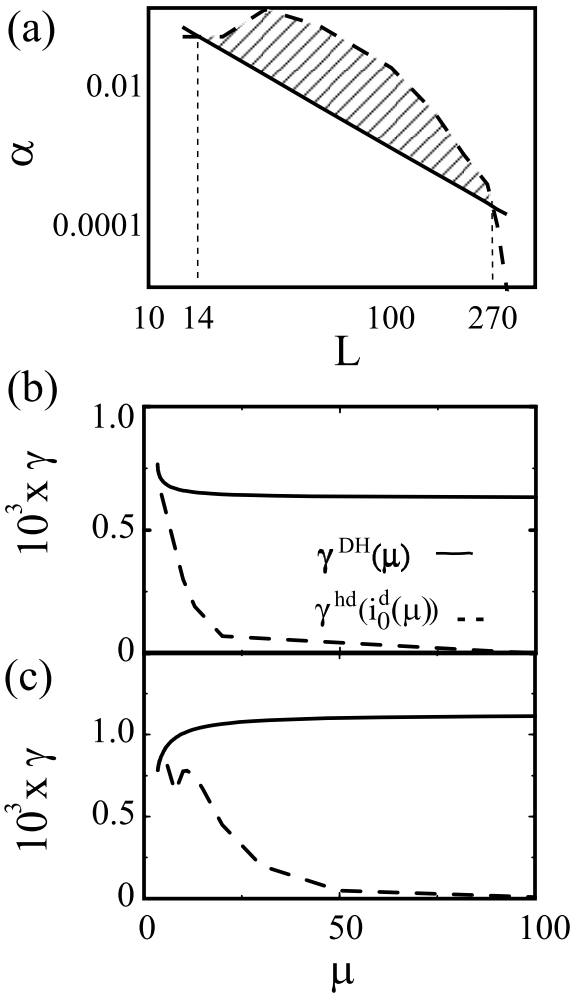

Figure 4.14: *Thresholds for oscillatory instabilities at imposed current density values at which the homogeneous steady state becomes unstable with respect to spatial fluctuations (effective three parameter continuation) to test condition (4.17). The threshold for an oscillatory instability of the domain ($\gamma^{hd}(j_0^d(\mu))$) and the codimension-two point (DH) ($\gamma^{DH}(\mu)$) are shown as dashed and solid lines, respectively. In (a) the two curves are shown for the semiconductor system (double logarithmic plot) for 2d domains at the lower turning point of the current-voltage characteristic. The hatched region indicates the region in which the sufficient condition (4.17) for complex spatio-temporal dynamics is fulfilled. In (b) and (c) $\gamma^{hd}(i_0^d(\mu))$ and $\gamma^{DH}(\mu)$ are shown for the electrochemical model for the two domain bifurcations at low and high current densities, respectively (cf. Fig. 4.4).*

loses stability and thus the trajectory of inhomogeneous oscillations never comes close to the unstable homogeneous fixed point.

4.1.5 Conclusions

The comparison of the two models presented allows us to identify bifurcations that exist in bistable systems subject to global inhibition. Apart from electrochemical and semiconductor systems such dynamics might be encountered in a variety of other systems, e.g., gas discharge devices [160].

Stationary large amplitude spatial patterns called domains or filaments appear via a subcritical spatial bifurcation of the uniform state and form attractors in the entire range of effective autocatalysis for common parameter values in such systems. A characteristic length scale can be defined that facilitates quantitative comparison of the respective models. For comparable timescales of activator and inhibitor stable homogeneous relaxation oscillations can be expected. For slow dynamics of the globally coupled inhibitor oscillatory instabilities of the domains occur, initially near the turning points of the current-potential(voltage) characteristic of the domain. However, the routes to complex spatio-temporal patterns depend on the local dynamics and might thus differ in each individual system under consideration.

We have identified the following scenarios: If the Hopf bifurcation of the domain is supercritical, the system will display stable breathing domains. In the case of a subcritical bifurcation the dynamics depends upon the further structure of the bifurcation diagram. If condition (4.17) is fulfilled, the onset of stable breathing or spiking modes can be expected. When inequality (4.17) is not fulfilled and the oscillatory instability of the domain is subcritical, no general statement regarding the resulting dynamics is possible. Either homogeneous relaxation oscillations or complex spatio-temporal dynamics may result in this case.

We have demonstrated the above general statements with two models exhibiting different scenarios leading to stable complex spatio-temporal dynamics, thus illustrating the general scheme. Condition (4.17), which ensures that stationary or uniform modes are either unstable or do not exist, is fulfilled for the semiconductor system in a wide parameter range, but it can never be satisfied in the specific electrochemical model, Eqs. (4.5),(4.6). As a consequence the electrochemical breathing current domains always coexist with homogeneous oscillations. Thus, they have a small basin of attraction compared to the situation in the semiconductor model, Eqs. (4.12),(4.13), in which no other mode is stable in a certain parameter range. As another consequence spiking current filaments are only present in the semiconductor system. Complex dynamics could only be found near the turning point of the current-potential(voltage) characteristic corresponding to the lower value of the imposed current density in both systems.

It is shown in section 5.2 that the sufficient condition (4.17) might be generalized even further. The generalization builds upon the apparent one parameter bifurcation of a homogeneous fixed point to complex dynamics reported here and earlier in the semiconductor

system [52, 82, 153, 161] when increasing j_0 from values below j_0^d to higher imposed current densities and condition (4.17) is fulfilled. Since similar results are described in section 5.2 for an electrochemical model, they are elaborated in the respective section.

Breathing current domains constitute a qualitatively new mode of complex spatio-temporal dynamics in electrochemical systems with S-shaped current-potential characteristic reported here for the first time. This mode may evolve to chaotic spatio-temporal dynamics via a period doubling cascade. Breathing current domains have been reported earlier by Christoph in the prototype N-NDR oscillator introduced in section 2.5.1 subject to NGC [104].

It should be noted that recent experimental studies of the CO-electrooxidation on Pt-single crystal electrodes have shown small amplitude oscillations of the potential in the range of negative differential resistance [162]. This system might be an experimental illustration of the above results, and therefore spatially resolved measurements would be desirable.

4.2 Turing Patterns Revisited

In [85] Turing patterns were predicted to exist in electrochemical systems with S-shaped current potential characteristic. The experimental observation of Turing patterns in such a system by Li *et al.* calls for a more detailed investigation of the model predictions. It turned out that the parameters used to calculate the bifurcation diagrams presented in [85, 107] did not match the experimental ones. Thus, we recalculate the characteristics of the Turing instability using the following set of equations, where the local functions are given by Eqs. (4.1),(4.2),

$$\dot{\theta} = f(\theta, \phi_{\mathrm{DL}}) + \frac{\partial^2 \theta}{\partial x^2} \tag{4.18}$$

$$\dot{\phi_{\mathrm{DL}}} = -i_r(\theta, \phi_{\mathrm{DL}}) + \frac{d}{\beta}(U - \phi_{\mathrm{DL}}) - \frac{d}{\beta}\left(\frac{\partial \phi}{\partial z} - \phi\right)\Bigg|_0 ; \tag{4.19}$$

the transformations of time, potentials and space as well as the definitions of the parameters are given in appendix A.1.2 and differ slightly from the ones used in the previous section since now periodic boundary conditions are used.

The conditions

$$\dot{\theta} = 0, \qquad \dot{\phi_{\mathrm{DL}}} = 0, \qquad \det J = 0, \qquad \frac{\partial \det J}{\partial n} = 0 \tag{4.20}$$

were used to perform the continuation of the Turing instability in parameter space. In Fig. 4.15(B) the calculated points of the Turing bifurcation are displayed in the $(1/\sigma$-$U)$-parameter plane in physical units for better comparability with the experiment, Fig.

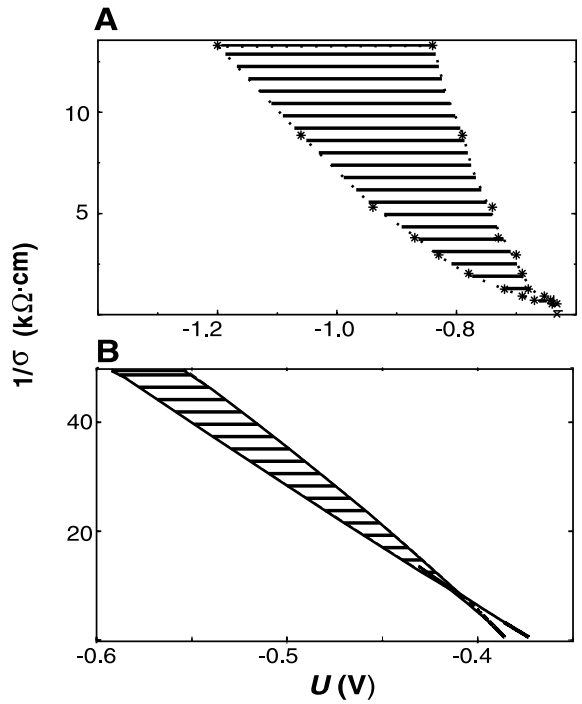

Figure 4.15: *(A) Measured existence region of stationary periodic potential patterns during periodate reduction in the presence of camphor in the* $(1/\sigma\text{-}U)$*-parameter plane. (B) Calculated Turing-unstable region in the same parameter plane. Dimensionless parameters used (for the retranslation see appendix A.1.2):* $\mu = 25$, $\beta = \gamma = 10$. *In the lower right corner the cusp of a bistable regime is also shown.*

4.15(A).[4] In Fig. 4.16 the value of the first mode to become unstable as a function of the applied voltage is given.

But, as mentioned earlier, the above treatment is an approximation. (i) Since $C_{DL} = C_{DL}(\theta)$ in general (cf. Eq. (2.57) on page 34), the double layer dynamics equation is given by (without global coupling)

$$\begin{aligned} &\frac{\partial}{\partial t}(C_{DL}\phi_{\mathrm{DL}}) = -i_r + \frac{d}{\beta}(U-\phi_{\mathrm{DL}}) - \frac{d}{\beta}\left(\frac{\partial\phi}{\partial z} - \phi\right)\Big|_0 \\ \Leftrightarrow \qquad &\dot{\phi}_{\mathrm{DL}} = \frac{1}{C_{DL}(\theta)}\left[-i_r + \frac{d}{\beta}(U-\phi_{\mathrm{DL}}) - \frac{d}{\beta}\left(\frac{\partial\phi}{\partial z} - \phi\right)\Big|_0\right] - \phi_{\mathrm{DL}}\frac{\partial C_{DL}}{\partial\theta}\frac{\partial\theta}{\partial t}. \end{aligned} \tag{4.21}$$

The local dynamics is left unchanged by this effect but the Jacobian of the extended system changes structurally and the implications are investigated in the next section. (ii) Modeling the spatial coupling of the adsorbate by simple diffusion neglects the attractive lateral interactions giving rise to the first order phase transition. It was shown already in

[4]The voltage was inverted to match the experiment. Note that σ stands for the physical conductivity in this case.

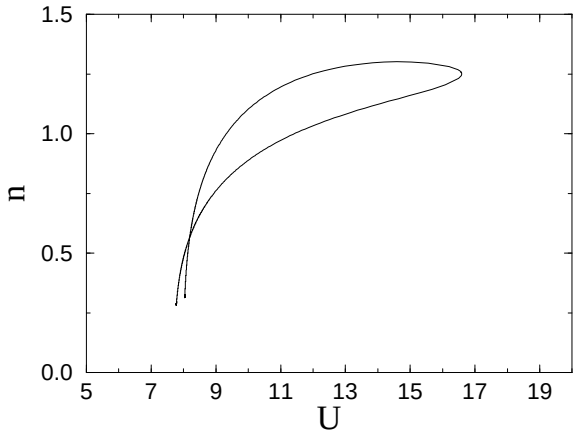

Figure 4.16: *Critical wavenumber n of the Turing bifurcation shown in Fig. 4.15 as a function of the applied voltage. Parameters as in Fig. 4.15.*

the early 80's that such interactions cause a desynchronizing spatial coupling in the autocatalytic region contrary to the homogenizing diffusive coupling assumed above [163]. In section 4.2.2 the consequences of such a more realistic model are explored.

4.2.1 Spatially Varying Double Layer Capacity

The general form of the equations to be investigated is, cf. Eq. (4.21),

$$\dot{\theta} = f(\theta, \phi_{\mathrm{DL}}) + K[\theta] \tag{4.22}$$

$$\dot{\phi}_{\mathrm{DL}} = 1/C_{DL}(\theta)\,\{g(\theta, \phi_{\mathrm{DL}}) + L[\phi_{\mathrm{DL}}]\} - C'_{DL}\phi_{\mathrm{DL}}\,\{f(\theta, \phi_{\mathrm{DL}}) + K[\theta]\}, \tag{4.23}$$

where $C'_{DL} := \partial C_{DL}/\partial\theta$ and L and K denote spatial operators. In the above system $K = \frac{\partial^2}{\partial x^2}$, $L = -\frac{\sigma}{\beta}\left(\frac{\partial\phi}{\partial z} - \phi\right)\Big|_0$. Thus, the Jacobian determining the stability if the homogeneous steady state is perturbed with $(\delta_\theta, \delta_{\phi_{\mathrm{DL}}})e^{\lambda t + inx}$ is given by (note that $(f+K)|_{ss} = 0 = (g+L)|_{ss}$)

$$J_n = \begin{pmatrix} f_\theta & f_{\phi_{\mathrm{DL}}} \\ C_{DL}^{-1}g_\theta - C'_{DL}\phi_{\mathrm{DL}}f_\theta & C_{DL}^{-1}g_{\phi_{\mathrm{DL}}} - C'_{DL}\phi_{\mathrm{DL}}f_{\phi_{\mathrm{DL}}} \end{pmatrix}\Bigg|_{(\theta^{ss},\phi^{ss}_{\mathrm{DL}})} + \begin{pmatrix} K_n & 0 \\ C'_{DL}\phi_{\mathrm{DL}}K_n & C_{DL}^{-1}L_n \end{pmatrix}\Bigg|_{(\theta^{ss},\phi^{ss}_{\mathrm{DL}})},$$

where K_n and L_n denote the eigenvalue of the n^{th} spatial mode of the respective spatial operator (e.g., for diffusion of θ, $K_n = -n^2$). Denoting the Jacobian of the system with constant capacity by J_0, the trace and determinant of J are given by

$$\mathrm{tr}J = \mathrm{tr}J_0 - C'_{DL}\phi_{\mathrm{DL}}f_{\phi_{\mathrm{DL}}} \tag{4.24}$$

$$\det J = \det J_0. \tag{4.25}$$

Considering the conditions for the Turing instability, Eqs. (4.20), it is apparent that the bifurcations points stay the same. Accordingly, *taking the coverage dependence of the double layer capacity into account does not change the region in parameter space where Turing patterns can be expected*, and Fig. 4.15 remains valid. Additionally, this statement is independent of the explicit form of the local dynamics and of the spatial coupling acting on the double layer as well as on the other variable.

However, the nonlinear dynamic equations as well as the spatial operator is changed. Thus, the observed patterns in the Turing unstable region might differ from the ones predicted with the simplified model.

4.2.2 Modeling Attractive Lateral Adsorbate Interactions

The linear response of the homogeneous steady state of an electrochemical system with S-shaped current-potential characteristic stemming from attractive lateral interactions of adsorbed molecules are investigated in this section. The approximations made in the previous sections are dropped in favor of a more realistic approach. (i) The Frumkin ansatz to model the dependence of the adsorption enthalpy with a global parameter, $G_{ad} = q'\theta$, is substituted by a local functional, $G_{ad} = U[\theta](x)/k_BT$, where $U[\theta](x)$ denotes a potential energy field. (ii) The potential energy field introduces a force acting towards higher concentrations of adsorbates, thus an intrinsically destabilizing spatial coupling is taken into account. This approach was first introduced by Mikhailov *et al.* to model pattern formation of adsorbates with strong lateral interactions [70,164–168]. Mesoscopic self-organized stationary and traveling structures were found in this model incorporating only one variable.

The potential energy field in the mean field approximation has the form

$$U[\theta](x) = \int_A u(x-x')\theta(x')\,\mathrm{d}x',$$

where a suitable choice of u is a Gaussian

$$u(x) = \frac{u_{max}}{\sqrt{\pi}x_0} e^{-\frac{x^2}{x_0^2}}$$

and boundary effects are neglected for simplicity in this section. $u_{max} < 0$ defines the maximum amplitude of the attractive interaction. The interaction radius is given by x_0. Together with the energy change caused by the change of the capacity of the double layer and including the shift of the PZC, the adsorption enthalpy is now given by (in physical units)

$$G_{ad} = \frac{N_A}{2N_{max}} \left[(C_{DL}^0 - C_{DL}^1)\ {\phi_{\mathrm{DL}}}^2 + C_{DL}^1 \phi_s \phi_{\mathrm{DL}} \right] + N_A U[\theta](x),$$

where ϕ_s quantifies the shift of the PZC during coverage changes.

The force $-\partial U/\partial x$ acting on an adsorbate particle results in a flow

$$j_U = -\frac{D}{k_B T}\theta(1-\theta)\frac{\partial U}{\partial x},$$

since it must be proportional not only to the available particles, θ, but also to the free sites, $1-\theta$. Additionally, diffusive fluxes are present on the surface, $j_d = -D\frac{\partial\theta}{\partial x}$.

Performing the usual transformations of time, space and potential and introducing dimensionless parameters (see appendix A.1.2), the adsorbate dynamics is given by

$$\dot{\theta} = \mu\left[(1-\theta)e^{-w-\varepsilon U[\theta](x)} + p\theta e^{w+\varepsilon U[\theta](x)}\right] + \frac{\partial}{\partial x}\left[\frac{\partial\theta}{\partial x} + 2\varepsilon\left(\theta(1-\theta)\frac{\partial U[\theta](x)}{\partial x}\right)\right]$$

with

$$w = \nu(1-C)\phi_{\mathrm{DL}}^2 + \phi_s C\phi_{\mathrm{DL}}.$$

The definitions of the dimensionless parameters are given in appendix A.1.2. To be able to calculate the homogeneous steady states of θ, the separation of the right hand side in the usual local term and a spatial interaction term has to be performed. The contribution of the potential field, U, in the homogeneous case is $\varepsilon U[\theta^{hom}] = \varepsilon\theta^{hom}$, thus retaining the Frumkin form with $q \to \varepsilon$. The separation can thus be achieved by artificially adding and subtracting $e^{\pm\varepsilon\theta}$

$$\begin{aligned}\dot{\theta} = {} & f(\theta,\phi_{\mathrm{DL}}) + \frac{\partial}{\partial x}\left[\frac{\partial\theta}{\partial x} + 2\varepsilon(\theta(1-\theta)\frac{\partial U[\theta](x)}{\partial x})\right] \\ & + \mu\left[(1-\theta)e^{-w}(e^{-\varepsilon U[\theta](x)} - e^{-\varepsilon\theta}) - \theta p e^{w}(e^{\varepsilon U[\theta](x)} - e^{\varepsilon\theta})\right] \qquad (4.26)\end{aligned}$$

with the local function

$$f(\theta,\phi_{\mathrm{DL}}) = \mu\left[(1-\theta)e^{-w-\varepsilon\theta} - \theta p e^{w+\varepsilon\theta}\right].$$

The double layer dynamics is left unchanged by these modifications and is still given by Eq. (4.21). To perform explicit calculations, a linear dependence of C_{DL} on θ is assumed (cf. section 2.5.2)

$$C_{DL}(\theta) = (C-1)\theta + 1.$$

Accordingly, the evolution of ϕ_{DL} is governed by

$$\dot{\phi_{\mathrm{DL}}} = \frac{1}{(C-1)\theta+1}\left[-\gamma(1-\theta)e^{\phi_{\mathrm{DL}}} + \frac{d}{\beta}(U-\phi_{\mathrm{DL}}) - \frac{d}{\beta}\left(\frac{\partial\phi}{\partial z} - \phi\right)\Big|_0\right] - \phi_{\mathrm{DL}}(C-1)\frac{\partial\theta}{\partial t},$$

where Eq. (4.26) is used to perform the separation in local and spatial terms also for the ϕ_{DL}-dynamics

$$\begin{aligned}\dot{\phi_{\mathrm{DL}}} = g(\theta,\phi_{\mathrm{DL}}) - \frac{1}{(C-1)\theta+1}\frac{d}{\beta}\left(\frac{\partial\phi}{\partial z}-\phi\right)\Big|_0 \\ -\phi_{\mathrm{DL}}(C-1)\left\{\left[\frac{\partial\theta}{\partial x}+2\varepsilon(\theta(1-\theta)\frac{\partial U[\theta](x)}{\partial x})\right]\right. \\ \left.+\mu\left[(1-\theta)e^{-w}(e^{-\varepsilon U(x)}-e^{-\varepsilon\theta})-\theta p e^{w}(e^{\varepsilon U(x)}-e^{\varepsilon\theta})\right]\right)\Big\} \qquad (4.27)\end{aligned}$$

with

$$g(\theta,\phi_{\mathrm{DL}}) = \frac{1}{(C-1)\theta+1}\left[-\gamma(1-\theta)e^{\phi_{\mathrm{DL}}}+\frac{d}{\beta}(U-\phi_{\mathrm{DL}})\right]-\phi_{\mathrm{DL}}(C-1)\,f(\theta,\phi). \quad (4.28)$$

Now the linear response of the homogeneous steady state $(\theta^{ss},\phi_{\mathrm{DL}}^{ss})$ of Eqs. (4.26),(4.27) to a perturbation $(\delta\theta,\delta\phi_{\mathrm{DL}}) = (\delta_\theta,\delta_{\phi_{\mathrm{DL}}})e^{\lambda t+inx}$ is tested. Inserting the perturbed steady state into the potential field yields [107, 169]

$$U[\theta^{ss}+\delta_\theta e^{\lambda t+inx}](x) = \varepsilon\left(\theta^{ss}+e^{\frac{-n^2x_0^2}{4}}\delta_\theta e^{\lambda t+inx}\right).$$

Finally, the entries in the Jacobian read

$$\begin{aligned}\frac{\delta}{\delta\theta}\dot{\theta}\Big|_{(\theta^{ss},\phi_{\mathrm{DL}}^{ss})} &= f_\theta + K_n + \varepsilon\mu\left(1-e^{\frac{-n^2x_0^2}{4}}\right)\left((1-\theta^{ss})e^{-w}+p\theta^{ss}e^{w})\right)|_{\phi_{\mathrm{DL}}^{ss},\theta^{ss}} \\ \frac{\delta}{\delta\theta}\dot{\phi_{\mathrm{DL}}}\Big|_{(\theta^{ss},\phi_{\mathrm{DL}}^{ss})} &= g_\theta - \phi_{\mathrm{DL}}^{ss}(C-1) \\ &\quad\cdot\left[K_n+\varepsilon\mu\left(1-e^{\frac{-n^2x_0^2}{4}}\right)\left((1-\theta^{ss})e^{-w}+p\theta^{ss}e^{w})\right)|_{\phi_{\mathrm{DL}}^{ss},\theta^{ss}}\right] \\ \frac{\delta}{\delta\phi_{\mathrm{DL}}}\dot{\theta}\Big|_{(\theta^{ss},\phi_{\mathrm{DL}}^{ss})} &= f_{\phi_{\mathrm{DL}}} \\ \frac{\delta}{\delta\phi_{\mathrm{DL}}}\dot{\phi_{\mathrm{DL}}}\Big|_{(\theta^{ss},\phi_{\mathrm{DL}}^{ss})} &= g_{\phi_{\mathrm{DL}}} + ((C-1)\theta^{ss}+1)^{-1}L_n\end{aligned}$$

with

$$\begin{aligned}K_n &= -n^2\left(1+2\varepsilon\theta^{ss}(1-\theta^{ss})e^{\frac{-n^2x_0^2}{4}}\right) \\ L_n &= -\left(dn\coth(n\beta)-\frac{d}{\beta}\right).\end{aligned}$$

The resulting typical dispersion relation is shown in Fig. 4.17

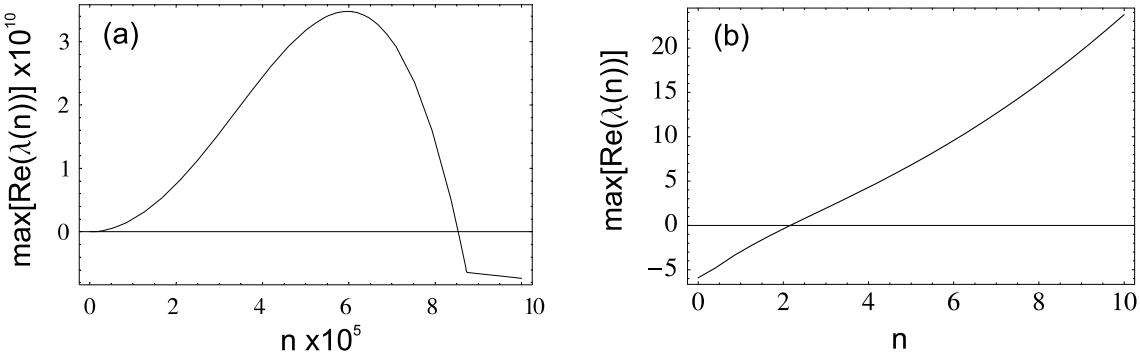

Figure 4.17: *Dispersion relation displaying the maximum growth rate of perturbations of the homogeneous steady state as a function of the wavenumber for model equations (4.26),(4.27). Parameters:* $\mu = 25$, $\gamma = 10$, $\varepsilon = -2.4$, $\nu = 0.025$, $p = 0.5$, $d = 4000$, $\beta = 10$, $U = 40$, $C = 0.1$, $\phi_s = 0.2$, $x_0 = 10^{-6}$.

4.2.3 Discussion

The unstable wavenumbers in Fig. 4.17(a) reach up to $\approx 10^6$ and also the wavenumber belonging to the maximum growth rate is of order x_0^{-1}. The huge region of unstable wavenumbers stems from the interplay of the long range interaction mediated by the electric potential in the electrolyte and the spatial coupling introduced by the attractive lateral interaction of the adsorbate molecules which acts on atomic scales. The dispersion relation suggests that stationary structures in the nanometer scale are present on the WE surface. However, Fig. 4.17(b) shows that also small wavenumbers are unstable, accordingly, in principle also large scale patterns are possible. Note that the system is far from the onset of the spatial instability for parameters corresponding to the dispersion relation shown in Fig. 4.17 and the coexistence of many different patterns is expected.

Nevertheless, a dispersion relation with a maximum at smaller wavenumbers would be a more convincing explanation of the observed patterns. Since x_0 is given by the radius of lateral interactions of the molecules adsorbed on the electrode surface, a value of $x_0 = 10^{-6}$, as used in Fig. 4.17, corresponds to the upper limit for x_0. We investigated if the inclusion of the concentration dynamics of the adsorbate and the reaction species or the N-NDR that is additionally present in the experiment [122] into the evolution equations yield more favorable descriptions. But it turned out that these have no considerable influence on pattern formation in the parameter regimes corresponding to the experiments.

4.2.4 Conclusions

In Fig. 4.15 the impressive agreement between the modeled and experimentally observed Turing unstable region is apparent. Also the low first unstable wavenumber, Fig. 4.16, matches well with the observation of modes with a maximum of three nodes in the ex-

periment [112]. It was proven that dropping the approximation of a constant double layer capacity does not shift the Turing bifurcation points to different values and thus the prediction made in Fig. 4.15(B) stays valid. This result is independent of the specific reaction and spatial coupling under consideration. However, the nonlinear dynamics changes and studies on electrochemical pattern formation including a non-constant double layer capacity will be an interesting topic in the future.

The dispersion relation derived using a potential energy field to model attractive interactions of adsorbate molecules displays a huge range of unstable eigenmodes in the S-NDR region. These include large wavelengths and are in principle compliant with experiments [112]. Additionally, it can not be excluded form experimental data that the observed periodic spatial structures with low wavenumbers coexist with small nanometer scale patterns [122]. In summary, it seems unlikely that the mechanisms included so far give the complete picture of the interactions involved. An additional spatial stabilization mechanism in effect for small length scales could not be identified.

Numerical investigations of the patterns predicted by Eqs. (4.26),(4.27) are very demanding since at least six orders of magnitude have to be covered in the spatial variable. Such simulations would yield valuable insight if the above description is indeed sufficient or if additional mechanisms have to be introduced to describe the formation of stationary structures in electrochemical systems with an S-shaped current potential characteristic caused by attractive lateral adsorbate-adsorbate interactions in detail.

Chapter 5

N-NDR Systems – Prototype Oscillator under Negative Global Coupling

After investigating the spatio-temporal dynamics of one variable supplemented with a global constraint in the previous chapter, this chapter deals with pattern formation in a true two variable system. We are going to study the dynamics of the prototype N-NDR oscillator introduced in section 2.5.1 under NGC focusing on instabilities of limit cycles. As mentioned in section 3, the new formulation of the double layer dynamics in terms of uncompensated and external resistance called for new experiments in which strictly negative global coupling is applied to an electrochemical system with a two dimensional WE. By means of a negative impedance device a desynchronizing global coupling acting with equal strength on the entire WE can be realized, cf. chapter 3. Such experiments were recently conducted by Li using a rectangular WE [122]. The chosen dimensions of the WE allowed pattern formation effectively only in 1d. Besides standing waves new phenomena were observed, namely pulse-like structures which apparently bifurcate from homogeneous oscillations on the one side and from anti-phase oscillations on the other side as a function of the applied potential. This findings motivated us to study the prototype N-NDR oscillator under NGC ($\rho < 0$) in 1d with no-flux boundary conditions.[1]

The transport processes acting on the concentration of the reacting species parallel to the electrode, migration and diffusion, are neglected in the following. This is well justified since the migration coupling acting on the activator variable, ϕ_{DL}, is much faster than diffusion of the inhibitor c. It is well known that the spatial coupling on the inhibitor can be neglected in this situation.

Recalling the derivation of the concentration dynamics given in section 2.5.1, the

[1] Note that, to the best knowledge of the author, all previous studies used periodic boundary conditions.

Table 5.1: *Parameter values used in Eqs. (5.3),(5.4)*

ε	=	0.0005	σ	=	0.2	β	=	3
k_0	=	$7.2932 \cdot 10^{-5}$	k_1	=	472.5	k_2	=	$5.5932 \cdot 10^4$

dynamical system describing pattern formation in the prototype N-NDR oscillator is

$$C_{DL}\frac{\partial \phi_{\mathrm{DL}}}{\partial t} = -i_r + \frac{\sigma}{\beta}\left(U - \phi_{\mathrm{DL}}\right) + \frac{\sigma\rho}{\beta}\left(\langle\phi_{\mathrm{DL}}\rangle - \phi_{\mathrm{DL}}\right) - \frac{\sigma(1+\rho)}{\beta}\left(\frac{\partial\phi}{\partial z} - \phi\right)\Big|_0 \tag{5.1}$$

$$\frac{\delta}{2}\frac{\partial c}{\partial t} = -\frac{1}{nF}i_r + \frac{D}{\delta}(c^b - c). \tag{5.2}$$

Eqs. (5.1),(5.2) are used in their dimensionless form in the following. The transformations of the variables and parameters are given in Appendix A.1.1 [107]. The resulting equations read (the new variables and parameters are relabeled to the old ones for clarity)

$$\varepsilon\frac{\partial \phi_{\mathrm{DL}}}{\partial t} = -i_r + \frac{\sigma}{\beta}\left(U - \phi_{\mathrm{DL}}\right) + \frac{\sigma\rho}{\beta}\left(\langle\phi_{\mathrm{DL}}\rangle - \phi_{\mathrm{DL}}\right) - \frac{\sigma(1+\rho)}{\beta}\left(\frac{\partial\phi}{\partial z} - \phi\right)\Big|_0 \tag{5.3}$$

$$\frac{\partial c}{\partial t} = -i_r + 1 - c \tag{5.4}$$

with

$$i_r = ck_0(\phi_{\mathrm{DL}}^3 + k_1\phi_{\mathrm{DL}}^2 + k_2\phi_{\mathrm{DL}}^3).$$

Fitting the parameters k_i to the reduction of peroxodisulfate on Ag yields the values given in Table 5.1. The other parameter values are determined by physical constants compiled in Table A.1.

A linear stability analysis of Eqs. (5.3),(5.4) along the lines developed in section 2.4 was performed by Christoph [36, 45, 103, 104, 115]. The resulting basic stability diagram in the (ρ-ε) parameter plane is presented schematically in Fig. 5.1. σ and U are chosen such that the system has one fixed point on the branch of negative differential resistance of the current-potential characteristic (cf. section 2.2.1 and Fig. 5.4). If the dynamics of the activator is faster than a threshold, $\varepsilon < \varepsilon^h$, the steady state is oscillatory unstable. ε^h is independent of the global coupling. The oscillatory motion stays homogeneous for small global coupling. If $|\rho| > |\rho_c|$ homogeneous oscillations are unstable ($|\rho|$ increases from top to bottom in Fig. 5.1 since $\rho < 0$.). Inhomogeneous oscillations will be observed. Additionally, the wave instability introduced in section 2.4 takes place at $\varepsilon > \varepsilon^h$ if $|\rho| > |\rho_c|$. In case of an oscillatory stable fixed point the system displays stationary domains if $|\rho|$ exceeds a critical NGC-strength $|\rho^d|$ [41].

In this chapter we give a complete picture of the instabilities of the oscillatory dynamics at intermediate global coupling strength as a function of U, i.e., for ρ and ε in the lower left corner of the diagram shown in Fig. 5.1.

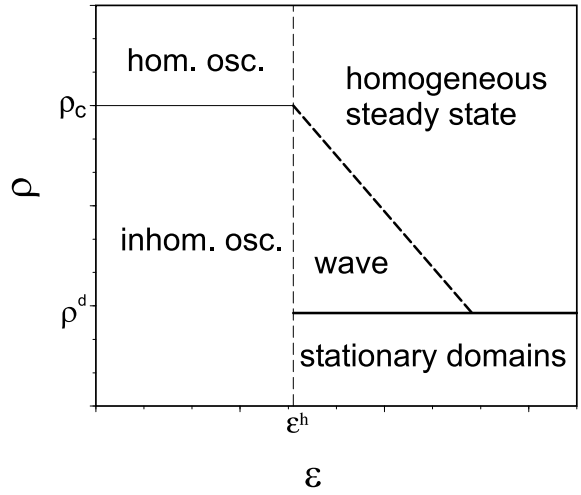

Figure 5.1: *Schematic skeleton stability diagram of Eqs. (5.3),(5.4) in the (ρ-ε) parameter plane. Homogeneous oscillations are observed for $|\rho| < |\rho_c|$ (note that $\rho < 0$ and thus, $|\rho|$ increases from top to bottom) and $\varepsilon < \varepsilon_h$. The homogeneous steady state is stable for more positive ε up to $\rho = \rho_d$ apart from a region where the wave instability destabilizes the fixed point before the Hopf bifurcation and standing waves or pulses are found. If $|\rho| > |\rho_d|$ and $\varepsilon > \varepsilon^h$ the homogeneous steady state is unstable with respect to the formation of stationary domains. In the region $|\rho| > |\rho_c|$ and $\varepsilon < \varepsilon^h$ inhomogeneous oscillations of a priori unknown kind will be found. After [104].*

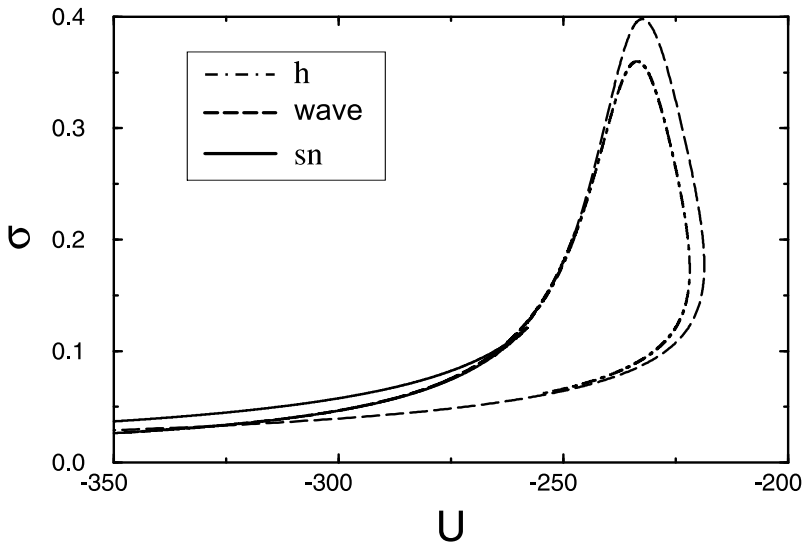

Figure 5.2: *sn, h and wave bifurcation for $\rho = -0.7$ in the (σ-U) parameter plane. Other parameters as in Table 5.1.*

Thus, the parameters ρ and σ have to be chosen accordingly. Fig. 5.2 displays the locations of sn, Hopf and wave bifurcations of Eqs. (5.3),(5.4) in the (σ-U) parameter

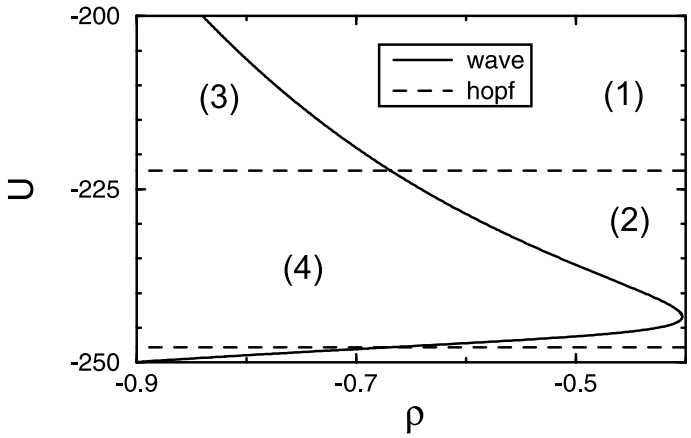

Figure 5.3: *Bifurcation diagram showing the points of Hopf (dashed line) and wave (solid line) instabilities in the (U-ρ) parameter plane. The numbers indicate the different attractors; (1) homogeneous steady state; (2) homogeneous oscillations; (3) standing waves; (4) inhomogeneous oscillations. Other parameters as given in Table 5.1.*

plane for $\rho = -0.7$. No bistability is found in the system for $\sigma \gtrsim 0.15$. Therefore, $\sigma = 0.2$ is used in the following. The homogeneous steady state always is destabilized in a wave bifurcation, then homogeneous oscillations bifurcate from the unstable fixed point at this NGC-strength. The points of the wave instability in (U-ρ) parameter space are shown together with the ρ-independent Hopf bifurcation points in Fig. 5.3 for parameter values given in Table 5.1. Hopf and wave bifurcation coincide in two double degenerate points (codimension-two bifurcations) at $\rho \approx -0.65$. Thus, stable standing wave solutions or anti-phase oscillations are expected to exist in the system for $\rho < -0.65$ in the upper and lower U-interval between the wave and Hopf bifurcation points, respectively.[2] In the following we denote the point of the wave bifurcation at lower U as U^w ($U^w = U^w(\rho)$).

Fig. 5.4 displays the current-potential characteristic of the N-NDR system together with a representative load line for the parameters given in Table 5.1. Since the parameters are fitted to the reduction of peroxodisulfate at Ag, the reaction current as well as the applied potential are negative.

The chapter is organized as follows. In the next section the bifurcation scenario as a function of U is given and is illustrated with numerical simulations. The other parameters are fixed at the values mentioned above. Section 5.2 compiles results that point to a generalization of a remarkable phase space structure found during the investigations in section 5.1 and also in the semiconductor S-NDR dynamics [52, 82, 153, 161] (cf. section 4.1.4). The presented findings are summarized in section 5.2.3 and an outlook to possible extensions is given.

[2] Traveling wave solutions do not exist since no-flux boundary conditions are used.

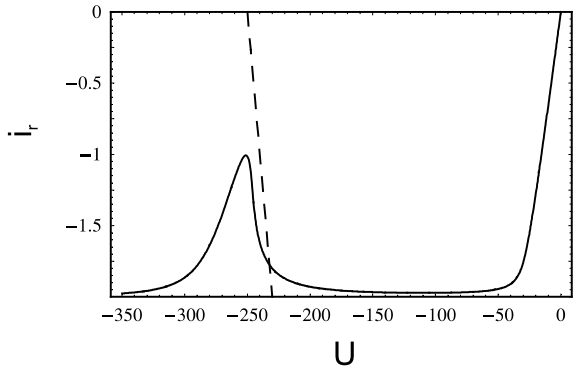

Figure 5.4: *Current-potential characteristic for the reduction of peroxodisulfate at Ag (solid line) together with a load line that intersects the N-NDR characteristic on the branch of negative differential resistance (dashed line). Parameters as given in Table 5.1.*

5.1 Spatio-temporal Dynamics

5.1.1 Bifurcation Analysis and Simulations

In this section the basic modes of spatio-temporal behavior observed in the prototype N-NDR oscillator at a certain strength of the NGC are presented. ρ is fixed at -0.7 throughout this section and the other parameters are given in Table 5.1. Simulations were performed using 15 cosine modes and an error tolerance of 10^{-8}.

Bifurcations displayed by Eqs. (5.3),(5.4) as a function of U are shown in Fig. 5.5 in the (max($\langle i_r \rangle$)-U) plane. The bifurcation diagram was calculated using seven cosine modes. The system exhibits one stable homogeneous stationary fixed point (solid line) for applied voltages $U \lesssim -248$ and $U \gtrsim -219$. As already shown in Figs. 5.2 and 5.3, the fixed point loses stability in wave bifurcations at lower and higher applied voltage.

The unstable homogeneous oscillations bifurcate from the unstable steady state just after the respective wave bifurcation at lower and higher values of the applied voltage, respectively. The increase of max($\langle i_r \rangle$) at the Hopf bifurcation at lower U is very steep until a plateau is reached which is attributed to the complex phase space structure at $U = U^w$ discussed in section 5.2.

The oscillatory instability with wavenumber one at $U \approx -219$ is supercritical and a branch of stable standing wave solutions is born (filled circles). An example of the observed spatio-temporal motion is given in Fig. 5.6(a). As can be seen in the third plate of Fig. 5.6(a), the oscillation amplitude of the homogeneous mode of the double layer potential, $a_0^{\phi_{\mathrm{DL}}}$, is small compared to the amplitude of the first cosine mode, $a_1^{\phi_{\mathrm{DL}}}$. Still, the amplitude of the homogeneous mode is not equal to zero. Consequently, the pattern shown in Fig. 5.6(a) does not resemble a standing wave in the strict sense. The oscillation

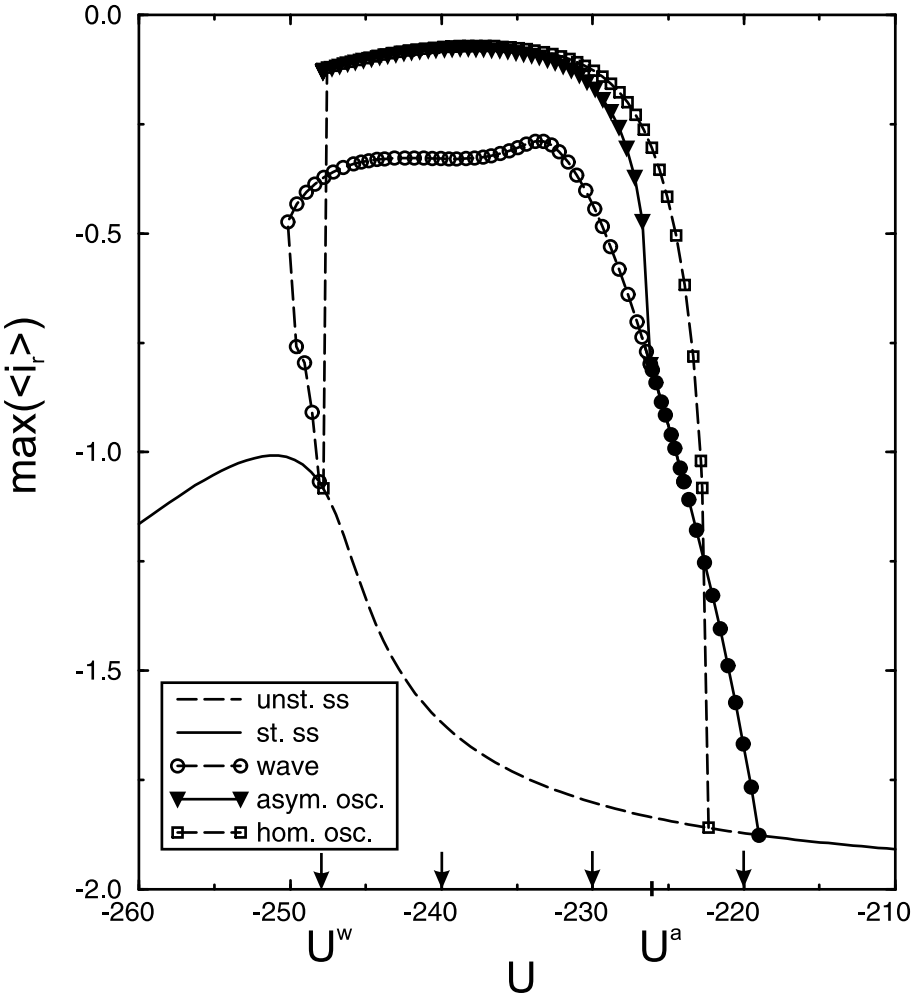

Figure 5.5: *Bifurcation diagram of the prototype N-NDR oscillator for intermediate NGC-strength. Displayed is the average (maximum) reaction current density, max$(\langle i_r \rangle)$, as a function of the applied voltage, U. Going down from more positive voltages, the homogeneous steady state (solid line) loses stability in a supercritical wave bifurcation. A more complex asymmetric spatio-temporal pattern (filled triangles, cf. Fig. 5.6(b)) bifurcates from the branch of standing wave solutions (filled circles, cf. Fig. 5.6(a)) in a supercritical pitchfork bifurcation of limit cycles at $U = U^a$. This branch terminates in a phase space region with complex structure discussed in detail in section 5.2. The unstable homogeneous oscillations (open squares) branch from the unstable homogeneous steady state (dashed line) after the wave bifurcation and return to the fixed point at lower voltages before the following subcritical wave bifurcation (open circles) at $U = U^w$. A set of unstable inhomogeneous limit cycles existing in a small U-interval is not shown here. Note that solutions were calculated at more U-values, but are omitted here for clarity. The arrows indicate the points at which spatio-temporal simulations are presented in Figs. 5.6-5.8.* $\rho = -0.7$*, other parameters see Table 5.1.*

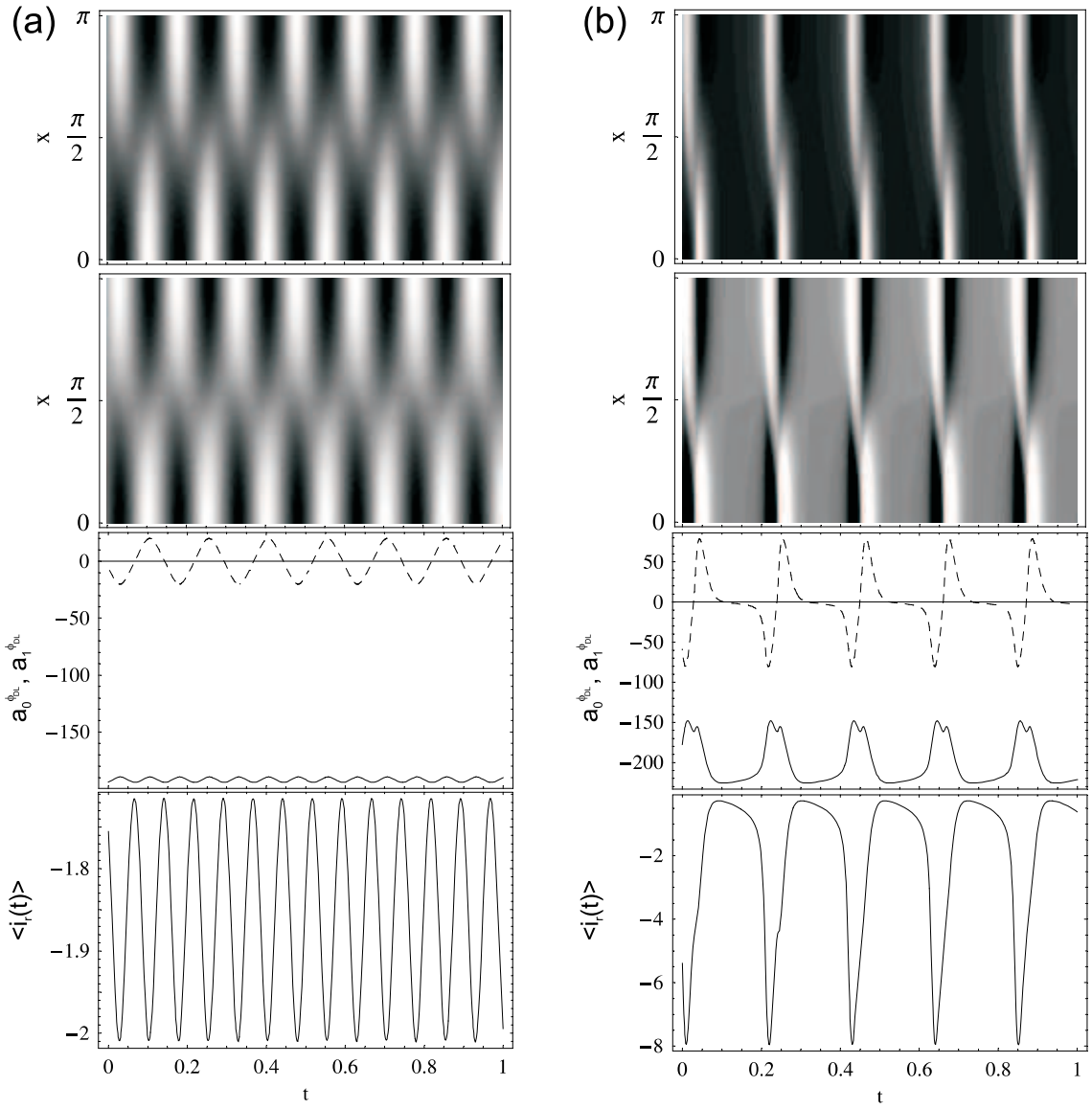

Figure 5.6: *(a) Standing wave pattern for $U = -220$. (b) Asymmetric spatio-temporal oscillation for $U = -230$. First plates: $\phi_{DL}(x,t)$, second plates: ϕ_{DL}-$\langle\phi_{DL}\rangle$, third plates: homogeneous ϕ_{DL}-mode, $a_0^{\phi_{DL}}(t)$, (solid line) and first cosine mode, $a_1^{\phi_{DL}}(t)$, (dashed line), fourth plates: $\langle i_r(t)\rangle$. $\rho = -0.7$, other parameters see Table 5.1. A linear gray scale map was used; white corresponds to the maximal ϕ_{DL} (active state) and black to the minimal ϕ_{DL}-value (passive state), respectively.*

frequency of the homogeneous mode is twice the one of the first cosine mode since $\langle\phi_{DL}\rangle$ is only sensitive to $|a_1^{\phi_{DL}}|$. This frequency doubled behavior is retained in the oscillations of the averaged reaction current density that are of relatively small amplitude.

The branch of stable standing wave solutions loses stability and gives rise to qual-

itatively new dynamics (filled triangles) in a supercritical pitchfork bifurcation of limit cycles at $U = U^a$. An example of the resulting pattern at a finite distance from the bifurcation point is shown in Fig. 5.6(b). Most remarkable is the spatial asymmetry in the spatio-temporal motion. The nodal line of the standing wave that is positioned at $\pi/2$ for $U > U^a$ moves closer to one of the borders. Additionally, the symmetry regarding the separation by half an oscillation period of the ϕ_{DL}-maxima appearing at the borders is also removed such that the excitations at the borders appear shortly one after the other separated by passive intervals (high $|\phi_{\mathrm{DL}}|$). This quite unusual behavior becomes clearer if one considers the first Fourier modes given in plate three of Fig. 5.6(b). The first cosine mode oscillates symmetrically to zero as expected. The asymmetry stems from the interplay of the first mode with the homogeneous mode. The homogeneous mode displays a two-peaked oscillation. The highest peak coincides with the maximum amplitude of the first mode. The maximum amplitude of the first mode with the opposite sign corresponding to the other half of the electrode occurs on the downward flank of the homogeneous mode. Consequently, the sum of homogeneous and first mode is smaller leading to an asymmetric nodal line. Herewith also the issue of the apparent change of the phase shift between the oscillations at $x = 0$ and $x = \pi$ is resolved.

The oscillation frequencies of the homogeneous and the spatial modes coincide for asymmetric standing waves. Starting from the bifurcation point, the amplitude of the two $a_0^{\phi_{\mathrm{DL}}}$ maximas in one period of $a_1^{\phi_{\mathrm{DL}}}$ evolve in different directions. Additionally, the lower maximum moves closer to the previous absolute one. Thus a smooth transition from standing waves to asymmetric standing waves is provided. Note also that the two-peaked structure of the homogeneous double layer potential time series is not retained in the mean reaction current density pointing at a non-vanishing contribution of capacitive currents.

At again lower applied voltages the dynamics evolves continuously to a pulse-like behavior as shown in Fig. 5.7. The amplitude of the first cosine mode increases fast as soon as the vicinity of the unstable homogeneous fixed point is left and leads to the spatio-temporal impression of a pulse-like motion. The pulse-like pattern results in an additional asymmetry in the first spatial modes, cf. dashed line in plate three of Fig. 5.7. Additionally, the current oscillations in this U-range exhibit long passive periods which hints at a possible proximity of a homoclinic orbit since the stationary state is also passive. Comparing the current and potential values of the long passive phase with the respective values of the unstable fixed point further supports this hypotheses. It is argued in detail in the next section that indeed a homoclinic connection terminates the branch of asymmetric standing wave solutions.

In Fig. 5.8 an orbit close to the homoclinic bifurcation is displayed. Due to the intricate phase space structure in this U-region it is not possible to continue the stable oscillatory dynamics up to these parameters. Nevertheless, it can be observed that the simple oscillatory motion found at $U = -240$ has lost stability and the dynamics at $U = -248$ resemble

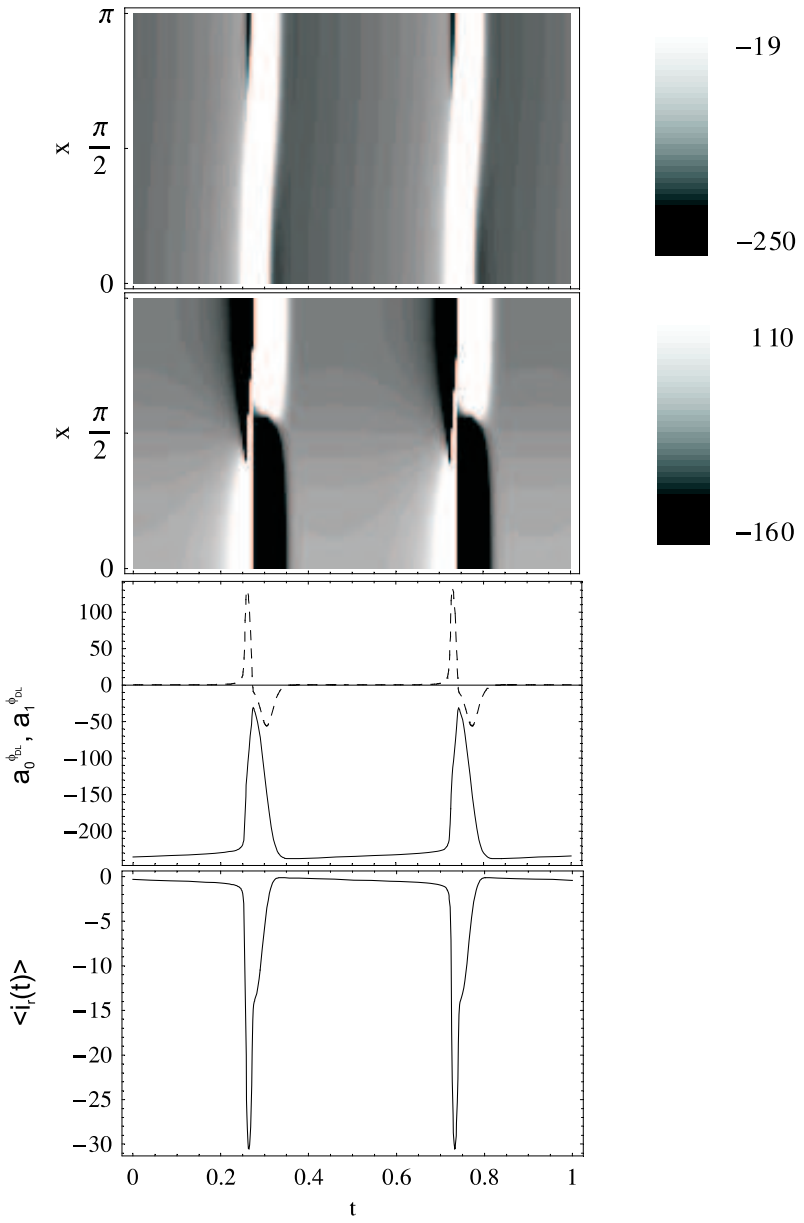

Figure 5.7: *Pulse-like behavior observed at $U = -240$. First plate: $\phi_{\mathrm{DL}}(x,t)$, second plate: ϕ_{DL}-$\langle\phi_{\mathrm{DL}}\rangle$, third plate: $a_0^{\phi_{\mathrm{DL}}}(t)$ (solid line) and $a_1^{\phi_{\mathrm{DL}}}(t)$ (dashed line), fourth plate: $\langle i_r(t)\rangle$. $\rho = -0.7$, other parameters see Table 5.1. The used gray scale maps are given next to the spatio-temporal data together with the maximum and minimum value of ϕ_{DL} and ϕ_{DL}-$\langle\phi_{\mathrm{DL}}\rangle$, respectively.*

a period doubled limit cycle. The period doubling is apparent in the difference plot, Fig. 5.8(b). The homogeneous fixed point is of the saddle-focus type at these parameter values, cf. Fig. 5.5, the focus being the unstable plane. The trajectory is brought into the vicinity of the fixed point by the stable directions and spirals out in the plane of the focus

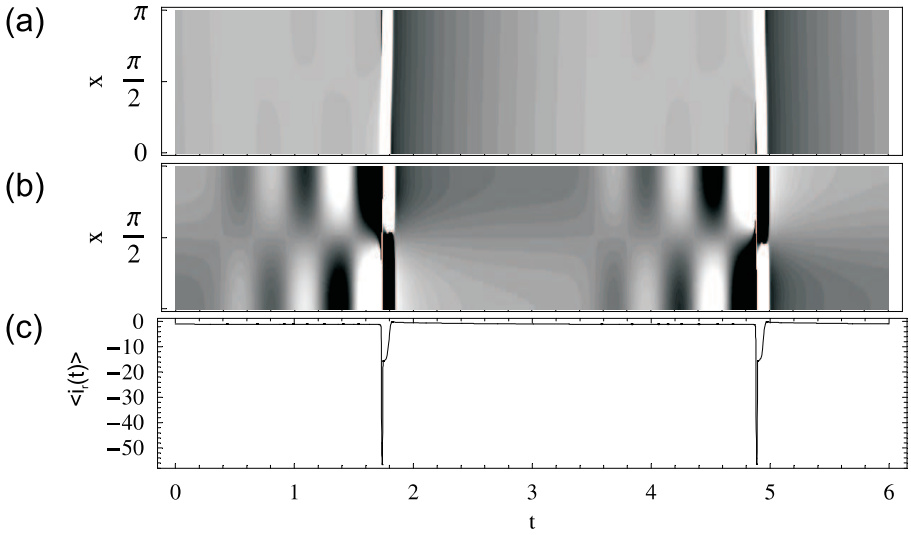

Figure 5.8: *Period doubled pulse at* $U = -248$. *(a)* $\phi_{\mathrm{DL}}(x,t)$, *(b)* ϕ_{DL}-$\langle\phi_{\mathrm{DL}}\rangle$, *(c)* $\langle i_r\rangle$. $\rho = -0.7$, *other parameters see Table 5.1.*

which is spanned by the first cosine modes of ϕ_{DL} and c, $a_1^{\phi_{\mathrm{DL}}}$ and a_1^c. This plane comprises the slow direction in phase space. Finally an excursion in phase space is observed in which the inhomogeneous modes again grow fast in the initial stage. Now, the sign of a_1 changes from one large excursion in phase space to the next one leading to a period doubled, alternating, behavior in space-time. A pulse is emitted at one boundary and travels to the opposite boundary where it is extinct. The next pulse is emitted at the boundary where the other one vanished. Consequently, also the spiraling out in the first modes is inverted in time, cf. Fig. 5.8(b). Note that (i) the period doubled behavior is not visible in the mean reaction current density (s.a.) and (ii) the dynamics are of the mixed-mode type (not visible since the high frequency current oscillations are of too small amplitude).

Decreasing the applied voltage further below U^w, the passive homogeneous steady state was found to be the only attractor.

5.1.2 Discussion and Conclusions

The spatio-temporal dynamics of the prototype N-NDR oscillator were investigated in the oscillatory regime subject to NGC. The instabilities of the emerging limit cycle motions were investigated with the use of numerical continuation techniques and through simulations for an intermediate NGC-strength as a function of the applied potential for no-flux boundary conditions.

The following sequence of stable attractors was observed with decreasing applied potential. The homogeneous steady state loses stability in a supercritical wave bifurcation leading to standing waves. A secondary (symmetry breaking) supercritical pitchfork bi-

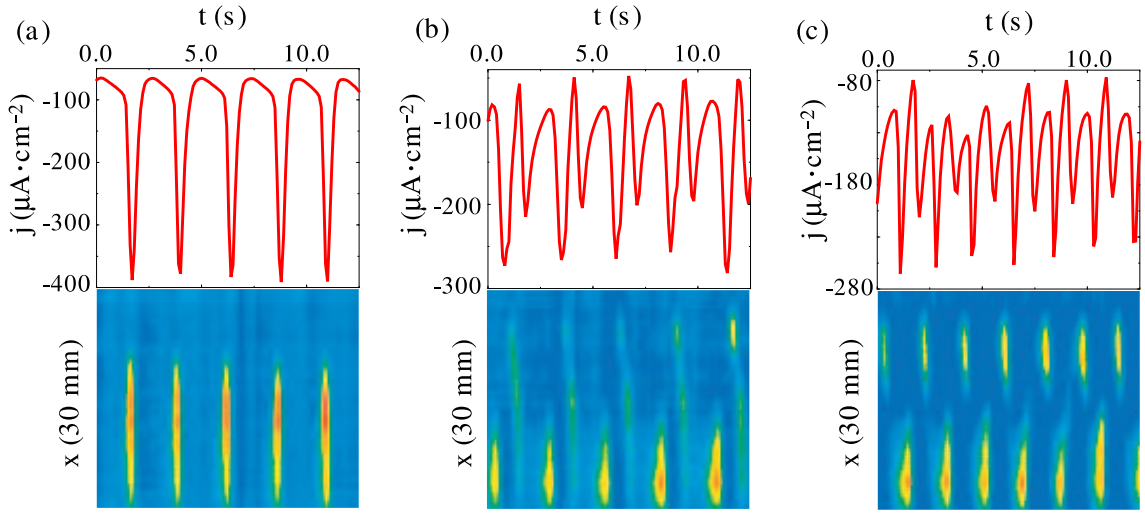

Figure 5.9: *Experimental data obtained during the oscillatory reduction of periodate at a Ag electrode under NGC employing a negative impedance device. The rectangular WE allowed pattern formation effectively only in one dimension. The average over the direction not participating in the spatial pattern formation is taken at every time moment. The upper plates display the total current density. The spatio-temporal dynamics on the WE is given in the lower plates. The data is obtained by surface plasmon resonance measurements [29]. For experimental details see Ref. [122] chapter 6. The upper part of the electrode does not seem to take part in the dynamics due to the chosen experimental setup. (a) Apparently homogeneous oscillations at the lower U-boundary of oscillatory behavior. (b) Pulse-like behavior in the middle of the oscillatory region. (c) Standing waves are observed at the upper voltage boundary of the oscillatory regime. After [122].*

furcation gives rise to asymmetric standing waves reported here for the first time. The dynamics underlying the occurrence of asymmetric standing waves could be clarified. Asymmetric standing waves continously transform to pulse-like behavior. Approaching the second subcritical wave bifurcation at lower U, the spatio-temporal dynamics become relaxation-like and period doubled pulses are observed. The stable pulse-like motion that corresponds to a limit cycle in phase space is removed from the system by means of a homoclinic orbit at the point of the wave bifurcation of the homogeneous steady state.

Experimental studies by Li exhibited the same bifurcation sequence [122], cf. Fig. 5.9, in particular the symmetry breaking bifurcation was also reported. A general trend of the electrode to display asymmetric patterns clearly visible in Fig. 5.9 has to be attributed to the experimental setup. See [122] chapter 6 for a comprehensive discussion.

Fig. 5.9(a) displays the apparently homogeneous oscillations that were observed at the lower boundary of oscillatory behavior. The discrepancy between model and experiment, i.e., the observation of homogeneous oscillations in the experiment opposed to pulse-like

behavior in the model, could have two reasons. The spatial inhomogeneity during pulse-like motion is only present with large amplitudes in the passive phase, cf. Fig. 5.7. The relaxation-like oscillations would require a better signal to noise ratio than available in the experiments to distinguish between pulse-like and homogeneous dynamics. Another possible explanation is that the sequence of Hopf and wave bifurcation at the lower U-boundary is reversed at different parameters in the sense that the homogeneous steady is first destabilized in a Hopf bifurcation thus giving rise to stable homogeneous oscillations. However, the relaxation-like form of the oscillations is observed in experiment and theory.

At higher voltages the behavior observed in experiment resembles the pulse-like dynamics apart from a region on the lower part of Fig. 5.9(b) that can be explained by the intrinsic asymmetry present in the experimental setup. In Fig. 5.9(c) a manifestation of standing waves is shown. Unfortunately, the distinction between standing waves and asymmetric standing waves is not possible in the experiment due to the intrinsic asymmetry. Nevertheless, the observation of the pulse-like motion and standing waves suggests the existence of the symmetry breaking pitchfork instability leading to asymmetric standing waves also in the experiments. Either the parameter interval in which asymmetric standing waves can be observed is small or the experimental asymmetry excludes the identification of asymmetric standing waves.

Christoph *et al.* performed similar studies concerning the prototype N-NDR oscillator under NGC using periodic boundary conditions [36, 104]. Standing waves were also reported. Christoph found stable target patterns and period doubled target patterns at higher voltages.[3] Target patterns are the analogon of pulse-like behavior in systems with periodic boundary conditions. Adding a reflected image of the pulse-like behavior to Fig. 5.7 to extend space to the interval from 0 to 2π target patterns are obtained. The transition from standing waves to target patterns involves a symmetry breaking bifurcation also in systems with periodic boundary conditions since the symmetry $\phi_{\mathrm{DL}}(x,t) = \phi_{\mathrm{DL}}(x+\pi, t+T/2)$ is lost at the transition.

Pulse-like behavior in oscillatory reaction-diffusion systems with no-flux boundary conditions under global coupling was reported earlier [58, 61]. Though a systematic study of the bifurcations using continuation techniques has not been presented before.

In conclusion, the prototype N-NDR oscillator successfully models the dynamics of the periodate reduction on Ag under NGC. The investigation of the spatio-temporal dynamics using bifurcation analysis provided valuable insight. Since the prototype N-NDR model is build on the most common electrochemical mechanisms for oscillatory behavior, cf. section 2.5.1, and the reaction rate constants were fitted to model peroxodisulfate reduction but agree with experimental data obtained during periodate reduction, the results presented here are expected to be transferable to other N-NDR oscillators.

[3] The authors considered an oxidation reaction.

5.2 Subcritical Bifurcations to a Homoclinic Saddle-Focus

The phase space in the vicinity of the homoclinic orbit is explored in detail in this section. It is demonstrated that the homoclinic connection coincides with the subcritical wave instability of the homogeneous fixed point. The simultaneous observation of a homoclinic orbit and a subcritical oscillatory instability is shown to exist for different values of the NGC-strength. Thus, the point in parameter space seems to be a codimension-one bifurcation rather than due to a double degeneracy. Realizing that Sch¨oll *et al.* reported a similar instability in the S-NDR semiconductor system [52, 82, 153, 161] (cf. section 4.1.4), some results regarding the semiconductor system will also be presented. The author is not aware of reports of such a coincidence in other dynamical systems. A generalization of the sufficient condition for the occurrence of complex spatio-temporal dynamics given in [52] (cf. section 4.1.4) motivated by the findings presented here is attempted in section 5.2.3.

Since general results concerning bifurcation points and not realistic modeling of spatio-temporal data is the aim in this section, the dimensionality of the dynamical systems, N, is reduced to the minimum wherever feasible by considering only the first spatial mode(s).

5.2.1 Electrochemical System

It was already argued in the previous section that the dynamics close to the homoclinic orbit observed in the N-NDR oscillator at U^w are of the saddle-focus type. Comparable dynamics were first investigated in three variables by Shil'nikov [87, 170, 171]. Fig. 5.10 gives an illustration of the typical phase space dynamics. In Fig. 5.10(a) a trajectory in a three dimensional projection of the, in this case, four dimensional dynamics (i.e., only the first cosine modes were used, $N = 4$) in the space of the homogeneous modes and the amplitude of the first mode of the concentration of the inhibitor in front of the WE, a_1^c, is shown for U slightly larger than U^w. As mentioned in the previous section, the leaving of the vicinity of the unstable fixed point (square in the lower right corner of Fig. 5.10(a)) is accompanied by a strong increase of the inhomogeneous mode. Note that the dynamics are not period doubled at this parameter value using $N = 4$. Due to the relaxation-like oscillations, the trajectory stays close to the homogeneous fixed point during the largest portion of the limit cycle motion. In Fig. 5.10(b) a zoom in the region of the saddle-focus in the plane of the inhomogeneous modes is presented. The spiraling out of the trajectory resembles an almost perfect Archimedian spiral in this plane.

In Fig. 5.11 the oscillation period of the pulse-like behavior is given as a function of U. Also shown is the point of the wave bifurcation at lower U, U^w. The period apparently diverges at the wave bifurcation point. It should be noted that continuations of the

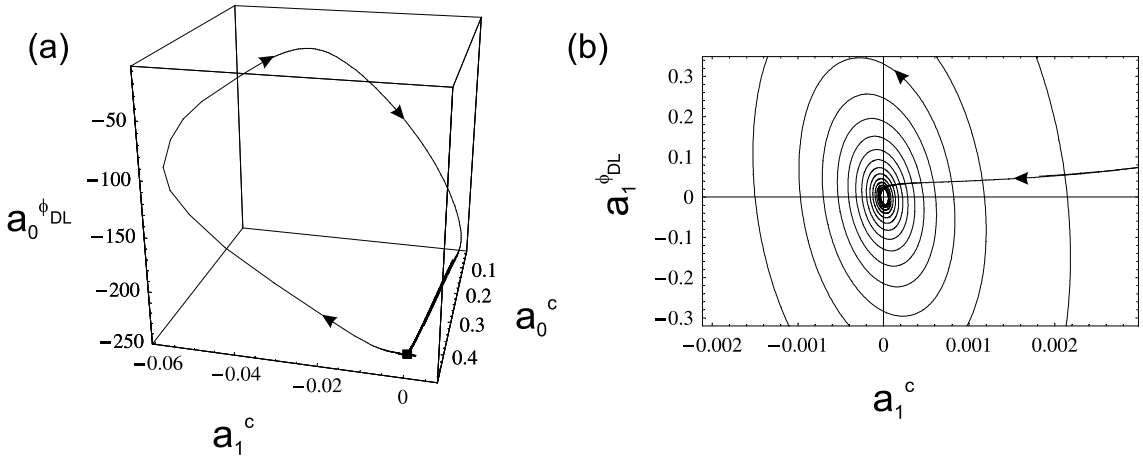

Figure 5.10: *Projections of the phase space trajectory of the N-NDR oscillator close to the homoclinic orbit. Only the first cosine mode was used in the simulations. Thus, the dynamics is four dimensional. (a) Full limit cycle in* $(a_0^{\phi_{\mathrm{DL}}}, a_0^c, a_1^c)$*-space. The unstable stationary fixed point is marked with a square in the lower right corner* $(a_1^c = 0)$*. (b) Zoom in the region of the fixed point in the* $(a_1^{\phi_{\mathrm{DL}}}, a_1^c)$*-plane.* $N = 4$*,* $U = -248.08$*,* $\rho = -0.7$*, other parameters as given in Table 5.1.*

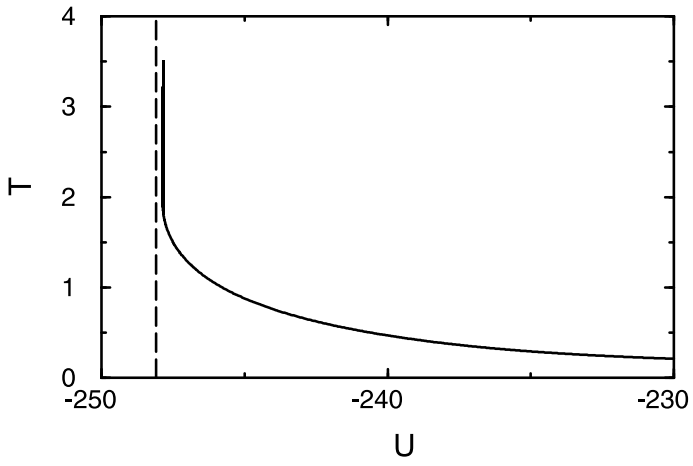

Figure 5.11: *Period* T *of periodic pulse-like motion as a function of the applied voltage* U *(solid line). The dashed line marks the point of the wave bifurcation of the homogeneous steady state,* $U^w = -248.088$*.* $N = 16$*,* $\rho = -0.7$*, other parameters as given in Table 5.1.*

relaxation-like oscillations close to U^w were only possible up to a distance of $\approx 10^{-3}U^w$ due to the relaxational form or due to the complex phase space structure in the vicinity of the homoclinic orbit. But simulations were performed up to a distance of $\approx 10^{-6}U^w$ to the wave bifurcation and the period was found to diverge further.

The bifurcation structure in the vicinity of U^w as obtained from the above arguments

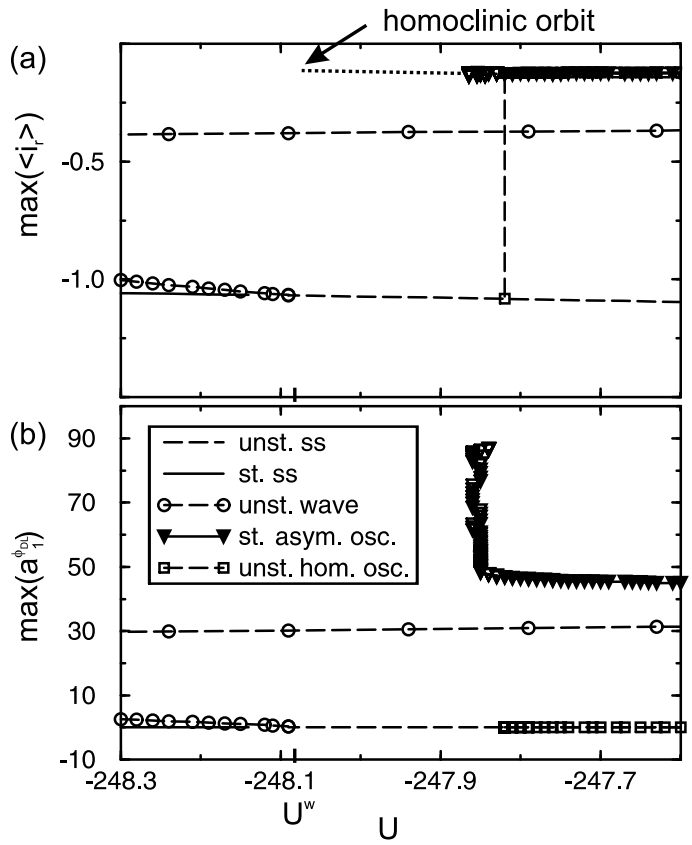

Figure 5.12: *Bifurcation diagrams in the vicinity of U^w. (a) Zoom corresponding to Fig. 5.5. The stable passive homogeneous steady state (solid line) undergoes a subcritical wave instability (open circles). Shortly after the wave bifurcation an unstable homogeneous oscillatory solution (open squares) branches from the unstable fixed point (dashed line). $max(\langle i_r \rangle)$ of the unstable homogeneous oscillations increases fast until it reaches the amplitude of the pulse-like solutions (triangles). The pulse-like solutions could not be continued up to the wave bifurcation. Simulations indicate that periodic relaxation-like pulse solutions exist up to U^w (indicated by a dotted line). (b) shows the same solution branches in the $(max(a_1^{\phi_{DL}})$-$U)$ parameter plane to resolve stable pulse-like solutions from the unstable homogeneous limit cycle. Parameters as in Fig. 5.5.*

and numerical calculations is summarized in Fig. 5.12. Fig. 5.12(a) displays a zoom corresponding to the full bifurcation diagram, Fig. 5.5. $\max(a_1^{\phi_{DL}})$ of the different branches is shown in Fig. 5.12(b) instead of $\max(\langle i_r \rangle)$ as in Fig. 5.12(a) to resolve unstable homogeneous and stable inhomogeneous limit cycles. These only come close to each other in the projection on the averaged reaction current density but are well separated in phase space. The unstable homogeneous limit cycle does not influence the flow in the vicinity of the limit cycle motion corresponding to pulse-like solutions.

In summary, it is shown that there seems to exist a homoclinic orbit at U^w and that

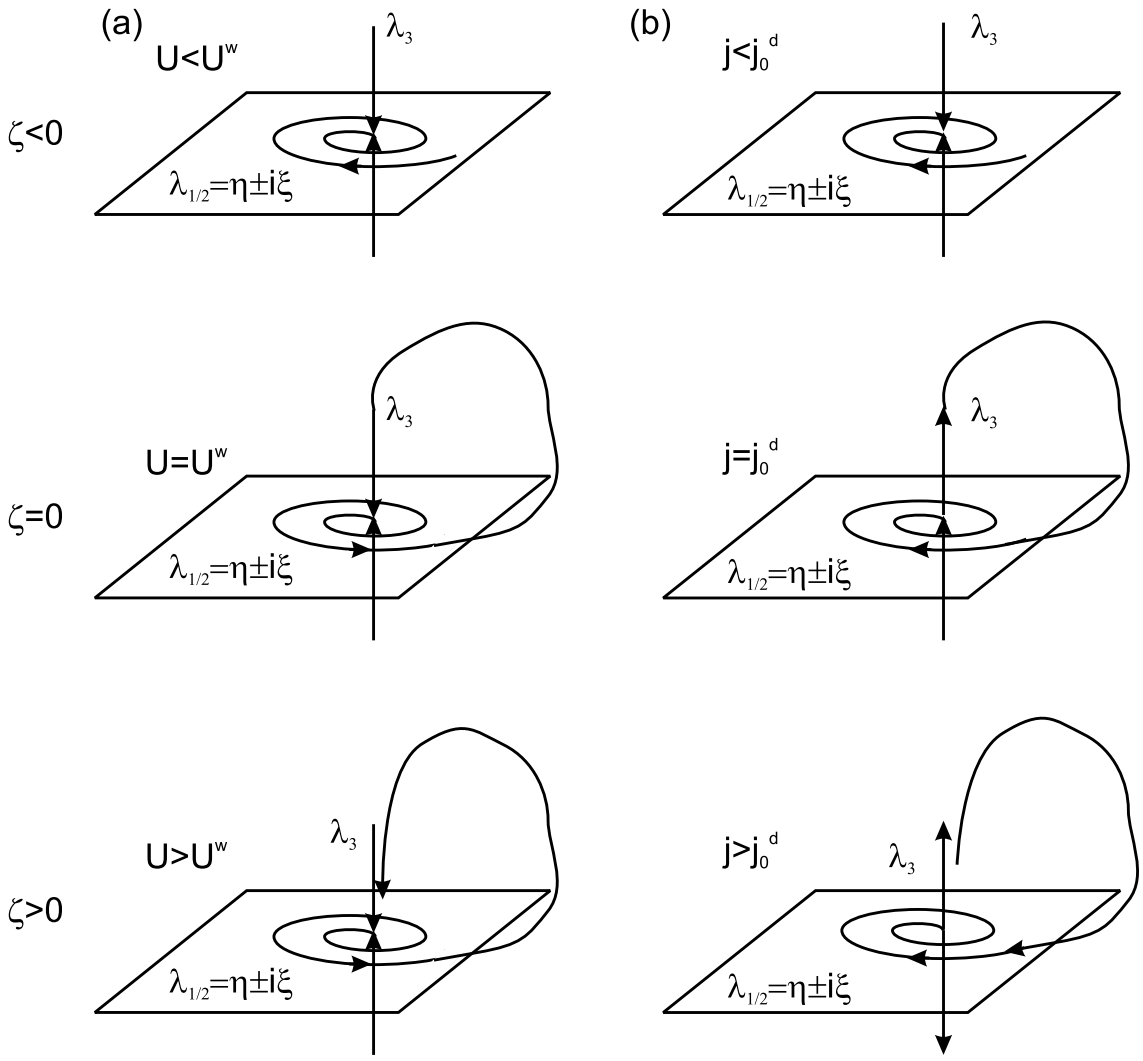

Figure 5.13: *Illustration of the flow in phase space close to the simultaneous occurrence of a Shil'nikov-type homoclinic orbit and a subcritical bifurcation. (a) For the electrochemical N-NDR oscillator (subcritical wave bifurcation,* $\eta(U = U^w) = 0$*);* $\eta < |\lambda_3|$*. (b) For the semiconductor S-NDR oscillator (subcritical pitchfork bifurcation,* $\lambda_3(j_0 = j_0^d) = 0$*);* $\lambda_3 < |\eta|$*.*

the attractor on the left of the bifurcation point is a stable stationary state whereas the dynamics resembles the Shil'nikov saddle-focus type on the right of U^w. Note however that the dynamics lives in a four dimensional phase space. At this stage, it is not clear whether the minimal phase space dimension of the phenomenon we are dealing with is three or four. The flow close to U^w is illustrated in Fig. 5.13(a). A distinct difference to the dynamics in the Shil'nikov situation has to be emphasized. The real part of the imaginary eigenvalues of the fixed point is zero at U^w and thus at the homoclinic connection. Hence, the topology of the phase space is expected to differ from the classic Shil'nikov situation.

As a consequence also the scaling, e.g., for the period of the limit cycle approaching the homoclinic orbit, might deviate from the standard scenario. The nonlinear analysis of the normal form of a subcritical Hopf bifurcation shows that the fixed point is unstable at $U = U^w$, cf. plate two in Fig. 5.13(a).

Let us consider Shil'nikov's condition for the observation of chaos in the proximity of a Shil'nikov homoclinic connection. For the case presented here the real part, η, of the imaginary eigenvalues $\lambda_{1/2} = \eta + i\xi$ is by definition smaller than the absolute value of the real eigenvalues, $\eta < |\lambda_3|$, in a neighborhood of the bifurcation point since $\eta = 0$ at the wave bifurcation. Thus, Shil'nikov's condition for chaotic dynamics in the vicinity of a homoclinic orbit is generically fulfilled. Still, dynamics of the mixed-mode type rather than chaos is observed to the right of U^w. Also the typical series of sn and period doubling bifurcations normally present with increasing period of the unstable periodic orbit close to a Shil'nikov homoclinic orbit for $\eta < |\lambda_3|$ is not observed, cf. Fig. 5.11 [87]. It is not yet clear whether the observation of mixed-mode oscillations instead of the expected chaotic dynamics has to be attributed to the different phase space topology or to the higher dimension of the phase space.

The above suggests to investigate if this bifurcation is of higher codimension, i.e., if the wave bifurcation and the homoclinic connection are found at the same point in parameter space by tuning two parameters, or if this behavior depends on only one parameter. The wave bifurcation was continued as a function of U and ρ, cf. Fig. 5.3, and simulations in the vicinity of the resulting respective U^w-values were performed in order to verify the hypothesis of a codimension-one bifurcation. An example of the results is given in Fig. 5.14. The wave bifurcation is shown to coincide with a homoclinic orbit in the (U-ρ) parameter plane up to an accuracy of $\approx 10^{-5}$. This behavior was found starting from (U,ρ)-values corresponding to the codimension-two bifurcation point at which h and wave bifurcation coincide up to $\rho = -0.9$. Simulations at lower ρ were not performed. Thus, the bifurcation at which the dynamics change from a stationary stable state to mixed-mode oscillations via a homoclinic orbit seems to be of codimension one.

An intuitive picture explaining the coincidence of the homoclinic orbit and the subcritical Hopf bifurcation using phase space arguments can be formulated as follows. If the fixed point is the only attractor left of U^w, the entire unstable manifold of the coexisting unstable limit cycle forms a heteroclinic connection to the stable fixed point. As the saddle limit cycle collapses onto the fixed point at $U = U^w$ this heteroclinic connection becomes a homoclinic one.

The sufficient condition for the occurrence of the bifurcation in the electrochemical system can thus be formulated as follows. If the homogeneous steady state is the only attractor for $U < U^w$ and the wave bifurcation at $U = U^w$ is subcritical, a homoclinic orbit to a saddle-focus is present at the bifurcation point. Complex spatio-temporal dynamics can be expected in the vicinity of the homoclinic orbit for $U > U^w$. Shil'nikov's

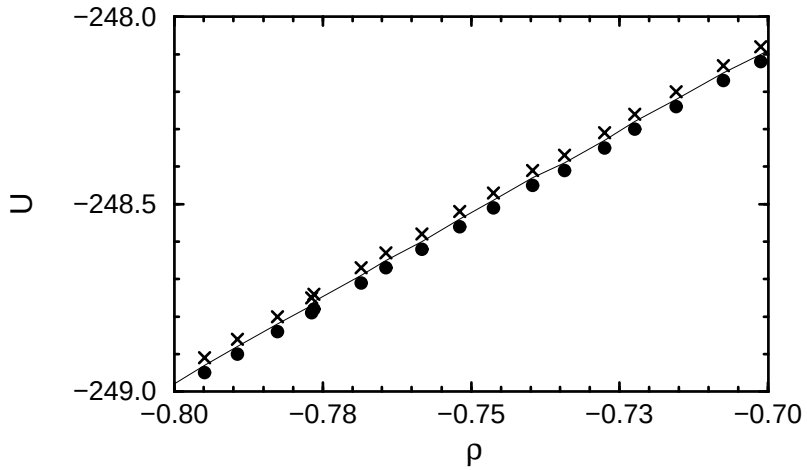

Figure 5.14: *U^w (solid line) together with results from simulations close to the wave bifurcation in the $(U$-ρ$)$ parameter plane. 'x' indicates inhomogeneous relaxation-like mixed-mode oscillations, dots the stationary passive state. Simulations were first conducted at $U = U^w + 0.02$ and then restarted with the solution from this run at $U = U^w - 0.02$. Other parameters see Table 5.1.*

condition for chaotic dynamics in the vicinity of an orbit homoclinic to a saddle-focus is by definition fulfilled in this situation. Due to a different phase space topology or due to the higher dimensionality of the system under consideration mixed-mode oscillations are observed for $U > U^w$.

In the next section a point in parameter space displaying a similar phase space structure in the semiconductor system introduced in section 4.1.4 is presented.

5.2.2 Semiconductor System

To the author's best knowledge, a codimension-one bifurcation similar to the one presented in the previous section has only been reported by Sch¨oll *et al.* in a dynamical system describing pattern formation in the HHED [52, 82, 153, 161] (cf. section 4.1.4). Some results emphasizing the similarities between electrochemical and semiconductor dynamics close to the bifurcation point are given in this section.

The equations used to model the S-NDR dynamics in the semiconductor system were given in section 4.1.4. We are going to use the renormalization of space to the interval $[0, \pi]$ as in the electrochemical system. The resulting equations were given in section 4.1.4 and are repeated here for clarity (Eqs. (4.14),(4.15) on page 67)

$$\dot{a} = \mu^s \left(\frac{u-a}{(u-a)^2+1} - 0.05a \right) + \frac{\partial^2 a}{\partial x^2}$$
$$\dot{u} = \gamma^s (j_0 - u + \langle a \rangle_\pi).$$

A bifurcation diagram of the solution branches as a function of the applied current density, j_0, at certain values of μ^s and γ^s was already displayed in Fig. 4.13 on page 68.

It will be seen below that a phase space structure similar to the electrochemical system can only be observed if the domain bifurcation destabilizing the homogeneous steady state at lower current values is subcritical. The domain bifurcation is found to be subcritical if at least two inhomogeneous cosine modes are taken into account. Four cosine modes are going to be used in this section resulting in a five dimensional dynamical system, $N = 5$.

As stated in section 4.1.4, the semiconductor model displays complex dynamics (periodically or chaotically spiking or breathing current domains) if the homogeneous steady state is unstable with respect to domain formation and the domains are oscillatory unstable for the same parameter values, cf. inequality (4.16) on page 69. In Fig. 5.15(a) the (maximum) potential drop over the semiconductor device, $\max(u)$, as a function of the applied current density is displayed for parameter values μ^s and γ^s at which the above condition is fulfilled. Complex spatio-temporal dynamics, i.e., spiking and breathing current domains, are observed in a wide j_0-interval (filled circles). In this interval the homogeneous steady state (thin lines) as well as stationary domains (thick lines) are unstable. As is apparent in Fig. 5.15(c) displaying the maximum of the first spatial mode of a, $\max(a_1^q)$, as a function of the applied current density, the fixed point loses stability in a subcritical pitchfork bifurcation. The respective current density was denoted by j_0^d. The symmetry necessary for the occurrence of a pf is a phase shift of π in Fourier space that corresponds to a reflection of the spatial pattern at $\pi/2$. Since such a reflection does not affect global properties, the two branches visible in Fig. 5.15(c) are projected on the same u-values in Figs. 5.15(a) and 5.15(b). The same is true for the branches corresponding to complex spatio-temporal solutions (circles) originating in a subcritical Hopf bifurcation of the domains. Stable and unstable breathing domains originate in a saddle node bifurcation of periodic orbits. The stable breathing domain branch undergoes a period doubling shortly after the saddle-node bifurcation but is stabilized again by the inverse period doubling bifurcation. For decreasing applied current density the maximum voltage drop during one oscillatory cycle of the breathing or spiking domain approaches the homogeneous fixed point. In Fig. 5.15(b) a zoom to the vicinity of the subcritical pitchfork bifurcation is displayed. Note the strong magnification used in Fig. 5.15(b). The trajectory of the spiking domain comes very close to the fixed point which is again of saddle-focus type (cf. section 4.1.4). The unstable eigen-direction leads to domain formation and the stable focus is given by the homogeneous modes.

A plot of the oscillation period versus the applied current density together with the point of the pitchfork bifurcation suggests the existence of a homoclinic orbit at the point of the pitchfork bifurcation, cf. Fig. 5.16(a). Simulations close and positive of j_0^d show that the complex dynamics are periodic also very close to the pf where AUTO failed to provide accurate Floquet multipliers.

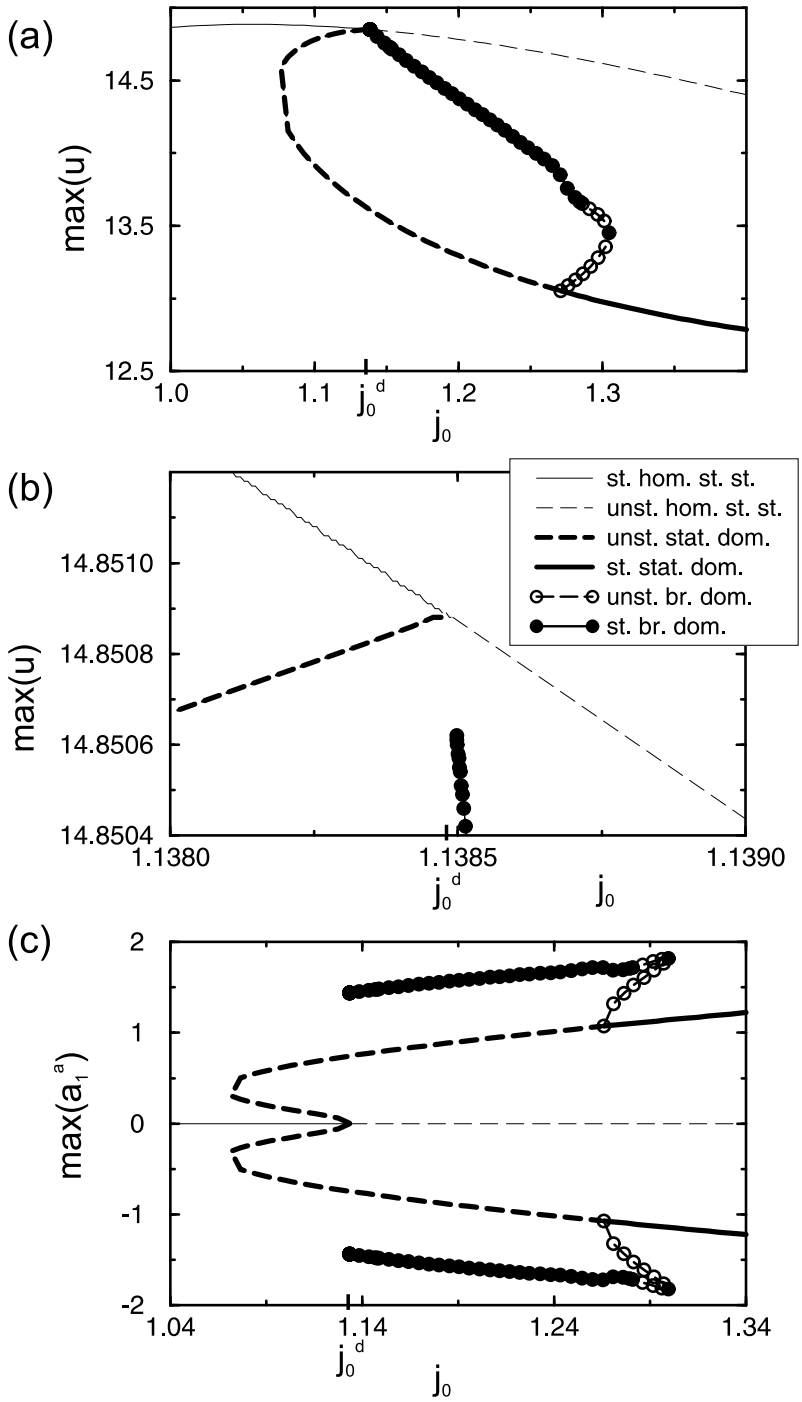

Figure 5.15: *Bifurcation diagrams of the semiconductor system for parameter values at which the sufficient condition* (4.16) *(page 69) is fulfilled. (a) (Maximum) potential drop across the semiconductor, max(u), versus the imposed current density, j_0, at the lower turning point of the current-voltage characteristic. (b) Zoom in the vicinity of the subcritical pitchfork bifurcation. (c) (Maximum) amplitude of a_1^q as a function of j_0 illustrating the subcritical pf together with the complex solutions. The description of the various solution branches and bifurcations is given in the text. Note that solutions were calculated at more j_0-values but are omitted here for clarity. Parameters: $N = 5$, $\gamma^s = (40/\pi)^2 0.06 \simeq 9.73$, $\mu^s = (40/\pi)^2 \simeq 162$.*

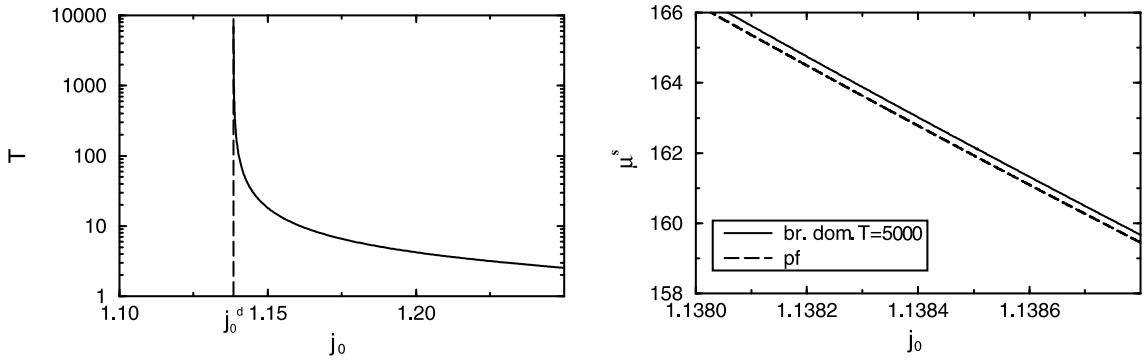

Figure 5.16: *(a) Period of complex spatio-temporal dynamics as a function of the applied current density (solid line). The dashed line indicates the pf. (b) Continuation of pf (solid line) and periodic orbit with T=5000 (dashed line) in $(\mu^s\text{-}j_0)$ parameter space. Parameter values as in Fig. 5.15.*

To reveal the codimension of the bifurcation at which apparently a subcritical pf and a homoclinic orbit coincide, the pf as well as an orbit with very long period (T=5000) is continued in j_0 and μ^s from $j_0 = 1.37$ to $j_0 = 1.41$. An exemplary j_0-range is displayed in Fig. 5.16(b). It is shown that the points of the pf and the periodic orbit with long period coincide in parameter space up to an accuracy of approximately 10^{-3} and evolve parallel to each other. This behavior is observed in the entire investigated j_0-interval.

In summary, it is shown that the semiconductor S-NDR dynamics seem to exhibit a codimension-one bifurcation similar to the bifurcation discussed in the previous section. Coming from lower applied current densities the homogeneous steady state loses stability in a subcritical bifurcation, in this case a subcritical pf. The homogeneous steady state is of the saddle-focus type with inversed time direction compared to the electrochemical dynamics, i.e., the real part, η, of the imaginary eigenvalues, $\lambda_{1/2} = \eta + i\xi$, is negative and the real eigenvalue λ_3 is positive for $j_0 > j_0^d$, cf. Fig. 5.13(b). A homoclinic orbit connecting the stable and unstable eigen-directions is present at the pf. Again, the topology of the phase space differs from the Shil'nikov homoclinic orbit since $\lambda_3(j_0 = j_0^d) = 0$. The intuitive picture of the phase flow given for the electrochemical system can be equally formulated in the semiconductor situation. Left of j_0^d the homogeneous fixed point is the only attractor and the unstable manifold of the unstable domain forms a heteroclinic connection with the steady state. As soon as the unstable domain collapses onto the fixed point a homoclinic orbit is formed.

Shil'nikov's condition for chaotic dynamics for this time inverted case, $\lambda_3 > |\eta|$, is by definition not fulfilled since $\lambda_3 = 0$ at the bifurcation point. Contrary to the electrochemical case, the observed dynamics reported here comply with this observation [82].[4]

[4]Note that Schöll *et al.* observed chaotic dynamics close to j_0^d for different parameter values. The authors attribute the observation of chaos to the flow close to the second fixed point present in the system.

5.2.3 Discussion and Conclusions

Two dynamical systems have been presented in which a subcritical bifurcation of a fixed point coincides with an orbit homoclinic to the same fixed point. The flow in the vicinity of the fixed points is of the saddle-focus type. It was investigated whether the coincidence of the two bifurcations is a codimension-two phenomenon or if the simultaneous occurrence of two instabilities can be observed at different parameter sets. All investigations undertaken point to a codimension-one bifurcation.

In the following the bifurcation sequence is sketched in general terms to underline the similarities found in the two systems and to point at a generalization of the sufficient condition for complex spatio-temporal dynamics for S-NDR systems [52, 161]. Let us denote the bifurcation parameter by ζ. Suppose that the fixed point is globally stable for $\zeta < 0$ and that the eigenvalue spectrum of the fixed point possesses a pair of complex eigenvalues $\lambda_{1/2} = \eta + i\xi$ and the other eigenvalues are real, cf. Fig. 5.13. λ_3 denotes the real eigenvalue that is closest to zero. At $\zeta = 0$ a subcritical codimension-one bifurcation, either an oscillatory instability, $\eta(\zeta = 0) = 0$, or a pitchfork bifurcation, $\lambda_3(\zeta = 0) = 0$, takes place. In both cases the unstable branch(es) emerging subcritically is not stabilized in the parameter region $\zeta < 0$ since global stability of the fixed point was assumed. (In the semiconductor system the second fixed point is oscillatory unstable at $j_0 \leq j_0^d$. Wave solutions are unstable with respect to the formation of pulse-like solutions at $U \leq U^w$ in the electrochemical N-NDR dynamics.) Thus a heteroclinic connection from the unstable manifold of the unstable solution to the fixed point has to present. It was demonstrated with two examples that this situation leads to the existence of a homoclinic orbit at $\zeta = 0$. Using phase space arguments, an intuitive picture of the possible reason behind the unusual coincidence of a local subcritical bifurcation and a homoclinic orbit was given. The homoclinic connection is of the saddle-focus type by assumption. The topology of the phase space is expected to differ structurally from the Shil'nikov situation since the real part of one eigenvalue associated with the fixed point is zero at the bifurcation. Shil'nikov's condition for the existence of a chaotic attractor in the vicinity of an orbit homoclinic to a saddle-focus in three dimensions is by definition fulfilled if the subcritical bifurcation is an oscillatory instability. The opposite holds for the pf.

It must be emphasized here that both systems considered in this section are of dimension greater than three ($N = 4$ in the electrochemical oscillator, $N = 5$ in the semiconductor model). The expected periodic dynamics are observed for $\zeta > 0$ in the $\lambda_3 = 0$ case. Still, the dynamics are complex since no stable fixed points or stable homogeneous oscillations are present for $\zeta > 0$. A different situation is found in the electrochemical case. Contrary to the above, mixed-mode oscillations instead of chaotic dynamics are observed. Either the higher dimension of the dynamics or the additional bifurcation taking place at

The eigenvalues at the stationary domain fulfi ll Shil'nikov's condition [52].

the point of the homoclinic connection account for this unexpected behavior.

In both systems the above formulated condition leads to a codimension-one bifurcation that mediates a direct transition from a stable fixed-point to mixed-mode oscillations without hysteresis.

In conclusion, the observed complex spatio-temporal dynamics in the electrochemical system together with the bifurcation analysis point at a possible generalization of the sufficient condition for complex dynamics given for the S-NDR system, cf. Eq. (4.17) [52, 161], along the line given above. Additionally, the quite spectacular coincidence of a homoclinic orbit and a subcritical bifurcation of a fixed point reported in the semiconductor system [82, 153] exists also in the prototype electrochemical N-NDR oscillator. It was shown that this coincidence it not due to a double degenerate point.

An extended analysis of the coincidence of the two bifurcations, especially the introduction of a normal form and the investigation of the phase space along the lines developed by Shil'nikov, will be the subject of future studies.

Chapter 6

HN-NDR Systems – Pattern Formation during Hydrogen Oxidation

In this chapter, a realistic model of hydrogen oxidation on platinum in the presence of poisons is derived and spatio-temporal simulations of pattern formation under desynchronizing global coupling are presented. The general mechanism and earlier models were given in section 2.5.3. However, these models fail to reproduce prominent features of the oscillatory behavior. The main features not captured are the form of the oscillations, especially the drop of the double layer potential to values near the equilibrium potential of the hydrogen oxidation/evolution reaction. A second important feature not described by the above model is the apparently hard onset of the oscillations at low voltages observed in the experiment during an anodic scan of the applied voltage (cf. Fig. 6.2(a) and [132, 133]). And finally, the phase relations given by the model in [135] were only matching the experimental ones close to the Hopf bifurcation and at high conductivity.

This calls for a more detailed description since the hydrogen oxidation on Pt in the presence of electrosorbing ions constitutes a prototype model for the study of dynamic instabilities in electrochemical systems for three reasons.

(a) The observed homogeneous as well as spatio-temporal dynamics is very rich. Period doubling cascades, chaotic dynamics and mixed-mode oscillations were reported [128–131]. In recent measurements of pattern formation during the hydrogen oxidation reaction (HOR) in the presence of Cu^{2+} and Cl^{-} (which are taken to be the metal respectively halide ions if not stated otherwise) Krischer *et al.* observed novel spatio-temporal phenomena which seem to be connected to the relaxation-like form of the underlying oscillations [132–134].

(b) The basic mechanism that leads to oscillations during the HOR is well understood (cf. section 2.5.2) and is made up of reaction steps that are independently studied. Recent investigations by Marković and Ross provided new insight into the interactions between the involved species [172–174] that were not accounted for in earlier models. We show

that these interactions are essential for realistic modeling of the HOR.

(c) The oscillatory dynamics of four quantities including three of the essential variables of the system are accessible experimentally and presented in [175] and in the next section. This exceptional situation allows the observation of the phase relations of these variables and thus a compelling test of a proposed model.

A quantitative model of the oscillatory HOR is thus both needed and feasible and the model can then be solidly verified with homogeneous as well as spatio-temporal experimental data.

In the next section we will show that, when including up to seven variables in the homogeneous dynamics, almost quantitative agreement with experiments can be reached. The model will then be reduced to the minimal model still capturing all features of the dynamics observed in experiment. The results obtained are then compared in detail with experiments using Cl^- or Br^- as halide ion. The reduced model forms the basis for modeling pattern formation during the HOR in section 6.2. Despite the rich behavior observed in experiments that points to this reaction as *the* prototype electrochemical oscillator in future studies of electrochemical nonlinear dynamics and its control, spatio-temporal pattern formation during the HOR has not been investigated before this thesis was resumed. We demonstrate the outstanding accuracy with which the reduced realistic model reproduces too a large extend novel experimental patterns. It is important to note that the model predictions are obtained using a large number of physical constants which are almost exclusively taken out of the literature and are thus obtained independently and not fitted to the experiment. Furthermore, it can be expected that the effects induced by a NGC acting on a relaxation oscillator presented here can be transferred to other relaxational systems.

6.1 Realistic Model and Homogeneous Dynamics

6.1.1 Model

The starting point for the subsequent modeling are the chemical processes which are taken into account:

$$Cu^{2+} + 2e^- + * \underset{k^d_{Cu}}{\overset{k^a_{Cu}}{\rightleftharpoons}} Cu_{ad} \tag{6.1}$$

$$Cl^- + * \underset{k^d_{Cl}}{\overset{k^a_{Cl}}{\rightleftharpoons}} Cl^{-+\delta}_{ad} + \delta e^- \tag{6.2}$$

$$H_2 + ** \underset{k^d_{H}}{\overset{k^a_{H}}{\rightleftharpoons}} 2H_{ad} \tag{6.3}$$

$$H_{ad} \underset{k^{r-}_{H}}{\overset{k^{r+}_{H}}{\rightleftharpoons}} H^+ + e^- \tag{6.4}$$

('*' denotes a free surface site). For reactions (6.1)-(6.3) the species on the left hand side are considered to be in the reaction plane and the transport from the bulk to the reaction plane has also to be taken into account (cf. section 2.5.1). We consider here the Tafel-Volmer mechanism, i.e., dissociative adsorption, for the HOR [91]. The variables included in the model to describe the mechanism (6.1)-(6.4) are the double layer potential, ϕ_{DL}, the coverage of the electrode by hydrogen, chloride and copper, θ_H,[1] θ_{Cl}, θ_{Cu}, and the concentrations in the reaction plane, c_H, c_{Cl}, and c_{Cu}.

The currents due to (partial) discharge of Cu^{2+} and Cl^- can be neglected. They contribute far less than 5% to the total current density. Thus, in the model, we take $i_r = i_{H_2}$. i_{H_2} is modeled using Butler-Volmer kinetics neglecting the hydrogen evolution reaction (HER). The change in coverages is given by the difference between adsorption and desorption velocities supplemented with 'consumptive' reaction in the case of hydrogen. H_{ad}, Cu^{2+} and Cl^- are considered to compete for the same surface sites with the exception that Cu^{2+} adsorption is not hindered by H_{ad}. Considering recent experiments by Stamenković *et al.* [172] we assume an attractive interaction between Cu^{2+} and Cl^- in the sense that anion adsorption is enhanced in the presence of copper on the electrode surface. This was not done in previous models and it turned out that it is essential for a correct description of the dynamics. We do not take any other interactions between the

[1] We only consider the reactive adsorbate H_{ad} (sometimes called H_{opd}) and neglect any influences on the dynamics by underpotentially adsorbed hydrogen, H_{upd}.

different species into account. The temporal changes of the concentrations of the individual species are given by the sum of adsorption, desorption and diffusion from the bulk solution to the 'reaction' plane.

The set of dynamic equations is thus

$$C_{DL}\dot{\phi}_{\mathrm{DL}} = -i_r + (RA)^{-1}(U - \phi_{\mathrm{DL}}) \tag{6.5}$$

$$\frac{\delta_H}{2}\dot{c}_H = \frac{D_H}{\delta_H}\left(c_H^b - c_H\right) - \left(v_H^a - v_H^d\right) \tag{6.6}$$

$$\frac{\delta_{Cu}}{2}\dot{c}_{Cu} = \frac{D_{Cu}}{\delta_{Cu}}\left(c_{Cu}^b - c_{Cu}\right) - \left(v_{Cu}^a - v_{Cu}^d\right) \tag{6.7}$$

$$\frac{\delta_{Cl}}{2}\dot{c}_{Cl} = \frac{D_{Cl}}{\delta_{Cl}}\left(c_{Cl}^b - c_{Cl}\right) - \left(v_{Cl}^a - v_{Cl}^d\right) \tag{6.8}$$

$$N\dot{\theta}_H = v_H^a - v_H^d - i_r/F \tag{6.9}$$

$$N\dot{\theta}_{Cu} = v_{Cu}^a - v_{Cu}^d \tag{6.10}$$

$$N\dot{\theta}_{Cl} = v_{Cl}^a - v_{Cl}^d \tag{6.11}$$

with

$$\begin{aligned}
v_H^a - v_H^d &= c_H k_H^a \left(1 - \theta_H - \theta_{Cu} - \theta_{Cl}\right)^2 - k_H^d \theta_H^2 \\
v_{Cu}^a - v_{Cu}^d &= k_{Cu}^a c_{Cu}\left(1 - \theta_{Cu} - \theta_{Cl}\right) - k_{Cu}^d \theta_{Cu} \\
v_{Cl}^a - v_{Cl}^d &= k_{Cl}^a c_{Cl}\left(1 + \chi\theta_{Cu}\right)\left(1 - \theta_H - \theta_{Cu} - \theta_{Cl}\right) - k_{Cl}^d \theta_{Cl} \\
i_r &= F k_H^{r+} \theta_H \left(e^{a_H \phi_{\mathrm{DL}}} - 1\right)
\end{aligned}$$

and

$$\begin{aligned}
k_{Cu/Cl}^a &= k_{Cu/Cl}^{a,0} e^{-a_{Cu/Cl}\left(\phi_{\mathrm{DL}} - \phi_{\mathrm{DL}}^{Cu/Cl,0}\right)} \\
k_{Cl/Cu}^d &= k_{Cu/Cl}^{d,0} e^{a_{Cu/Cl}\left(\phi_{\mathrm{DL}} - \phi_{\mathrm{DL}}^{Cu/Cl,0}\right)}.
\end{aligned}$$

c_{Cu}^b and c_{Cl}^b denote the bulk concentrations of copper and chloride, respectively. c_H^b is the bulk concentration of hydrogen for a saturated solution. v_x^a and v_x^d are the adsorption and desorption velocities of species x, respectively. N denotes the number of free surface sites per unit area on Pt. δ_H, δ_{Cu} and δ_{Cl} are the thicknesses of the diffusion layers for hydrogen, copper and chloride, respectively. We use physical units in this section for later quantitative comparison with experiment. The values of the numerous constants used in Eqs. (6.5)-(6.11) are given in Table 6.1. The respective sources are also indicated. The parameters that were used for the calculations if not stated otherwise are shown in Table 6.2. The model parameters refer to a ring WE since the ultimate goal of this chapter is the

Table 6.1: *Physical constants*

c_H^b	=	$7.14 \cdot 10^{-6}$ mol cm^{-3} [a]
ν	=	$1.07 \cdot 10^{-2}$ cm^2 s^{-1} [174]
k_H^{r+}	=	$5 \cdot 10^{-6}$ mol s^{-1} cm^{-2} [176]
k_H^a	=	$2.17 \cdot 10^{-2}$ cm s^{-1} [177]
k_H^d	=	$1 \cdot 10^{-5}$ mol s^{-1} cm^{-2} [176]
a_H	=	19.5 V^{-1} [136]
N	=	$2.2 \cdot 10^{-9}$ mol cm^{-2} [176]
$k_{Cl}^{a,0}/N$	=	$1 \cdot 10^4$ cm^3 (mol s)$^{-1}$ [e]
D_{Cu}	=	$1.2 \cdot 10^{-5}$ cm^{2}s^{-1} [178]
a_{Cl}	=	-3 V^{-1} [136]
$\phi_{\mathrm{DL}}^{Cl,0}$	=	-0.5 V [b]
$k_{Cl}^{d,0}/k_{Cl}^{a,0}$	=	$1 \cdot 10^{-3}$ mol cm^{-3} [e]
$k_{Cu}^{a,0}/N$	=	$1 \cdot 10^2$ cm^3 (mol s)$^{-1}$ [c]
F	=	$9.64 \cdot 10^4$ C mol^{-1}
a_{Cu}	=	38 V^{-1} [136]
$\phi_{\mathrm{DL}}^{Cu,0}$	=	0.5 V [b]
$k_{Cu}^{d,0}/k_{Cu}^{a,0}$	=	$1 \cdot 10^{-3}$ mol cm^{-3} [e]
C	=	$2.0 \cdot 10^{-5}$ A s V^{-1} cm^{-2} [176]
D_H	=	$3.7 \cdot 10^{-5}$ cm^2 s^{-1}[a]
χ	=	50
D_{Cl}	=	D_{Cu} [f]
δ_{Cl}	=	δ_{Cu} [f]
δ_H	=	$\frac{1.61 D_H^{1/3} \nu^{1/6} w^{-1/2} (r_3^3 - r_2^3)^{1/3}}{r} = 3.76 \cdot 10^{-4}$ cm [d]
δ_{Cu}	=	$\left(\frac{D_{Cu}}{D_H}\right)^{1/3} \delta_H = 2.54 \cdot 10^{-4}$ cm

[a] Taken from [174] for $T = 25°C$ and a solution of 0.5 M H_2SO_4. Conway *et. al* give slightly different values [177].

[b] In [136] $\phi_{\mathrm{DL}}^{Cl,0}$ and $\phi_{\mathrm{DL}}^{Cu,0}$ were given as -0.6 and 0.6, respectively, but they depend on multiple parameters like crystal orientation and electrolyte composition. I.e., $\phi_{\mathrm{DL}}^{Cl,0}$ was also reported to be more positive, e.g., in [179], and in [180, 181] $\phi_{\mathrm{DL}}^{Cu,0}$ was reported to be more negative.

[c] Factor 10 lower than in [136]. This value agrees with the observed transient times.

[d] The thickness of the diffusion layers is calculated assuming a ring geometry with the outer and inner diameters r_3 and r_2 respectively and a rotation rate of ω [91].

[e] No reliable data could be found in the literature, we thus take the values given in [136].

[f] This is a good approximation and the dynamcis do not depend on these values (see section Model reduction).

Table 6.2: *Typical parameter values used in the experiments*

c_{Cl}	=	$1\cdot10^{-7}$ mol cm^{-3} = 0.1 mM	R_t	=	450 Ω
c^b_{Cu}	=	$1\cdot10^{-9}$ mol cm^{-3} = $1\cdot10^{-3}$ mM	A	=	0.911 cm^2
ω	=	$2\pi\cdot20$ s^{-1}	r_3	=	1.5 cm
r_2	=	1.45 cm	c_1	=	$1.226\cdot10^{-2}$ A cm^{-2}
c_2	=	118.7 V^{-1}			

understanding of the spatio-temporal dynamics observed on a Pt-ring. Experiments presented in this section were conducted using a small disk electrode to assure homogeneous dynamics.

The voltages are measured relative to the equilibrium potential of the HOR/HER. a_x quantifies the potential dependence of the adsorption/desorption processes which (since $\alpha_x = 0.5$ for simplicity) are determined by $a_x = \alpha_x n_x F(RT)^{-1} = (1-\alpha_x) n_x F(RT)^{-1}$ and n_x is the number of transfered electrons during the adsorption/desorption process. The enhanced Cl^- adsorption in the presence of Cu^{2+} is modeled by multiplying the adsorption term with $(1+\chi\theta_{Cu})$ where χ is a dimensionless phenomenological constant measuring the strength of the interaction (cf. e.g. [182]). χ is the only parameter used to match model and experiment.

The time integrations presented in the next section were performed using a relative tolerance of 10^{-15} and a time step of 10^{-4} s, which proved necessary due to the stiffness of the equations.

6.1.2 Results

Stationary Behavior

In Fig. 6.1(b) the stationary states of Eqs. (6.5)-(6.11) are shown in the intuitive (i,ϕ_{DL})-plane for three situations: a) In hydrogen saturated sulfuric acid (c_{Cu}=c_{Cl}=0, solid line). b) In hydrogen saturated sulfuric acid solution containing Cl^- (c_{Cu}=0, dashed line) and c) in the presence of all three species (dotted line). The stationary states are then compared to the experiment, Fig. 6.1(a). For steady state conditions the capacitive current, I_C, vanishes and the HOR-current density exactly equals the total current density set by the control condition without any contributions from adsorption or desorption currents. Thus, the concentrations of copper and chloride in the reaction plane equal the bulk ones. In the absence of poisons the hydrogen current density reaches a diffusion limited plateau already for very small overpotentials (ca. 50 mV) reflecting that the HOR is one of the

[3] ϕ_{DL} or more precisely the potential micro-probe signal is measured with respect to the reversible hydrogen electrode (RHE).

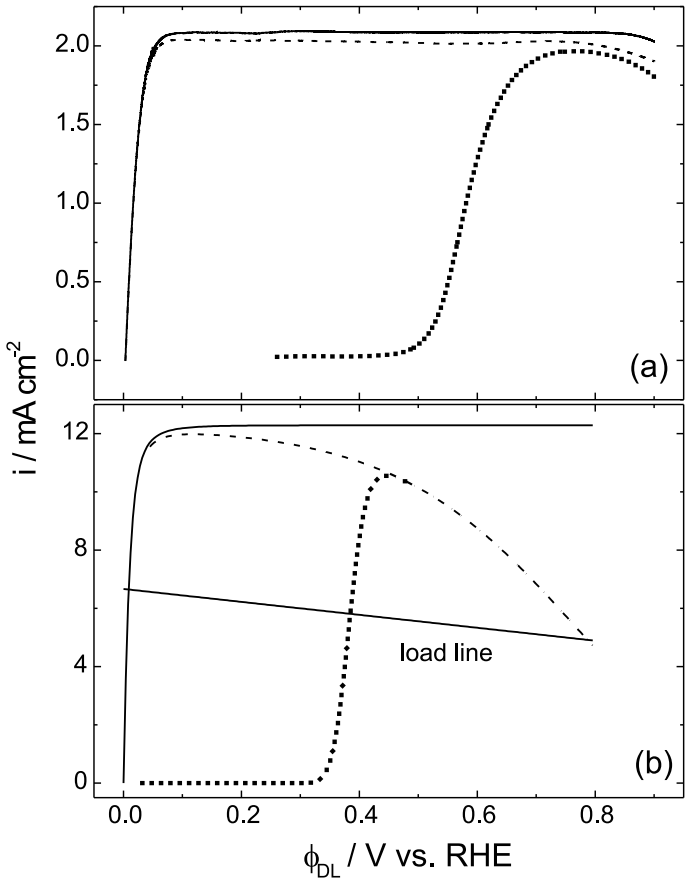

Figure 6.1: *(a) Stationary states in the experiment (a) and the model (b) in the presence of both poisons (dotted line), without Cu^{2+} (dashed line) and without Cl^- and Cu^{2+} (solid line) in the (i, ϕ_{DL})-plane.*[3] *The data with Cu^{2+} were obtained using 1 mM H_2SO_4, 0.025 mM $CuSO_4$ and 1 mM Cl^- electrolyte solution thus being identical to those in Fig. 6.2. The two other curves where recorded with 0.1 M H_2SO_4. In (b) the load line is also shown for $U = 3\,V$. The same concentrations were used for the computations and the other constants are given in Tables 6.1 and 6.2 except that $\phi_{\mathrm{DL}}^{Cl,0} = -0.3V$.*

fastest known electrochemical reactions so that mass transport becomes the rate determining step. The measured and modeled maximum diffusion limited current densities, i_{diff}, agree within a factor of approximately six, which is due to different transport conditions in model (large ring electrode) and experiment (small disk electrode). Additionally, the experimental data obtained using a ring electrode with the dimensions given in Table 6.2 suggest that a smaller value of $k_H^a \approx 8 \cdot 10^{-3}$ cm s^{-1} would match model and experiment.

Adding chloride yields a large NDR-region following the steep current increase. The NDR gives rise to an autocatalytic loop composed of ϕ_{DL} and Cl^- (cf. Fig. 2.17 on page 38). Adding copper to the electrolyte solution inhibits H_2 oxidation almost completely

at potentials negative to approximately 400 mV due to underpotential deposition of one monolayer of Cu. Starting from $\phi_{DL} \approx 400\,\mathrm{mV}$ copper is stripped from the electrode and H_2 oxidation sets in until almost all copper left the surface and the current density corresponding to a copper-free solution is reached. Thus, the NDR due to Cl^- adsorption is hidden in a certain potential interval.

Calculating the dependence of the hydrogen current on the total coverage of the working electrode, the assumption made in Ref. [135] that, due to the Tafel mechanism, the hydrogen current density is only significantly reduced for total coverages above ≈ 0.8 has to be dropped in favor of a standard langmuiric behavior.

Comparing the curves with Cu^{2+} and Cl^- in experiment and model it becomes apparent that the adsorption isotherm of Cu^{2+} underpotential deposition seems to be more positive than reported in [136]. Additionally the current decrease at higher potentials due to chloride adsorption is more pronounced in the model. A behavior closer to the model was observed in experiments using a ring working electrode. The ring electrode was not used for the comparison with the homogeneous model since spatial patterns can be expected which would lead to discrepancies in the time series of the oscillations (s.b.).

Oscillatory Behavior

For sufficiently high series resistance oscillations are observed in a wide range of applied voltages, U, on the branch of positive differential resistance in both, model and experiment (cf. section 2.2.1). In Fig. 6.2(b) the stationary and periodic solutions of the reduced model obtained by a continuation in the parameter U are shown in the (i-ϕ_{DL})-plane. For low applied voltages the stationary low current state loses stability in a supercritical Hopf bifurcation. The amplitude of the oscillations increases very fast and soon extends from $\phi_{DL} \approx 0\,\mathrm{V}$ to $\phi_{DL} \approx 500\,\mathrm{mV}$. The same characteristics are obtained in experiment as can be seen in Fig. 6.2(a) where i is shown as a function of ϕ_{DL} for an anodic potential scan. It should be noted that the concentrations of Cl^- and Cu^{2+} used in the calculations were different from the ones used in the experiments. Especially the copper concentration had to be reduced by a factor of approximately 20 to reproduce the diffusion limited adsorption as further discussed below. This could also be due to a slower adsorption rate constant $k_{Cu}^{a,0}$ or a lower diffusion constant for our experimental situation which is reported in [92]. Another reason are the different transport conditions for a ring and a disk electrode (transport to a ring is more efficient than to a disk).

For the parameter values used in this thesis oscillations do not exist for vanishing metal-halide interaction strength, χ, illustrating the importance of the Cu^{2+}-Cl^- interaction. Note that in earlier publications oscillations were also observed without taking the Cl^--Cu^{2+} interaction into account using different and for the studied experimental situation unrealistic model parameters. The fast increase of the oscillation amplitude can

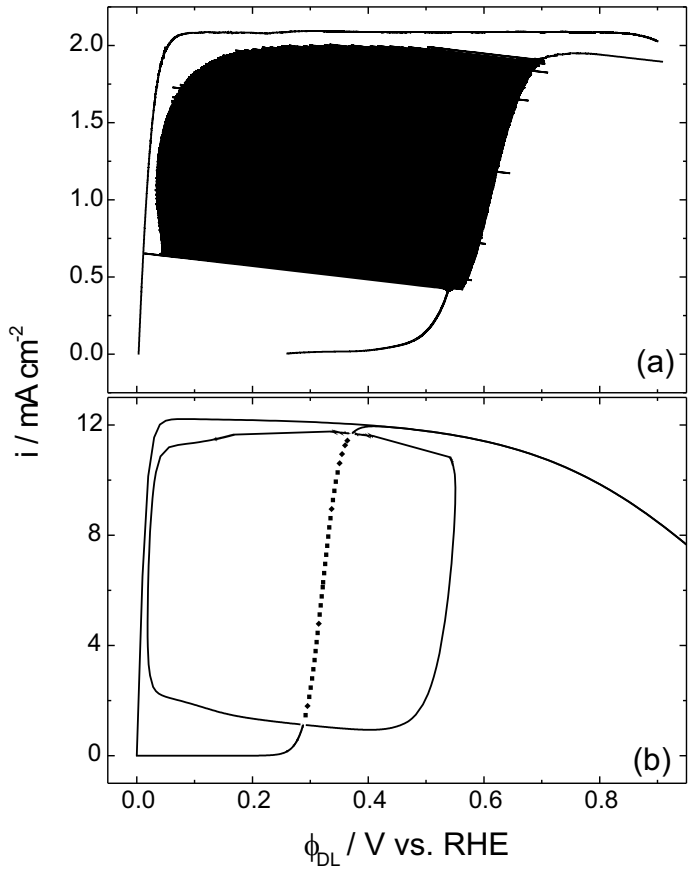

Figure 6.2: *(a) i as a function of* ϕ_{DL} *for an anodic potential scan in experiment.*[3] *(b) Oscillation amplitude and stationary states in the same plane calculated with the reduced four variable model using the parameters from Tables 6.1 and 6.2. Also shown are the curves without copper in the solution in both graphs to illustrate the importance of the potential dependence of the hydrogen current since the oscillations almost reach the* Cu^{2+}*-free curve, cf. Fig. 6.1.*

only be captured for $\chi \gtrsim 10$ and was thus always absent in previous models. The drop of the double layer potential to $\phi_{\mathrm{DL}} \approx 0$ can only be modeled by taking c_{Cu} into account (s.b.). At current densities just below the maximum current density the oscillations vanish again in a Hopf bifurcation. The amplitude of the oscillations close to this second Hopf bifurcation again decreases fast, though not as fast as for lower voltages.

In Fig. 6.3 the time dependence of all seven variables is shown for a few oscillatory cycles. The almost exact similarity of the oscillatory form of ϕ_{DL} and $-i_r$ seen in Fig. 6.3(a) stems from the fast double layer dynamics, i.e., capacitive currents remain small. The long active period of the current is caused by the slow diffusion limited adsorption of Cu^{2+} which can be seen in Figs. 6.3(b) and (c). While the copper concentration in the reaction plane is practically zero (dashed line in Fig. 6.3(b)), θ_{Cu} rises linearly until a

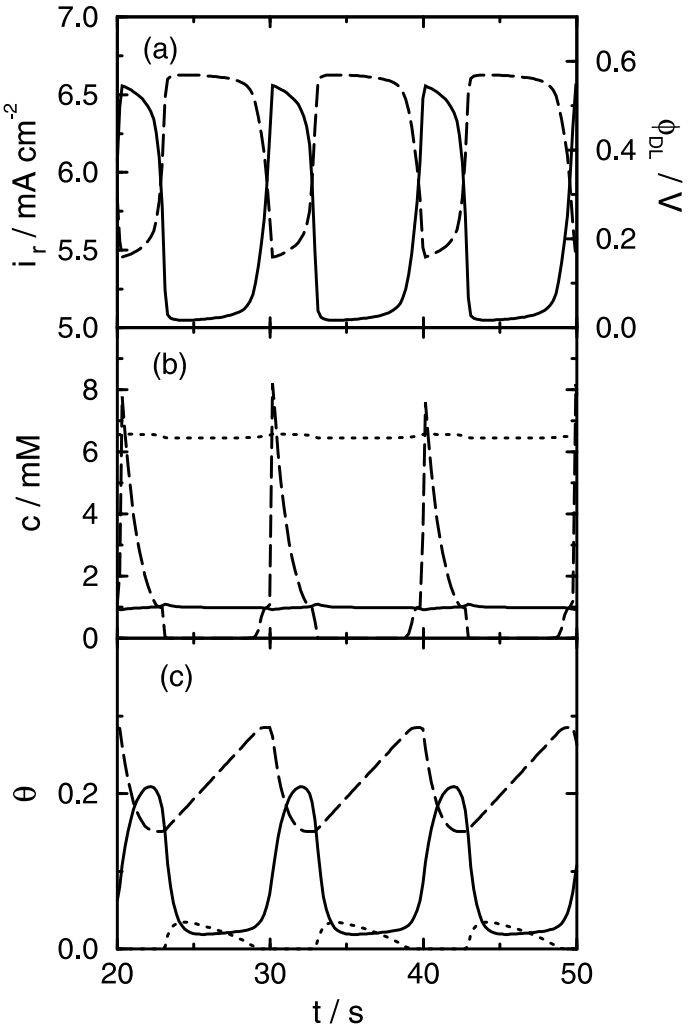

Figure 6.3: *Time evolution of i_r and the seven variables of model* (6.5)-(6.11) *for U=3V, other parameter values as in Tables 6.1 and 6.2. (a) ϕ_{DL} (solid line), i_r (dashed line). (b),(c) $1000c_{Cu}$, θ_{Cu} (dashed lines), $10c_{Cl}$, θ_{Cl} (solid lines) and c_H, θ_H (dotted lines).*

threshold is reached and ϕ_{DL} increases fast. In the next section these findings are used to simplify the model (6.5)-(6.11) considerably.

Model reduction

For the chloride concentrations used in experiments ($c_{Cl} \geq 0.1\,\mathrm{mM}$) the chloride adsorption never becomes diffusion limited. Looking at Fig. 6.3 this becomes apparent through the absence of linear increases in the chloride coverage, which would be indicative of diffusion limited adsorption. It follows that the chloride concentration in the reaction plane remains almost constant (Fig. 6.3(b), solid line). In the following c_{Cl} is thus taken as constant ($c_{Cl} \to c_{Cl}^b$).

Substantial simplifications are also suggested by the time series of the variables governing the HOR, c_H and θ_H. The hydrogen coverage remains small during the whole cycle whereas c_H adjusts to a diffusion controlled value and stays approximately constant with changes below 2%. Rather than taking the hydrogen current density in the hydrogen saturated solution as a constant, as was done in [135] (see footnote 11 on page 39), we conclude from these findings that the hydrogen current density can be modeled by

$$i_{H_2} = (1 - \theta_{Cl} - \theta_{Cu})\, f(\phi_{\mathrm{DL}}) \tag{6.12}$$

with a function $f(\phi_{\mathrm{DL}})$ fitted to simulated data using the above model or to experimental data (cf. Fig. 6.1). This approach keeps in mind that low potentials are reached during the oscillations and thus, the dependence of the hydrogen current density on the potential comes into play which was neglected in [135]. A suitable fit function is

$$f(\phi_{\mathrm{DL}}) = c_1 \left(1 - 2(1 + e^{c_2 \phi_{\mathrm{DL}}})^{-1}\right).$$

In order to keep the model based on the known reaction steps, $f(\phi_{\mathrm{DL}})$ was fitted to the theoretical hydrogen current density curve displayed in Fig. 6.1(b) (solid line) yielding $c_1 = 1.226 \cdot 10^{-2}$ A cm^{-2} and $c_2 = 118.7$ V^{-1}.

The reduced model thus consists of four equations, namely Eq. (6.5), which now reads

$$C_{DL}\dot{\phi}_{\mathrm{DL}} = -(1 - \theta_{Cl} - \theta_{Cu}) c_1 \left(1 - 2(1 + e^{c_2 \phi_{\mathrm{DL}}})^{-1}\right) + (RA)^{-1}(U - \phi_{\mathrm{DL}}), \tag{6.13}$$

and Eqs. (6.7), (6.10), and (6.11) where c_{Cl} has to be substituted by c_{Cl}^b in the evolution equation for the chloride coverage, Eq. (6.11).

In Figs. 6.4(a)-(c) the time evolutions of ϕ_{DL}, θ_{Cu} and θ_{Cl} are shown as obtained with the above reduced model. Comparing Figs. 6.4(a)-(c) to the data obtained with the full model Eqs. (6.5)-(6.11), Fig. 6.3, it becomes apparent that, apart from a slight change in period, no deviation between the two models can be observed. The above four variable model is used in the next section for a detailed comparison with experiments.

Comparison of Theory and Experiment

In Fig. 6.4 theoretical and experimental data are compared. Shown are the total current density, the copper coverage and the halide coverage (using rate constants for Cl^- in the model but Br^- in experiment) for a few oscillatory cycles. The oscillation periods differ by about a factor of two, which is an exceptionally good agreement considering the use of 21 constants out of the literature, i.e., obtained by independent measurements,[4] and

[4] Note however that the six constants governing the chloride and copper adsorption velocities are poorly known (cf. 6.1).

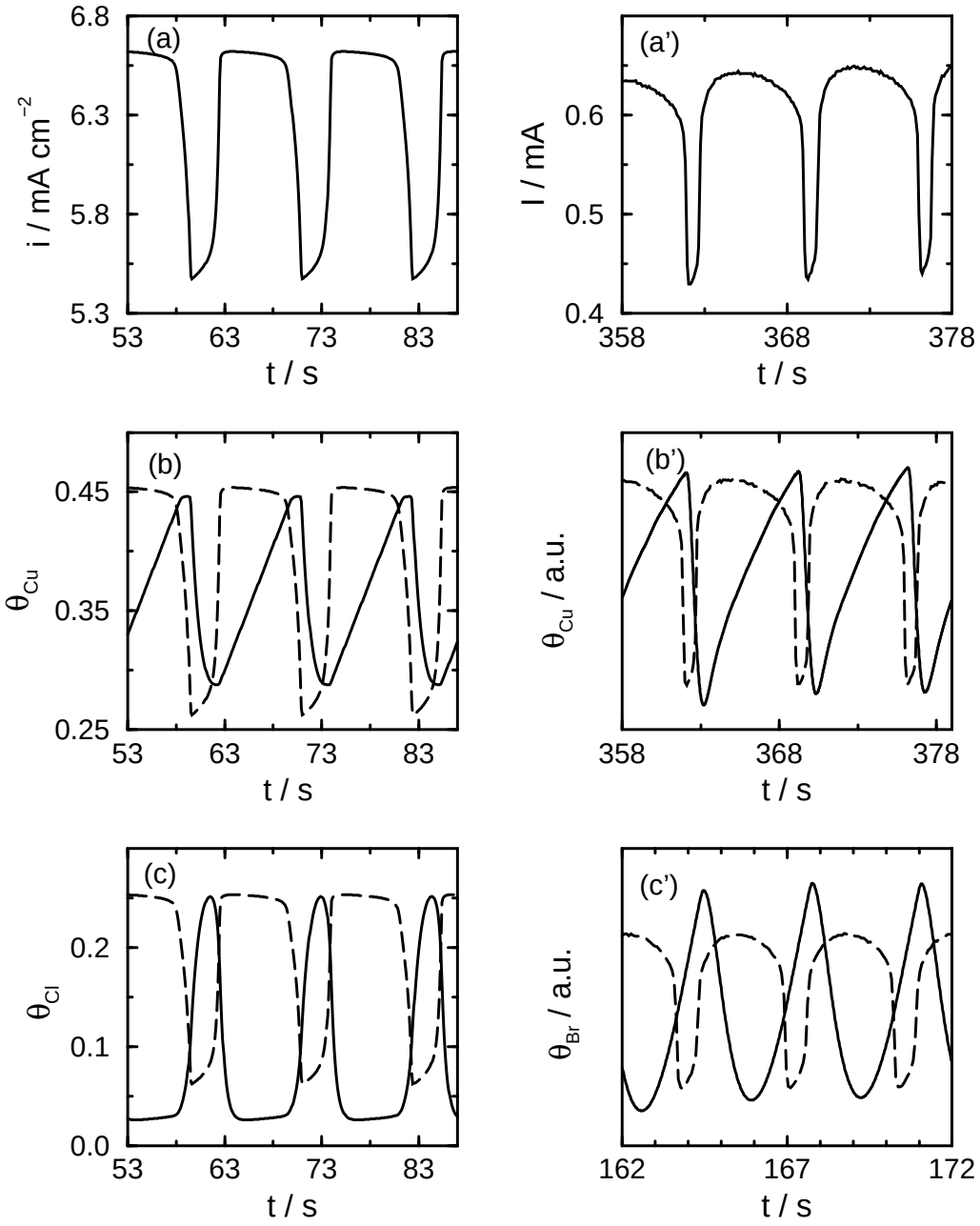

Figure 6.4: *(a)-(c) Oscillatory behavior of the four variable model to be compared with the full model, cf. Fig. 6.3, and with the experimental data (a')-(c'). The parameters used are given in Tables 6.1 and 6.2 and $U = 3$ V. (a')-(c') Experimental data obtained with the halide Br^- during an anodic potential scan. See [175] for experimental details. The dashed curves in ($b^{(\prime)}$) and ($c^{(\prime)}$) display the total current (density) such that the phase relations of the individual variables can be compared.*

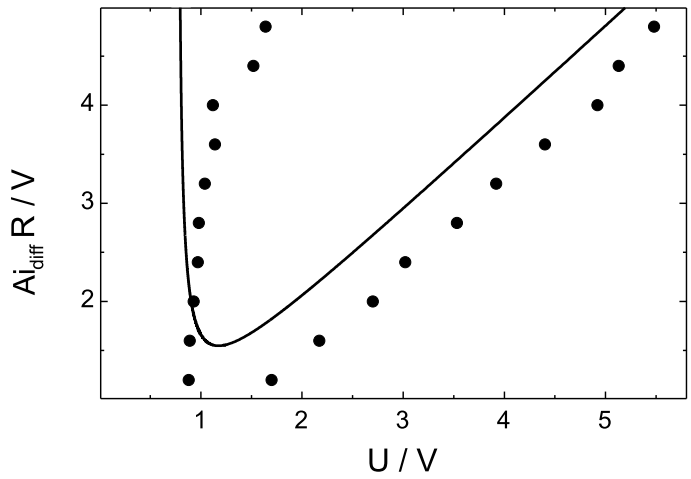

Figure 6.5: *Oscillatory region in the $(i_{\mathrm{diff}}R\text{-}U)$-plane. Solid line: Calculated Hopf bifurcations. Points: Experimentally observed locations of Hopf bifurcations for 10 different series resistances.*

only one free parameter, the interaction strength χ. The agreement regarding the oscillatory form of all three quantities is apparent.[5] The full descriptive power of the model, however, is displayed in the precise coincidence of the phase relations of calculated and experimental time series. In Figs. 6.4(b$^{(\prime)}$),(c$^{(\prime)}$) the current density is also plotted as a guide to the eye to compare the phase relations. Agreement exists concerning maxima and minima and slow and fast stages of the evolution of the coverages with respect to the evolution of ϕ_{DL}.

The precise agreement regarding the onset and amplitude of the oscillations was already demonstrated in Fig. 6.2 for a certain external resistance. In Fig. 6.5 the set of calculated Hopf bifurcation points in the *R-U* parameter plane in the model is compared with the points of onset of oscillations in experiment for 10 different values of the series resistance. The series resistance, *R*, in Fig. 6.5 is multiplied by the maximum diffusion limited reaction current, Ai_{diff}, observed in experiment and model, respectively (cf. Fig. 6.1), to correct for different transport conditions. The remaining quantitative mismatch is due to the mismatch of the onset of Cu^{2+} desorption already discussed above (cf. Fig. 6.1).

6.1.3 Conclusions

The oscillatory mechanism during hydrogen oxidation on Pt is well understood. It is based on the opposite potential dependence of two poisons that adsorb at the working electrode and inhibit the hydrogen oxidation. This simple picture makes it an ideal model

[5] Note that the copper concentration in the model is again lower as in experiment (s.a.).

system since the dynamics can be controlled in model and experiment in a straight forward manner.

In earlier models these findings were used in a rough approximation that captured the basic oscillation mechanism [127, 135, 136]. Recent experiments reported in [132–134] and experimental time series of i, ϕ_{DL}, θ_{Cu} and θ_{Br} presented here showed that these earlier models failed to predict several features of the experiments, including the amplitude, form, potential range, and phase relations of the oscillations. These features have to be captured by a model that is capable of describing the interesting spatio-temporal behavior observed in this system (cf. section 6.2 and [132–134]).

In this section we presented a detailed model of the oscillatory HOR in which all terms are well understood in their physical meaning. New experimental observations were included that describe an attractive interaction of chloride and copper on the electrode surface [172]. This proved to be essential even for the occurrence of oscillations for realistic model parameters.

We took into account the mass balance and transport equations for all three reacting species, H_2, Cl^- and Cu^{2+}, and the charge balance at the working electrode, thus arriving at a seven variable model. All constants that enter the seven evolution equations were taken from independent measurements out of the literature where possible. The unknown interaction strength between Cl^- and Cu^{2+} was adjusted to match model and experiments.

It was shown that the initial seven variable model could be reduced to a four variable one which is sufficient and minimal to give a quantitative description of the observed experimental oscillations. Also the bifurcation diagrams calculated with the four variable model were shown to agree quantitatively with the experimental ones.

The thus solidly verified model can now be used in the next section to study the rich spatio-temporal dynamics exhibited by this system in the presence of different spatial couplings [132–134].

6.2 Pattern Formation under Desynchronizing Global Coupling

In this section spatio-temporal simulations are presented that yield considerable insight in the origin of experimentally observed patterns during the HOR in the presence of poisons. The dynamics is modeled by the reduced four variable model presented in the previous section. The spatial coupling mediated by the electric field is by far more effective than diffusion of Cu^{2+} (which is practically immobile on a Pt WE) or Cl^- on the WE surface. The same holds for fluxes due to Cu^{2+} concentration gradients in the plane just in front of the WE. Additionally, ϕ_{DL} plays an activatory role in the oscillatory HOR. Genuine spatial bifurcations such as the Turing bifurcation are not present in electrochemical systems in

Table 6.3: *Values of the non-dimensional parameters used if not stated otherwise*

σ	=	0.8368950770951986	β	=	2.827433388230814
τ_{Cl}	=	83760.0902552427	τ_{Cu}	=	21.03215159159541
p_{Cl}	=	497.8642409711874	p_{Cu}	=	$p^0_{Cu} := 3.13913279204803 \cdot 10^{-11}$
ν	=	17401.49196751466	c_1	=	4.89745966763657
c_2	=	39.553360429673866	a_{Cu}	=	38/3

which ϕ_{DL} is the activator [107] and thus, spatial couplings on the inhibitory variables can be neglected. Accordingly, the migration coupling is the only coupling taken into account.[6] Since pattern formation during the HOR was investigated experimentally on a platinum ring, the simulations are carried out in 1d and periodic boundary conditions are used.

In the following a dimensionless form of the reduced model equations is used. The transformations of time, space, potential and concentrations as well as the definitions of the dimensionless parameters are given in Appendix A.1.3. The resulting dynamical system is

$$\begin{aligned}
\dot{\phi_{\mathrm{DL}}} &= -i_r + \frac{\sigma}{\beta}\left(U - \phi_{\mathrm{DL}}\right) \\
&\quad + \frac{\sigma\rho}{\beta}\left(\langle\phi_{\mathrm{DL}}\rangle - \phi_{\mathrm{DL}}\right) - \frac{\sigma(1+\rho)}{\beta}\left(\frac{\partial\phi}{\partial z} - \phi\right)\Big|_0 && (6.14)\\
\tau_{Cl}\dot{\theta}_{Cl} &= (1+\chi\theta_{Cu})\,(1-\theta_{Cu}-\theta_{Cl})\,e^{\phi_{\mathrm{DL}}} - p_{Cl}\theta_{Cl}e^{-\phi_{\mathrm{DL}}} && (6.15)\\
\tau_{Cu}\dot{\theta}_{Cu} &= \nu^a_{Cu} - \nu^d_{Cu} && (6.16)\\
\dot{c}_{Cu} &= 1 - c_{Cu} - \nu\tau^{-1}_{Cu}\left(\nu^a_{Cu} - \nu^d_{Cu}\right) && (6.17)
\end{aligned}$$

with

$$\begin{aligned}
\nu^a_{Cu} - \nu^d_{Cu} &= c_{Cu}\,(1-\theta_{Cu}-\theta_{Cl})\,e^{-a_{Cu}\phi_{\mathrm{DL}}} - p_{Cu}\theta_{Cu}e^{a_{Cu}\phi_{\mathrm{DL}}}\\
i_r &= c_1(1-\theta_{Cu}-\theta_{Cl})\left(1 - 2(1+e^{c_2\phi_{\mathrm{DL}}})^{-1}\right).
\end{aligned}$$

The values of the non-dimensional parameters as obtained from the constants and parameters from Tables 6.1 and 6.2 are given in Table 6.3. τ_{Cl}, τ_{Cu}, p_{Cl}, ν, c_1, c_2, and a_{Cu} are fixed at the given values throughout this section. The main bifurcation parameters are the applied voltage, U, and the global coupling strength, ρ. The homogeneous steady states and the maximum amplitude of oscillatory solutions of ϕ_{DL} are shown as a function of U in Fig. 6.6(a). Since the above parameter definitions fix the steady state

[6] It was tested if the diffusion of the other activatory variable, θ_{Cl}, would introduce new effects, which was not the case.

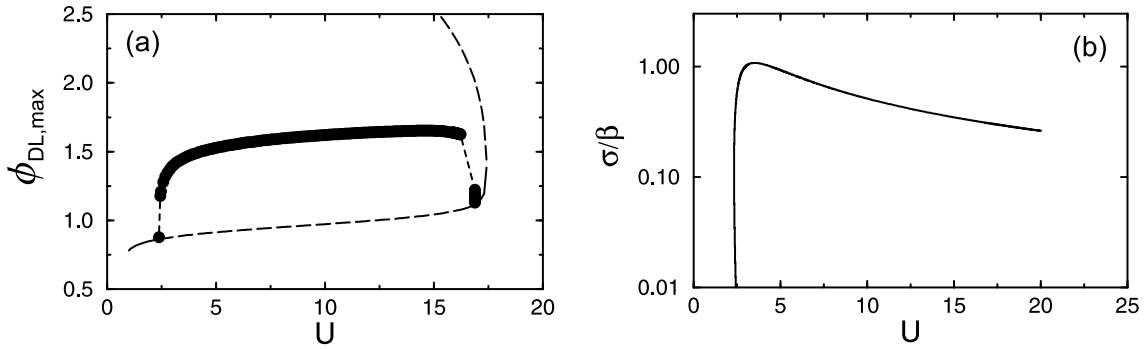

Figure 6.6: *(a) One parameter continuation of the homogeneous steady states and periodic solutions for the dimensionless model, Eqs. (6.14)-(6.17). Solid line and dashed lines: Stable and unstable stationary steady state, respectively; dots: Maximal amplitude of homogeneous periodic solutions (stable or unstable depending on* ρ*, s.b.). Parameters see Table 6.3. (b) Location of Hopf bifurcation points in the* $(\sigma/\beta$-$U)$*-parameter plane for the same parameter set.*

for changing global coupling at the cost of implicitly changing the physical conductivity when changing ρ, also σ is varied in the following sections to be able to compare systems with identical physical conductivity under different global couplings. The continuation of the two Hopf bifurcations present for the parameter values of Table 6.3 is presented in Fig. 6.6(b) in the $(\sigma/\beta$-$U)$-plane. The point of the Hopf bifurcation at lower U, i.e. lower i_r, is almost independent of σ/β in a wide σ/β-interval. At higher U the limit cycle is destroyed via a second Hopf bifurcation for high conductivities, cf. Fig. 6.6(a), and via a saddle-loop bifurcation involving the coexisting saddle present at higher ϕ_{DL} for lower σ/β (not shown in Fig. 6.6(b), cf. upper right corner in Fig. 6.6(a)).

Additionally, the aspect ratio β and p_{Cu} are varied. p_{Cu} essentially determines the bulk concentration of copper which proved to be an important parameter in experiments.

An overview of the observed spatio-temporal patterns at different values of the above parameters is presented in the next section. The properties of the most significant patterns are then explored in the following sections. The results are put into a general frame and compared with experiments in the discussion. Section 6.2.7 summarizes the findings presented.

Eqs. (6.14)-(6.17) represent a stiff dynamical system for physically meaningful parameters as given in Table 6.3. For this reason continuations of the spatial extended system proved to be not feasible. Furthermore due to long integration times, simulations could only be carried out for a limited number of points in parameter space. Integrations were performed until transients decayed. Typically about 50 oscillation periods of the homogeneous system sufficed to observe stable spatio-temporal behavior. Simulations were carried out with a relative and absolute tolerance of 10^{-14} and 31 or 63 Fourier modes.

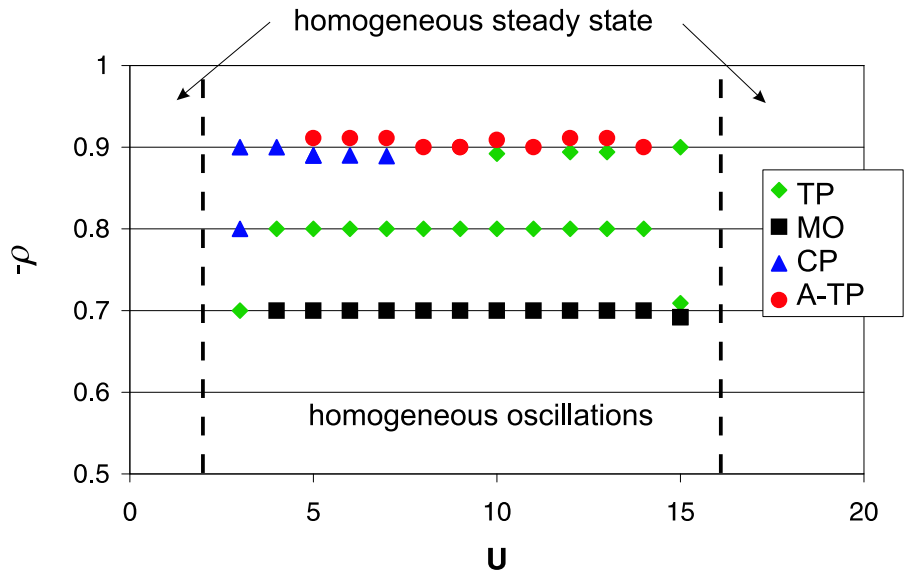

Figure 6.7: *Spatio-temporal patterns in the U-ρ-parameter plane for $p_{Cu} = p^0_{Cu} \cdot 10^{-4}$ (other parameters see Table 6.3). The homogeneous steady state is observed on the left and right borders of the figure (dashed lines) and homogeneous oscillations are found for $\rho \geq -0.6$. Bistability is indicated by stacking the respective symbols.*

Different initial conditions were employed (s.b.).

6.2.1 Overview of Observed Patterns

The spatio-temporal dynamics of the HOR in the presence of Cl^- and Cu^{2+} was investigated on a grid over the two main bifurcation parameters, U and ρ, using model Eqs. (6.14)-(6.17) and parameter values given in Table 6.3 if not stated otherwise. U was varied in the oscillatory region of the HOR and ρ-values were chosen in the NGC-interval $\rho \in]-1, 0[$. The parameter grid was evaluated at three different values of p_{Cu} and the results are summarized in Figs. 6.7, 6.8, and 6.9.

Simulations without global coupling yield homogeneous dynamics for aspect ratios β of the order of one. Systems with smaller aspect ratios also display pulses. Homogeneous oscillations stay stable up to $\rho \approx -0.65$ for $\beta \simeq 2.8$. For $U \lesssim 2.3$ and $U \gtrsim 17.8$ the system relaxes to the homogeneous stationary fixed point, cf. Fig. 6.6. For U in the oscillatory interval and $\rho \lesssim -0.65$ a variety of spatio-temporal patterns are observed, which are characterized in detail in the following sections. They include *pulses*, *anti-phase oscillations*, *modulated oscillations (MO)*, so called *cluster patterns (CP)*, one dimensional *target patterns (TP)* and patterns that were termed *asymmetric target patterns (A-TP)* [133]. Several parameter combinations support multiple spatio-temporal patterns such that the final pattern depends on the initial condition (cf. Fig. 6.7).

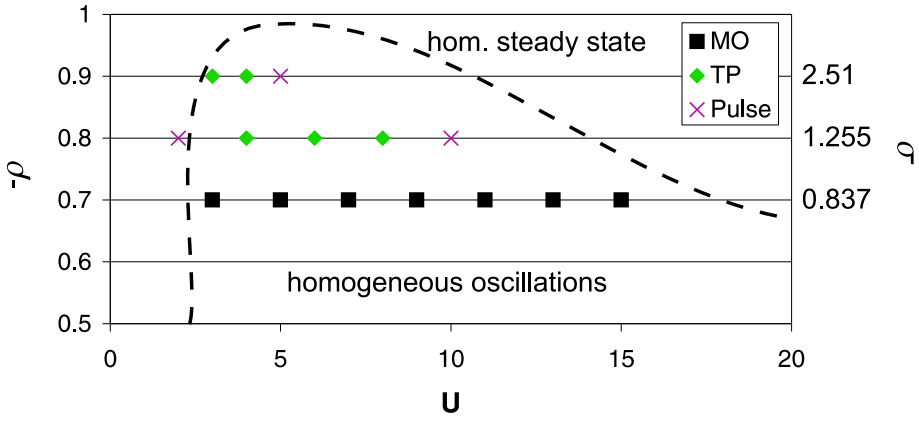

Figure 6.8: *Pattern formation under varying global coupling* ρ *and adjusting* σ *at the same time to investigate the system behavior for fixed physical conductivity* $(\sigma(1+\rho) = \text{const.})$. *The homogeneous steady state is globally stable outside the region marked with the dashed line (cf. Fig. 6.6).* $p_{Cu} = p^0_{Cu} \cdot 10^{-2}$, *other parameters see Table 6.3.*

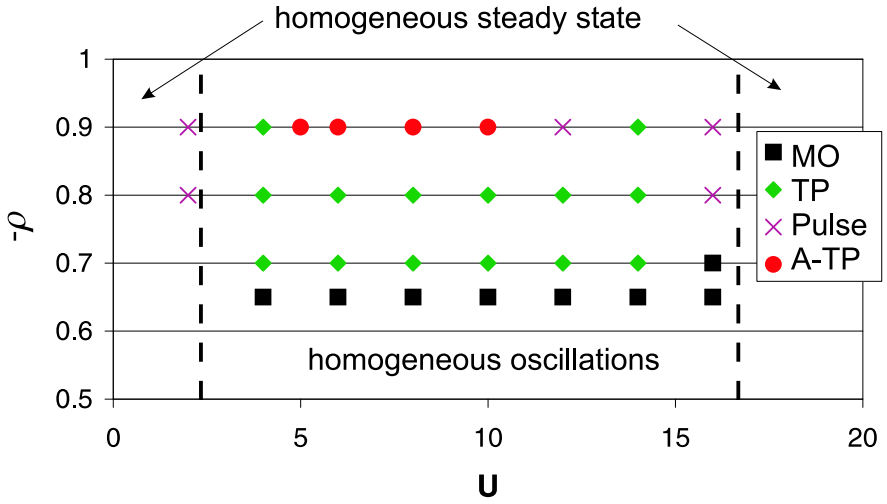

Figure 6.9: *Approximate regions where various patterns induced by the negative global coupling are observed for* $p_{Cu} = p^0_{Cu}$ *(other parameters see Table 6.3).*

Fig. 6.7 summarizes the findings for $p_{Cu} = p^0_{Cu} \cdot 10^{-4}$ and thus corresponds to the lowest investigated copper concentration. The behavior in this region proved to be the richest one, especially for strong negative global coupling, $\rho = -0.9$.

In Fig. 6.8 pattern formation as a function of the applied potential and the global coupling was investigated for a fixed physical conductivity at $p_{Cu} = p^0_{Cu} \cdot 10^{-2}$. Consequently, σ had to be changed for different values of ρ. Ergo, also the homogeneous dynamics and hence the U-range where oscillations could be observed at all change with changing global coupling (cf. Fig. 6.6).

The observed dynamics for $p_{Cu} = p_{Cu}^0$ are displayed in Fig. 6.9. It corresponds to parameter values investigated in the previous section dealing with the homogeneous dynamics.

A few general trends apart from the mere existence region of inhomogeneous spatio-temporal behavior can be observed in Figs. 6.7-6.9. Pulses are favored at the lower and upper U-boundary of oscillatory behavior. Pulses are also observed for U-values outside the oscillatory region at the lower U-boundary. Thus, these pulses indicate that either excitable dynamics exist in a small parameter region before the Hopf bifurcation or that the wave instability destabilizes the homogeneous steady state at lower U. A similar behavior is not exhibited at the upper U-boundary. MOs and TPs are found for lower values of the negative global coupling. The richest behavior is displayed at $\rho = -0.9$ where A-TPs, CPs and multistability between those and other afore mentioned patterns exists.

In the next sections characteristics and different forms of occurrence of the above mentioned patterns are studied in detail.

6.2.2 Pulses and Anti-phase Oscillations

As mentioned above the most basic patterns to be expected in an oscillatory system under NGC, namely pulses and anti-phase oscillations (cf. section 2.4) are only observed near the boundaries of oscillatory behavior. In both cases however, the simplest form of these patterns was hardly observed at all. Instead, the anti-phase oscillations were found to be translatory unstable, i.e., the entire pattern rotates around the ring as depicted in Fig. 6.10. A common characteristic of the observed pulses is that they exhibit an oscillatory instability resulting in breathing of the pulse width and a non-constant pulse speed. These pulses are usually termed *modulated pulses*. After the wave bifurcation giving rise to traveling wave solutions, modulated pulses stem from a second oscillatory instability introducing a second frequency into the system. This is apparent in the time series of the total current density that oscillates with a frequency which is independent from the circulation time of the pulse.

Pulses during oscillatory oxidation of hydrogen under NGC always display apparently chaotic modulations resulting in a chaotic total current density, see Fig. 6.11(a).[7] These chaotically modulated pulses coexist with A-TPs in certain parameter regions (s.b.).

Pulses traveling with constant shape and speed are found only in the regime in which the mode of homogeneous oscillations is not yet present in the system and for high p_{Cu}. The same is true for modulated pulses displaying a periodic modulation. The modulation amplitude of the periodically modulated pulse is strongly decreased as compared to the chaotic situation, cf. Fig. 6.11.

[7] Chaotic dynamics are assumed since no periodicity was observed during $\sim$ 500 oscillations periods.

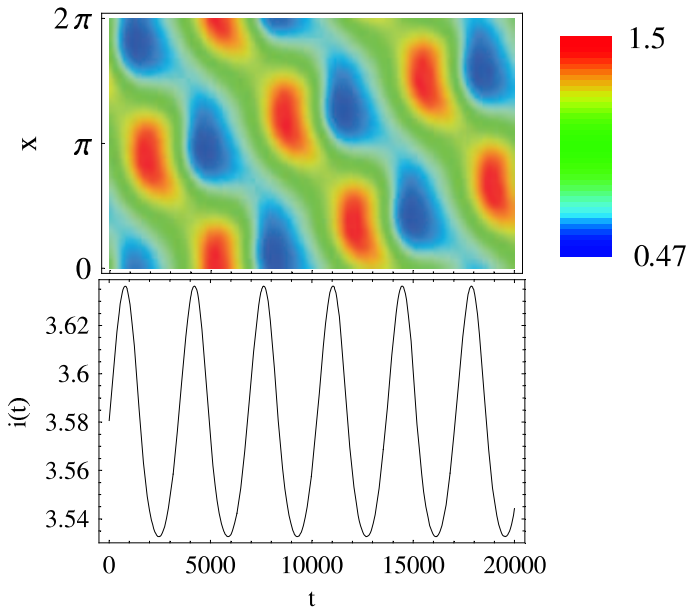

Figure 6.10: *Rotating anti-phase oscillation. Upper plate:* $\phi_{\mathrm{DL}}(x,t)$*; Lower plate:* $i(t)$*. Parameters:* $U = 5$, $\sigma = 2.51069$, $p_{Cu} = p^0_{Cu}$, $\rho = -0.7$. *The color map used here and in the following is also displayed with minimum and maximum values of* ϕ_{DL}*. Other parameters see Table 6.3*

6.2.3 Modulated Oscillations (MOs) and Target Patterns (TPs)

The most common patterns displayed by Eqs. (6.14)-(6.17) in the region of intermediate NGC are MOs and TPs (cf. Figs. 6.7-6.9). An example of an MO is depicted in Fig. 6.12. The pattern is practically homogeneous apart from the fast stages of the oscillations. The inhomogeneous part of the spatio-temporal motion can be made visible by subtracting the space averaged value of ϕ_{DL} at every time moment, see Fig. 6.12(b). It becomes clear that the homogeneous oscillations are modulated with a spatial wavenumber one which only shows up on the fast transitions connecting active and passive state. The representation of the dynamics as in Fig. 6.12, i.e., the (x,t)-plot of ϕ_{DL} and ϕ_{DL}-$\langle\phi_{\mathrm{DL}}\rangle$ supplemented with the total current density as a function of time, is used in all plots from now on.

MOs are observed for low NGC-strengths, i.e., the desynchronizing effect is not effective enough to promote inhomogeneities at all times. The 'pumping' into inhomogeneous modes is strong enough to promote spatial patterns only during the fast stages of the relaxation oscillations. MOs are thus genuine patterns to be observed in systems under NGC displaying relaxation-like oscillations in the homogeneous system.

Increasing the NGC, the inhomogeneities become more pronounced until the passive stage of the oscillation is completely inhomogeneous. Such a pattern is shown in Fig. 6.13(a). It apparently resembles an 1d TP. Two waves are emitted from a source point

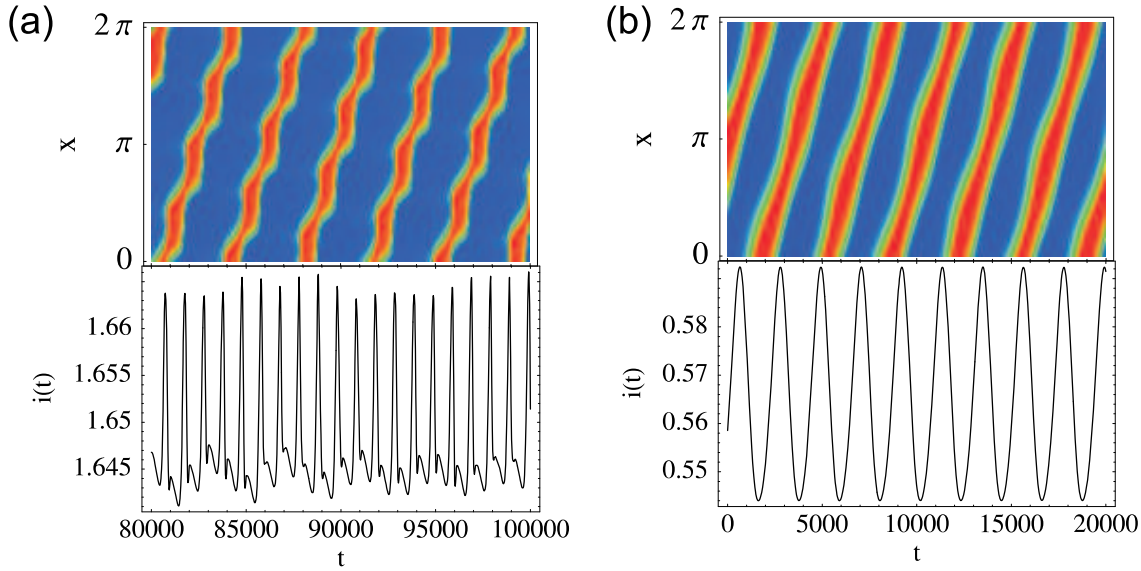

Figure 6.11: *Typical pulse forms observed in the (a) oscillatory and (b) non-oscillatory regime. A second independent frequency is visible in the total current density. Upper plates:* $\phi_{\mathrm{DL}}(x,t)$*; Lower plates:* $i(t)$*. (a) Chaotically modulated pulse. Parameters:* $U = 6$, $p_{Cu} = p^0_{Cu}$, $\rho = -0.9$. *(b) Periodically modulated pulse. Parameters:* $U = 2$, $\sigma = 1.125534$, $p_{Cu} = p^0_{Cu} \cdot 10^{-2}$, $\rho = -0.9$. *Other parameters see Table 6.3*

and travel along the ring until they annihilate on the opposite side of the ring.[8] The waves are decelerated which yields an asymmetric pattern in time and facilitates the distinction between TPs and MOs. Whether the NGC or the nonlocal migration coupling is responsible for the deceleration could not be completely clarified. To shed light on this matter, the aspect ratio is decreased to values where the migration coupling can be approximated by a diffusional term (cf. section 2.3.2). The resulting TP is displayed in Fig. 6.13(b) and the constant speed of the traveling waves suggests that the migration coupling causes the deceleration. Note however that the global coupling strength in Fig. 6.13(b) is decreased compared to Fig. 6.13(a).

A further apparent difference between MOs and TPs is the reoccurrence of the TP in the inhomogeneous part of the double layer potential, cf. Fig. 6.13, caused by the joining of the inhomogeneities in the uprising and falling flanks that is clearly absent in the subtracted data of the MO shown in Fig. 6.12. However, the transition from MOs to TPs is continuous. A suitable quantitative measure to decide whether a pattern should be classified as an MO or a TP is the time average over one oscillation of the total current density. TPs exhibit a more pronounced spatial symmetry breaking. On average the total current density in the region in which the two waves meet is higher than on the rest of the ring. Also MOs show some asymmetry, but less pronounced than TPs. Thus, a threshold

[8] Note that these TPs are not connected to excitable dynamics or inhomogeneities on the ring.

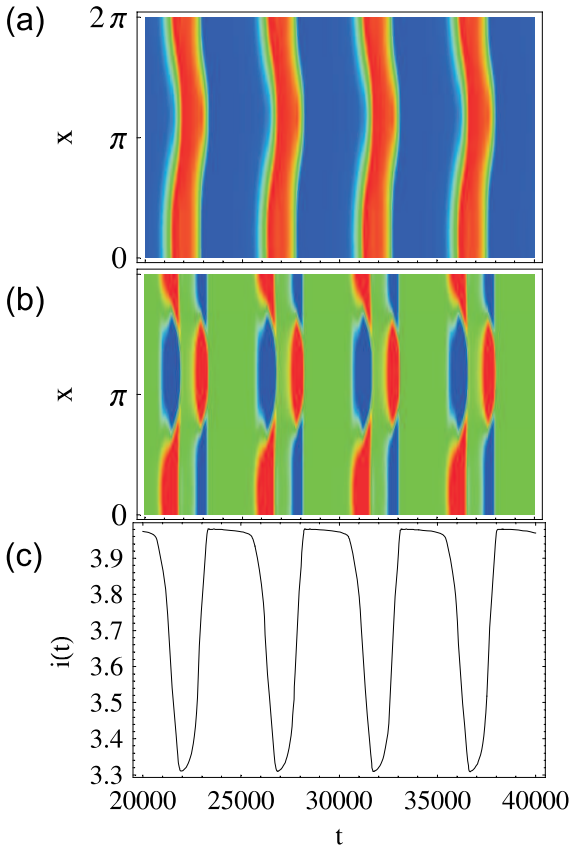

Figure 6.12: *Modulated oscillation. (a)* $\phi_{\mathrm{DL}}(x,t)$*; (b) Inhomogeneous part of the double layer potential,* $\phi_{\mathrm{DL}} - \langle\phi_{\mathrm{DL}}\rangle$*; (c) Total current density as a function of time displaying the relaxation-like behavior of the underlying oscillations. Parameters:* $U = 14$, $p_{Cu} = p^0_{Cu} \cdot 10^{-4}$, $\rho = -0.7$, *other parameters see Table 6.3.*

r_t on the basis of the maximum of

$$h(x) := \left(\int_t^{t+T}\int_0^{\pi} i(x,t)\,\mathrm{d}x\mathrm{d}t\right)^{-1}\left(\int_t^{t+T} i(x,t)\,\mathrm{d}t - \int_t^{t+T}\int_0^{\pi} i(x,t)\,\mathrm{d}x\mathrm{d}t\right)$$

could be defined to classify patterns with $r = \max_x h(x) < r_t$ as MOs and the ones above this threshold as TPs. A systematic study of the evolution of r as a function of the model parameters could not be performed due to the long integration times.

The passivation of the source point, which actually would be better characterized as a source region in this case, is accompanied by a steep fall in the total current density. The current minimum is reached as soon as the two waves meet on the opposite side of the ring. The active current plateau is reached after the annihilation.

For $\rho = -0.9$, $p_{Cu} = p^0_{Cu} \cdot 10^{-4}$, and $U > 10$ the rising flank is interrupted by a small peak. The small peak continously grows with increasing voltage until a qualitatively new form of TP as depicted in Fig. 6.14(a) is observed. The type-2 TP almost completely lacks

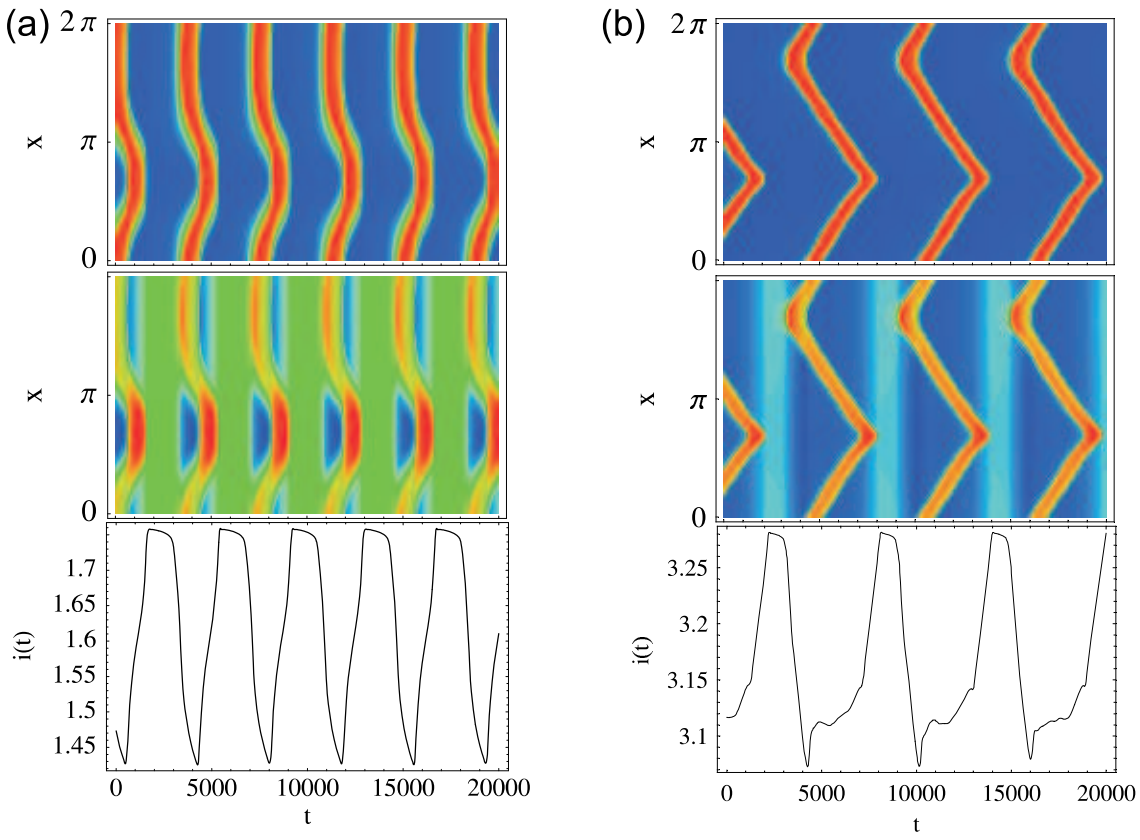

Figure 6.13: *Two examples of type-1 TPs. Upper plates:* $\phi_{DL}(x,t)$*; middle plates:* ϕ_{DL}-$\langle\phi_{DL}\rangle$*; lower plates:* $i(t)$*. (a) Typical TP observed for most* U, ρ *and* p_{Cu} *values. Parameters:* $U = 12$, $p_{Cu} = p^0_{Cu}$, $\rho = -0.9$*. (b) TP as observed for larger aspect ratios (smaller* β*) to compare with TPs in 1d reaction-diffusion systems. Parameters:* $U = 11$, $\beta = 0.1$, $\sigma = 0.03$, $p_{Cu} = p^0_{Cu} \cdot 10^{-4}$, $\rho = -0.5$*. Other parameters see Table 6.3*

the above mentioned asymmetry in time. Source and annihilation region are of the same size. The growth of the 'pre-peak' is accompanied by a shortening of the active period. Finally no active period remains and the two waves annihilate at the same time at which two new waves are send out.

Fig. 6.14(b) depicts a third type of TP that is identified at the lower voltage boundary of oscillatory behavior. Again no active period is present. Despite the substantial similarity in the spatio-temporal pictures of the TP type-2 and the TP type-3 the total current density reveals that they are indeed quite different. TP type-3 almost resembles a cluster pattern since the annihilation region becomes active as soon as the source region goes passive. TP type-3 was classified as a TP rather than a CP for continuity reasons.

TP type-1 tends to coexist with the A-TP. Note that in case the TP type-1 exhibits a small 'pre-peak' it is indistinguishable from an A-TP on the basis of the global time series (s.b.).

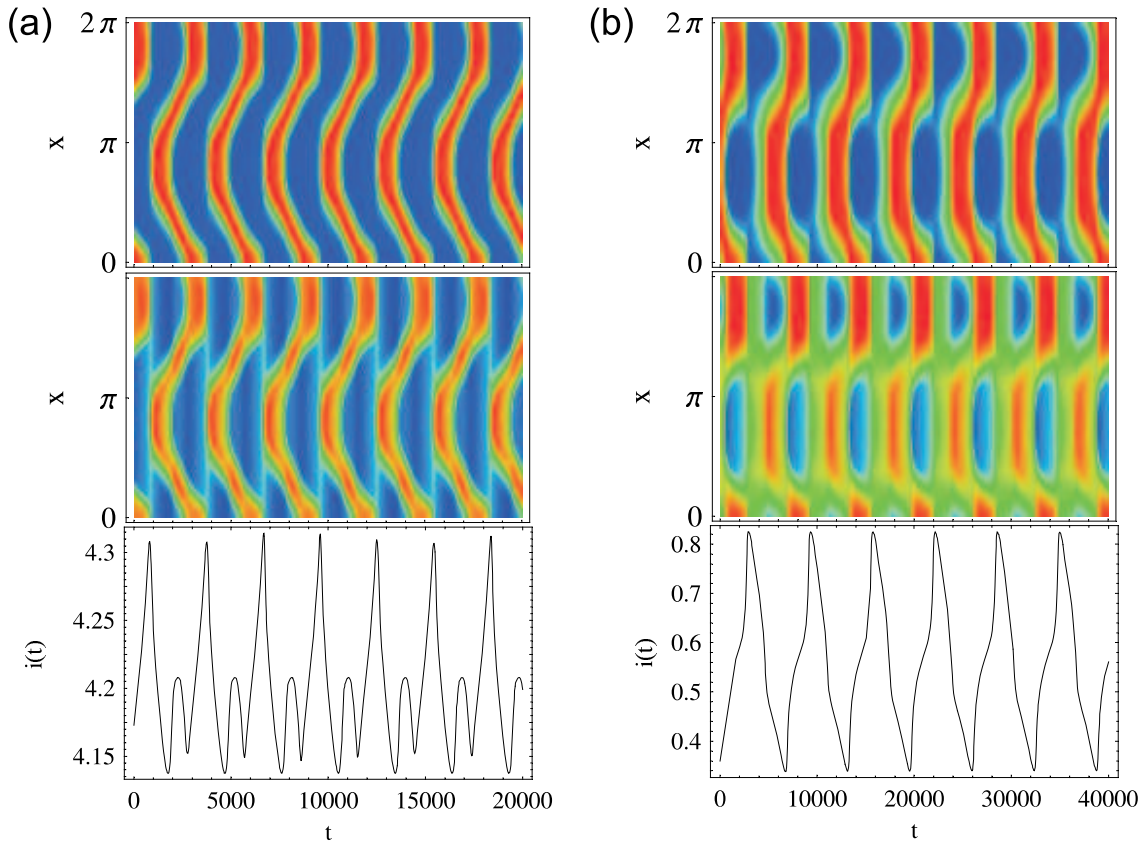

Figure 6.14: *(a) Second type of TP found during the HOR. Parameters:* $U = 15$, $p_{Cu} = p^0_{Cu} \cdot 10^{-2}$, $\rho = -0.9$. *(b) TP type-3 observed at the lower U-boundary. Parameters:* $U = 3$, $p_{Cu} = p^0_{Cu} \cdot 10^{-4}$, $\rho = -0.7$. *Other parameters see Table 6.3. Upper plates:* $\phi_{DL}(x,t)$*; middle plates:* ϕ_{DL}-$\langle\phi_{DL}\rangle$*; lower plates:* $i(t)$.

6.2.4 Asymmetric Target Patterns (A-TPs)

In Fig. 6.15(a) a typical periodic A-TP is displayed. The term 'asymmetric target pattern' stems from the fact that two waves originate at a source point but only one of them travels around the ring. The other one is pinned at a certain position close to the wave source and stays approximately at this position until it annihilates with the wave emitted in the opposite direction [133]. The source point can also behave in the opposite way as presented in Fig. 6.15(a). Instead of staying passive after emitting a wave it stays passive after annihilation and goes active after a wave is emitted (not shown). The source point is traveling along the ring with constant speed for all periodic A-TPs found. The typical speed of the source point is of the order 10^{-4}.

The pulse emitted in one direction undergoes shape modulations on its way around the ring resembling the chaotic pulse modulations reported in section 6.2.2. Indeed, periodic A-TPs coexist with chaotically modulated pulses of the type shown in Fig. 6.11(a) in

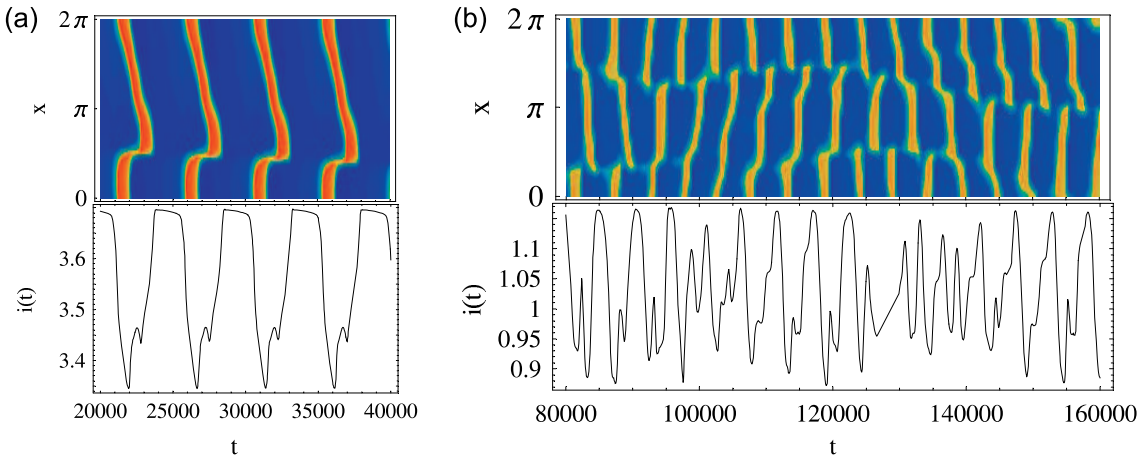

Figure 6.15: *(a) Periodic A-TP. Parameters:* $U = 13$, $p_{Cu} = p_{Cu}^0 \cdot 10^{-4}$, $\rho = -0.9$. *(b) Irregular A-TP. Parameters:* $U = 4$, $p_{Cu} = p_{Cu}^0 \cdot 10^{-2}$, $\rho = -0.9$. *Upper plates:* $\phi_{\mathrm{DL}}(x,t)$*; Lower plates:* $i(t)$.

certain parameter regimes. On the other hand periodic A-TPs also coexist with TPs of type-1 in different regions in parameter space. As can be expected due to the presence of a strong spatial defect in the A-TP, A-TPs are favored for initial conditions also exhibiting such an inhomogeneity. Nevertheless, periodic A-TPs can also be observed starting from homogeneous initial conditions.

Note however that the so termed periodic A-TPs still display apparently chaotic time series (not visible in Fig. 6.15(a) but verified with long time integrations).

Apart from periodic A-TPs also irregular A-TPs are found. During irregular A-TP dynamics the source point travels in irregular motions along the ring. Additionally, the pulse modulations are strong enough to promote the formation and extinction of a second source point. The resulting dynamics can be observed in Fig. 6.15(b). Short periods of cluster-like behavior interrupt the A-TP motion. After such a cluster-like phase the direction of the pulse traveling around the ring might be interchanged, cf. Fig. 6.15(b).

6.2.5 Cluster Patterns (CPs)

The last building block of pattern formation induced by NGC during the HOR are cluster patterns. CPs are characterized by the presence of a small number of domains in which the oscillation phase and amplitude are constant. Two examples of CPs found are presented in Fig. 6.16. The phase relation between two neighboring domains stays constant in time. Since the amplitudes of the individual oscillations in each domain are of the same size, cf. Fig. 6.17, these CPs are termed *phase clusters*.

The phase domains are connected by sharp transition fronts. Since the oscillations

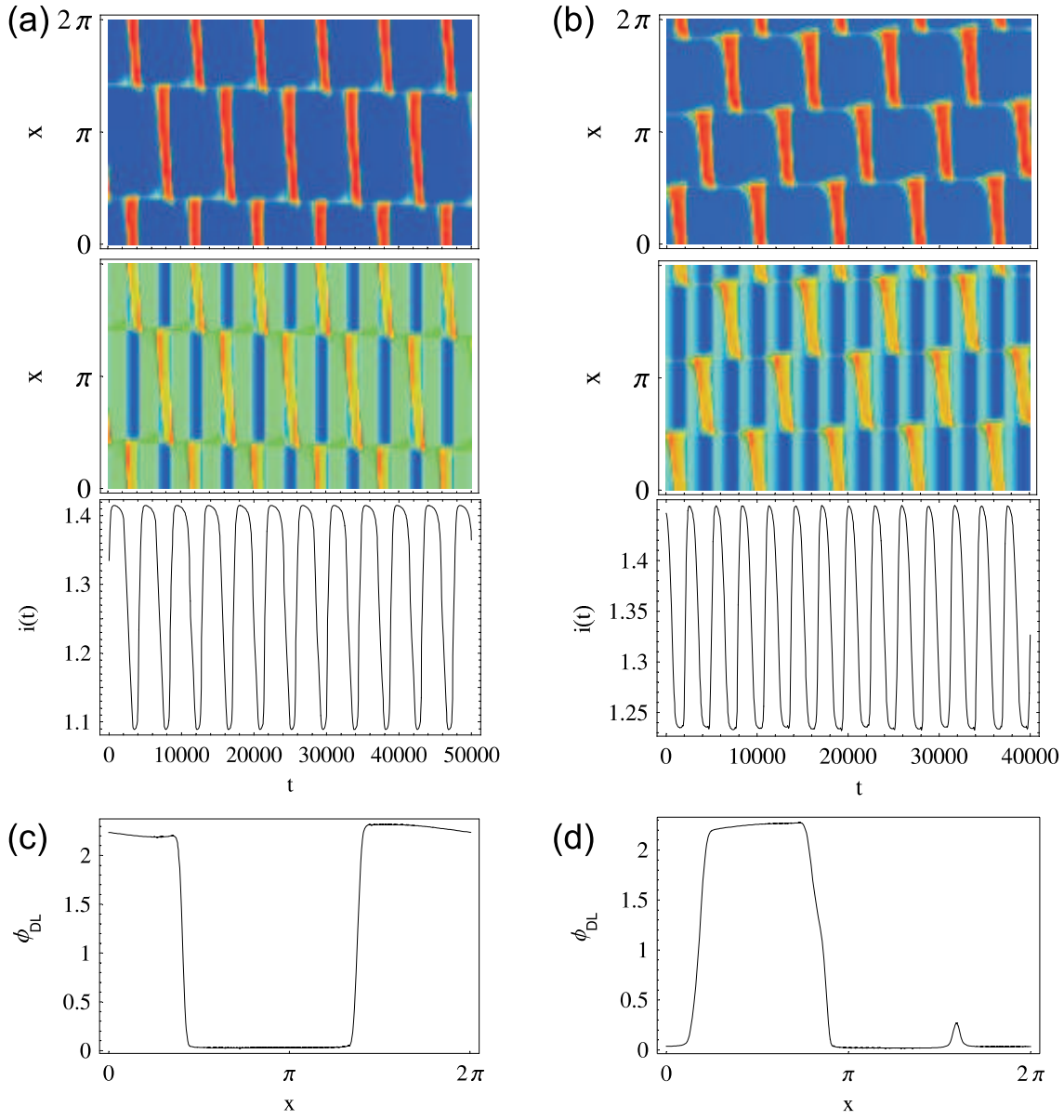

Figure 6.16: *(a) Traveling two phase CP. (b) Traveling three phase CP observed for the same parameter values. Upper plates:* $\phi_{DL}(x,t)$*; middle plates:* ϕ_{DL}-$\langle\phi_{DL}\rangle$*; lower plates:* $i(t)$*. (c)* $\phi_{DL}(x,t)$ *at* $t = 21000$ *and (d) at* $t = 15200$ *for the CPs presented in (a) and (b), respectively. Parameters:* $U = 5$, $p_{Cu} = p^0_{Cu} \cdot 10^{-4}$, $\rho = -0.9$, *other parameters see Table 6.3.*

are relaxation-like, the amplitudes of the different phase clusters are almost identical at certain stages of a full oscillatory cycle. During these active intervals the phase clusters are separated by a slightly more passive potential 'wall'. In all observed CPs the fronts were not stationary in time but traveling with a constant velocity. Due to work by Ising

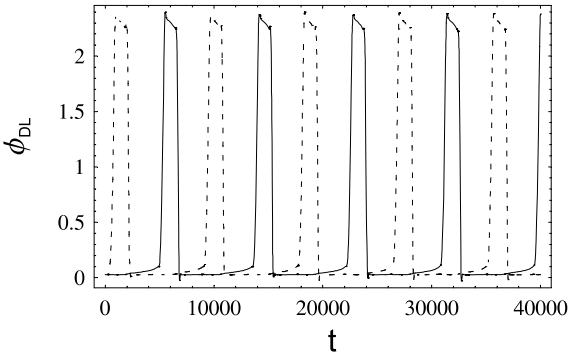

Figure 6.17: *Time series $\phi_{\mathrm{DL}}(x_{1/2},t)$ at two different points $x_{1/2}$ in space representing the two phase domains for the CP presented in Fig. 6.16(a).*

and Bloch, traveling fronts are also called Bloch fronts [183]. The symmetry breaking instability leading to traveling fronts is called Ising-Bloch bifurcation.

The global time series and thus the spatio-temporal motion is found to be periodic in all CPs.

In Fig. 6.16(a) a CP consisting of two phase domains is presented. The oscillatory medium is divided into two regions of equal size, as is clearly visible in Fig. 6.16(c) in which a snapshot of the spatio-temporal motion at a certain time moment of the evolution is presented. This property is also called phase balance. It is a well known characteristic of cluster behavior in reaction-diffusion systems and reflects the absence of an intrinsic length scale.

Apart from the two phase CP also three phase CPs are observed, actually the three phase CP shown in Fig. 6.16(b) coexist with the two phase CP discussed above. The three phase CP displays the same properties as the two phase CP. Only Bloch fronts are stable and phase balance is reached after transients decayed, cf. Fig. 6.16(d).

6.2.6 Discussion

In this section the results obtained by numerical simulation of pattern formation during the HOR in the presence of poisons are compared with experiments and put into the general frame of nonlinear dynamics in reaction-diffusion systems.

Modulated Pulses and Anti-phase Oscillations

Experimental observations of modulated pulses during the HOR in the presence of poisons are presented in [133]. However, the modulation frequency coincides with the time of circulation of the pulse. Thus, the modulations might stem from inhomogeneities on the ring and hence, do not originate from an intrinsic dynamic instability. It is also conceivable that the intrinsic dynamics supports modulated oscillations but the inhomogeneities

lead to the pinning of the modulation frequency to the circulation frequency. This hypothesis is supported by the varying amplitude of the modulation with the applied potential observed in experiment. The time series presented in Fig. 4 in [133] hint at a complex interaction between the non-uniformities on the ring and the nonlinear dynamics. A comprehensive discussion of this matter is given in [133]. Additionally, these two possibilities are very difficult to distinguish experimentally since precise information regarding the absolute position on the ring during rotating ring experiments became available only recently.

A similar situation was reported by Luss *et al.* during hydrogen oxidation on a nickel ring [184] and was modeled using a nonuniformly active ring [185]. Rotating pulses with a modulation not connected to the rotation period were observed during the oscillatory electro-dissolution of Co under NGC [36]. Reports on modulated pulses during theoretical investigations of pattern formation in reaction-diffusion systems include, e.g., Dolnik *et al.* who were not modeling global coupling but a wave instability in the BZ-system [119, 186] or theoretical work from Luss *et al.* [58].

Anti-phase oscillations stemming from an instability of the homogeneous fixed point have been reported earlier in experiments concerning the oxidation of formic acid (HN-NDR oscillator) under NGC with periodic boundary conditions [45, 115]. The interaction of a global coupling and unstable limit cycle motion in an HN-NDR oscillator apparently resulted in anti-phase oscillations during Ni-electrodissolution [28]. N-NDR oscillators display anti-phase oscillations under positive global coupling both, in theory and experiment [103, 104]. Note that these anti-phase oscillations are manifestations of the effect of the global coupling on the limit cycle motion opposed to the anti-phase oscillations reported here that stem from a wave instability of the homogeneous fixed point.

MOs and TPs

MOs were recently reported to exist during the oscillatory HOR in the presence of NGC [132, 134]. A representative example of the experimental pattern is displayed in Fig. 6.18(a). The theoretical data given in Fig. 6.12 matches the the experimental spatio-temporal picture. The mechanism behind the long passive periods observed in the experiment does not seem to be captured by the model presented here. MOs in an HN-NDR oscillator modeling Ni electro-dissolution were reported earlier by Christoph [103, 104] but have a different origin since positive global coupling was applied on a Benjamin-Feir unstable system.

The agreement between the presented TP type-1 which is by far the most common type observed in the simulations with the patterns found during experimental investigations of the same system is excellent in the spatio-temporal picture as well as the total current, cf. Figs. 6.18(b) and 6.13(a). Thus, the appearance of TPs in relaxation oscillators subject

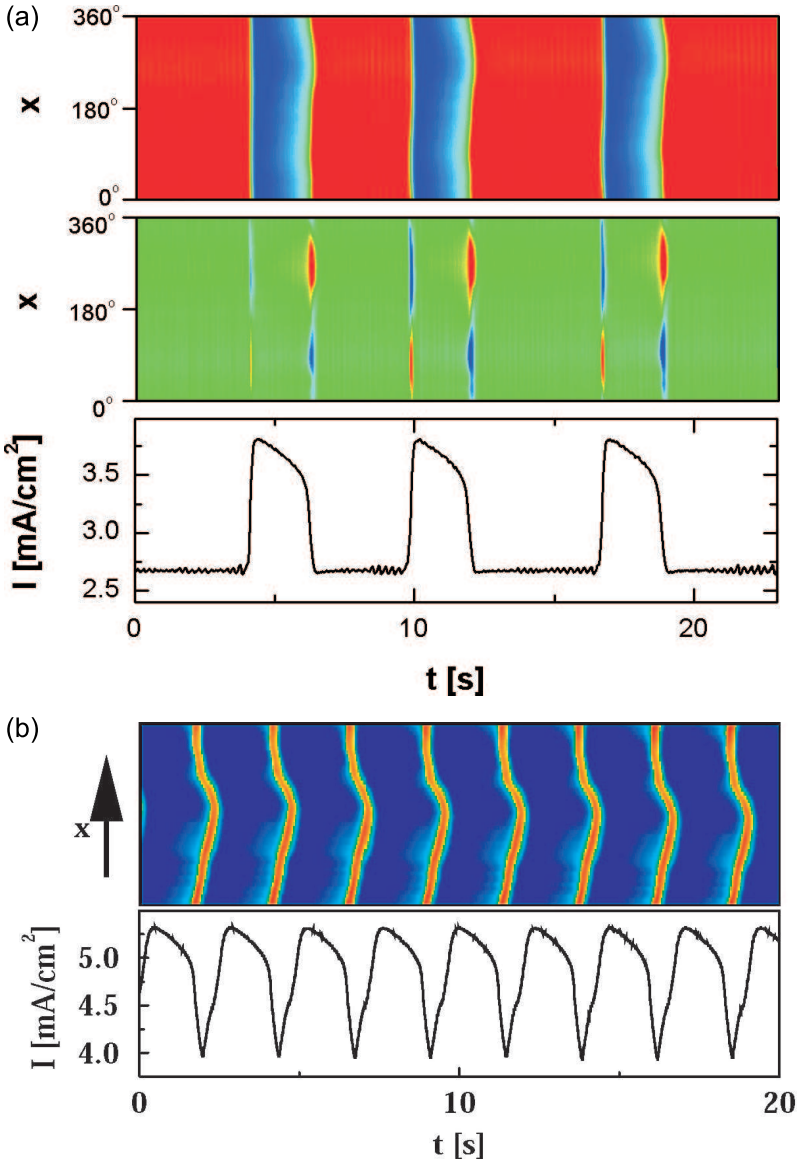

Figure 6.18: *Experimental manifestations of (a) MOs and (b) TPs. (a) First plate: Potential micro-probe signal corresponding to ϕ_{DL}; second plate: Corresponding difference plot; third plate: Total current density. (b) First plate: Potential micro-probe signal; second plate: Total current density. Taken from [133].*

to global coupling is explained and high consilience between model and experiment is reached. Also the general trend in the (U-ρ)-bifurcation parameter plane is retained.

1d TPs were found in an N-NDR oscillator under NGC theoretically [36] as well as experimentally during HCOOH-oxidation (HN-NDR) [45]. Other observations of 1d TPs in reaction-diffusion systems are reported in, e.g., [58, 118]. Luss *et al.* studied the catalytic hydrogen oxidation under NGC [58]; Zhabotinsky *et al.* investigated a model of

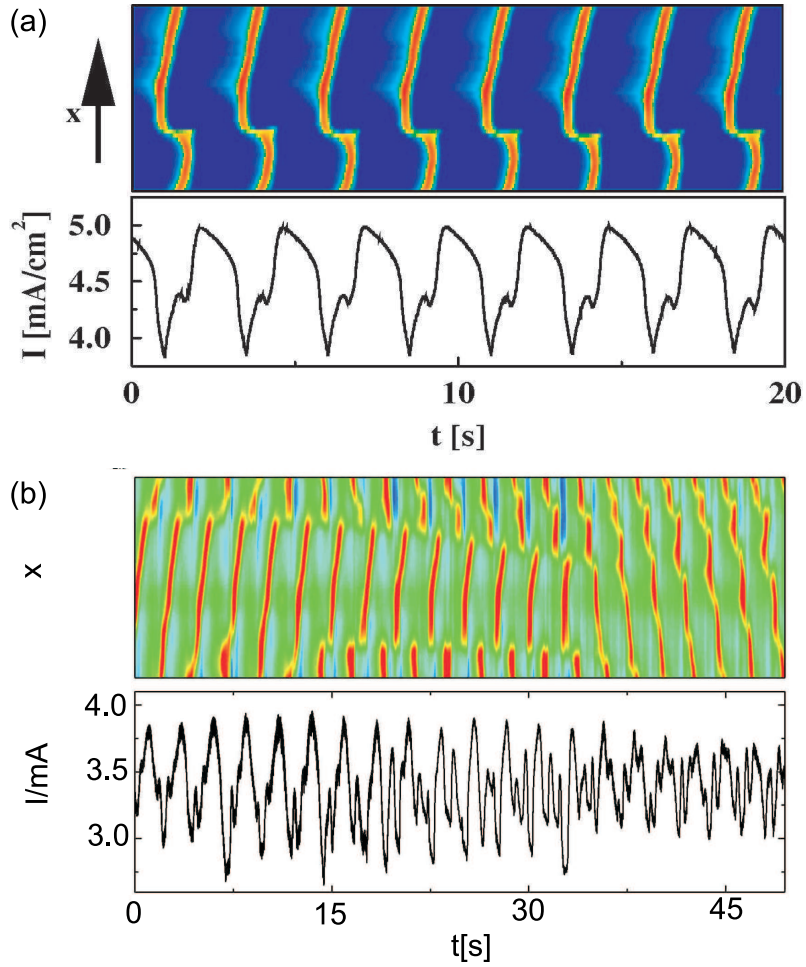

Figure 6.19: *(a) Periodic and (b) irregular A-TP as observed in experiments. First plates: Potential micro-probe signal (in (b) only the inhomogeneous part is shown); second plates: Total current (density). (a) taken from [133]; (b) after [134].*

the BZ-reaction with wave instability [118] .

A-TPs

The first experimental observation of an A-TP was reported in [133] and is reprinted in Fig. 6.19(a) for a convenient comparison with the theoretical data given in Fig. 6.15(a). The model presented here reproduced the spatio-temporal behavior and the global current for the first time. Thus, the question if the asymmetric behavior observed in experiment is due to spatial inhomogeneities can be negated. It could be further shown that the A-TP coexist with TPs and modulated pulses. It is important to note that the global time series does not necessarily differ between A-TPs and TPs. In the view of these new results the data presented in [133] can be reinterpreted as follows. The occurrence of A-TP, TP and

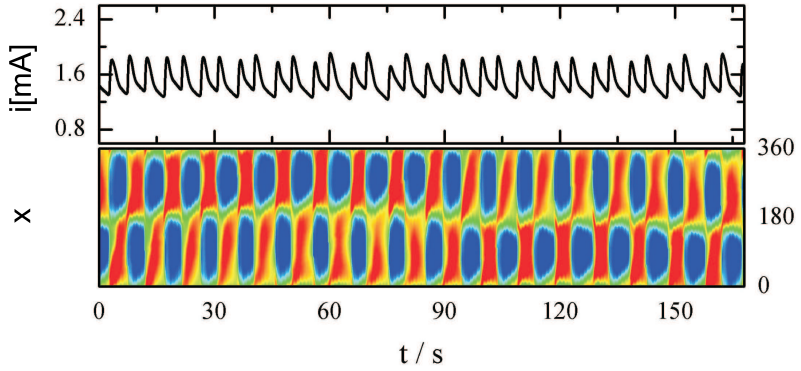

Figure 6.20: *Two phase CP observed during the HOR under NGC. First plate: Total current; second plate: Potential micro-probe signal.*

a mixture of the two patterns for increasing applied voltage as reported in [133] is not due to different global attractors but due to different initial conditions and the mixed state seems to be a long transient close to equistability of the two patterns. This hypotheses is supported by recent experiments conducted by Varela [187].

Note however, that the source point in the experiments as presented in [133] is stationary and the global time series apparently is periodic. We suggest that the wave source is pinned at a certain location by the inhomogeneities present on the WE since stationary dislocations were never observed in the simulations and inhomogeneities seem to be present on the ring surface (s.a.). Furthermore, the statement made above regarding the experimental difficulties of absolute positioning stays valid and thus the experimental source point dynamics are not fully clarified.

The irregular A-TP presented in section 6.2.4 perfectly resembles the experimental pattern presented in Fig. 6.19(b). Note the eminent similarity of the total current time series.

CPs

CPs are reported here for the first time in an electrochemical model. CPs with similar characteristics were also found in experiments during the oscillatory HOR under NGC [134]. As can be seen in Fig. 6.20 the two phase CPs observed in the experiment apparently also exhibit phase balance. The position of the phase fronts seems to be unstable. The correspondence regarding the global time series and the detailed characteristics of the experimental and theoretical CPs is not as perfect.

In [188] the authors investigated the role the local and the global coupling play for different characteristics of CPs and concluded that the dynamics are governed mainly by the global coupling [189, 190]. Two and three phase CPs have been reported to exist in various oscillatory reaction-diffusion systems subject to global coupling, most prominently in

the complex Ginzburg-Landau equation, during the BZ-reaction and during CO oxidation on platinum [75, 77–79, 188, 191–194].

6.2.7 Conclusions

Numerical investigations of spatio-temporal pattern formation during the oscillatory oxidation of hydrogen in the presence of Cu^{2+} and Cl^{-} have been presented. The results given here present the first study of the influence of NGC on an HN-NDR relaxation oscillator of which class the hydrogen oxidation on Pt in the presence of poisons is the most prominent example. The reduced four variable model introduced in section 6.1 was used for the modeling. The system displays homogeneous relaxation oscillations without global coupling for almost all parameter values tested. The existence of pulses was reported in a region of smaller aspect ratios in the absence of NGC in the oscillatory regime.

With increasing NGC four distinct spatio-temporal patterns are observed. Pulses and anti-phase oscillations and MOs and TPs are found for intermediate NGC. Additionally, we present the observation of CPs and A-TPs at high NGC. To our knowledge this is the first report of A-TPs in a reaction-diffusion model. The regime of their existence as well as their dynamical nature was clarified. The first theoretical evidence of CPs in electrochemistry was given.

The theoretical results reproduce the novel experimentally observed patterns with outstanding consilience. Thus, it was shown that not only the homogeneous dynamics are captured by the model Eqs. (6.14)-(6.17), but that the reduced model also is sufficient to describe the rich previously uncaptured spatio-temporal dynamics during the HOR in the presence of NGC. The only spatial coupling mechanism taken into account is the migration coupling acting on ϕ_{DL}. It should be noted that some trends in the experiments could not yet be reproduced and that the NGC-strengths used in the simulations exceed those in the experiments.

The presented model can now be used for extended investigations of pattern formation during the HOR. Especially the influence of distributed parameters on the front motion in A-TPs and the modulation frequency of the modulated pulses is an interesting question. Also the introduction of a 'toy-model' that preserves the phenomenological spatio-temporal behavior but lacks the numerical difficulties would be desirable to gain deeper insight into the dynamics by computing bifurcation diagrams. A second unresolved issue is the turbulent dynamics observed in experiments without global coupling [26, 133, 134].

Chapter 7

Summary and Outlook

Theoretical aspects of pattern formation in electrochemistry were studied with a special emphasis on effects induced by global coupling. In a first step, a generalization of the electrochemical global coupling term revealed that global coupling plays a role in experimental situations much more frequently than realized before. This implies that the electrode does not respond uniformly but exhibits spatial patterns in many experimental investigations. In this thesis mechanisms that break spatial symmetry were investigated in the three types of electrochemical oscillators employing analytical and numerical methods. In all three cases two aspects were elaborated. On the one hand, the universal features governing dynamical systems under global coupling were extracted and were put into the general frame of nonlinear dynamics. On the other hand, quantitative predictions regarding the spatio-temporal evolution of the electrochemical variables were given and were compared with experiments.

The results of the present work can be summarized in five main points which are elaborated in the following paragraphs. (i) An expression for the strength of the global coupling introduced by the control mode as a function of the resistances between working, reference, and counter electrode was derived. (ii) Contributions to the realistic modeling of electrochemical systems in general as well as for a specific reaction are presented. (iii) The spatio-temporal dynamics of three electrochemical systems subject to different forms of global coupling has been investigated. (iv) During these investigations a, to the best of the author's knowledge, novel transition from a fixed point to complex dynamics was unrevealed. (v) The generality and transferability of the derived results was elaborated by means of extensive comparisons with other dynamical systems.

(i) The strength of the global coupling due to the external control either using an external resistor or a close reference electrode was derived in chapter 3 as a function of experimentally easily accessible parameters and independent of the specific electrode geometry.

It was shown that the effect of a close reference electrode manifests itself in the evolution equation of the double layer potential in exactly the same way an external resistor with negative impedance of the same magnitude as the compensated resistance would do. It is argued that the common control mode of ohmic drop compensation is equivalent to the insertion of such a negative impedance. Hence, the formation of nonuniform potential distributions at the working electrode is expected if ohmic drop compensation is invoked, in particular if the reaction under consideration displays a region of negative differential resistance.

(ii) Four contributions to the realistic modeling of electrochemical systems are presented. The first two concern systems with an S-shaped current potential curve in which the 'S' arises due to attractive lateral adsorbate-adsorbate interactions. These systems exhibit stationary periodic spatial patterns (Turing patterns) without global coupling.

The points in parameter space in which the homogeneous fixed point is unstable with respect to the formation of Turing patterns were calculated using realistic parameters modeling the reduction of periodate in the presence of camphor. Almost quantitative agreement with experiment was demonstrated (section 4.2).

Secondly, a model of the coverage dynamics of adsorbates with attractive lateral adsorbate-adsorbate interactions, explicitly taking the interactions on the nanometer scale into account, was derived. Dispersion relations were calculated, and the system is found to be unstable with respect to a huge range of wavenumbers from macroscopic to mesoscopic scales (section 4.2.2) .

Third, the unrealistic assumption of a constant double layer capacity, e.g., in the presence of adsorbing organic molecules, was dropped. It was shown that the points of the onset of the Turing instability are not changed when a spatially varying double layer capacity is included in the dynamics. This statement is independent of the specific electrochemical reaction under consideration and of the spatial coupling mechanisms in effect (section 4.2.1).

Finally, a quantitative model of the hydrogen oxidation on Pt in the presence of poisons was given. Hydrogen oxidation in the presence of poisons is a system of fundamental importance owing to basic research interests and technological relevance since hydrogen oxidation takes place in the $H_2|O_2$ fuel cell. Furthermore, the exceptional situation that four quantities governing the dynamics can be measured independently if Cu and halides are taken as poisons renders the hydrogen oxidation reaction the ideal prototype electrochemical oscillator since model predictions can be compellingly tested. In section 6.1 existing experimental data were evaluated to derive a quantitative model for the homogeneous dynamics. The model was verified by means of a detailed comparison with the experimental data. Quantitative agreement with the experiment in the four observables and with bifurcation diagrams was demonstrated. Thus, the mechanistic view of

the oscillations observed during the hydrogen oxidation reaction could be clarified, and the importance of the recently reported attractive interaction between Cu^{2+} and Cl^{-} was revealed. A minimal set of evolution equations build upon well studied reaction steps was given. This model formed the basis for the subsequent spatio-temporal investigations (s.b.).

(iii) Pattern formation in electrochemical systems subject to global coupling was studied in the three different electrochemical oscillators. The roles of the activator and the inhibitor as well as the resulting form of the global coupling differ in each system. Thus, general contributions to the impact of global coupling on intrinsically bistable as well as oscillatory systems and on a relaxation-like oscillator are presented.

The dynamics of a bistable system with S-shaped current-potential characteristic subject to a global constraint was investigated. The global constraint stems from a high electrolyte conductivity such that spatial variations of the double layer potential are damped out on timescales much faster than the rest of the dynamics. Consequently, the spatial degree of freedom can be eliminated adiabatically. The formation of stationary current domains and an oscillatory instability of the domains leading to periodically as well as chaotically breathing domains is reported for the first time (section 4.1).

A bifurcation analysis and numerical simulations of the prototype system displaying an N-shaped current-potential curve under negative global coupling in the oscillatory regime were performed using no-flux boundary conditions (section 5.1). In this case the global coupling acts on the activator. We reported standing waves, asymmetric standing waves, pulse-like behavior and spatially inhomogeneous mixed-mode oscillations including a period doubling. Asymmetric standing waves present a previously unreported means of a smooth transition from standing waves to pulse-like behavior. A symmetry breaking pitchfork bifurcation going from standing waves to asymmetric standing waves could be identified. Since a prototype model is used, the results are expected to be of general nature. This is illustrated by the excellent agreement of the theoretical data with experiments even though the free parameters used for the calculations were fitted to a different reaction than the one used in the experiment.

Third, also the dynamics displayed by a system with a current-potential characteristic of the hidden negative differential resistance-type under desynchronizing global coupling was explored (section 6.2). The solidly verified model of the oscillatory hydrogen oxidation reaction (s.a.) was used in these studies. The resulting dynamics of a relaxation-like limit cycle oscillator subject to negative global coupling displays rich spatio-temporal behavior. As a function of the applied voltage and the negative global coupling strength the following, to a large extend novel, patterns were found to exist in one dimensional domains with periodic boundary conditions. Pulses of constant shape and speed, modulated pulses, and traveling anti-phase oscillations were observed in the regime in which the ho-

mogeneous fixed point is stable with respect to homogeneous oscillations. The system exhibits aperiodically modulated pulses in the oscillatory regime with global coupling. For low global coupling strength the relaxation-like oscillations display inhomogeneities only on the fast flanks of the oscillations (modulated oscillations). Strong global coupling leads to the formation of one dimensional target patterns. It was demonstrated that target patterns as well as aperiodically modulated pulses coexist with asymmetric target patterns which had been observed in experiments during the hydrogen oxidation in the presence of poisons but have never before been reported in simulations. Additionally, two and three phase cluster patterns are reported to exist during the hydrogen oxidation reaction. Cluster patterns were so far unknown in electrochemical models. The success of the model becomes apparent in view of the fact that indeed all these patterns were observed experimentally during the oscillatory oxidation of hydrogen in the presence of Cu^{2+} and Cl^{-} and that moreover, qualitative agreement regarding bifurcation sequences was demonstrated.

These results emphasize the necessity to incorporate the spatial degree of freedom when studying electrochemical systems, in particular if a negative differential resistance is present and/or ohmic drop compensation is invoked.

(iv) During the investigation of the dynamics displayed by the prototype N-shaped negative differential resistance oscillator the coincidence of a subcritical wave bifurcation and a homoclinic orbit was discovered. This unusual point in parameter space provides means of a transition from a stable stationary steady state to complex spatio-temporal dynamics that does not involve a hysteresis. Hints pointing to a generalization of this mechanism for the occurrence of complex dynamics have been elaborated. Utilizing two examples, it was shown that a subcritical pitchfork or Hopf bifurcation of a stable homogeneous fixed point coincides with a homoclinic connection at the bifurcation point if the homogeneous steady state is globally stable (section 5.2). To the author's knowledge such a bifurcation point is not discussed in the mathematical literature. It is well known that complex spatio-temporal motion is to be expected in the proximity of a homoclinic connection to a saddle focus which is illustrated by the observation of spatially inhomogeneous mixed-mode oscillations in the cases presented here. Thus, a mechanism for the abrupt onset of complex dynamics coming from a homogeneous steady state by means of tuning just one parameter is presented.

(v) The transferability of results derived during the investigation of self-organization phenomena was elaborated by a detailed comparison of the obtained findings with other models thus emphasizing the universal nature of this work. Nevertheless, the importance of a throughout study of each individual system is underlined by the differences in the "fine-structure" between the respective models.

Stationary and breathing current domains were reported earlier to exist in a model derived to describe pattern formation in semiconductors displaying an S-shaped current-voltage characteristic. A sufficient condition for the occurrence of complex spatio-temporal dynamics originally derived for the semiconductor system was successfully applied in the electrochemical system (section 4.1.4). Even though this condition is never fulfilled in the electrochemical system, complex spatio-temporal motion is exhibited also by the electrochemical dynamics.

Stationary current domains also exist in electrochemical models of systems displaying an S-shaped current-potential characteristic subject to positive global coupling. In studies of a bistable electrochemical system displaying an N-shaped negative differential resistance subject to negative global coupling also stationary and breathing current domains were observed. Thus, the basic effects induced by a global constraint acting on an intrinsically bistable variable are similar to phenomena due to a global coupling acting on a two component system either if a NGC on the inhibitor or a positive global coupling on the activator is present, cf. section 2.4.

The cluster patterns observed if a negative global coupling acts on a relaxation oscillator are a common pattern displayed by (oscillatory) reaction-diffusion systems subject to global coupling. Still, the specific properties, e.g., if phase balance is displayed or if the clusters are of the amplitude or phase cluster type, depends on the system under consideration, cf. section 6.2.6.

The coincidence of a subcritical Hopf bifurcation and a homoclinic connection reported to exist in the dynamics of an oscillator with N-shaped current-potential characteristic closely resembles the simultaneous observation of a pitchfork bifurcation and a homoclinic orbit reported earlier in a semiconductor system. This points to a possible further generalization in terms of bifurcation theory and to a general mechanism for the occurrence of complex spatio-temporal dynamics (section 5.2).

The results presented in this thesis motivate further investigations regarding several aspects. A main focus of future work will be the elaboration of the afore mentioned bifurcation point. The enormous wealth in the dynamics of the hydrogen oxidation in the presence of poisons observed in experiments with and without global coupling is not yet fully captured by the model presented here. Numerical simulations of the adsorbate coverage dynamics in the Turing unstable region of the S-NDR oscillator and experiments with other systems displaying an S-NDR (e.g., CO-electrooxidation on Pt) could bring further insight. The detailed comparison with experiment might also benefit from including a non-constant double layer capacity in the electrochemical modeling.

The results should also be seen in a broader framework. Electro-transfer reactions involving a first order phase transition play an important role in the study of biological membranes and their model systems such as lipid layers. Furthermore, controlled elec-

trochemical reactions are processes of technological importance, e.g., electropolishing, electroplating, metal corrosion, and electrocatalytic reactions, especially the $H_2|O_2$ and methanol fuel cell. Dynamical instabilities have been known to exist in all these applications for a long time. The studies shown here make it very likely that also spatial patterns exist in these systems due to the general nature of the positive feedback and global coupling mechanisms in electrochemistry. Oscillations and spatial patterns are usually undesired in industrial processes. Thus, insight into the conditions under which spatial patterns have to be anticipated and the development of control strategies using appropriate feedback schemes is needed. Even though general aspects of pattern formation constituted the main focus in this thesis the results presented here also point to potential routes of technological exploitation. The manufacturing of structured electrodes by means of spatial symmetry breaking could be one such route. Also the detailed understanding of the oscillation mechanism during the hydrogen oxidation reaction in the presence of poisons might open opportunities to find optimal reaction conditions in the $H_2|O_2$ fuel cell, perhaps under non-stationary operation, especially in the view of the common problem of CO poisoning. These considerations illustrate that the investigation of electrochemical pattern formation contributes not only to fundamental research in nonlinear dynamics and electrochemistry but additionally has the potential for technological applications.

Appendix A

Appendix

A.1 Non-dimensionalization

A.1.1 N-NDR Model

The set of equations describing the dynamics in an NDR system in physical units given in section 5, Eqs. (5.1),(5.2), can be cast into dimensionless form. With the transformations of the variables (since Neumann boundary conditions are used in chapter 5, x is rescaled accordingly)

$$\begin{aligned} 2D\delta^{-2}t &\to t \\ c &\to c/c^b \\ \phi_{\mathrm{DL}} &\to f\phi_{\mathrm{DL}} \\ x &\to x\pi/L \\ z &\to z/w \end{aligned}$$

(all voltages are scaled accordingly) and the definitions of the parameters

$$\begin{aligned} \varepsilon &= 2C_{DL}(c^b nF\delta f)^{-1} \\ \sigma &\to \sigma\pi\delta(fnFc^bDL)^{-1} \\ U &\to fU \\ \beta &= \pi L w^{-1} \end{aligned}$$

Eqs. (5.1),(5.2) transform to the dimensionless dynamical system given by Eqs. (5.3),(5.4). The physical parameter values are given in Table A.1. The resulting dimensionless parameters are compiled in Table 5.1. The constants k_i were fitted to experimental data obtained during $S_2O_8^{2-}$-reduction on Ag [39].

Table A.1: *Physical parameter values used in the N-NDR dynamics*

L	=	1cm	C_{DL}	=	0.2 F/m	w	=	1.05 cm
D	=	10^{-9} m^2/s	δ	=	10^{-5} m	U	$\in$	[-1,-3] V
c^b	=	0.05 mol/m^3	σ	=	0.065 $(\Omega$ m$)^{-1}$	f	=	38 V^{-1}

Table A.2: *Typical parameter values used in the S-NDR model*

k_{ad}=$1\cdot10^4\,\frac{\text{cm}^3}{\text{mol s}}$	C^0_{DL}=$20\cdot10^{-6}\,\frac{\text{C}}{\text{V cm}^2}$
k_d=$5\cdot10^{-3}\,\text{s}^{-1}$	C^1_{DL}=$2\cdot10^{-6}\,\frac{\text{C}}{\text{V cm}^2}$
$k_r\exp(-\alpha f\phi^0_{\text{DL}})$=$2\cdot10^{-8}\,\frac{\text{cm}}{\text{s}}$	c^b_{ad}=$1\cdot10^{-6}\,\frac{\text{mol}}{\text{cm}^3}$
N_{max}=$1\cdot10^{14}\,\text{cm}^{-2}$	D_θ=$1\cdot10^{-5}\,\frac{\text{cm}^2}{\text{s}}$
n=1	q'=$-1.2\cdot10^5\,\frac{\text{J}}{\text{mol}}$
χ=1	α=$1/2$
T=300 K	σ=$1\cdot10^{-3}\,\Omega^{-1}$
L=10 cm	w=4.5 cm

A.1.2 S-NDR Model

In this section we give the transformations yielding the dimensionless model equations (4.5),(4.6). Note that the transformations leading to dimensionless units differ from the ones given in [85]. In physical units the equations for current controlled conditions read (cf. section 2.5.2) [85]

$$C_{DL}\frac{\mathrm{d}\phi_{\text{DL}}}{\mathrm{d}t} = i'_0 - \chi nF c^b_r k_r(1-<\theta>)e^{\chi\alpha f(\phi_{\text{DL}}-\phi^0_{\text{DL}})}$$
$$\frac{\partial\theta}{\partial t} = k_{ad}c^b_{ad}(1-\theta)\exp\left(-\alpha w'(\phi_{\text{DL}},\theta)\right) - k_d\theta\exp\left((1-\alpha)w'(\phi_{\text{DL}},\theta)\right)$$

with

$$w'(\phi_{\text{DL}},\theta) = \frac{C^0_{DL}-C^1_{DL}}{2N_{max}k_BT}\phi^2_{\text{DL}} + \frac{q'\theta}{RT}.$$

The meaning of the numerous constants is given in Table 2.1 and typical values of the constants are shown in Table A.2. The model equations (4.1),(4.2) are retained via the transformations of the variables according to

$$\phi_{\text{DL}} \to \phi'_{\text{DL}} = \alpha f\phi_{\text{DL}}$$
$$t \to t' = \frac{c_x^2 D_\theta}{L^2}t$$
$$x \to x' = \frac{c_x}{L}x.$$

c_x accounts for the different boundary conditions used in sections 4.1 and 4.2, respectively. x is rescaled to fit Neumann boundary conditions in section 4.1, $c_x = \pi$; Dirichlet boundary conditions are used in the other sections, $c_x = 2\pi$.

Additionally the parameters

$$\begin{aligned}
\mu &= \frac{L^2 k_{ad} c_{ad}^b}{c_x^2 D_\theta} \\
p &= \frac{k_d}{k_{ad} c_{ad}^b} \\
\nu &= \frac{R(C_{DL}^0 - C_{DL}^1)}{2N_{max} k_B \alpha f n F} \\
q &= \frac{\alpha q'}{RT} \\
\gamma &= \frac{\alpha L^2 n F f}{c_x^2 D_\theta C_{DL}^0} c_r^b k_r e^{-\chi \alpha f \phi_{\mathrm{DL}}^0} \\
i_0 &= \frac{i_0'}{n F c_r^b k_r \exp(-\chi \frac{\alpha n F}{RT} \phi_{\mathrm{DL}}^0)} \\
d &= L\sigma (c_x D_\theta C_{DL})^{-1} \\
C &= C_{DL}^1 / C_{DL}^0 \\
\phi_s &\to \frac{C_{DL}^0 \phi_s}{f} \\
\varepsilon &= \frac{w_{max}}{2 k_B T} \\
x_0 &\to 2\pi x_0 / L
\end{aligned}$$

are introduced. Again, slight differences in the definitions accounting for different boundary conditions are included with the use of c_x.

With the values given in table A.2 the parameters p, ν, C, ϕ_s and q are fixed to $\nu = 0.025$, $p = 0.5$, $C = 0.1$, $\phi_s = 0.2$ and $q = -2.4$.[1]

ν is defined slightly different in section 4.2.2: $\nu = \frac{R C_{DL}^0}{2N_{max} k_B \alpha f n F}$.

[1] Note that the values of ν and g were given as $\nu = 2$ and $g = -4$ in previous papers [46, 85], but the above values fit the physical situation better.

A.1.3 HN-NDR Model

Eqs. (6.14)-(6.17) are obtained from the reduced four variable model via the transformations

$$\begin{aligned}
\phi_{\mathrm{DL}} \to \phi'_{\mathrm{DL}} &= |a_{Cl}|\phi_{\mathrm{DL}} \\
c \to c' &= c/c_{Cu}^{b} \\
t \to t' &= 2D_{Cu}\delta_{Cu}^{-2}t \\
x \to x' &= (2\pi L)^{-1}x \\
z \to z' &= z/w.
\end{aligned}$$

All voltages are rescaled accordingly. Primes are omitted in Eqs. (6.14)-(6.17) for clarity.

The new parameters used are composed of the old one as follows (again primes where omitted at the obvious places)

$$\begin{aligned}
\nu &= 2N(\delta_{Cu}c_{Cu}^{b})^{-1} \\
\tau_{Cl} &= 2D_{Cu}Ne^{-a_{Cl}\phi_{\mathrm{DL}}^{Cl,0}}(\delta_{Cu}^{2}c_{Cl}^{b}k_{Cl}^{a})^{-1} \\
\tau_{Cu} &= 2D_{Cu}Ne^{-a_{Cu}\phi_{\mathrm{DL}}^{Cu,0}}(\delta_{Cu}^{2}c_{Cu}^{b}k_{Cu}^{a})^{-1} \\
p_x &= k_x^{d}e^{-2a_x\phi_{\mathrm{DL}}^{x,0}}(k_x^{a}c_x^{b})^{-1} \\
\sigma \to \sigma' &= \frac{\sigma\delta_{Cu}^{2}}{LC_{DL}D_{Cu}(1+\rho)} \\
\beta &= 2\pi L w^{-1} \\
a_x \to a'_x &= a_x/a_{Cl}
\end{aligned}$$

Parameter values as obtained from the constants and parameters from Tables 6.1 and 6.2 are given in Table 6.3.

A.2 The Jacobian in Pseudo Spectral Space - An Explicit Example

As an illustration of the pseudo spectral method introduced in section 2.6.1 the Jacobian in Fourier space for the S-NDR system presented in section 4.1, Eqs. (4.5),(4.6) will be computed explicitly. Periodic boundary conditions will be imposed on the space interval $[0, 2\pi]$, thus N Fourier modes are used to expand θ (no expansion is needed for ϕ_{DL} since it does not depend on space in this approximation). The modes and variables are arranged in the following form into a set of odes

vector		mode	symbol
u(1)	$\hat{=}$	homogenous mode of θ	$u_{\theta_{\text{hom}}}$
u(2)	$\hat{=}$	cos 1 – mode of θ	$u_{\theta_{\text{cos1}}}$
u(3)	$\hat{=}$	cos 2 – mode of θ	$u_{\theta_{\text{cos2}}}$
⋮		⋮	⋮
u(N+1)	$\hat{=}$	cos N – mode of θ	$u_{\theta_{\text{cosN}}}$
u(N+2)	$\hat{=}$	sin 1 – mode of θ	$u_{\theta_{\text{sin1}}}$
u(N+3)	$\hat{=}$	sin 2 – mode of θ	$u_{\theta_{\text{sin2}}}$
⋮		⋮	
u(2N+1)	$\hat{=}$	sin N – mode of θ	$u_{\theta_{\text{sinN}}}$
u(2N+2)	$\hat{=}$	double layer potential ϕ_{DL}	$u_{\phi_{\text{DL}}}$

According to section 2.6.1 the Jacobian of the system can be written in the following form

$$
\begin{aligned}
J &= \frac{\partial \dot{\boldsymbol{u}}}{\partial \boldsymbol{u}} \\
&= \begin{pmatrix}
\frac{\partial \dot{u}_{\theta_{\text{hom}}}}{\partial u_{\theta_{\text{hom}}}} & \frac{\partial \dot{u}_{\theta_{\text{hom}}}}{\partial u_{\theta_{\text{cos1}}}} & \cdots & \frac{\partial \dot{u}_{\theta_{\text{hom}}}}{\partial u_{\theta_{\text{cosN}}}} & \frac{\partial \dot{u}_{\theta_{\text{hom}}}}{\partial u_{\theta_{\text{sin1}}}} & \cdots & \frac{\partial \dot{u}_{\theta_{\text{hom}}}}{\partial u_{\theta_{\text{sinN}}}} & \frac{\partial \dot{u}_{\theta_{\text{hom}}}}{\partial u_{\phi_{\text{DL}}}} \\
\frac{\partial \dot{u}_{\theta_{\text{cos1}}}}{\partial u_{\theta_{\text{hom}}}} & \cdots & & & & & & \\
\vdots & & & & & & & \vdots \\
\frac{\partial \dot{u}_{\theta_{\text{cosN}}}}{\partial u_{\theta_{\text{hom}}}} & \cdots & & & & & & \\
\frac{\partial \dot{u}_{\theta_{\text{sin1}}}}{\partial u_{\theta_{\text{hom}}}} & \cdots & & & & & & \\
\vdots & & & & & & & \vdots \\
\frac{\partial \dot{u}_{\theta_{\text{sinN}}}}{\partial u_{\theta_{\text{hom}}}} & \cdots & & & & & & \\
\frac{\partial \dot{u}_{\phi_{\text{DL}}}}{\partial u_{\theta_{\text{hom}}}} & \cdots & & & & & \frac{\partial \dot{u}_{\phi_{\text{DL}}}}{\partial u_{\theta_{\text{sinN}}}} & \frac{\partial \dot{u}_{\phi_{\text{DL}}}}{\partial u_{\phi_{\text{DL}}}}
\end{pmatrix} \\
&= -\boldsymbol{\lambda} + \frac{\partial \boldsymbol{f}}{\partial \boldsymbol{a}}
\end{aligned}
$$

with

$$\frac{\partial \boldsymbol{f}}{\partial \boldsymbol{a}} = \begin{pmatrix} \mathrm{dft}\left(\left.\frac{\partial f}{\partial \theta}\right|_{x_1}, \ldots, \left.\frac{\partial f}{\partial \theta}\right|_{x_N}\right) & \mathrm{dft}\left(\cos 1x_1 \left.\frac{\partial f}{\partial \theta}\right|_{x_1}, \ldots, \cos 1x_N \left.\frac{\partial f}{\partial \theta}\right|_{x_N}\right) & \cdots & \mathrm{dft}\left(\cos Nx_1 \left.\frac{\partial f}{\partial \theta}\right|_{x_1}, \ldots, \cos Nx_N \left.\frac{\partial f}{\partial \theta}\right|_{x_N}\right) & \mathrm{dft}\left(\sin 1x_1 \left.\frac{\partial f}{\partial \theta}\right|_{x_1}, \ldots, \sin 1x_N \left.\frac{\partial f}{\partial \theta}\right|_{x_N}\right) & \cdots & \mathrm{dft}\left(\sin Nx_1 \left.\frac{\partial f}{\partial \theta}\right|_{x_1}, \ldots, \sin Nx_N \left.\frac{\partial f}{\partial \theta}\right|_{x_N}\right) & \mathrm{dft}\left(\left.\frac{\partial f}{\partial \phi_{\mathrm{DL}}}\right|_{x_1}, \ldots, \left.\frac{\partial f}{\partial \phi_{\mathrm{DL}}}\right|_{x_N}\right) \\ \frac{\partial g}{\partial \theta} & 0 & \cdots & 0 & 0 & \cdots & 0 & \frac{\partial g}{\partial \phi_{\mathrm{DL}}} \end{pmatrix}.$$

dft() denotes the discrete Fourier transform of the enclosed series (homogenous mode coefficients in the first row, coefficients of the cosine modes in the following N rows and the sine coefficients last (consistent with the ordering in the columns)). Finally it follows that

$$J = \begin{pmatrix} \frac{\partial f_1}{\partial a_1} & \frac{\partial f_1}{\partial a_2} & \cdots & & & & \frac{\partial f_1}{\partial a_{2N+2}} \\ \frac{\partial f_2}{\partial a_1} & \frac{\partial f_2}{\partial a_2} - 1^2 & \frac{\partial f_2}{\partial a_3} & \cdots & & & \\ \vdots & & \ddots & & & & \vdots \\ \cdots & & \frac{\partial f_{N+1}}{\partial a_{N+1}} - N^2 & \cdots & & & \\ \cdots & & & \frac{\partial f_{N+2}}{\partial a_{N+2}} - 1^2 & \cdots & & \\ \vdots & & & & \ddots & & \vdots \\ \cdots & & & & & \frac{\partial f_{2N+1}}{\partial a_{2N+1}} - N^2 & \cdots \\ \frac{\partial g}{\partial \theta} & 0 & \cdots & 0 & 0 & \cdots 0 & \frac{\partial g}{\partial \phi_{\mathrm{DL}}} \end{pmatrix}$$

The last line originates from the somewhat degenerated case of the variable ϕ_{DL} which has no spatial dependence and thus, the discrete Fourier transform yields the above ex-

pressions for the last line

$$\begin{aligned}
\frac{\partial \dot{u_{\phi_{\mathrm{DL}}}}}{\partial u_{\theta_{\mathrm{hom}}}} &= \frac{1}{M}\sum_{i=1}^{M}\frac{\partial g}{\partial \theta}\Big|_{x_i} \\
&= \frac{\partial g}{\partial \theta} \\
\frac{\partial \dot{u_{\phi_{\mathrm{DL}}}}}{\partial u_{\theta_{\cos m}}} &= \frac{1}{N}\sum_{i=1}^{M}\cos\left(m x_i \frac{\partial g}{\partial \theta}\Big|_{x_i}\right) \\
&= \frac{\partial g}{\partial \theta}\frac{1}{M}\sum_{i=1}^{M}\cos\left(m(i-1)\frac{2\pi}{M}\right) \\
&= 0
\end{aligned}$$

which also holds for the sine modes. The last step originates from the spatial periodicity of the Fourier basis functions. But is it intuitively clear that a derivation of a spatially homogenous variable with respect to a spatially inhomogeneous mode should yield 0.

List of Abbreviations

h	Hopf bifurcation of the homogeneous steady state
sn	saddle-node bifurcation
pf	pitchfork bifurcation
d	domain bifurcation of the homogeneous steady state
sn-d	saddle-node bifurcation of domains
hd	Hopf bifurcation of the domain state
snp	saddle-node bifurcation of periodic orbits
DH	domain-Hopf codimension-two point (d and h)
TB	Takens-Bogdanov codimension-two point
DHD	degenerate Hopf bifurcation
NDR	negative differential resistance
NGC	negative global coupling
N-NDR	‘N-type’ NDR
HN-NDR	hidden NDR of the ‘N-type’
S-NDR	‘S-type’ NDR
WE	working electrode
CE	counter electrode
RE	reference electrode
PZC	point of zero charge
NHE	normal hydrogen electrode
RHE	reversible hydrogen electrode
upd	under potential deposition
HOR	hydrogen oxidation reaction
HER	hydrogen evolution reaction
ODE	ordinary differential equation
PDE	partial differential equation
HHED	heterostructure hot electron diode

BZ	Belousov-Zhabotinsky
MO	modulated oscillation
TP	target pattern
A-TP	asymmetric target pattern
CP	cluster pattern

Bibliography

[1] E. Schr¨odinger. *What is Life?* Cambridge University Press (1948).

[2] H. Haken. *Synergetics*. Springer, Berlin (1977).

[3] G. Nicolis and I. Prigogine. *Self-organization in Nonequilibrium Systems*. Wiley, New York (1977).

[4] Y. Kuramoto. *Chemical Oscillations, Waves and Turbulence*, vol. 19 of *Springer Series in Synergetics*. Springer, Berlin (1984).

[5] M. C. Cross and P. C. Hohenberg. Pattern formation outside of equilibrium. *Rev. Mod. Phys.* 65 (1993) 851.

[6] G. Nicolis. *Introduction to Nonlinear Science*. Cambridge University Press, Cambridge (1995).

[7] J. D. Murray. *Mathematical Biology*, vol. 19 of *Biomathematics*. Springer, Berlin (1989).

[8] A. S. Mikhailov. *Foundations of Synergetics I*, vol. 51 of *Springer Series in Synergetics*. Springer, Berlin (1990).

[9] H. Poincaré. *Les méthodes nouvelles de la méchanique celeste*, vol. 1. Gauthier-Villars, Paris (1890,1893,1899).

[10] E. N. Lorenz. Deterministic nonperiodic flow. *J. Atmos. Sci.* 20 (1963) 130.

[11] H. G. Schuster. *Deterministic Chaos*. Physik Verlag, Weinheim (1984).

[12] R. Kapral and K. Showalter. *Chemical Waves and Patterns*. Kluwer Academic Publishers, Dordrecht (1995).

[13] R. Imbihl and G. Ertl. Oscillatory kinetics in heterogeneous catalysis. *Chem. Rev.* 95 (1995) 697.

[14] A. T. Winfree. Sudden cardiac death: A problem in topology. *Sci. Americ.* 248 (1983) 118.

[15] E. Sch¨oll. *Nonlinear Spatio-Temporal Dynamics and Chaos in Semiconductors*, vol. 10 of *Cambridge Nonlinear Science Series*. Cambridge University Press, Cambridge (2001).

[16] A. M. Turing. The chemical basis of morphogenesis. *Philos. Trans. R. Soc. London Ser. B* 237 (1952) 37.

[17] G. T. Fechner. Über Umkehrungen der Polarit¨at in der einfachen Kette. *Schweigg J. für Chemie und Physik* 53 (1828) 129.

[18] H. L. Heathcoat. Vorl¨aufiger Bericht ¨uber Passivierung, Passivit¨at und Aktivierung des Eisens. *Z. Phys. Chem.* 37 (1901) 368.

[19] R. S. Lillie. Transmission of activation in passive metals as a model of the protoplasmatic or nervous type of transmission. *Science* 48 (1918) 51.

[20] A. L. Hodgkin and A. F. Huxley. A quantitative description of membrane current and its application to conduction and excitation of nerve. *J. Physiol.* 117 (1952) 500.

[21] R. FitzHugh. Impulses and physiological states in theoretical models of nerve membrane. *Biophys. J.* 1 (1961) 445.

[22] J. Wojtowicz. Oscillatory behavior in electrochemical systems. In J. O. Bockris and B. E. Conway, editors, *Modern Aspects of Electrochemistry*, vol. 8. Butterworths, London (1973), 47.

[23] J. L. Hudson and T. T. Tsotsis. Electrochemical reaction dynamics: A review. *Chem. Eng. Sci.* 49 (1994) 1493.

[24] M. T. M. Koper. The theory of electrochemical instabilities. *Electrochim. Acta* 37 (1992) 1771.

[25] M. T. M. Koper. Oscillations and complex dynamical bifurcations. In I. Prigogine and S. A. Rice, editors, *Advances in Chemical Physics*, vol. 92. Wiley, New York (1996), 161.

[26] K. Krischer. Nonlinear dynamics in electrochemical systems. In R. C. Alkire and D. M. Kolb, editors, *Advances in Electrochemical Science and Engineering*. Wiley-VCH (2003), 89.

[27] M. T. M. Koper. Stability study and categorization of electrochemical oscillators by impedance spectroscopy. *J. Electroanal. Chem.* 409 (1996) 175.

[28] O. Lev, M. Sheintuch, L. M. Pismen, and C. Yarnitzky. Standing and propagating wave oscillations in the anodic dissolution of nickel. *Nature* 336 (1988) 458.

[29] G. Fl¨atgen, K. Krischer, B. Pettinger, K. Dobelhofer, H. Junkes, and G. Ertl. 2d-imaging of potential waves in electrochemical systems by means of surface-plasmon microscopy. *Science* 269 (1995) 668.

[30] G. Fl¨atgen, K. Krischer, and G. Ertl. Investigation of front propagation in an electrochemical system: Experiments and numerical simulations. *Z. Naturforsch.* 50a (1995) 1097.

[31] G. Fl¨atgen and K. Krischer. Accelerating fronts in an electrochemical system due to global coupling. *Phys. Rev. E* 51 (1995) 3997.

[32] Z. Fei, R. G. Kelly, and J. L. Hudson. Spatiotemporal patterns on electrode arrays. *J. Phys. Chem* 100 (1996) 18986.

[33] G. Fl¨atgen and K. Krischer. A general model for pattern formation in electrode reactions. *J. Chem. Phys.* 103 (1995) 5428.

[34] M. T. M. Koper and J. H. Sluyters. A simplified approach to the modeling of wave propagation at electrode/electrolyte interfaces. *Electrochim. Acta* 38 (1993) 1535.

[35] D. Haim, O. Lev, L. M. Pismen, and M. Sheintuch. Modelling periodic and chaotic dynamics in anodic nickel dissolution. *J. Phys. Chem.* 96 (1992) 2676.

[36] J. Christoph, R. D. Otterstedt, M. Eiswirth, N. I. Jaeger, and J. L. Hudson. Negative coupling during oscillatory pattern formation on a ring electrode. *J. Chem. Phys.* 110 (1999) 8614.

[37] A. Birzu, B. J. Green, R. D. Otterstedt, N. I. Jaeger, and J. L. Hudson. Modelling of spatiotemporal patterns during metal electrodissolution in a cell with a point reference electrode. *Phys. Chem. Chem. Phys.* 2 (2000) 2715.

[38] A. Karantonis, L. Bieniasz, and S. Nakabayashi. The combined unidirectional and local coupling in a spatially one–dimensional model of oscillatory metal electrodissolution. Patch-adaptive simulation study. *Phys. Chem. Chem. Phys.* 5 (2003) 1831.

[39] N. Mazouz, K. Krischer, G. Fl¨atgen, and G. Ertl. Synchronization and pattern formation in electrochemical systems: Model calculations. *J. Phys. Chem. B* 101 (1997) 2403.

[40] N. Mazouz, G. Fl¨atgen, and K. Krischer. Tuning the range of coupling in an electrochemical system: From local via nonlocal to global coupling. *Phys. Rev. E* 55 (1997) 2260.

[41] P. Grauel, J. Christoph, G. Fl¨atgen, and K. Krischer. Stationary potential patterns during the reduction of peroxodisulfate at Ag ring electrodes. *J. Phys. Chem. B* 102 (1998) 10264.

[42] N. Mazouz, G. Fl¨atgen, K. Krischer, and I. G. Kevrekidis. The impact of the operation mode on pattern formation in electrode reactions: From potentiostatic to galvanostatic control. *J. Electrochem. Soc.* 145 (1998) 2404.

[43] J. Christoph, P. Strasser, M. Eiswirth, and G. Ertl. Remote triggering of waves in an electrochemical system. *Science* 284 (1999) 291.

[44] I. Z. Kiss, W. Wang, and J. L. Hudson. Experiments on arrays of globally coupled periodic electrochemical oscillators. *J. Phys. Chem. B* 103 (1999) 11433.

[45] P. Strasser, J. Christoph, W.-F. Lin, M. Eiswirth, and J. L. Hudson. Standing wave oscillation in an electrocatalytic reaction. *J. Phys. Chem. A* 104 (2000) 1854.

[46] K. Krischer, N. Mazouz, and G. Fl¨atgen. Pattern formation in globally coupled electrochemical systems with S-shaped current-potential curve. *J. Phys. Chem. B* 104 (2000) 7545.

[47] A. F. Volkov and S. M. Kogan. Physical phenomena in semiconductors with negative differential conductivity. *Usp. Fiz. Nauk* 96 (1968) 633. [Sov. Phys. Usp. **11**, 881 (1969)].

[48] F. G. Bass, V. S. Bochkov, and Y. G. Gurevich. The effect of sample dimension on current voltage characteristic of media with ambigious filed dependence on electron temperature. *Sov. Phys. JETP* 31 (1970) 972. [Zh. Eksp. Teor. Fiz. **58**, 1814 (1970)].

[49] A. Alekseev, S. Bose, P. Rodin, and E. Sch¨oll. Stability of current filaments in a bistable semiconductor system with global coupling. *Phys. Rev. E* 57 (1998) 2640.

[50] M. Meixner, P. Rodin, A. Wacker, and E. Sch¨oll. Lateral current density fronts in globally coupled bistable semiconductors with S- or Z-shaped current voltage characteristics. *Eur. Phys. J. B* 13 (2000) 157.

[51] M. Meixner, P. Rodin, and E. Sch¨oll. Fronts in a bistable medium with two global constraints: Oscillatory instability and large-amplitude limit cycle motion. *Phys. Rev. E* 58 (1998) 5586.

[52] S. Bose, P. Rodin, and E. Sch¨oll. Competing spatial and temporal instabilities in a globally coupled bistable semiconductor system near a codimesion-two bifurcation. *Phys. Rev. E* 62 (2000) 1778.

[53] L. Schimansky-Geier, C. Z¨ulicke, and E. Sch¨oll. Domain formation due to Ostwald ripening in bistable systems far from equilibrium. *Z. Phys. B* 84 (1991) 433.

[54] H. Willebrand, T. H¨unteler, F.-J. Niedernostheide, R. Dohmen, and H.-G. Purwins. Periodic and turbulent behavior of solitary structures in distributed active media. *Phys. Rev. A* 45 (1992) 8766.

[55] V. Barelko, I. I. Kurochka, A. G. Merzhanov, and K. G. Shkadinskii. Investigation of travelling waves on catalytic wires. *Chem. Eng. Sci.* 33 (1977) 805.

[56] S. A. Zhukov and V. V. Barelko. Spatially nonhomogeneous stationary states of a catalyst in oxidation reactions on a platinum filament. *Sov. J. Chem. Phys.* 1982 (1984) 883.

[57] M. D. Graham, S. L. Lane, and D. Luss. Proper orthogonal decomposition analysis of spatiotemporal temperature patterns. *J. Phys. Chem.* 97 (1993) 889.

[58] U. Middya, M. D. Graham, D. Luss, and M. Sheintuch. Pattern selection in controlled reaction-diffusion systems. *J. Chem. Phys.* 98 (1993) 2823.

[59] U. Middya and D. Luss. Impact of global interactions on patterns in a simple system. *J. Chem. Phys.* 100 (1994) 6386.

[60] J. Annamalai, M. A. Liauw, and D. Luss. Temperature patterns on a hollow cylindrical catalytic pellet. *Chaos* 9 (1999) 36.

[61] F. Mertens, R. Imbihl, and A. Mikhailov. Breakdown of global coupling in oscillatory chemical reactions. *J. Chem. Phys.* 99 (1993) 8668.

[62] F. Mertens, R. Imbihl, and A. Mikhailov. Turbulence and standing waves in oscillatory chemical reactions with global coupling. *J. Chem. Phys.* 101 (1994) 9903.

[63] M. Falcke and H. Engel. Influence of global coupling through the gas phase on the dynamics of CO oxidation on Pt(110). *Phys. Rev. E* 50 (1994) 1353.

[64] K. C. Rose, D. Battogtokh, A. S. Mikhailov, R. Imbihl, W. Engel, and A. M. Bradshaw. Cellular structures in catalytic reactions with global coupling. *Phys. Rev. Lett.* 76 (1996) 3582.

[65] G. Veser, F. Mertens, A. S. Mikhailov, and R. Imbihl. Global coupling in the presence of defects: Synchronization in an oscillatory surface reaction. *Phys. Rev. Lett.* 71 (1993) 935.

[66] M. Falcke and H. Engel. Travelling pulses in anisotropic media with global coupling. *Phys. Rev. E* 56 (1997) 635.

[67] F. J. Elmer. Nonlocal dynamics of domains and domain-walls in dissipative systems. *Phys. Rev. A* 41 (1990) 4174.

[68] K. H. Seung, C. Kurrer, and Y. Kuramoto. Dephasing and bursting in coupled neural oscillators. *Phys. Rev. Lett.* 75 (1995) 3190.

[69] I. Schebesch and H. Engel. Influence of a light-induced global coupling on the dynamics of waves in the Belousov-Zhabotinsky reaction. In H. Engel, F.-J. Niedernostheide, H.-G. Purwins, and E. Sch¨oll, editors, *Self-Organization in Activator-Inhibitor Systems: Semiconductors, Gas-Discharges and Chemical Active Media*. Wissenschaft & Technik-Verlag, Berlin (1996), 120.

[70] D. Battogtokh, M. Hildebrand, K. Krischer, and A. S. Mikhailov. Nucleation kinetics and global coupling in reaction-diffusion systems. *Phys. Rep.* 288 (1997) 435.

[71] D. Lima, D. Battogtokh, A. S. Mikhailov, P. Borckmans, and G. Dewel. Pattern selection in oscillatory media with global coupling. *Europhys. Lett.* 42 (1998) 631.

[72] H. Hempel, I. Schebesch, and L. Schimansky-Geier. Travelling pulses in reaction-diffusion systems under global constraints. *Eur. Phys. J. B* 2 (1998) 399.

[73] Y. Kuramoto. Phase- and center-manifold reductions for large populations of coupled oscillators with application to non-locally coupled systems. *Int. J. Bifurcation Chaos* 7 (1997) 789.

[74] D. Battogtokh and A. S. Mikhailov. Controlling turbulence in the complex Ginzburg-Landay equation. *Physica D* 90 (1996) 84.

[75] D. Battogtokh, A. Preusser, and A. S. Mikhailov. Controlling turbulence in the complex Ginzburg-Landay equation II. Two dimensional systems. *Physica D* 106 (1997) 327.

[76] G. Franceschini, S. Bose, and E. Sch¨oll. Control of chaotic spatio-temporal spiking by time-delay autosynchronisation. *Phys. Rev. E* 60 (1999) 5426.

[77] V. K. Vanag, Y. Lingfa, M. Dolnik, A. M. Zhabotinsky, and I. R. Epstein. Oscillatory cluster patterns in a homogeneous chemical system with global feedback. *Nature* 406 (2000) 389.

[78] M. Bertram and A. S. Mikhailov. Pattern formation in a surface chemical reaction with global delayed feedback. *Phys. Rev. E* 63 (2001) 066102.

[79] M. Kim, M. Bertram, M. Pollmann, A. Oertzen, A. S. Mikhailov, H. H. Rotermund, and G. Ertl. Controlling chemical turbulence by global delayed feedback: Pattern formation in catalytic CO oxidation reaction on Pt(110). *Science* 292 (2001) 1357.

[80] O. Beck, A. Aman, E. Sch¨oll, J. E. S. Socolar, and W. Just. Comparison of time-delayed feedback schemes for spatiotemporal control of chaos in a reaction-diffusion system with global coupling. *Phys. Rev. E* (2002) 016213.

[81] W. Just, H. Benner, and E. Reibold. Theoretical and experimental aspects of chaos control by time delayed feedback. *Chaos* 13 (2003) 259.

[82] S. Bose, A. Wacker, and E. Sch¨oll. Bifurcation scenarios of spatiotemporal spiking in semiconductor-devices. *Phys. Lett. A* 195 (1994) 144.

[83] A. Wacker and E. Sch¨oll. Spiking at vertical electrical-transport in a heterostructure device. *Semicond. Sci. Technol.* 9 (1994) 592.

[84] A. Wacker and E. Sch¨oll. Criteria for stability in bistable electrical devices with S- or Z-shaped current voltage characteristic. *J. Appl. Phys.* 78 (1995) 7352.

[85] N. Mazouz and K. Krischer. A theoretical study on Turing patterns in electrochemical systems. *J. Phys. Chem. B* 104 (2000) 6081.

[86] P. Glendinning. *Stability, Instability and Chaos: An Introduction to the Theory of Nonlinear Differential Equations*. Cambrige University Press (1994).

[87] J. Guckenheimer and P. Holmes. *Nonlinear Oscillations, Dynamical Systems, and Bifurcations of Vector Fields*, vol. 42 of *Applied Mathematical Sciences*. Springer, Berlin (1983).

[88] S. H. Strogatz. *Nonlinear Dynamics and Chaos*. Addison Wesley, Reading (MA) (1994).

[89] A. Bard and L. Faulkner. *Electrochemical Methods*. Wiley & Sons, New York (1980).

[90] W. Schmickler. *Interfacial Electrochemistry*. Oxford University Press, New York (1996).

[91] C. H. Hamann, A. Hamnett, and W. Vielstich. *Electrochemistry*. Wiley/VCH, Weinheim (1998).

[92] J. Newman. *Electrochemical Systems*. Prentice Hall, Englewood Cliffs, second edn. (1991).

[93] K. Krischer. Spontaneous formation of spatiotemporal patterns at the electrode|electrolyte interface. *J. Electroanal. Chem.* 501 (2001) 1.

[94] K. Krischer, N. Mazouz, and P. Grauel. Fronts, waves, and stationary patterns in electrochemical systems. *Angew. Chem.-Int. Ed.* 40 (2001) 851.

[95] K. Krischer. Principles of spatial and temporal pattern formation in electrochemical systems. In B. E. Conway, J. O. Bockris, and R. White, editors, *Modern Aspects of Electrochemistry*, vol. 32. Kluwer Academic/Plenum, New York (1999), 1.

[96] J. Newman. *Advances in Electrochemistry and Electrochemical Engineering*, vol. 5. Interscience, New York (1967). P. 87.

[97] A. Birzu, B. J. Green, N. I. Jaeger, and J. L. Hudson. Spatiotemporal patterns during electrodissolution of a metal ring: Three-dimensional simulations. *J. Electroanal. Chem.* 504 (2001) 126.

[98] A. Birzu, B. J. Green, R. D. Otterstedt, J. L. Hudson, and N. I. Jaeger. Spatiotemporal patterns on a disk electrode: Effects of cell geometry and electrolyte properties. *Z. Phys. Chem.* 216 (2002) 459.

[99] N. I. Jaeger, R. D. Otterstedt, A. Birzu, B. J. Green, and J. L. Hudson. Evolution of spatiotemporal patterns during the electrodissolution of metals: Experiments and simulations. *Chaos* 12 (2002) 231.

[100] A. Birzu, F. Plenge, N. I. Jaeger, J. L. Hudson, and K. Krischer. Complex spatiotemporal antiphase oscillations during electrodissolution of a metal disk electrode: Model calculations. *J. Phys. Chem., in print* .

[101] A. Birzu, F. Plenge, N. I. Jaeger, J. L. Hudson, and K. Krischer. Excitable dynamics during electrodissolution of a metal disk electrode: Model calculations. *submitted to Phys. Chem. Chem. Phys.* .

[102] K. Krischer, H. Varela, A. Birzu, F. Plenge, and A. Bonnefont. Stability of uniform electrode states in the presence of ohmic drop compensation. *Electrochem. Acta, in print* .

[103] J. Christoph and M. Eiswirth. Theory of electrochemical pattern formation. *Chaos* 12 (2002) 215.

[104] J. Christoph. *Musterbildung auf Elektrodenoberflächen*. Ph.D. thesis, FU Berlin (1999). Http://www.diss.fu-berlin.de/2000/11.

[105] G. Fl¨atgen. *Musterbildung in einer elektrokatalytischen Reaktion: Eine Untersuchung mittels Oberflächenplasmonen-Mikroskopie und Potentialsonden sowie Modellbildung und Simulation*. Ph.D. thesis, FU Berlin (1995).

[106] R. Otterstedt, P. J. Plath, N. I. Jaeger, J. C. Sayer, and J. L. Hudson. Accelerating fronts during the electrodissolution of cobalt. *Chem. Eng. Sci.* 51 (1996) 1747.

[107] N. Mazouz. *Fronten, Wellen und stationäre Strukturen in elektrochemischen Systemen*. Ph.D. thesis, FU Berlin (1999).

[108] V. Castets, E. Dulos, J. Boissonade, and P. deKepper. Experimental evidence of a sustained standing Turing-type nonequilibrium chemical pattern. *Phys. Rev. Lett.* 64 (1990) 2953.

[109] I. R. Epstein, I. Lengyel, S. Kadar, M. Kagan, and M. Yokohama. New systems for pattern formation studies. *Physica A* 188 (1992) 26.

[110] Q. Ouyang and H. L. Swinney. Transition from a uniform state to hexagonal and striped Turing patterns. *Nature* 352 (1991) 610.

[111] J. Ross, A. P. Arkin, and S. C. M¨uller. Experimental evidence for Turing structures. *J. Phys. Chem.* 99 (1995) 10417.

[112] Y.-J. Li, J. Oslonovitch, N. Mazouz, F. Plenge, K. Krischer, and G. Ertl. Turing-type patterns on electrode surfaces. *Science* 291 (2001) 2395.

[113] E. M. Nicola, M. Or-Guil, W. Wolf, and M. B¨ar. Drifting pattern domains in a reaction-diffusion system with nonlocal coupling. *Phys. Rev. E* 65 (2002) 055101.

[114] P. Grauel and K. Krischer. Fronts and stationary domains during electrochemical H_2 oxication on Pt: The impact of the position of the reference electrode on the spatiotemporal behaviour. *Phys. Chem. Chem. Phys.* 3 (2001) 2497.

[115] J.-Y. Lee, J. Christoph, P. Strasser, M. Eiswirth, and G. Ertl. Spatio-temporal interfacial potential patterns during the electrocatalyzed oxidation of formic acid on Bi-modified Pt. *J. Chem. Phys.* 115 (2001) 1485.

[116] Y. Kuramoto, H. Nakao, and D. Battogtokh. Multi–scaled turbulence in large populations of oscillators in a diffusive medium. *Physica A* 288 (2000) 244.

[117] M. Stich. *Target patterns and pacemakers in reaction-diffusion systems*. Ph.D. thesis, TU Berlin (2003).

[118] A. M. Zhabotinsky, M. Dolnik, and I. R. Epstein. Pattern formation arising from wave instability in a simple reaction-diffusion system. *J. Chem. Phys.* 103 (1995) 10306.

[119] M. Dolnik, A. M. Zhabotinsky, A. B. Rovinsky, and I. R. Epstein. Spatio-temporal patterns in a reaction-diffusion system with wave instability. *Chem. Eng. Sci.* 55 (2000) 223.

[120] O. Lev, M. Sheintuch, H. Yarnitsky, and L. M. Pismen. Spatial current distribution during nickel anodic dissolution in sulfuric acid. *Chem. Eng. Sci.* 45 (1990) 839.

[121] M. T. M. Koper and J. H. Sluyters. Electrochemical oscillators: Their description through a mathematical model. *J. Electroanal. Chem.* 303 (1991) 73.

[122] Y.-J. Li. *Adsorption processes and spatiotemporal pattern formation during electrochemical reaction on Au(111) film electrodes*. Ph.D. thesis, FU Berlin (2003).

[123] H. Striegler, D. Krznaric, and D. M. Kolb. Two–dimensional condensation of camphor and its derivatives on Au(111) electrodes. *J. Electroanal. Chem.* 532 (2002) 227.

[124] A. Frumkin and A. Gorodetzkaya. Kapillarelektrische Erscheinungen an Amalgamen. *Z. Phys. Chem.* 136 (1926) 451.

[125] M. Thalinger and M. Volmer. Untersuchungen an der Platin-Wasserstoffelektrode. *Zeit. Phys. Chem.* 150 (1930) 401.

[126] G. Horányi and C. Visy. Potential oscillations in the course of galvanostatic oxidation of hydrogen at platinum electrode in the presence of electrosorbing cations. *J. Electroanal. Chem.* 103 (1979) 353.

[127] W. Wolf, M. L¨ubke, M. T. M. Koper, K. Krischer, M. Eiswirth, and G. Ertl. Experimental and theoretical description of potentiostatic current oscillations during H_2 oxidation. *J. Electroanal. Chem.* 399 (1995) 185.

[128] K. Krischer, M. L¨ubke, W. Wolf, M. Eiswirth, and G. Ertl. Chaos and interior crisis in an electrochemical reaction. *Ber. Bunsenges. Phys. Chem.* 95 (1991) 820.

[129] M. Eiswirth, M. L¨ubke, K. Krischer, W. Wolf, J. L. Hudson, and G. Ertl. Structural effects on the dynamics of an electrocatalytic oscillator. *Chem. Phys. Lett.* 192 (1992) 254.

[130] K. Krischer, M. L¨ubke, M. Eiswirth, W. Wolf, J. L. Hudson, and G. Ertl. A hierarchy of transitions to mixed mode oscillations in an electrochemical system. *Physica D* 62 (1993) 123.

[131] W. Wolf. *Ozillatorische Dynamik zweier elektrochemischer Reaktionen*. Ph.D. thesis, Freie Universit¨at Berlin, Berlin, Germany (1994).

[132] H. Varela and K. Krischer. Nonlinear phenomena during electrochemical oxidation of hydrogen on platinum electrodes. *Catal. Today* 70 (2001) 411.

[133] P. Grauel, H. Varela, and K. Krischer. Spatial bifurcations of fixed points and limit cycles during the electrochemical oxidation of H_2 on Pt ring-electrodes. *Faraday Disc.* 120 (2001) 165.

[134] H. Varela. *Nonlinear phenomena during electrochemical oxidation of Hydrogen on platinum electrodes*. Ph.D. thesis, FU Berlin (2003).

[135] K. Krischer, M. L¨ubke, W. Wolf, M. Eiswirth, and G. Ertl. Oscillatory dynamics of the electrochemical oxidation of H_2 in the presence of Cu^{2+}. *Electrochim. Acta* 40 (1995) 69.

[136] W. Wolf, K. Krischer, M. L¨ubke, M. Eiswirth, and G. Ertl. Modeling oscillations in galvanostatic H_2 oxidation at Pt in the presence of metal ions. *J. Electroanal. Chem.* 385 (1995) 85.

[137] G. Horányi and G. Vértes. Study of the adsorption of chloride ions in the course of electrosorption on platinized platinum electrodes. *J. Electroanal. Chem.* 45 (1973) 295.

[138] C. Canuto, M. Y. Hussaini, A. Quarteroni, and T. A. Zang. *Spectral Methods in Fluid Dynamics*. Springer series in computational physics. Springer, Berlin, 3. edn. (1993).

[139] H. S. Brown. *A computer assisted, nonlinear dynamic study of instabilities and pattern formation for interfacial waves*. Ph.D. thesis, Princeton University (1992).

[140] W. H. Press, B. P. Flannery, S. A. Teukolsky, and W. T. Vetterling. *Numerical Recipes*. Cambridge University Press, Cambridge (1989).

[141] A. C. Hindmarsh. ODEPACK, a systematized collection of ODE solvers. In R. S. Stepleman, editor, *Scientific Computing*, vol. 1 of *IMACS Transactions on Scientific Computation*. North-Holland, Amsterdam (1983), 55. Lsode is available from the netlib library http://www.netlib.org/odepack/.

[142] E. J. Doedel and J. P. Kevernez. *AUTO: Software for continuation and bifurcation problems in ordinary differential equations*. Applied mathematics report, California Institut of Technology (1986). AUTO is available from http://indy.cs.concordia.ca/auto/.

[143] M. Kohout, I. Schreiber, and M. Kubíček. A computational tool for nonlinear dynamical and bifurcation analysis of chemical engineering problems. *Comput. Chem. Eng.* 26 (2002) 517.

[144] R. D. Otterstedt, P. J. Plath, N. I. Jaeger, and J. L. Hudson. Rotating waves on disk and ring electrodes. *Faraday Trans.* 92 (1996) 2933.

[145] J.-Y. Lee, J. Christoph, M. Eiswirth, and G. Ertl. Spatiotemporal mixed-mode oscillations on a ring electrode. *Z. Phys. Chem.* 216 (2002) 479.

[146] J.-Y. Lee, J. Christoph, P. Strasser, M. Eiswirth, and G. Ertl. Existence regions of spatiotemporal patterns in the electro-oxidation of formic acid. *Phys. Chem. Chem. Phys.* 5 (2003) 935.

[147] G. Dewel, P. Borckmans, A. DeWit, B. Rudovics, J. J. Perraud, E. Dulos, J. Boissonade, and P. DeKepper. Pattern selection and localized structures in reaction-diffusion systems. *Physica A* 213 (1995) 181.

[148] A. DeWit, D. Lima, G. Dewel, and P. Borckmans. Spatiotemporal dynamics near a codimension-two point. *Phys. Rev. E* 54 (1996) 261.

[149] M. Meixner, A. DeWit, S. Bose, and E. Sch¨oll. Generic spatiotemporal dynamics near codimension-two Turing-Hopf bifurcations. *Phys. Rev. E* 55 (1997) 6690.

[150] J. Boissonade, E. Dulos, and P. DeKepper. Turing patterns: From myth to reality. In R. Kapral and K. Showalter, editors, *Chemical Waves and Patterns*. Kluwer Academic, Dodrecht (1995), 221.

[151] D. P. Valette, W. S. Edwards, and J. P. Gollub. Transition to spatio-temporal chaos via spatially subharmonic oscillations of a periodic front. *Phys. Rev. E* 49 (1994) R4783.

[152] G. Heidemann, M. Bode, and H. G. Purwins. Fronts between Hopf-type and Turing-type domains in a 2-component reaction-diffusion system. *Phys. Lett. A* 177 (1993) 225.

[153] A. Wacker and E. Sch¨oll. Spiking in an activator-inhibitor model for elements with S-shaped negative differential conductivity. *Z. Phys. B* 93 (1994) 431.

[154] E. Sch¨oll. *Nonequilibrium Phase Transitions in Semiconductors*, vol. 35 of *Springer Series in Synergetics*. Springer, Berlin (1987).

[155] B. A. Glavin, V. A. Kochelap, and V. V. Mitin. Patterns in bistable resonant-tunneling structures. *Phys. Rev. B* 56 (1997) 13346.

[156] D. V. Mel'nikov and A. I. Podlivaev. Lateral traveling wave as a type of transient process in a resonant-tunneling structure. *Semiconductors* 32 (1998) 206.

[157] A. V. Gorbatyuk and P. B. Rodin. Effect of distributed-gate control on current filamentation in thyristors. *Solid-State Electron.* 35 (1992) 1359.

[158] B. S. Kerner and V. V. Osipov. *Autosolitons: A new approach to problems of self-organization and turbulence*. Kluwer Academic Publishers, Dordrecht (1994).

[159] E. Sch¨oll and D. Drasdo. Nonlinear dynamics of breathing current filaments in n-GaAs and p-Ge. *Z. Phys. B* 81 (1990) 183.

[160] Y. P. Raizer. *Gas Discharge Physics*. Springer (1997).

[161] F. Plenge, P. Rodin, E. Sch¨oll, and K. Krischer. Breathing current domains in globally coupled electrochemical systems: A comparison with a semiconductor model. *Phys. Rev. E* 64 (2001) 056229.

[162] M. T. M. Koper, T. J. Schmidt, N. M. Marković, and P. N. Ross. Potential oscillations and S-shaped polarization curve in continuous electro-oxidation of CO on platinum single-crystal electrodes. *J. Phys. Chem. B* 105 (2001) 8381.

[163] I. Kevrekides, L. D. Schmidt, and R. Aris. Rate multiplicity and oscillations in single species surface-reactions. *Surf. Sci.* 137 (1984) 151.

[164] A. Mikhailov and G. Ertl. Pattern formation by adsorbates with attractive lateral interactions. *Chem. Phys. Lett.* 238 (1995) 104.

[165] M. Hildebrand, A. S. Mikhailov, and G. Ertl. Nonequilibrium stationary microstructures in surface chemical reactions. *Phys. Rev. E* 58 (1998) 5483.

[166] M. Hildebrand, A. S. Mikhailov, and G. Ertl. Traveling nanoscale structures in reactive adsorbates with attractive lateral interactions. *Phys. Rev. Lett.* 81 (1998) 2602.

[167] M. Hildebrand, M. Kuperman, H. Wio, A. S. Mikhailov, and G. Ertl. Self-organized chemical nanoscale microreactors. *Phys. Rev. Lett.* 83 (1999) 1475.

[168] M. Hildebrand and A. Mikhailov. Mesoscopic modeling in the kinetic theory of adsorbates. *J. Phys. Chem.* 100 (1996) 19089.

[169] M. Hildebrand. *Selbstorganisierte Nanostrukturen in katalytischen Oberflächenreaktionen*. Ph.D. thesis, HU Berlin (1999).

[170] S. Wiggins. *Global Bifurcations and Chaos*, vol. 73 of *Applied Mathematical Sciences*. Springer, Berlin (1988).

[171] Y. A. Kuznetsov. *Elements of Applied Bifurcation Theory*, vol. 112 of *Applied Mathematical Series*. Springer, New York, 2 edn. (1998).

[172] V. Stamenković and N. M. Marković. Oxygen reduction and hydrogen oxidation reactions on Pt(111) and Pt(100) in solutions containing copper ions. *Langmuir* 17 (2001) 2388.

[173] N. Marković and P. N. Ross. Effect of anions on the underpotential deposition of Cu on Pt(111) and Pt(100) surfaces. *Langmuir* 9 (1993) 580.

[174] N. M. Marković, B. N. Grgur, and P. N. Ross. Temperature-dependent hydrogen electrochemistry on platinum low-index single-crystal surfaces in acid solutions. *J. Phys. Chem. B* 101 (1997) 5405.

[175] F. Plenge, H. Varela, M. L¨ubke, and K. Krischer. Quantitative modeling of the oscillatory electrooxidation of hydrogen on Pt in the presence of poisons. *Z. Phys. Chem.* 217 (2003) 365.

[176] Y. Mukouyama, S. Nakanishi, T. Chiba, K. Murakoshi, and Y. Nakato. Mechanisms of two electrochemical oscillations of different types, observed for H_2O_2 reduction on a Pt electrode in the presence of a small amount of halide ions. *J. Phys. Chem. B* 105 (2001) 7246.

[177] J. Barber, S. Morin, and B. E. Conway. Specificity of the kinetics of H_2, evolution to the structure of single-crystal Pt surfaces, and the relation between opd and upd H. *J. Electroanal. Chem.* 446 (1998) 125.

[178] R. Mills and V. M. M. Lobo. *Self-Diffusion in Electrolyte Solutions*. Elsevier, New York (1989). P. 320.

[179] G. Horányi. Recent developments in the application of the radiotracermethod to the investigation of adsorption and electrocatalytic phenomena. *Electrochim. Acta* 25 (1980) 43.

[180] N. M. Marković, H. A. Gasteiger, and P. N. Ross. Copper electrodeposition on Pt(111) in the presence of chloride and (bi)sulfate: Rotating ring-Pt(111) disk electrode studies. *Langmuir* 11 (1995) 4098.

[181] N. M. Marković, H. A. Gasteiger, C. A. Lucas, I. M. Tidswell, and P. N. Ross. The effect of chloride on the underpotential deposition of copper on Pt(111) - AES, LEED, RRDE, and X-ray-scattering studies. *Surf. Sci.* 335 (1995) 91.

[182] S. Nakanishi, Y. Mukouyama, K. Karasumi, A. Imanishi, N. Furuya, and Y. Nakato. Appearance of an oscillation through the autocatalytic mechanism by control of the atomic-level structure of electrode surfaces in electrochemical H_2O_2 reduction at Pt electrodes. *J. Phys. Chem. B* 104 (2000) 4181.

[183] P. Coullet, J. Lega, B. Houchmanzadeh, and J. Lajzerowicz. Breaking chirality in nonequilibrium systems. *Phys. Rev. Lett.* 65 (1990) 1352.

[184] M. Somani, M. A. Liauw, and D. Luss. Evolution and impact of temperature patterns during hydrogen oxidation on a Ni ring. *Chem. Eng. Sci.* 52 (1997) 2331.

[185] M. A. Liauw, J. Ning, and D. Luss. Pattern formation on a nonuniformly active ring. *J. Chem. Phys.* 104 (1996) 5657.

[186] M. Dolnik, A. M. Zhabotinsky, and I. R. Epstein. Modulated and alternating waves in a reaction-diffusion model with wave instability. *J. Chem. Soc.-Faraday Trans.* 92 (1996) 2919.

[187] H. Varela. priv. com.

[188] M. B¨ar, M. Hildebrand, M. Eiswirth, M. Falcke, H. Engel, and M. Neufeld. Chemical turbulence and standing waves in a surface reaction model: The influence of global coupling and wave instabilities. *Chaos* 4 (1994) 499.

[189] V. Hakim and W. J. Rappel. Dynamics of the globally coupled Ginzburg-Landau equation. *Phys. Rev. A* 46 (1992) R7437.

[190] D. Golomb, D. Hansel, B. Shraiman, and H. Sompolinsky. Clustering in globally coupled phase oscillators. *Phys. Rev. A* 45 (1992) 3516.

[191] M. Falcke, H. Engel, and M. Neufeld. Cluster formation, standing waves, and stripe patterns in oscillatory active media with local and global coupling. *Phys. Rev. E* 52 (1995) 763.

[192] M. Falcke and H. Engel. Pattern formation during the CO oxidation on Pt(110) surfaces under global coupling. *J. Chem. Phys.* 101 (1994) 6255.

[193] V. K. Vanag, A. M. Zhabotinsky, and I. R. Epstein. Oscillatory clusters in the periodically illuminated, spatially extented Belousov-Zhabotinsky reaction. *Phys. Rev. Lett.* 86 (2001) 552.

[194] L. Y. Yang, M. Dolnik, A. M. Zhabotinsky, and I. R. Epstein. Oscillatory clusters in a model of the photosensitive Belousov-Zhabotinsky reaction system with global feedback. *Phys. Rev. E* 62 (2000) 6414.

I would like to thank...

Prof. Katharina Krischer for suggesting this work and for her continuing interest and support.

Prof. Gerhard Ertl for giving me the opportunity to prepare this work in an excellent scientific environment.

Prof. Eckehard Sch¨oll and Dr. Pavel Rodin for a fruitful collaboration and helpful discussions.

Hamilton Varela for reading the manuscript and for the opportunity of an outstanding collaboration with experiment.

all members of Katharina Krischers group and the neighboring groups of Prof. Winterlin, Prof. Rotermund and Prof. Mikhailov for making the stay at the Fritz a pleasant experience and for helpful discussions.

the Deutsche Forschungsgemeinschaft for financial support in the framework of the SFB 555 “Complex Nonlinear Processes”.

Publications

Part of this work has been published in

F. Plenge, P. Rodin, E. Sch¨oll, and K. Krischer. Breathing current domains in globally coupled electrochemical systems: A comparison with a semiconductor model. *Phys. Rev. E* 64 (2001) 056229.

F. Plenge, H. Varela, M. L¨ubke, and K. Krischer. Quantitative modeling of the oscillatory electrooxidation of hydrogen on Pt in the presence of poisons. *Z. Phys. Chem.* 217 (2003) 365.

Y.-J. Li, J. Oslonovitch, N. Mazouz, F. Plenge, K. Krischer, and G. Ertl. Turing-type patterns on electrode surfaces. *Science* 291 (2001) 2395.

K. Krischer, H. Varela, A. Birzu, F. Plenge, and A. Bonnefont. Stability of uniform electrode states in the presence of ohmic drop compensation. *Electrochem. Acta, in print.*

Further publications

A. Birzu, F. Plenge, N. I. Jaeger, J. L. Hudson, and K. Krischer. Excitable dynamics during electrodissolution of a metal disk electrode: Model calculations. *submitted to Phys. Chem. Chem. Phys.* .

A. Birzu, F. Plenge, N. I. Jaeger, J. L. Hudson, and K. Krischer. Complex spatiotemporal antiphase oscillations during electrodissolution of a metal disk electrode: Model calculations. *J. Phys. Chem., in print*.

Curriculum Vitae

Personal Details

Florian Moritz Plenge
Waldemarstr. 103
D-10997 Berlin
Germany
Email: Florian.Plenge@gmx.de
Place and date of birth: Berlin, 09/05/74

School Education

1981–1985	Primary school in 82544 Egling
1985–1994	Secondary school in 82538 Geretsried
07/1994	“Abitur”
1990–1991	International School, Atlanta, Georgia, USA

Higher Education

10/94–02/00	Physics student at the Ruprecht-Karls University Heidelberg
07/10/96	“Vordiplom”
02/08/00	“Hauptdiplom”; diploma-thesis at the MPI for nuclear physics, Heidelberg; title: “Design and set up of an experiment to investigate the negative positronium-ion”; thesis advisor: Prof. D. Schwalm
05/00–today	Ph.D. student at the Fritz-Haber-Institute, Berlin; thesis title: “Theory of Electrochemical Pattern Formation under Global Coupling”; thesis advisor: Prof. K. Krischer